Advanced 2D Materials Integrated Optical and Optoelectronic Sensors for Biochemical Sensing

Jiaxing Sun

Supervisor: Dr Xianfeng Chen

School of Science and Technology

Nottingham Trent University

A thesis submitted in partial fulfilment of the requirements of Nottingham Trent University for the degree of Doctor of Philosophy

July 2025

Copyright statement

Declaration

I hereby declare that the work presented in this thesis is the results of my own investigations, except where otherwise stated. All other sources are acknowledged by bibliographic references. This work has not previously been submitted for a degree or other qualification.

Abstract

This thesis presents a systematic investigation on the development of two-dimensional (2D) materials integrated optoelectronic sensors for the advanced biomedical and chemical sensing applications. The major contributions presented in this thesis are summarised as below.

The development of nanotechnologies for the synthesis and characterisation of various 2D materials, including graphene oxide (GO), $Ti_3C_2T_x$ MXene, black phosphorus (BP), orthorhombic molybdenum trioxide (α-MoO_3), $BiTiS_3$, and small gold nanorods (sAuNRs), using a suite of top-down and bottom-up methods. Material properties such as flake thickness, lateral dimension, and surface chemistry were finely tuned to meet the functional demands of different sensing platforms. 2D materials were integrated with optoelectronic devices by the optimised deposition techniques including in-situ layer-by-layer (i-LbL) assembly, PMMA-assisted wet transfer, spin coating, and drop casting.

The functionalised nano-photonic platforms were developed to achieve high-performance for biochemical and biomedical applications. A GO-coated long-period grating (LPG) biosensor enabled label-free quantification of breast cancer cell. The first perovskite/graphene heterostructure-based biosensor was proposed for cytokine detection with an ultrahigh sensitivity achieving attomolar level. A hybrid LPG/FBG grating was designed to detect the haemoglobin. A $Ti_3C_2T_x$ MXene-functionalised fibre-optic Fabry–Perot interferometer was developed to detect heavy metal ions, demonstrating a high sensitivity with a wide detection range. Additionally, a GO-coated fibre probe was constructed for bioimaging detection, exhibiting strong signal amplification and reusability.

Overall, these results establish a modular and adaptable framework for integrating 2D materials with advanced photonic and optoelectronic devices. The findings highlight the synergy between materials design, device engineering, and application-driven biochemical sensing performance, contributing to the next generation of bio-nano-photonic platforms for early diagnostics, environmental monitoring, and bioimaging applications.

Key words: 2D materials, Nanotechnology, Optoelectronic, Fibre gratings, Optical biosensors, Label-free, Biosensing, Chemical sensing, Bioimaging

Acknowledgements

I would like to express my sincere thanks to my supervisor, Dr. Xianfeng Chen, for his continuous support during my research and studies in the UK. He has great passion for scientific work and has guided me patiently from a beginner to an independent researcher. Whenever I faced challenges, he was always willing to discuss problems with me and help find possible solutions. He also gave me the courage to explore new research directions that few had been previously investigated. Besides academic supervision, Dr. Chen also cared about my life and mental health, offering encouragement and support with kindness and warmth. I feel truly lucky to have had him as my supervisor.

I would like to express my sincere gratitude to Prof. Carole Perry, Prof. John Hunt, Dr. Amanda Coutts, and Dr. Lei Xu for their invaluable collaboration and co-supervision throughout my PhD research. I also extend my thanks to SST and MTIF for providing access to state-of-the-art laboratories and equipment, which greatly supported the progress of my research.

I am deeply grateful to Dr. Graham J. Hickman and Dr. Domanic Eberl-Craske for their generous support in training me on the use of AFM, SEM, and TEM. Their guidance greatly improved my research skills and helped me to obtain high-quality images for publication.

In addition, I would like to sincerely thank Prof. Zhipei Sun (Aalto University, Finland), Prof. Jianlong Zhao, Dr. Lin Zhou (SIMIT, Chinese Academy of Sciences), Prof. Xuefeng Yu, and Dr. Jiahong Wang (SIAT, Chinese Academy of Sciences) for hosting and supporting my international visiting research. They generously provided access to advanced laboratory facilities and created a highly collaborative research environment. Their valuable advice and guidance played a crucial role in advancing my research. I am especially grateful for their openness, and for the excellent coordination and assistance throughout the experimental work.

Finally, I would like to thank close friends, Mr. Sangchu Quan, Mr. Yifei Zhang, Mr. Xiaoyi Ding, Mr. Hongxiao Zhang for their invaluable support and encouragement through my PhD journey.

I would like to thank the support from the European Union's Horizon 2020 research and innovation programme under the Marie Skłodowska-Curie grant agreement No 872049.

Table of Contents

List of Figures

List of Tables

List of abbreviations and acronyms

2D	Two-dimensional
AFM	Atomic force microscopy
AFP	Alpha-fetoprotein
ALB	Albumin
APTES	(3-Aminopropyl)triethoxysilane
AuNPs	Gold nanoparticles
AuNRs	Gold nanorods
BN	Boron Nitride
BP	Black phosphorus
CEA	Carcinoembryonic antigen
CNM	Carbon nanomembrane
COVID-19	Coronavirus disease 2019
CRP	C-reactive protein
CTAB	Cetyltrimethylammonium bromide
CVD	Chemical vapor deposition
DI	Deionised
DMEM	Dulbecco's modified eagle's medium
DMF	Dimethylformamide
DOS	Density of states
EDC	1-Ethyl-3-(3-dimethylaminopropyl)carbodiimide
EDS	Energy Dispersive X-ray Spectroscopy
EIS	Electrochemical impedance spectroscopy
ELISA	Enzyme-linked immunosorbent assay
EV	Extracellular vesicles

FBG	Fibre Bragg grating
FBS	Fetal bovine serum
FET	Field-effect transistor
FFPI	Fibre-optic Fabry-Perot interferometer
FFT	Fast Fourier transform
FIB	Focused ion beam
FP	Fabry-Perot
FPI	Fabry-Perot interferometer
FSR	Free spectral range
FTIR	Fourier transform infrared
FWHM	Full width at half maximum
g-C_3N_4	Graphitic Carbon Nitride
GO	Graphene oxide
GPC1	Glypican-1
Hb	Haemoglobin
h-BN	Hexagonal Boron Nitride
HRI	High refractive index
HR-TEM	High-resolution transmission electron microscopy
IARC	International agency for research on cancer
IgG	Immunoglobulin G
IL6	Interleukin 6
i-LbL	In situ layer-by-layer
LOD	Limit of detection
LPG	Long-period grating
LSPR	Localised surface plasmon resonance
MILD	Minimally intensive layer delamination
MOS	Metal Oxide Semiconductor

NA	Neutravidin
NaOL	Sodium Oleate
NHS	N-Hydroxysuccinimide
NIR	Near Infrared
NMP	N-methyl-pyrrolidone
OFG	Oxygen-containing functional group
OSA	optical spectrum analyser
PBS	Phosphate-buffered saline
PC	Polarisation controller
PDAC	Pancreatic ductal adenocarcinoma
PMMA	Polymethyl methacrylate
POCT	Point-f-care testing
PQD	Perovskite quantum dot
PTT	Photothermal therapy
PVC	Polyvinyl chloride
PVD	Physical vapor deposition
RI	Refractive index
RIU	Refractive index unit
RMS	Root-mean-square
RPM	Revolutions per minute
SAED	Selected area electron diffraction
SEM	Scanning electron microscopy
SERS	Surface-enhanced Raman scattering
SLG	Single layer graphene
SMF	Single-mode fibre
SPR	Surface plasmon resonance
SRI	Surrounding refractive index

TBAB	Tetrabutylammonium bromide
TE	Transverse Electric
TEM	Transmission electron microscopy
TFG	Tilted fibre grating
TIR	Total internal reflection
TM	Transverse Magnetic
TMD	Transitional metal dichalcogenide
TRI	Transition refractive index
UV	Ultraviolet
vdW	van der Waals
VIS	Visible
WHO	World health organization
XPS	X-ray Photoelectron Spectroscopy
XRD	X-ray Diffraction

List of symbols

α_c	Critical angle
β	Propagation constant
ε	Medium permittivity
ε_r	Relative permittivity
ε_0	Vacuum permittivity
θ	Angle
κ	“ac” coupling coefficient
λ	Wavelength
Λ	Grating period
μ	Medium permeability
μ_r	Relative permeability
μ_0	Vacuum permeability
ν	Fringe visibility of the index change
ρ	Charge density
σ	“dc” coupling coefficient
ω	Angular frequency
A_{1g}	Non-degenerate total-symmetric vibration
c	Speed of light in vacuum
d	Distance
E_g	Doubly-degenerate symmetric vibrational
F	Finesse coefficient
$\mathcal{F}$	Finesse
I	Irradiance
I_{ds}	Drain-source current
I_{ph}	Photocurrent

k	Wave number
K_d	Dissociation constant
L	Length
m	Diffraction order
n	Refractive index or Hill coefficient
n_{eff}	Effective refractive index
$P6_3/mmc$	Hermann-Mauguin notation for the hexagonal space group 194
r	Reflection coefficient
R	Reflectance
sp^2	Trigonal planar hybridisation (one s + two p orbitals)
sp^3	Tetrahedral hybridisation (one s + three p orbitals)
V_{ds}	Drain-source voltage
$\vec{\mathbf{E}}$	Electric field
$\vec{\mathbf{H}}$	Magnetic field
$\vec{J}$	Current density
$\vec{K}$	Wave vector

Chapter 1 Introduction

1.1. Background and motivation

Two-dimensional (2D) materials, characterised by their atomic-scale thickness, high surface-to-volume ratio, and tuneable electronic and optical properties, have emerged as versatile candidates for a wide range of advanced applications. Their unique properties enable them to host surface functional groups and interact strongly with external analytes, making them highly attractive for chemical and biochemical sensing applications. Over the past two decades, 2D materials such as graphene, graphene oxide (GO), MXenes, black phosphorus (BP), transition metal dichalcogenides (TMDs), gold nanoparticles (AuNPs), and gold nanorods (AuNRs) have been into sensing schemes [1–7]. Meanwhile, optoelectronic devices offer an excellent platform for high-performance sensing applications, such as optical fibre technologies, field-effect transistor (FET) sensors [8], surface plasmon resonance (SPR) [9], surface-enhanced Raman scattering (SERS) [10], and electrochemical impedance spectroscopy (EIS) [11], etc. Notably, the sensing performances have been greatly enhanced by the integration of 2D materials due to their capabilities of surface functionality improvement, signal amplification, and analyte recognition. In particular, optical fibre technologies have emerged as a powerful subclass of optical sensors, revolutionising fields ranging from telecommunications to environmental and biomedical monitoring due to their inherent advantages, including compact size, high sensitivity, resistance to electromagnetic interference, real-time, and cost-effectiveness [12–15]. Various configurations, such as long-period gratings (LPGs) [16], tilted fibre gratings (TFGs) [3], and fibre-optic Fabry-Perot interferometers (FFPIs) [17], have been developed and integrated with 2D materials to enable applications in refractive index (RI) sensing, chemical sensing, biosensing, and biomedical imaging. 2D materials have shown great potential for enhancing sensitivity, improving selectivity, and enabling more efficient signal transduction. However, the practical integration of 2D materials with optoelectronic devices remains a challenge due to their ultrathin, fragile nature and the difficulty in achieving uniform, stable, and functional coatings across different device geometries.

1.2. State-of-the-art and challenges

While numerous 2D material-based sensors have been proposed, several key technical bottlenecks hinder their reproducibility, robustness, and practical deployment. Firstly, one of the key bottlenecks lies in the rational control of critical material parameters, despite the availability of various synthesis methods. although a variety of synthesis techniques have been developed, including top-down approaches such as sonication-assisted exfoliation, electrochemical exfoliation, and selective etching, as well as bottom-up methods such as chemical vapor deposition (CVD), hydrothermal synthesis, and seed-mediated growth, these synthesis techniques enable the preparation of 2D materials with tuneable properties including lateral size, thickness, and surface chemistry. Nevertheless, achieving precise and application-specific control over parameters such as flake thickness, lateral dimensions, and crystallographic phase remains challenging. These properties often need to be optimised to ensure strong and reliable interactions with device structures, including fibre gratings, interferometers, and transistor channels, where material integration and interface quality are crucial. To address this bottleneck, synthesis strategies with a focus on practical device compatibility were systematically explored to ensure effective integration and optimal sensing performance. Secondly, the integration of 2D materials onto optical fibre and optoelectronic devices presents the distinct challenges in coating uniformity, adhesion, and functional stability. Conventional methods, such as drop-casting or spin-coating, often lead to poor repeatability and incomplete surface coverage, especially for the cylindrical or curved devices (i.e., optical fibre). While wet transfer is commonly used for placing nanosheets onto planar substrates (e.g., FETs) [6], it is not always suitable for fibre devices with cylindrical geometries. An in situ layer-by-layer (i-LbL) assembly has been proposed for achieving uniform coatings with controlled thickness [1], However, its systematic evaluation across different devices and materials is underexplored. Finally, although significant progress has been made in integrating 2D materials with various optoelectronic sensor devices, a more complete understanding of how material characteristics interface with specific device architectures is still evolving. It is well known that the light-matter interaction could be influenced by the parameters such as 2D materials' coating thickness, surface roughness, and crystallinity, but their role remains underexplored in many integrated photonic systems.

1.3. Research objectives and achievements

The thesis aims to develop next generation photonic-nano-bio platform for biochemical sensing and biomedical imaging applications. The research objectives include: 1) to develop versatile fibre-optic and optoelectronic architectures; 2) to develop nanotechnologies for 2D materials' synthesis, integration and characterisation; 3) to implement the ultrasensitive, real-time, label-free biosensing and biomedical imaging applications.

In this investigation, significant progresses have been achieved across device fabrication, nanomaterial synthesis and integration, and biochemical and bioimaging applications. The fibre optic and optoelectronic devices including LPG, FPI, LPG/FBG hybrid sensors, TFG/TFG interferometers, and photonic filter functionalised-FET have been developed for ultrasensitive, label-free detection of cytokines, cancer cells, haemoglobin, and heavy metal ions, forming the basis for diverse biomedical and chemical sensing. A variety of 2D materials, including GO, $Ti_3C_2T_x$ MXene, BP, α-MoO_3, $BiTiS_3$, and sAuNRs were successfully synthesised using the developed top-down and bottom-up methods. 2D materials have been successfully deposited on both planar and fibre-based devices by the developed deposition techniques, including in-situ layer-by-layer assembly, wet transfer, spin coating, and drop casting.

The 2D materials-functionalised devices have been implemented in a series of biochemical sensing and bioimaging applications. The first perovskite quantum dots (PQDs)/single layer graphene (SLG) heterostructure FET biosensor enabled highly sensitive cytokine detection. A GO-coated LPG sensor allowed label-free detection of breast cancer cell density. The MXene-assisted FFPI sensor achieved rapid and broad-range mercury ion detection. A GO-coated fibre optic probe was developed for reusable fluorescence bioimaging. Additionally, an LPG-FBG hybrid sensor enabled label-free haemoglobin detection. These developments demonstrate the versatility of 2D material-assisted platforms for advanced biochemical sensing.

1.4. Thesis structure

This thesis is organised into seven chapters, covering the theoretical foundation, 2D materials development, device integration, and applications of biomedical and chemical sensing.

Chapter 1 introduces the background and motivation of this research, followed by a discussion of the key challenges and research gaps. It concludes with a statement of the research objectives and a summary of the main achievements.

Chapter 2 presents the theoretical framework for light propagation and mode coupling in optical fibre gratings. It starts from Maxwell's equations and proceeds to establish the coupled-mode theory and corresponding phase-matching conditions covering fibre Bragg gratings (FBGs), long-period gratings (LPGs), and tilted fibre gratings (TFGs). In addition, the principles underlying Fabry–Perot interferometers (FPIs) are introduced.

Chapter 3 provides an overview of the 2D materials used in this work, including their structures, physical and chemical properties, and relevant applications. Various synthesis strategies are discussed, encompassing both top-down and bottom-up approaches such as sonication-assisted exfoliation, electrochemical exfoliation, selective etching, and one-pot seedless synthesis. The chapter then presents the synthesis of various 2D materials such as BP, $BiTiS_3$, α-MoO_3, GO, $Ti_3C_2T_x$, and sAuNRs, where the surface morphologies and structural composition are characterised using SEM, EDS, TEM, AFM, XRD, UV-Vis-NIR spectroscopy, Raman spectroscopy, etc.

Chapter 4 focuses on the 2D materials deposition and integration with fibre optic and optoelectronic devices. Several deposition techniques are reviewed, including wet transfer, dry transfer, spin coating, drop casting, and dip coating. In particular, an in-situ layer-by-layer (i-LbL) method is employed for achieving uniform and controllable coatings on cylindrical optical fibres. Subsequently, the morphology, thickness, and uniformity of the nano-coatings are comprehensively characterised using SEM, AFM, EDS, XPS, and Raman spectroscopy.

Chapter 5 demonstrates the label-free biosensing applications: a GO-LPG biosensor for label-free quantification of breast cancer cells; the first PQDs/SLG-based FET biosensor for highly sensitive IL-6 cytokine detection; and an LPG-FBG hybrid sensor for human haemoglobin monitoring.

Chapter 6 shows two functionalised fibre-optic probes: a MXene-assisted FFPI for heavy metal ion detection, and a GO-coated fibre probe for fluorescence-based bioimaging application.

Chapter 7 concludes the thesis by summarising the key findings and proposing future research directions.

Chapter 2 Theory of fibre optics

2.1. Introduction of fibre optic waveguide

Optical fibres are cylindrical dielectric waveguides. A standard single-mode fibre (SMF) consists of a high refractive index core surrounded by a lower refractive index cladding. Light propagation within an optical fibre relies on total internal reflection (TIR) at the interface between the core and the cladding, which confines the light within the core. To describe the propagation of electromagnetic waves in optical fibres, it is necessary to derive the wave equation from Maxwell's equations. For an ideal optical fibre, the medium is considered as non-conductive (i.e., $\rho = 0$, $\vec{J} = 0$), non-magnetic ($\mu = \mu_0$), and with constant permittivity ($\varepsilon = \varepsilon_r \varepsilon_0$). Here, ρ and $\vec{J}$ represent charge density and current density, respectively; μ and μ_0 are the permeabilities of the medium and vacuum, respectively; and ε_r and ε_0 represent the relative permittivities of the medium and the permittivity of vacuum, respectively. Hence, the wave equations for the electric field and magnetic field can be derived as [18]:

$$\nabla^2 \vec{\mathbf{E}} - \frac{n^2}{c^2} \frac{\partial^2 \vec{\mathbf{E}}}{\partial t^2} = 0 \qquad (2.1-1a)$$

$$\nabla^2 \vec{\mathbf{H}} - \frac{n^2}{c^2} \frac{\partial^2 \vec{\mathbf{H}}}{\partial t^2} = 0 \qquad (2.1-1b)$$

where c is the speed of light in vacuum which equals to $\frac{1}{\sqrt{\varepsilon_0 \mu_0}}$, and n is the refractive index (RI), given by $\sqrt{\varepsilon_r}$.

Assuming the time-harmonic solutions, where the field quantities exhibit sinusoidal time dependence at a single angular frequency, the electromagnetic field in complex exponential form are given by:

$$\vec{\mathbf{E}}(\vec{\mathbf{r}}, t) = \vec{\mathbf{E}}(\vec{\mathbf{r}}) e^{i\omega t} \qquad (2.1-2a)$$

$$\vec{\mathbf{H}}(\vec{\mathbf{r}}, t) = \vec{\mathbf{H}}(\vec{\mathbf{r}}) e^{i\omega t} \qquad (2.1-2b)$$

By substituting Eq. 2.1-2 into wave equations of Eq. 2.1-1, the Helmholtz equations can be derived as follows:

$$\nabla^2 \vec{\mathbf{E}} + k^2 n^2 \vec{\mathbf{E}} = 0 \qquad (2.1-3a)$$

$$\nabla^2\vec{\mathbf{H}} + k^2n^2\vec{\mathbf{H}} = 0 \qquad (2.1-3b)$$

where k is the wave number, defined as $\frac{\omega}{c} = \frac{2\pi}{\lambda}$, describing the spatial frequency of the propagating wave in free space, and n represents the refractive index of the medium.

In the context of optical fibre, it is more appropriate to express the wave equations in cylindrical coordinates (r, ϕ, z), which conform to the geometry of a typical step-index fibre. Then the scalar field $U(r, \phi, z)$, representing the electric or magnetic field component, can be separated into radial, azimuthal, and longitudinal components (Fig. 2.1-1). Accordingly, the solution takes the form:

$$U(r, \phi, z) = R(r)e^{il\phi}e^{i\beta z} \qquad (2.1-4)$$

where $R(r)$ is the radial field distribution, l is the azimuthal mode number, and β is the propagation constant along the fibre axis. This separable solution simplifies the analysis of mode propagation within the fibre optical waveguide. By substituting this expression, the Helmholtz equation in cylindrical coordinates can be expressed as [19]:

$$\frac{d^2R}{dr^2} + \frac{1}{r}\frac{dR}{dr} + \left(k^2n^2(r) - \beta^2 - \frac{l^2}{r^2}\right)R = 0 \qquad (2.1-5)$$

This differential equation describes the radial field distribution of guided modes in step-index fibres and serves as the basis for deriving linearly polarized modes under the weakly guiding approximation.

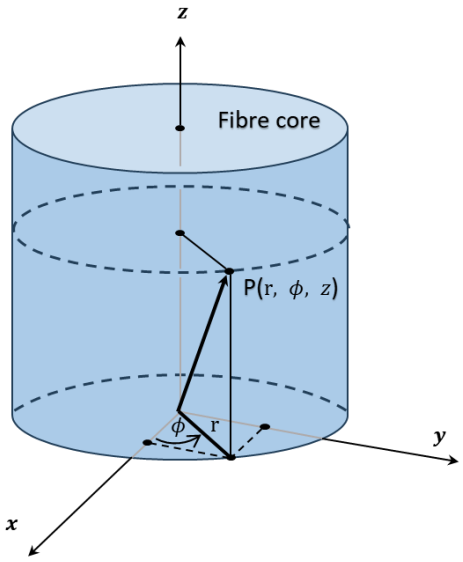

Figure 2.1 - 1 *The geometry of cylindrical coordinates in the fibre core, illustrating the radial r, azimuthal ϕ, and longitudinal z, directions.*

2.2. Coupled-mode theory

Having established the theoretical basis for light propagation in optical fibres through the scalar Helmholtz equation in cylindrical coordinates. Subsequently, the discussion will focus on how periodic perturbations in the refractive index profile result in distributed reflection or mode coupling, thereby giving rise to structures known as fibre gratings. Fibre gratings are structures featuring periodic modulations of the refractive index within the fibre core along the fibre axis, which are capable of altering the propagation characteristics of guided modes through mode coupling mechanisms. Depending on the period and geometric configuration of the fibre grating, distinct mode-coupling phenomena may arise. In general, these include (1) fibre Bragg gratings (FBGs) with core mode backward-propagating; (2) long-period gratings (LPGs) with mode coupling between the core mode and co-propagating cladding modes; and (3) tilted fibre gratings (TFGs), where the mode coupling is influenced by the tilt angles of grating [20,21]. To fully understand these interactions, the framework of coupled-mode theory is introduced, providing a systematic method to describe power transfer between modes in the presence of perturbations.

Coupled-mode theory serves as a fundamental analytical framework for quantitatively assessing the diffraction efficiency and spectral characteristics of fibre gratings. When a grating is inscribed in an optical fibre, it introduces a dielectric perturbation, disrupting the orthogonality condition of fibre modes and consequently enabling energy exchange among the modes. These coupling phenomena play a key role for understanding the fibre grating behaviours. Based on the model introduced by Erdogan [22–24], the coupled-mode theory of fibre gratings will be discussed.

Firstly, an unperturbed optical fibre is considered, which no axial refractive index modulation is present. Under the ideal-mode approximation, the electric field can be expressed as a superposition of orthogonal modes, possessing a well-defined transverse profile and propagation constant. The transverse electric field can be written as:

$$\vec{\mathbf{E}}_t(r,\phi,z,t) = \sum_j \left[A_j(z)e^{i\beta_j z} + B_j(z)e^{-i\beta_j z}\right] \cdot \vec{\boldsymbol{e}}_{jt}(r,\phi)e^{-i\omega t} \qquad (2.2-1)$$

Here, $A_j(z)$ and $B_j(z)$ represent the slowly varying amplitudes of the j th mode propagating in the $+z$ and $-z$ directions, respectively. β is the mode propagation constant. The transverse field distribution $\vec{\boldsymbol{e}}_{jt}(r,\phi)$ defines the spatial mode (bound-core, cladding, or radiation modes) in the radial and azimuthal dimensions. In an ideal waveguide, these

modes are orthogonal without energy exchange. However, this condition is altered when a periodic refractive index modulation is introduced into the fibre optical waveguide, breaking the modal orthogonality and enabling the couplings, such that the forward and backward amplitudes $A_j(z)$ and $B_j(z)$ of the jth mode vary along the z-axis according to:

$$\frac{dA_j}{dz} = i\sum_k A_k(K_{kj}^t + K_{kj}^z)e^{i(\beta_k-\beta_j)z} + i\sum_k B_k(K_{kj}^t - K_{kj}^z)e^{-i(\beta_k+\beta_j)z} \quad (2.2-2)$$

$$\frac{dB_j}{dz} = -i\sum_k A_k(K_{kj}^t - K_{kj}^z)e^{i(\beta_k+\beta_j)z} - i\sum_k B_k(K_{kj}^t + K_{kj}^z)e^{-i(\beta_k-\beta_j)z} \quad (2.2-3)$$

Each of the two equations consists of two summation terms representing the coupling contributions from all other modes k. In Eq. 2.2-2, the first term describes co-propagating coupling between the k and j modes, representing energy transfer between components of forward-propagating modes. The exponential term $e^{i(\beta_k-\beta_j)z}$ indicates the phase difference between the k and j modes. The second term represents counter-propagating coupling, where components of forward-propagating mode j is coupled into the backward mode k, governed by a phase term $e^{-i(\beta_k+\beta_j)z}$. By contrast, Eq. 2.2-3 involves coupling contributions to the mode j, with the first and second terms corresponding to counter-propagating and co-propagating modes, respectively. In Eq. 2.2-2 and Eq. 2.2-3, K_{kj}^t and K_{kj}^z represent the transverse and longitudinal coupling coefficient, respectively. Although K_{kj}^z is analogous to K_{kj}^t, it is generally much smaller than K_{kj}^t for fibre guided modes and therefore normally neglected. Hence, the coupling coefficient is dominated by the transverse coefficient K_{kj}^t:

$$K_{kj}^t(z) = \frac{\omega}{4}\int_0^{2\pi}\int_0^{\infty} \Delta\varepsilon(r,\phi,z)\vec{e}_{kt}(r,\phi)\cdot\vec{e}_{jt}^*(r,\phi)rdrd\phi \quad (2.2-4)$$

where $\vec{e}_{kt}(r,\phi)$ and $\vec{e}_{jt}(r,\phi)$ denote the transverse electric field distributions of k and j modes, respectively. $\Delta\varepsilon(r,\phi,z)$ represents the permittivity perturbation. When $\delta n_{\text{eff}} \ll n_{\text{eff}}$, where δn_{eff} represents the effective refractive index modulation induced by the grating, $\Delta\varepsilon$ can be approximated as:

$$\Delta\varepsilon(r,\phi,z) = 2n_{eff}\overline{\delta n_{eff}}(z)\left\{1 + v\cos\left[\frac{2\pi}{\Lambda}z + \phi(z)\right]\right\} \quad (2.2-5)$$

where n_{eff} is the effective refractive index, and $\overline{\delta n_{eff}}$ denotes the longitudinally averaged change in n_{eff} over a grating period, often referred as "dc" index change, which

defines the slowly varying envelope of the grating. ν is the fringe visibility of the index change. Λ is the grating period. $\phi(z)$ introduces a local phase shift along the propagation axis, describing the grating chirp. In most fibre gratings, the refractive index modulation $\delta n(r, \phi, z)$ is assumed to be radially uniform across the fibre core and negligible in the cladding region. Hence, the core index variation can be described using Eq. 2.2-5 with n_{eff} replaced by n_{co}, and $\overline{\delta n_{eff}}(z)$ replaced by $\overline{\delta n_{co}}(z)$. By substituting the modified expressions into Eq. 2.2-4, the transverse coefficient K_{kj}^{t} can be written as:

$$K_{kj}^{t}(z) = \frac{\omega n_{co}}{2} \cdot \overline{\delta n_{co}}(z) \left\{1 + \nu \cos\left[\frac{2\pi}{\Lambda} z + \phi(z)\right]\right\} \cdot \int_{0}^{2\pi} \int_{0}^{\infty} \vec{e}_{kt}(r, \phi) \cdot \vec{e}_{jt}^{*}(r, \phi) r dr d\phi \qquad (2.2-6)$$

The terms are taken outside the transverse integral since they depend only on the longitudinal coordinate z, and can be treated as constants within the cross section. For simplicity, two coefficients are defined as follows [22]:

$$\sigma_{kj}(z) = \frac{\omega n_{co}}{2} \cdot \overline{\delta n_{co}}(z) \int_{0}^{2\pi} \int_{0}^{\infty} \vec{e}_{kt}(r, \phi) \cdot \vec{e}_{jt}^{*}(r, \phi) r dr d\phi \qquad (2.2-7)$$

$$\kappa_{kj}(z) = \frac{\nu}{2} \sigma_{kj}(z) \qquad (2.2-8)$$

where σ denotes the so-called "dc" coupling coefficient, which represents the average or slowly varying component of the refractive index modulation. In contrast, κ is to the "ac" coupling coefficient, corresponding the periodic variation introduced by the grating structure. Hence, the general coupling coefficient can be expressed as:

$$K_{kj}^{t}(z) = \sigma_{kj}(z) + 2\kappa_{kj}(z) \cos\left[\frac{2\pi}{\Lambda} z + \phi(z)\right] \qquad (2.2-9)$$

Equation 2.2 - 9 shows that the total coupling coefficient consists of a slowly varying 'dc' term and a periodically modulated 'ac' term arising from the grating structure, indicating that the coupling strength varies periodically along the fibre axis.

2.2.1. Backward mode coupling

To derive the simplified coupled-mode equations describing the dominant reflection mechanism in backward mode coupling, one starts from the general coupled-mode equations (Eq. 2.2-2 and Eq. 2.2-3), which govern the evolution of the forward- and backward-propagating mode amplitudes $A_j(z)$ and $B_j(z)$ along the longitudinal axis z.

These equations contain coupling terms between the mode j and all other modes k, each is accompanied by a phase factor of the form $e^{\pm i(\beta_k \pm \beta_j)z}$, which may exhibit rapid oscillations along the propagation direction.

In the case of backward mode coupling, the dominant interaction arises near the wavelength at which a mode of amplitude $A(z)$ is reflected into an identical counter-propagating mode of amplitude $B(z)$. Consequently, only the intra-modal terms with $j = k$ are retained, while intermodal coupling terms with $j \neq k$ are neglected due to their typically weak interaction and phase mismatch. Furthermore, under the synchronous approximation [25], only the terms with slow longitudinal phases are preserved, whereas rapidly oscillating terms are discarded. This approximation is justified by the fact that fast-varying components tend to average out over a grating period, exerting minimal influence on net energy transfer between modes. By applying these assumptions to Eq. 2.2-2 and Eq. 2.2-3, the simplified coupled-mode equations then take the form:

$$\frac{dA}{dz} = iBK_{jj}^{t} e^{-i2\beta z} \qquad (2.2-10)$$

$$\frac{dB}{dz} = iAK_{jj}^{t} e^{+i2\beta z} \qquad (2.2-11)$$

To eliminate the fast-varying phase terms, the slowly varying envelopes are introduced as:

$$R(z) = A(z)e^{i\delta z - i\phi(z)/2} \qquad (2.2-12)$$

$$S(z) = B(z)e^{-i\delta z + i\phi(z)/2} \qquad (2.2-13)$$

where $\delta \equiv \beta - \frac{\pi}{\Lambda} = \beta - \beta_D = 2\pi n_{eff}\left[\frac{1}{\lambda} - \frac{1}{\lambda_D}\right]$ is the detuning parameter, which quantifies the deviation of the operating wavelength from the exact resonance condition, and determines the spectral position of the reflection peak in the grating response. λ_D represents the "design wavelength" for Bragg scattering by an extreme weak grating ($\delta n_{eff} \to 0$), which is defined as $\lambda_D = 2n_{eff}\Lambda$. In this case, the grating induces negligible phase shift and energy exchange, allowing λ_D to represent a purely geometric resonance condition that serves as a reference point, independent of the grating strength. While $\phi(z)$ describes the local phase shift (chirp) of the grating. Substituting Eq. 2.2–12 and Eq. 2.2–13 into Eq. 2.2–10 and Eq. 2.2–11, the resulting equations can be expressed in terms of the slowly varying envelopes, which are given by:

$$\frac{dR}{dz} = i\hat{\sigma}R(z) + i\kappa S(z) \qquad (2.2-14)$$

$$\frac{dS}{dz} = -i\hat{\sigma}S(z) - i\kappa^* R(z) \qquad (2.2-15)$$

where $\hat{\sigma} = \delta + \sigma - \frac{1}{2}\frac{d\phi(z)}{dz}$ is the general "dc" self-coupling coefficient. κ represents the "ac" coupling coefficient from Eq. 2.2-8. These equations describe the evolution of the forward and backward propagating envelopes, incorporating both the amplitude coupling due to the index modulation and the local phase variation of the grating structure.

For a single-mode fibre Bragg grating, the simplified relations can be expressed as follows:

$$\sigma = \frac{2\pi}{\lambda}\overline{\delta n_{eff}} \qquad (2.2-16)$$

$$\kappa = \kappa^* = \frac{\pi}{\lambda}v\overline{\delta n_{eff}} \qquad (2.2-17)$$

If the grating is uniform along the z direction, the effective RI modulation $\overline{\delta n_{eff}}$ remains constant, and the derivative of the phase shift $\frac{d\phi(z)}{dz} = 0$, indicating the absence of grating chirp. Consequently, the "ac" coupling coefficient κ, "dc" coupling coefficient σ, and the general "dc" self-coupling coefficient $\hat{\sigma}$ become constants. This results in the simplification of equations Eq. 2.2-14 and Eq. 2.2-15 into coupled first-order ordinary differential equations with constant coefficients. The closed-form solutions can be obtained by specifying appropriate boundary conditions.

2.2.2. Forward mode coupling

For the forward mode coupling, when a mode "1" with amplitude $A_1(z)$ is strongly coupled to a co-propagating mode "2" with amplitude $A_2(z)$ near a specific wavelength, the coupling equations (Eq. 2.2-2 and Eq. 2.2-3) can be simplified using the synchronous approximation. This approximation retains only the terms that relate to the amplitudes of these two modes, resulting in the coupled-mode equations:

$$\frac{dR}{dz} = i\hat{\sigma}R(z) + i\kappa S(z) \qquad (2.2-18)$$

$$\frac{dS}{dz} = -i\hat{\sigma}S(z) + i\kappa^* R(z) \qquad (2.2-19)$$

where the new amplitudes R and S are defined as:

$$R(z) = A_1(z)e^{-i(\sigma_{11}+\sigma_{22})z/2} \cdot e^{i\delta z-\phi/2} \qquad (2.2-20)$$

$$S(z) = A_2(z)e^{-i(\sigma_{11}+\sigma_{22})z/2} \cdot e^{-i\delta z+\phi/2} \qquad (2.2-21)$$

In the questions above, σ_{11} and σ_{22} represent "dc" coupling coefficients as defined in the previous section (Eq. 2.2-7). The coefficient κ, which satisfies $\kappa = \kappa_{21} = \kappa_{12}^*$, denotes the "ac" cross-coupling coefficient in Eq. 2.2-8. Additionally, $\hat{\sigma}$ serves as a general "dc" self-coupling coefficient, which is now defined as:

$$\hat{\sigma} = \delta + \frac{\sigma_{11}-\sigma_{22}}{2} - \frac{1}{2}\frac{d\phi}{dz} \qquad (2.2-22)$$

The detuning parameter here is assumed to be constant along the z axis, which is given by:

$$\delta = \frac{1}{2}(\beta_1 - \beta_2) - \frac{\pi}{\Lambda} = \pi\Delta n_{eff}\left[\frac{1}{\lambda} - \frac{1}{\lambda_D}\right] \qquad (2.2-23)$$

Similarly, $\lambda_D = \Delta n_{eff}\Lambda$ is the "design wavelength" for an infinitesimally weak grating.

$\hat{\sigma}$ and κ are constants for a uniform forward-coupled grating. Unlike the case of Bragg reflection involving a single mode, the coupling coefficient κ here generally cannot be expressed as in a simple form as in Eq. 2.2-17. In the case where coupling occurs between two different modes, whether in reflection or transmission gratings, the overlap integrals (Eq. 2.2-7 and Eq. 2.2-8) typically require numerical evaluations. Similar to the analogous Bragg grating equations, Eq. 2.2-18 and Eq. 2.2-19 are coupled first-order ordinary differential equations with constant coefficients are specified. Therefore, the closed-form solutions can be obtained with appropriate initial conditions.

2.3. Phase matching conditions

In the study of optical gratings, the phase matching conditions play a crucial role in understanding the coupling between different modes or the efficient light reflection at specific wavelengths. To introduce this concept systematically, it is beneficial to begin with the fundamental diffraction phenomenon observed in conventional optical gratings and then extend the discussion to fibre gratings.

Consider two parallel light beams are diffracted by a uniform grating with a period of Λ (Figure 2.3-1). The incident rays, labelled as Ray 1 and Ray 2, incident to the grating at the same angle θ_1. The grating then diffracts these rays into different diffraction orders. Now consider the first-order diffracted wave with diffraction angle of θ_2. The

constructive interference occurs when the first-order diffraction of ray 1 and ray 2 are in-phase. The orange crosses (A_1, A_2, B_1, B_2, C_1, and C_2) in Figure 2.3-1 mark the points where the wave fronts of the two rays are in-phase.

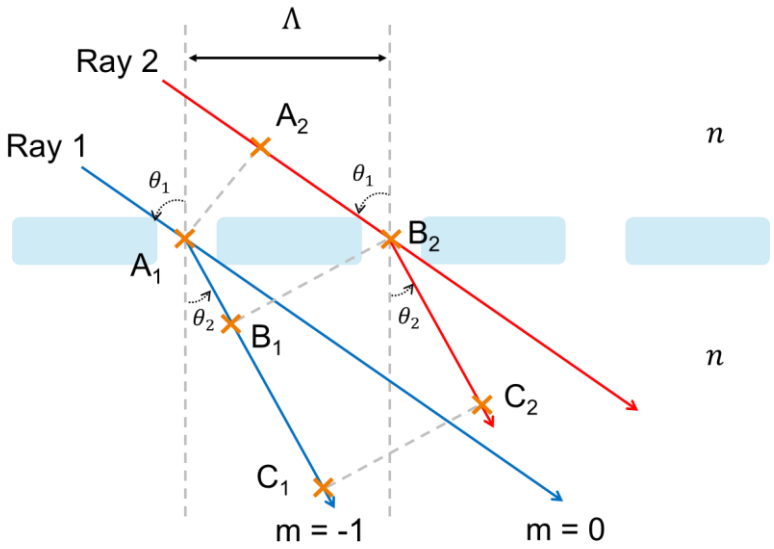

Figure 2.3 - 2 *The diffraction of light wave by a grating.*

To achieve constructive interference, the optical path difference (OPD) between the two light beams must satisfy the following relationship:

$$\Delta L = m\frac{\lambda}{\mathrm{n}} \qquad (2.3-1)$$

where ΔL represents the optical path difference, m is the diffraction order. In the context of in Figure 2.3-1, $\Delta L = \overrightarrow{A_2B_2} + \overrightarrow{B_2C_2} - \overrightarrow{A_1C_1} = \overrightarrow{A_2B_2} - \overrightarrow{A_1B_1} = \Lambda(\sin\theta_2 - \sin\theta_1)$. Therefore, the grating equation can be derived as [26]:

$$n\sin\theta_2 = n\sin\theta_1 + m\frac{\lambda}{\Lambda} \qquad (2.3-2)$$

Fiber gratings can be classified based on the mode coupling direction into backward-coupled and forward-coupled gratings. Backward-coupled gratings, such as FBGs of normal and small-tilt uniform and chirped structures, couple light in opposite directions. Forward-coupled gratings, including LPGs and largely tilted FBGs, couple light in the same direction, resulting in transmission without significant reflection.

2.3.1. Fibre Bragg gratings

In the case of FBGs where the backward-coupling occurs (Figure 2.3-2), the diffracted light propagates in the opposite direction to the incident wave. The dominant first-order diffraction corresponds to $m = -1$. Therefore, the Eq. 2.3-2 can be rewrite as:

$$-n_{eff,2} = n_{eff,1} - \frac{\lambda}{\Lambda} \qquad (2.3-3)$$

where the effective refractive index n_{eff} is defined as $n \sin\theta$ (given that $\theta = 90^{\circ}$, hence $\sin\theta = 1$). The negative sign of $n_{eff,2}$ describes the modes that propagate in the $-z$ direction. Given that $n_{eff,2} = n_{eff,1}$, the well-known phase matching condition of FBGs can be expressed as:

$$\lambda = 2n_{eff}\Lambda \qquad (2.3-4)$$

Where the n_{eff} is the effective RI of fibre core.

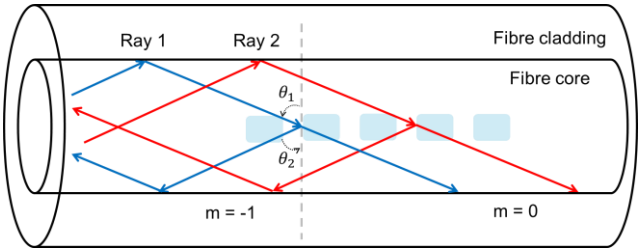

Figure 2.3 - 3 *Ray-optic illustration of the backward-coupling in an FBG.*

2.3.2. Long-period gratings

When the core mode is forward-coupled with a bounce angle θ_1 into a co-propagating cladding mode with a bounce angle θ_2 induced by a transmission grating (i.e., an LPG here) is depicted in Figure 2.3-3.

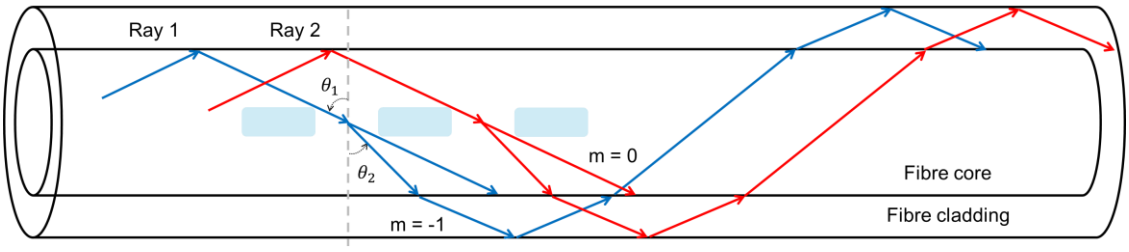

Figure 2.3 - 4 *Ray-optic illustration of the forward-coupling in an LPG.*

Since the first-order diffracted light propagates in the same direction as the incident wave, the grating equation can be expressed as follows:

$$n_{eff,2} = n_{eff,1} - \frac{\lambda}{\Lambda} \qquad (2.3-5)$$

Hence the resonant wavelength for a transmission grating is

$$\lambda = (n_{eff}^{co} - n_{eff}^{cl,j})\Lambda \qquad (2.3-6)$$

where n_{eff}^{co} and $n_{eff}^{cl,j}$ are the effective RIs of fibre core and j th cladding mode, respectively. Since the difference in effective RIs between the core and cladding modes is significantly smaller than unity, the grating period required for forward-coupled gratings at a given wavelength is much larger than that of backward-coupled gratings (i.e., FBGs). Typically, LPGs have grating periods of hundreds of micrometres, while FBGs exhibit periods of less than one micrometre.

2.3.3. Tilted fibre gratings

Tilted fibre gratings (TFGs) are formed by inscribing grating planes at an angle to the fibre axis, as illustrated in Figure 2.3-4.

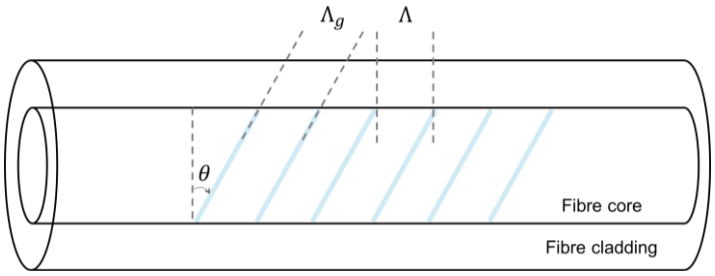

Figure 2.3 - 5 *Schematic illustration of a tilted fibre grating.*

where Λ and Λ_g represent the effective grating period and the inscribed period, respectively. The resonant wavelength is determined by Λ instead of Λ_g. Therefore, the phase matching condition of a TFG can be expressed as:

$$\lambda = (n_{eff}^{co} \pm n_{eff}^{cl,j}) \frac{\Lambda_g}{\cos\theta} \qquad (2.3-7)$$

where n_{eff}^{co} and $n_{eff}^{cl,j}$ are the effective refractive indices of fibre core and jth cladding mode, respectively. The Λ along the fibre axial is defined as $\Lambda = \frac{\Lambda_g}{\cos\theta}$. The signs "+" and "−" indicate the mode propagates in the $-z$ and $+z$ directions, corresponding to the backward- and forward-coupling, respectively. As the tilt angle varies, the grating can support backward coupling, side radiation, or forward coupling. According to wavevector-based ray optics [27], the direction of strongest coupling is given by [26]:

$$\vec{K}_R = \vec{K}_{\text{core}} + \vec{K}_G \qquad (2.3-8)$$

Here, the wave vectors $\vec{K}_R$, $\vec{K}_{\text{core}}$, and $\vec{K}_G$ correspond to the radiated light, the core mode, and the grating structure, respectively. Given the typically small difference between the refractive indices of the fibre core and cladding, the amplitude difference between $\vec{K}_R$ and

$\vec{K}_{\text{core}}$ is assumed to be negligible. Figure 2.3-5a demonstrates the phase matching conditions for a TFG with different tilt angles, where θ is less than, equal to, or greater than 45˚, respectively. The coupling direction of a TFG is highly dependent on the tilt angle of the grating (Figure 2.3-5b). When the tilt angle is less than 45˚, the core mode preferentially couples to backward-propagating cladding modes. In contrast, for the tilt angles greater than 45˚, the core mode is primarily coupled to forward-propagating cladding modes. When θ equals to 45˚, the corresponding radiation angle δ becomes 90˚, indicating that the coupled light propagates perpendicularly to the fibre axis and be radiated out of the fibre as the radiation mode.

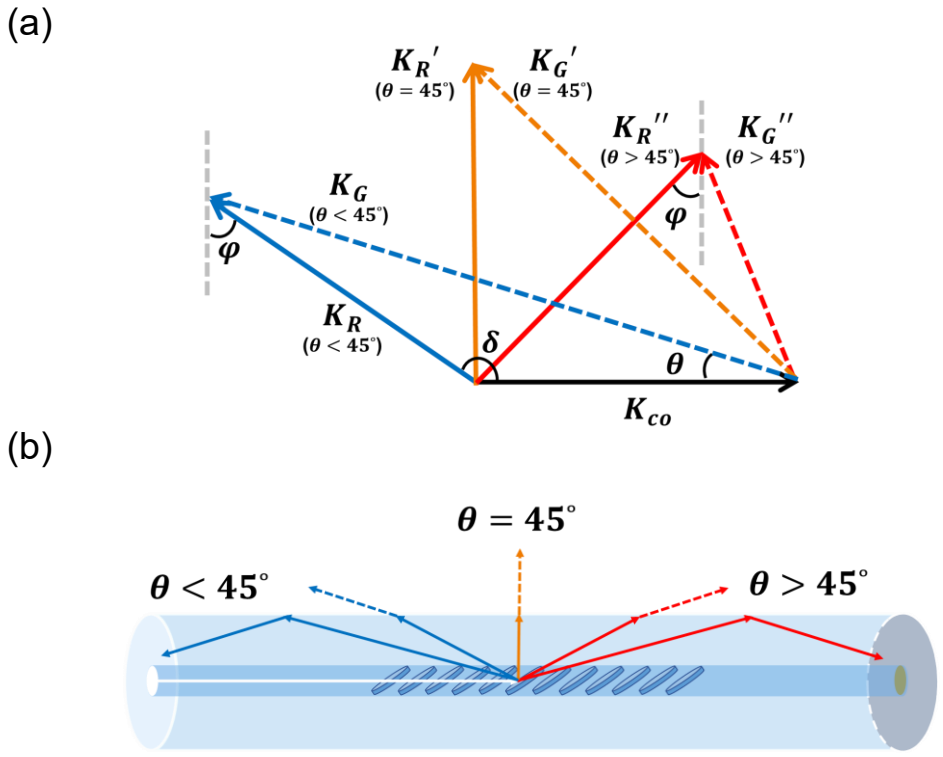

Figure 2.3 - 6 *(a) Phase matching conditions defined by wavevectors. (b) Mode coupling regimes for TFGs with tilt angles* $\theta < 45^\circ$, $\theta = 45^\circ$, *and* $\theta > 45^\circ$.

However, the propagation behaviour of the coupled light is also influenced by total internal reflection at the cladding–medium interface. Only when the radiation angle satisfies the requirement for total internal reflection will the coupled light remain confined within the cladding and propagate as guided cladding modes. Otherwise, the light is no longer guided and will be coupled into radiation modes, which tapped out of the fibre. The range over which radiation mode coupling occurs is determined by the critical angle, which is defined as:

$$\alpha_c = \arcsin \frac{n_1}{n_2} \qquad (2.3-9)$$

where n_1 and n_2 are refractive indices of the surrounding medium and the fibre cladding, respectively. Assuming the refractive index of the cladding is approximately $n_2 \approx 1.445$, the critical angle is calculated to be 43.8˚ when the fibre is surrounded by air ($n_1 \approx 1.000$). When the surrounding medium is changed to water ($n_1 \approx 1.330$), the corresponding critical angle is found to be 67.0˚ [20].

To describe the angular range for radiation mode coupling, the incident angle φ (as shown in Figure 2.3-5a) is defined based on the grating tilt angle θ by the relation of $\varphi = |2\theta - \pi/2|$. Radiation mode coupling occurs when φ is smaller than the critical angle α_c, corresponding to the angular range $\theta_{1c} < \theta < \theta_{2c}$, where:

$$\theta_{1c} = \frac{1}{2}\left(\frac{\pi}{2} - \alpha_c\right), \theta_{2c} = \frac{1}{2}\left(\frac{\pi}{2} + \alpha_c\right) \qquad (2.3-10)$$

By substituting the critical angles calculated in air and in water, the radiation mode coupling range can be determined as $\theta \in (23.1°, 66.9°)$ in air ($n_1 \approx 1.000$), and $\theta \in (11.5°, 78.5°)$ in water ($n_1 \approx 1.330$), respectively. Within these angular ranges, the light cannot be confined by total internal reflection at the cladding boundary and will radiate outward as radiation modes. Beyond those angular ranges, the light remains within the fibre and is coupled to backward- or forward- propagating cladding modes, depending on the tilt angle.

2.4. Fabry-Perot interferometer (FPI)

In 1899, the first Fabry-Perot interferometer was proposed by Charles Fabry and Alfred Perot [28,29]. The Fabry-Perot interferometer is an optical instrument in which the light interference principle is used to measure wavelength, frequency, or spectral resolution. The setup includes an optical cavity formed by two parallel-facing highly reflective surfaces (i.e., mirrors), spaced a distance *d* apart. Light is repeatedly reflected off the two precisely aligned mirrors, producing an interference fringe pattern.

Two-beam interference. Optical interference is developed based on wave theory as the phenomenon which describes the distribution of light intensity when two or more coherent light waves meet [26]. The formation of interference fringes depends on the phase relationship of the waves in establishing either constructive or destructive interference, which gives rise to periodic intensity variations in dimensional space or

frequency domain. In an ideal situation, two coherent monochromatic light waves are considered. At an observation point *P*, located sufficiently far from the sources, their plane wave expressions can be represented as [18]:

$$\vec{\mathbf{E}}_1(\vec{\mathbf{r}}, t) = \vec{\mathbf{E}}_{01}\cos\left(\vec{\mathbf{k}}_1 \cdot \vec{\mathbf{r}} - \omega t + \varepsilon_1\right) \qquad (2.4-1\text{a})$$

$$\vec{\mathbf{E}}_2(\vec{\mathbf{r}}, t) = \vec{\mathbf{E}}_{02}\cos\left(\vec{\mathbf{k}}_2 \cdot \vec{\mathbf{r}} - \omega t + \varepsilon_2\right) \qquad (2.4-1\text{b})$$

According to the superposition principle, the electrical field intensity at point *P* can be expressed as:

$$\vec{\mathbf{E}} = \vec{\mathbf{E}}_1 + \vec{\mathbf{E}}_2 \qquad (2.4-2)$$

Hence, the Squared magnitude of the total electric field is

$$\vec{\mathbf{E}}^2 = \vec{\mathbf{E}}_1^2 + \vec{\mathbf{E}}_2^2 + 2\vec{\mathbf{E}}_1 \cdot \vec{\mathbf{E}}_2 \qquad (2.4-3)$$

By substituting Eq. 2.4-1, the interference related term $\vec{\mathbf{E}}_1 \cdot \vec{\mathbf{E}}_2$ can be expressed as:

$$\begin{aligned}\vec{\mathbf{E}}_1 \cdot \vec{\mathbf{E}}_2 = \frac{1}{2}\vec{\mathbf{E}}_{01} \cdot \vec{\mathbf{E}}_{02}[&\cos((\vec{\mathbf{k}}_1 - \vec{\mathbf{k}}_2) \cdot \vec{\mathbf{r}} + (\boldsymbol{\varepsilon}_1 - \boldsymbol{\varepsilon}_2)) \\ &+ \cos((\vec{\mathbf{k}}_1 + \vec{\mathbf{k}}_2) \cdot \vec{\mathbf{r}} + (\boldsymbol{\varepsilon}_1 + \boldsymbol{\varepsilon}_2)) - 2\omega t)]\end{aligned} \qquad (2.4-4)$$

By taking the time average,

$$\langle \vec{\mathbf{E}}_1 \cdot \vec{\mathbf{E}}_2 \rangle_{\mathrm{T}} = \frac{1}{2}\vec{\mathbf{E}}_{01} \cdot \vec{\mathbf{E}}_{02}\cos((\vec{\mathbf{k}}_1 - \vec{\mathbf{k}}_2) \cdot \vec{\mathbf{r}} + (\boldsymbol{\varepsilon}_1 - \boldsymbol{\varepsilon}_2)) \qquad (2.4-5)$$

And,

$$\langle \vec{\mathbf{E}}_1^2 \rangle_{\mathrm{T}} = \frac{\vec{\mathbf{E}}_{01}^2}{2} \qquad (2.4-6)$$

$$\langle \vec{\mathbf{E}}_2^2 \rangle_{\mathrm{T}} = \frac{\vec{\mathbf{E}}_{02}^2}{2} \qquad (2.4-7)$$

By substituting Eq. 2.4-5, Eq. 2.4-6, and Eq. 2.4-7 into Eq. 2.4-3, the total irradiance can be expressed as:

$$\langle \vec{\mathbf{E}}^2 \rangle_{\mathrm{T}} = \frac{\vec{\mathbf{E}}_{01}^2}{2} + \frac{\vec{\mathbf{E}}_{02}^2}{2} + \vec{\mathbf{E}}_{01} \cdot \vec{\mathbf{E}}_{02}\cos((\vec{\mathbf{k}}_1 - \vec{\mathbf{k}}_2) \cdot \vec{\mathbf{r}} + (\boldsymbol{\varepsilon}_1 - \boldsymbol{\varepsilon}_2)) \qquad (2.4-8)$$

which can be simplified as:

$$I = I_1 + I_2 + 2\sqrt{I_1 I_2}\cos\delta \qquad (2.4-9)$$

where I represents the total irradiance, and I_1 and I_2 correspond to the terms $\frac{\vec{\mathbf{E}}_{01}^2}{2}$ and $\frac{\vec{\mathbf{E}}_{02}^2}{2}$, respectively. The phase difference δ equals to $(\vec{\mathbf{k}}_1 - \vec{\mathbf{k}}_2) \cdot \vec{\mathbf{r}} + (\boldsymbol{\varepsilon}_1 - \boldsymbol{\varepsilon}_2)$, resulting from the combination of path length variation and initial phase offset.

Multiple-beam interference. Now, consider a beam with the amplitude E_0 incident on a non-absorbing transparent dielectric thin film with RI of n_{film} as shown in Figure 2.4-1. For simplicity, the surrounding media on both sides have the same refractive index $n_1 = n_2$. Consider a set of parallel reflected rays where ray maintains a fixed phase relationship with all others. These phase differences result from variations in the optical path length and phase shifts introduced at each reflection. Since these waves are coherent, they could interfere when collected or focused at either point P (reflection) or point P′ (transmission) by lens. The amplitude transmission coefficients t and t' represent the fractions of the wave amplitude transmitted when entering and leaving the film, respectively. Similarly, the amplitude reflection coefficients r and r' correspond to the fractions of wave amplitude reflected from the film's outer and inner surfaces, respectively. Since the thin film is assumed to be non-absorbed, it follows that $tt' = 1 - r^2$, indicating the incident beam either be reflected or transmitted without loss. Additionally, $r = -r'$ where the negative sign refers to the phase shift upon reflection.

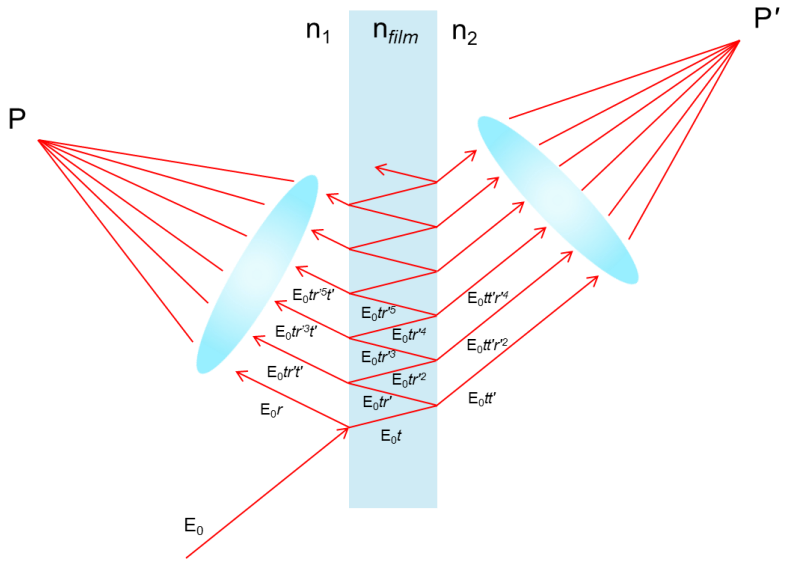

Figure 2.4 - 1 *Schematic illustration of multiple-beam interference from a transparent dielectric thin film.*

Hence, the total reflected scalar wave can be expressed as:

$$\tilde{E}_r = E_0 r e^{i\omega t} + E_0 t r' t' e^{i(\omega t - \delta)} + E_0 t r'^3 t' e^{i(\omega t - 2\delta)} + \cdots + E_0 t r'^{(2N-3)} t' \times e^{i[\omega t - (N-1)\delta]} \quad (2.4-10)$$

where δ represents the phase difference between two adjacent reflected rays, resulting from the optical path length difference while the incident beam undergoes different times of reflection in the thin film. Due to the series converges when it approaches infinity, and by substituting $tt' = 1 - r^2$ and $r = -r'$, Eq. 2.4-10 can be simplified as follows:

$$\tilde{E}_r = E_0 e^{i\omega t}\left[\frac{r(1-e^{-i\delta})}{1-r^2e^{-i\delta}}\right] \qquad (2.4-11)$$

By substituting $I_r = \frac{\tilde{E}_r\tilde{E}_r^*}{2}$ and noticing that the total incident irradiance is $I_i = \frac{E_0^2}{2}$, the total reflected irradiance can be derived as follows:

$$I_r = I_i \frac{2r^2(1-\cos\ \delta)}{(1+r^4)-2r^2\cos\ \delta} \qquad (2.4-12)$$

Similarly, the total irradiance of transmission can be expressed as:

$$I_t = I_i \frac{(1-r^2)^2}{(1+r^4)-2r^2\cos\ \delta} \qquad (2.4-13)$$

Hence, the irradiance distribution of reflection and transmission are determined by the total incident irradiance I_i, the reflectance of the thin film r^2, and phase difference δ, which is given as follows:

$$\delta = \frac{4\pi n_{film}}{\lambda_0} d\cos\theta \qquad (2.4-14)$$

where n_{film} is the RI of the thin film, λ_0 is the central wavelength, d is the distance between the two surfaces where light beams reflected, and θ is angle between the incident light ray and the normal to the reflecting surface.

Fabry-Perot interferometer. Now consider the FPI with a pair of distance-adjustable mirrors. The reflectance $R = r^2$ of the mirrors is determined by their coating materials. Again, if the absorbance is ignored, the formulas for the reflected and transmitted irradiance of the F-P interferometer can be written as:

$$\frac{I_r}{I_i} = \frac{2\sqrt{R_1R_2}(1-\cos\ \delta)}{1+R_1R_2-2\sqrt{R_1R_2}\cdot\cos\ \delta} \qquad (2.4-15)$$

and,

$$\frac{I_t}{I_i} = \frac{(1-\sqrt{R_1R_2})^2}{1+R_1R_2-2\sqrt{R_1R_2}\cdot\cos\ \delta} \qquad (2.4-16)$$

where R_1 and R_2 represent reflectance of two mirrors.

The finesse $\mathcal{F}$, which describes the sharpness of reflection or transmission peaks, is defined as the ratio of the separation of adjacent maxima to the half-width and is given by:

$$\mathcal{F} = \frac{\pi(R_1R_2)^{\frac{1}{4}}}{1-(R_1R_2)^{\frac{1}{2}}} \qquad (2.4-17)$$

From Eq. 2.4-17, the finesse is found determined only by the reflectance of mirrors. Figure 2.4-2 shows the irradiance distribution of reflected beam in a F-P interferometer with different mirror reflectance R. For simplicity, the two parallel mirrors in the resonant cavity are assumed to have identical reflectance ($R = R_1 = R_2$). Recall that $R = r^2$, an increase in mirror reflectance leads to a greater finesse coefficient F, which is defined as $F = \frac{4R}{(1-R)^2} = (\frac{2\mathcal{F}}{\pi})^2$. As the mirror reflectance increases, the reflection peaks become sharper, indicating an enhanced selectivity of the resonances within the F-P cavity.

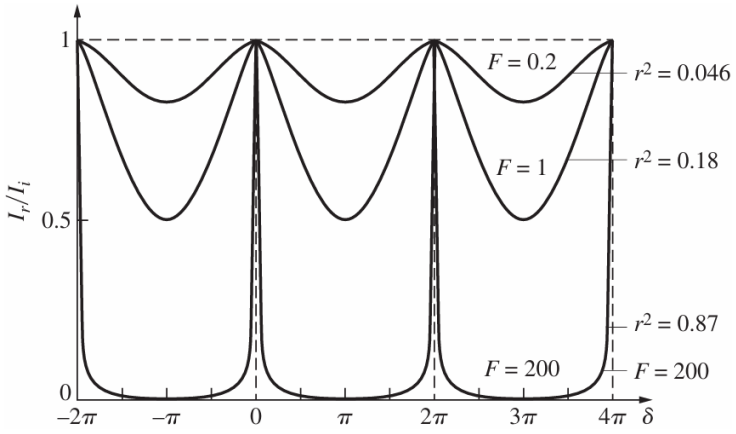

Figure 2.4 - 2 *Irradiance distribution of reflection as a function of phase difference in a F-P interferometer with mirrors of varying reflectance [18].*

Another key parameter of the FPI is the free spectral range (FSR), which characterises the spectral spacing between adjacent transmission or reflection peaks. It defines the periodicity of resonance conditions within the interferometric cavity and thus plays a central role in determining the spectral response of the device, which is given by:

$$\Delta\lambda = \frac{\lambda_0^2}{2nL} \qquad (2.4-18)$$

where n is the RI within the F-P cavity, L is the cavity length, and λ_0 is the central wavelength. For a given λ_0, FSR is inversely proportional to both n and L.

2.5. Chapter summary

This chapter established the theoretical foundation for light propagation and mode interaction in fibre optic waveguides. Starting from the derivation of the wave equation under the weakly guiding approximation, the analysis focused on understanding how guided modes behave in step-index fibre waveguides. Coupled-mode theory was introduced to explain the resonance mechanisms in FBGs, LPGs, and TFGs, with particular emphasis on phase matching and mode coupling dynamics. The FPI was also examined, highlighting how cavity parameters influence spectral characteristics in reflection-based fibre sensors. Together, these theoretical insights support the design and analysis of the fibre-optic sensing platforms explored in this thesis.

Chapter 3 Two-dimensional (2D) materials synthesis and characterisation

3.1. Introduction of 2D materials

Two-dimensional (2D) materials are defined as materials with one dimension being single- or few-atoms thick whilst the other two dimensions are significantly larger, ranging from 100 nm to micrometres or even centimetres [30]. 2D materials have gained great interests since the successful isolation of single-layer graphene from graphite in 2004 [31]. The extremely thin nature of 2D materials endows them with characteristics such as high surface-to-volume ratio, flexibility, optical transparent, tuneable bandgaps, and quantum-size effect compared to their bulk counterparts [32]. Confined electrons on monolayer nanosheets enable efficient transport without interlayer interactions, resulting in high conductivity [33]. Additionally, strong in-plane chemical bonds contribute to the outstanding mechanical strength of 2D materials [34]. Furthermore, surface engineering can be easily performed to enhance or modify their intrinsic properties, thanks to the large fraction of surface atoms [35]. As illustrated in Fig. 3.1-1, various 2D materials such as graphene, 2D MOS, TMDs, 2D polymer, BP, BN, g-C_3N_4, and MXene have been widely explored and investigated among fields of physics, materials science, chemistry, and nanotechnology [36].

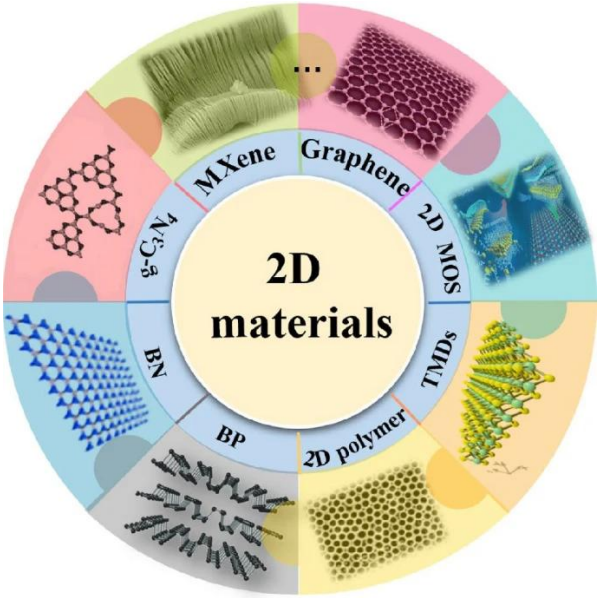

Figure 3.1 - 1 *Schematic illustration of various 2D materials including graphene, 2D MOS, TMDs, 2D polymer, BP, BN, g-C_3N_4, and MXene [36].*

In this chapter, several 2D materials will be introduced in section 3.1, followed by a review of various synthesis techniques for 2D materials in section 3.2. Moreover, in section 3.3 to 3.6, we demonstrate our development on 2D materials synthesis and characterisation.

Graphene is a single-atom-thick two-dimensional carbon nanomaterial, which was firstly reported by isolating from bulk graphite with micromechanical cleavage [31]. As an allotrope of carbon, graphene is composed of a hexagonal close-packed network of carbon atoms with sp^2 hybridisation.

As the crystal structure illustrated in Fig. 3.1-2, along the in-plane direction of a single-layer graphene sheet, each carbon atom covalently bonds to three adjacent atoms via σ-bond, with a bond length of 1.42 Å (Fig. 3.1-2a). The strong covalent in-plane bond features graphene extraordinary mechanical strength. Additionally, the remaining p_z electrons from individual carbon atoms form π-bonds. The advanced electron properties of graphene come from the hybridisation of π-bands and π*-bands [37]. In the out-of-plane direction (Fig. 3.1-2b), the individual layers of graphene stack together through the van der Waals (vdW) forces to form multiple layers of graphene or graphite, with the interlayer distance of 3.35 Å [38,39].

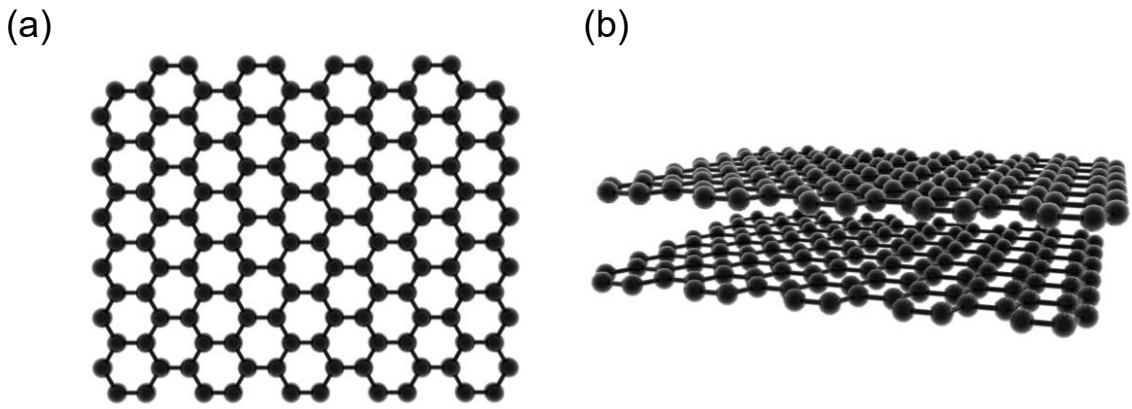

Figure 3.1 - 2 *Schematic illustration of crystal structure of graphene (a) The top view of single-layer graphene. (b) Bilayer graphene stacked together through the van der Waals force.*

The relationship between energy and momentum in graphene is determined by its unique band structure, where the valence and conduction bands meet at the Dirac point (located at the edge of the Brillouin zone in momentum space), resulting in graphene being a zero-bandgap semiconductor. Additionally, near the Dirac points, a cone-like linear dispersion relation is observed, which can be accurately described by the Dirac equation for massless fermions. The effective mass of the charge carriers in this region is zero, resulting

ultrahigh carrier mobility of graphene, which was reported as high as 200,000 $cm^2/V{\cdot}s$ at room temperature. This value is about 100 times larger than that in silicon [40–43]. Moreover, graphene exhibits broadband absorption ranging from the visible to near-infrared spectrum, with a single graphene sheet absorbing 2.3% of white incident light. This highlights graphene's strong light-matter interaction [44,45].

Graphene Oxide (GO) is one of the graphene derivatives, which contains conducting π-states from carbon atoms with sp^2 hybridisation as well as large energy gaps between σ-bonds of carbon atoms with sp^3 hybridisation. Unlike the ideal graphene sheet with fully sp^2-hybridised carbon atoms, sp^3-hybridised carbon atoms feature the basal plane and sheet edges of GO with different oxygen-containing functional groups (OFGs) such as epoxy, hydroxyl and carboxyl (Fig. 3.1-3) [46].

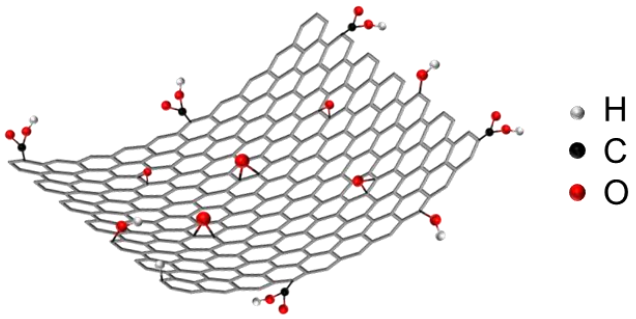

Figure 3.1 - 3 *Schematic illustration of a single sheet of graphene oxide.*

These OFGs provide GO with excellent dispersibility in aqueous media and exceptional biocompatibility, enabling a wide range of reactions and surface functionalisation and making GO an appealing candidate for chemical and biomedical applications [47]. The ratio of sp^2 and sp^3 fractions can be tuned by chemical reduction, providing a powerful method to adjust GO's bandgap and enabling its controlled transformation from an insulator to a semiconductor or even to a graphene-like semi-metallic material [48]. Moreover, GO has unique optical properties such as high in-plane RI in the telecommunications band, resulting in higher loss in-plane (TE) electric field compared to out-of-plane (TM) loss. In addition, the enriched oxygen functional groups (OFGs) provide GO films with an ultra-low extinction coefficient in telecommunications band, leading to low material absorption [49,50].

MXenes, known as 2D transition metal carbides, nitrides, and carbonitrides, have attracted great interest and exhibited outstanding performance in energy storage [51],

optoelectronics [52], biomedical and environmental applications [53,54] since the $Ti_3C_2T_x$ was firstly reported in 2011 [55]. Fig. 3.1-4 illustrates the crystal structure of MAX phase and MXene. The MAX phase exhibits a layered hexagonal structure including two formula units per unit cell, which follows the space group $P6_3/mmc$. Near-close-packed M-layers are interleaved with layers of pure A-group elements, whilst X-atoms occupy the octahedral sites between the M-layers [55]. MXenes are synthesised with a top-down approach by selectively etching the A-layer atoms from the MAX phase precursor ($M_{n+1}AX_n$) to form loosely stacked 2D layers with the formular of $M_{n+1}X_nT_x$ (n = 1-4), where "M" is an early transition metal, "A" is an element mainly from group IIIA or IVA in the periodic table, “X” is carbon and/or nitrogen, and "T_x" represents surface termination groups (-O, -OH, -F, etc.) [56,57]. The loosely stacked MXene layers can be further exfoliated into single-layer or few-layer flakes with delamination due to the removal of the A-layer significantly weakens the interactions between the $M_{n+1}X_n$ layers [58]. The surface termination groups (such as -F, and -Cl) are induced during the etching and delamination steps, which can be utilised for surface modification of MXenes.

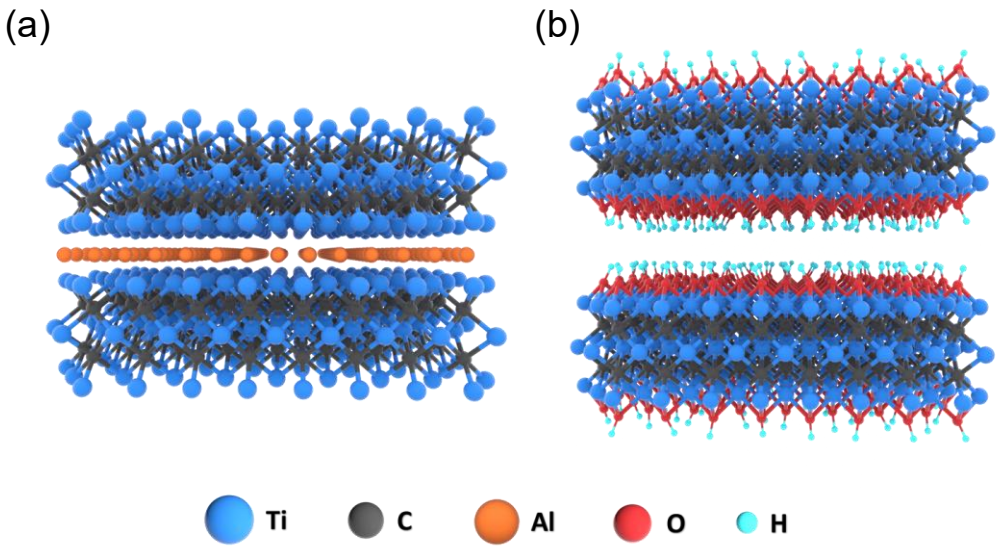

Figure 3.1 - 4 *Schematic illustration of crystal structure of (a) MAX, and (b) MXene.*

Furthermore, MXenes combine metallic conductivity, attributed to the free electrons in their transition metal carbide or nitride backbone, with hydrophilicity which arises from their surface terminations [59]. Moreover, the density of states (DOS) and Fermi level of MXenes can be modified by their surface terminations, making MXenes electronically tuneable. Due to numerous combinations of "M_{n+1}" and "X_n" as well as various values of n, more than 100 types of MXenes have been theoretically predicted, and more than 30 different MXenes have been experimentally synthesised [60].

α-phase molybdenum trioxide (α-MoO_3) is a natural vdW material with strong in-plane anisotropy. Fig. 3.1-5a illustrates the crystal structure of α-MoO_3 which demonstrated double layers of edge-sharing, with distorted MoO_6 octahedra weakly bound by vdW forces along the (010) plane to form α-MoO_3 [61]. As shown in Fig. 3.1-5b, the orthorhombic unit cell exhibits unequal lattice constant of a = 0.396 nm, b = 1.385 nm, and c = 0.369 nm, respectively, with interaxial angles of 90˚ [62]. The 7.2 % difference between the interlayer spacing of the (100) and (001) facets results in the strong in-plane anisotropy of α-MoO_3 [63]. The direction-dependent refractive index, known as birefringence, was reported as $n_a = 2.21 + 0i$ along the a-axis and $n_c = 2.30 + 0i$ along the c-axis. The ~0.1 difference of Δn between two axes demonstrates that α-MoO_3 is a strongly birefringent material [64]. Such in-plane anisotropic structure features α-MoO_3 unique optical properties. Elliptic and hyperbolic in-plane polariton dispersion were observed along the surface of α-MoO_3 slides [62]. Based on this, mid-infrared polaritons with negative refraction were observed in α-MoO_3, which were used for the generation of reversed Cherenkov radiation [65,66]. Moreover, with a wide band gap (~3.3eV), α-MoO_3 is quasi-transparent in the visible spectrum and remains electrically conductive [67]. 2D layers of α-MoO_3 have been synthesised with bottom-up methods including chemical vapor deposition (CVD) [68], physical vapor deposition (PVD) [69], vdW epitaxy growth [70], and rapid flame growth [71], as well as top-down exfoliation methods, such as ion intercalation-assisted liquid exfoliation [72] and mechanical force-assisted liquid exfoliation [73].

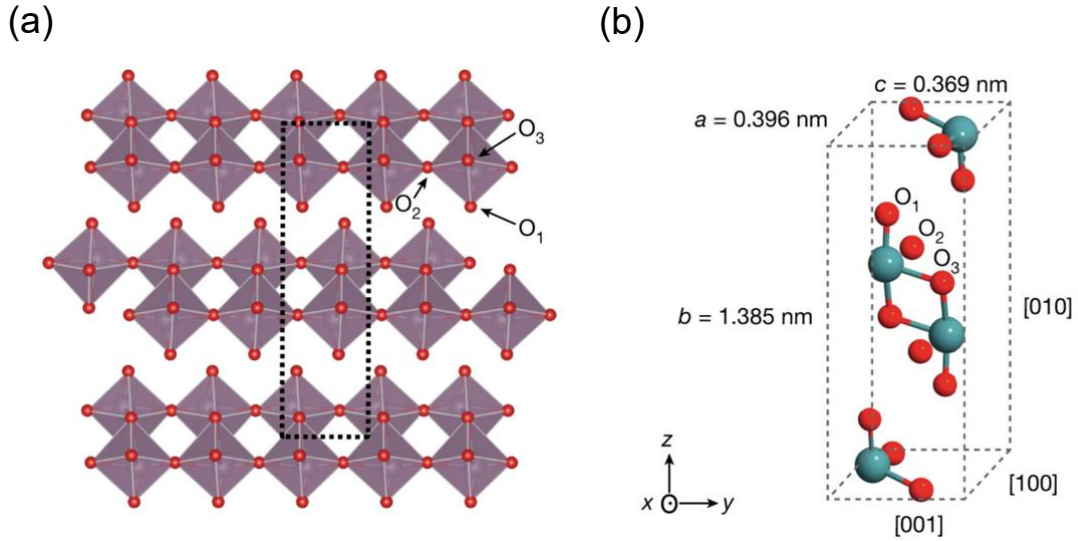

Figure 3.1 - 5 *Schematic illustration of (a) the orthorhombic lattice structure of layered α-MoO_3, (b) the unit cell of α-MoO_3 extracted from the dashed box in (a) [62].*

3.2. Current methods for 2D materials synthesis

Various synthesis methods have been widely explored to obtain ultrathin 2D nanomaterials with desired thickness, lateral size, composition, and surface properties. This is essential for the investigation of their unique physical, chemical, and optoelectronic properties, as well as for the exploration of diverse applications [30]. The reported synthesis methods can be allocated into two categories: top-down and bottom-up approaches. The top-down methods utilise various exfoliation strategies to obtain atomically ultrathin 2D materials by breaking the weak interplane interactions (e.g., vdW forces) in their bulk counterparts with layered structures. These exfoliation methods mainly include mechanical cleavage [74] and liquid exfoliation, which can be further categorised based on their exfoliation mechanisms. To date, the liquid exfoliation has been reported for the synthesis of various 2D materials by assisting with sonication [75], shear force [76], ion intercalation [77], ion exchange [78], oxidation [79], and selective etching [80]. The bottom-up methods rely on chemical reactions involving certain precursors under given experimental conditions, offering practical approaches for direct 2D materials synthesis [32]. As two typical bottom-up methods, CVD and wet-chemical syntheses offer greater versatility in principle [30]. The wet-chemical techniques such as hydrothermal synthesis [81], 2D-oriented attachment [82], self-assembly [83], 2D-templated synthesis [84], seed-growth [85], and hot-injection [86] have been explored for the bottom-up synthesis of 2D materials.

In this section, several synthesis methods will be discussed along with their advantages and disadvantages.

Mechanical cleavage, a traditional method using Scotch tape to exfoliate layered bulk crystals, which is widely employed to produce ultrathin 2D flakes while preserving the in-plane covalent bonds [87]. The first single-layer graphene was successfully exfoliated from graphite using the mechanical cleavage method in 2004 [31]. The typical process is demonstrated in Fig. 3.2-1. In brief, the bulk crystal was firstly attached to the adhesive surface of a piece of Scotch tape followed by attaching another adhesive surface to peel the bulk crystal into two thinner flakes. Then another adhesive surface was attached to these two flakes to further cleavage them. This procedure was repeated numerous times until single-layer flakes appear. Then, with gentle pressure, the Scotch tape attached single-layer flakes was sticked to substrates (e.g., SiO_2/Si) followed by peeling off the tape. Finally, the single- or few-layer nanosheets were found under an optical microscope.

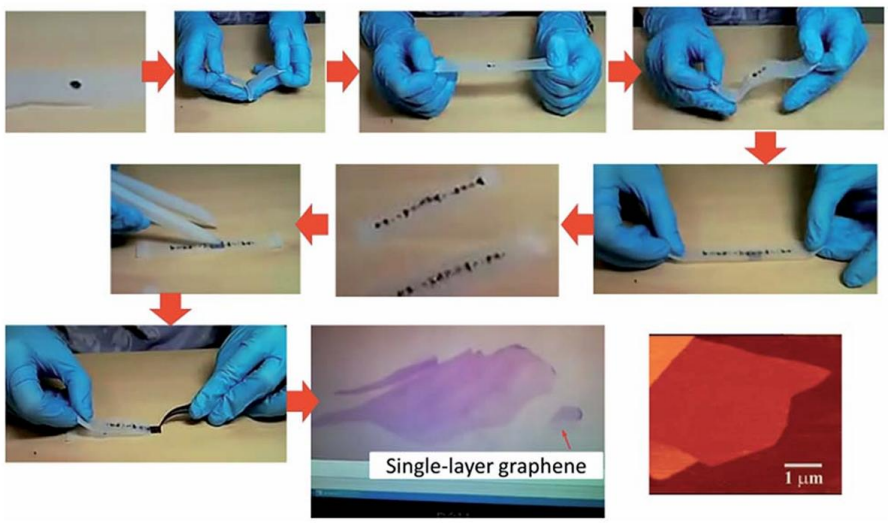

Figure 3.2 - 1 *Schematic procedure of the Scotch-tape-assisted mechanical cleavage of graphene [74].*

During the exfoliation process, the force in the in-plane direction was repeatedly applied to break the weak interplane vdW interactions. Therefore, the obtained nanosheets preserved excellent crystal structure of their parent bulk crystal, as no chemical reactions were introduced. Moreover, the exfoliated nanosheets can reach up to tens of micrometres, making them ideal for the downstream exploration of their intrinsic electronic, optical, and mechanical properties. However, some limitations of this method restricted its practical applications. Firstly, the low production yield prevents it from meeting the demands for large quantities of 2D materials. Secondly, it is a challenge to precisely control the thickness, shape, and lateral size of the produced 2D nanosheets. Lastly, a substrate is always needed to support the exfoliated nanosheets [30,34].

Sonication-assisted liquid exfoliation is an effective method to exfoliated 2D nanosheets from layered bulk crystals in liquid phase (Fig. 3.3-1). By applying external forces (i.e., sonication), vdW interactions are broken between layers, whilst the in-plane covalent bonding of each layer is preserved. In a typical sonication process, the layered bulk crystals are dispersed in organic solvents such as Ethanol, N-methyl-pyrrolidone (NMP), and dimethylformamide (DMF) to stabilise the exfoliated nanosheets and prevent aggregation. Moreover, the use of aforementioned organic solvents is intended to match the surface tension between the layered bulk crystal and the solvent system, which is a key factor in achieving efficient exfoliation.

Liquid cavitation could be induced during the sonication, which brings bubbles into the liquid system. When the bubbles collapse, shock waves and microjets will pass through the layered bulk crystals hence being dispersed in the solvent. This process generates

intense tensile stress on the crystals, resulting in their exfoliation into thinner nanosheets [30]. The concentration, lateral size, and thickness of the exfoliated nanosheets can be tailored by modifying parameters such as sonication time, solvent system, ultrasonic power, sonication temperature, and even container shape [88]. The exfoliated nanosheets are further purified by centrifugation. Nanosheets with varying lateral sizes and thicknesses can be selectively collected by tuning the centrifugation time and speed. Compared to the mechanical cleavage, sonication-assisted liquid exfoliation has been widely used for the efficient and cost-effective high-yield production of 2D materials. However, there are some disadvantages of this method whilst preparing 2D materials. Firstly, fewer monolayer nanosheets can be obtained from the exfoliation suspension, which restricts fundamental research on 2D materials, as certain extraordinary properties can only be observed in their monolayer form. Secondly, as the strong sonication force breaks larger sheets into smaller fragments during the exfoliation process, the lateral size of exfoliated nanosheets is relatively small. Thirdly, the organic solvents or surfactants might be induced to absorb on the surface of exfoliated nanosheets, which are difficult to be completely removed. The undesired residual could affect downstream applications. Finally, some defects might be induced on the exfoliated nanosheets during the sonication process, potentially altering their intrinsic properties.

Chemical vapor deposition (CVD) is a typical bottom-up approach to grow high-purity 2D materials. In a typical CVD process (Fig. 3.2-2), certain substrates are put in a furnace chamber with high temperature and high vacuum environments. One or more precursors are placed at designed locations where varying temperatures are applied. With the assistance of high temperature and an inert gas flow (i.e., nitrogen or argon), the vaporised precursors are transported to the surface of target substrates, reacting and/or decomposing to form 2D nanosheets or large-scale thin films [89].

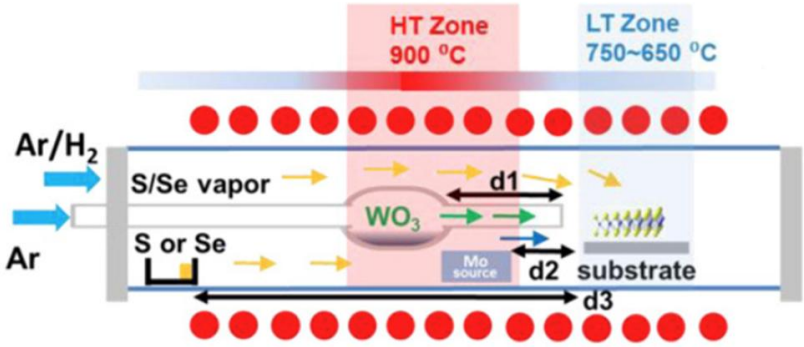

Figure 3.2 - 2 *Schematic illustration of CVD for the synthesis of 2D heterostructures [89].*

It is worth to note that the substrate types, temperature, distance between various precursors, the ratio of precursors, and surrounding atmospheres are crucial factors in determining the structure features of the synthesised 2D nanomaterials. By finely tuning the parameters, CVD method enables the synthesis of 2D materials or 2D heterostructures with high purity, good crystal quality, scalable lateral size, tuneable layer numbers, controllable thickness, and limited defects [30]. As a promising method, CVD has been used for the growth of many 2D materials including graphene [90], h-BN [91], TMDs (MoS_2, WS_2, WSe_2, $MoSe_2$, $MoTe_2$, ReS_2, etc.) [92–97], and 2D heterostructures ($MoSe_2$−WSe_2, MoS_2−WS_2, and WSe_2−$MoSe_2$) [98–100]. Unlike the mechanical cleavage technique suffering from low yield and production rate, CVD enables the large-scale production of 2D materials suitable for industrial applications. However, the CVD method still faces the challenges, such as the necessity of substrates to support the grown 2D materials, requiring an additional transfer process to move the grown nanomaterials onto desired substrates for further investigation and applications. Moreover, the high temperature, high vacuum, and inert gas flow result in a relatively higher cost compared to the liquid-based methods.

3.3. Development of sonication-assisted liquid phase exfoliation method

Sonication-assisted liquid phase exfoliation was selected in this work due to its simplicity, scalability, and compatibility with solution-based processing. This approach enables the preparation of single- and few-layer nanosheets with preserved in-plane crystal structure, making it suitable for subsequent material integration and device fabrication.

3.3.1. Black Phosphorus (BP)

Black phosphorus (BP) was selected as a representative layered two-dimensional material due to its puckered crystal structure and strong thickness-dependent electronic properties. In particular, the bandgap of BP varies significantly with layer number, making it highly sensitive to exfoliation conditions and well suited for demonstrating the sonication-assisted liquid phase exfoliation approach. The BP nanosheets were obtained by a basic-NMP solvent exfoliation method as shown in Fig. 3.3-1. Firstly, 100.0 mg of bulk BP (obtained from SIAT, Shenzhen, China, Fig. 3.3-2a) was ground thoroughly in a quartz mortar for 30 minutes with the assist of NMP (Fig. 3.3-2b). Secondly, the ground BP was

dispersed in 100 mL of NMP and subjected to probe sonication at 1,200 W, operated in a cycle of 2 seconds on and 4 seconds off, for a duration of 20 hours. During sonication, the temperature was maintained at 6 °C using a cooling bath. Finally, the differential centrifugation was implemented for collecting the BP nanosheets. After centrifuging at 7,000 rpm, the supernatant was extracted and subsequently subjected to centrifugation at 13,000 rpm for 10 minutes. The desired BP nanosheets were obtained by collecting the resulting sediment. The obtained sample was rinsed three times with ethanol to remove residual NMP and then re-suspended in an aqueous solution. Figure 3.3-2c shows the BP suspensions before and after the probe sonication. The suspension obtained after sonication exhibits a brighter and smoother texture, attributed to the exfoliation of BP bulk material into smaller nanosheets. The aggregated BP nanosheets were shown in Fig. 3.3-2d.

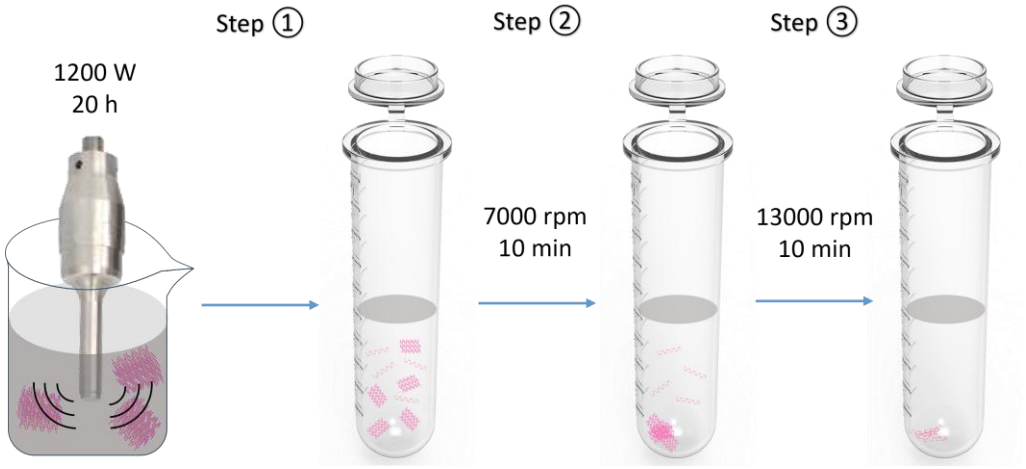

Figure 3.3 - 1 *Schematic illustration of BP exfoliation in liquid phase with probe sonication differential centrifugation.*

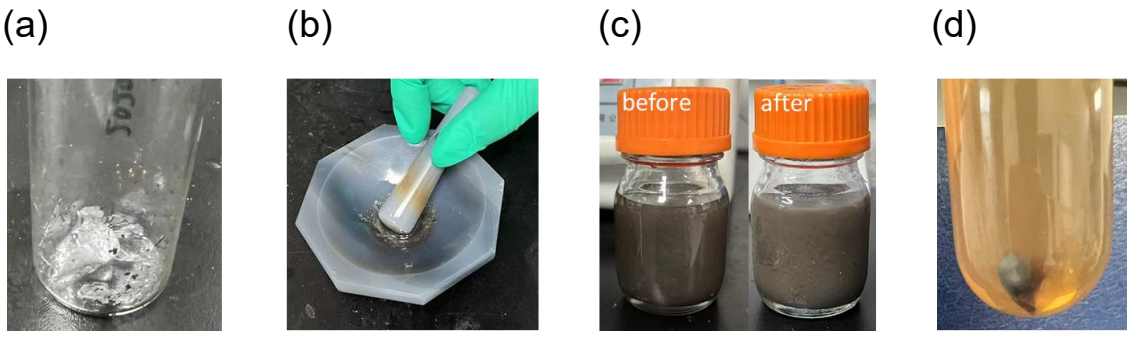

Figure 3.3 - 2 *Digital photos of (a) bulk BP, (b) BP in grinding, (c) BP suspensions before & after probe sonication, and (d) the desired BP sediment after centrifugation of 13000 rpm.*

3.3.2. $BiTiS_3$

$BiTiS_3$ is a layered chalcogenide material with a van der Waals crystal structure, making it amenable to liquid phase exfoliation into 2D nanosheets. In this context, $BiTiS_3$ nanosheets are introduced owing to their broad optical absorption across the NIR-I and NIR-II regions and their favourable photothermal response in the NIR-II window, while also serving to demonstrate the applicability of the sonication-assisted exfoliation approach to layered materials beyond those introduced in Section 3.1. (The bulk $BiTiS_3$ was obtained from SIAT, Shenzhen, China). The $BiTiS_3$ nanosheets were obtained by a basic-NMP solvent exfoliation method. To obtain nanosheets with a uniform size distribution, a modified centrifugation method incorporating additional differential steps was employed after 20-hour sonicating. The differential centrifugation process was conducted in several steps to prepare the desired materials. The $BiTiS_3$ suspension after sonication was centrifuged sequentially at 1,000 rpm for 3 minutes, 3,000 rpm for 5 minutes, and 5,000 rpm for 10 minutes. The resulting supernatant was then collected and subjected to further centrifugation at 7,000 rpm for 5 minutes, followed by 9,000 rpm for 15 minutes. The sediment obtained was re-dispersed in NMP and centrifuged again at 4,000 rpm for 5 minutes, with the supernatant retained for subsequent processing. This supernatant was further centrifuged at 13,000 rpm for 10 minutes to collect the sediment. To remove residual NMP, the sediment was washed three times with ethanol, where each washing step involved re-dispersing the sediment in ethanol, centrifuging at 13,000 rpm for 10 minutes, and then collecting the sediment. Finally, the washed sediment was re-dispersed in deionized (DI) water, making it ready for downstream processes.

Fig. 3.3-3 presents the SEM images of the $BiTiS_3$ layered structures before exfoliation with different magnifications, clearly displaying a well-organized arrangement of layers. As confirmed by EDS in Fig. 3.3-3c, the atomic concentrations of Bi, Ti, and S are

21.15%, 19.65%, and 59.20%, respectively, aligning with the theoretical stoichiometric ratio of 1:1:3 [101].

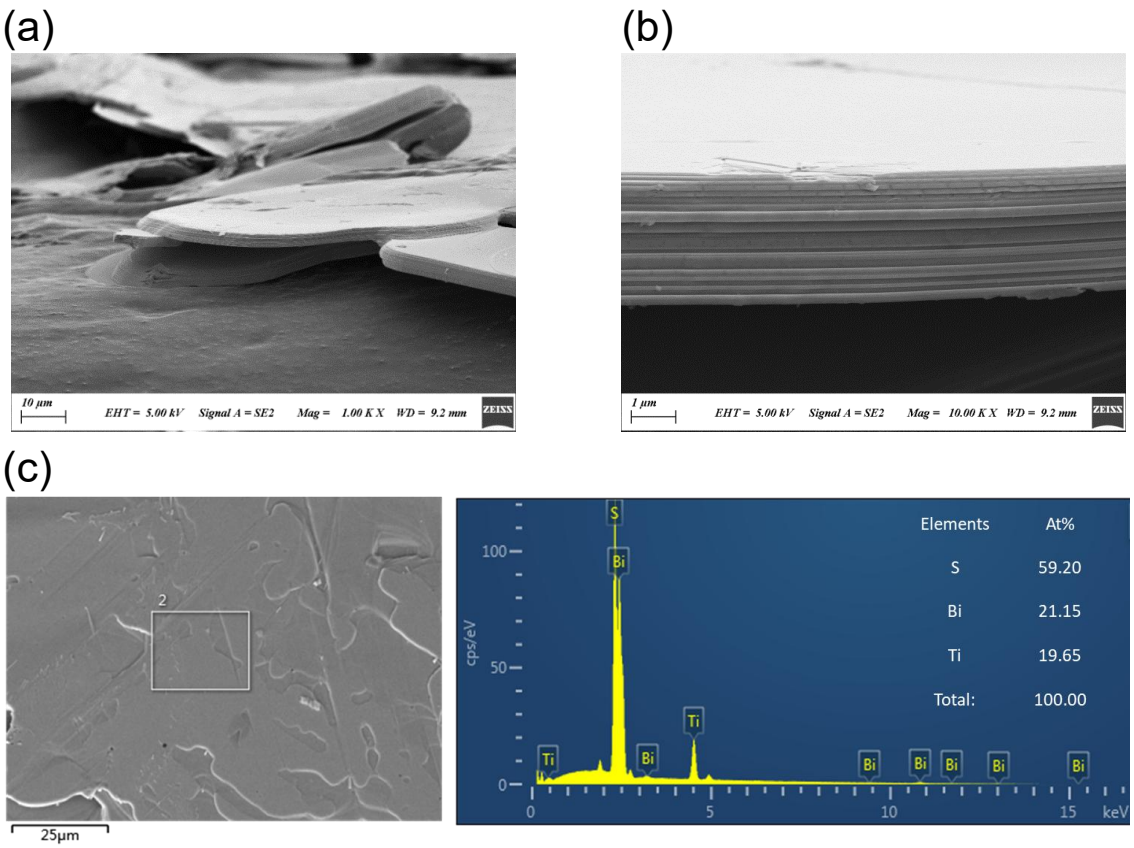

Figure 3.3 - 3 *(a, b) SEM images of $BiTiS_3$ layered structure before exfoliation with different magnifications. (c) SEM image of the layered $BiTiS_3$ nanosheets with EDS spectrum extracted from the box with solid line (inset).*

A piece of $BiTiS_3$ was extracted from the bulk material using the focused ion beam (FIB) technique. Then the cross-section of $BiTiS_3$ was characterised with TEM. As shown in the high-resolution TEM (HR-TEM) image (Fig. 3.3-4), a well-organised alternating stacking of BiS and TiS_2 layers was observed.

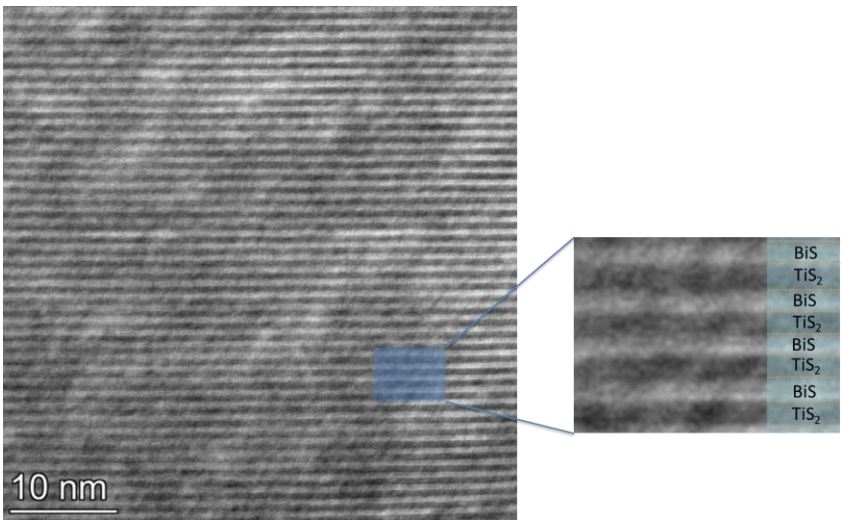

Figure 3.3 - 4 *Cross-sectional HR-TEM image of $BiTiS_3$ representing its layered structure.*

$BiTiS_3$ nanosheets after exfoliation were characterised by AFM for the identification of the height and lateral size of the synthesised nanosheets (Fig. 3.3-5). The thinnest nanosheets have a height of approximately 8 nm, corresponding to a few layers of $BiTiS_3$. In contrast, the thicker nanosheets, with a height of around 80 nm, likely result from layer aggregation or incomplete exfoliation. The lateral sizes of $BiTiS_3$ nanosheets were 50 – 250 nm.

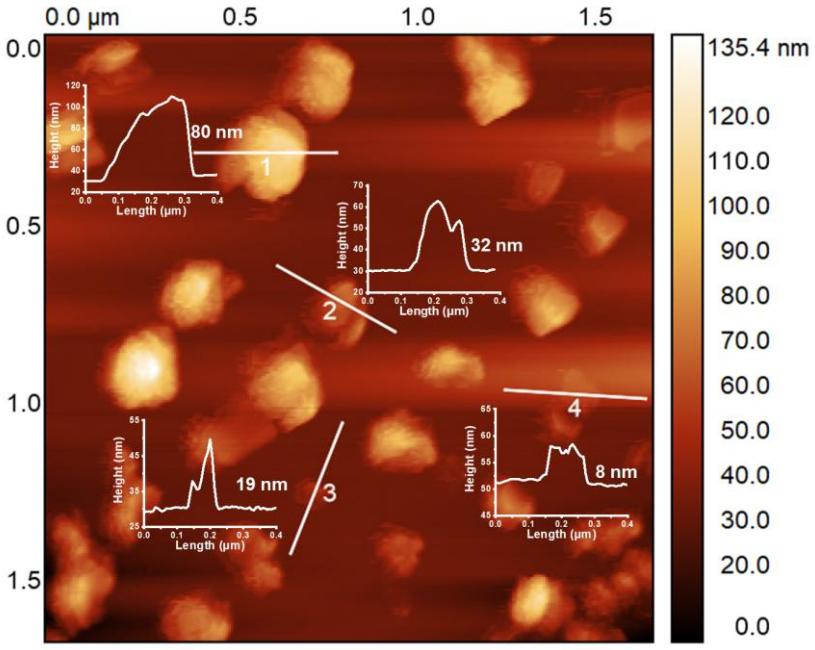

Figure 3.3 - 5 *AFM image of $BiTiS_3$ nanosheets with corresponding height profiles extracted from white lines (inset).*

The UV-Vis-NIR spectra of suspensions with different concentrations of $BiTiS_3$ nanosheets exhibited a broad absorption band ranging from 500 – 1100 nm region (Fig.

3.3-6), promising $BiTiS_3$ as a photothermal agent for NIR-II mild photothermal therapy (PTT).

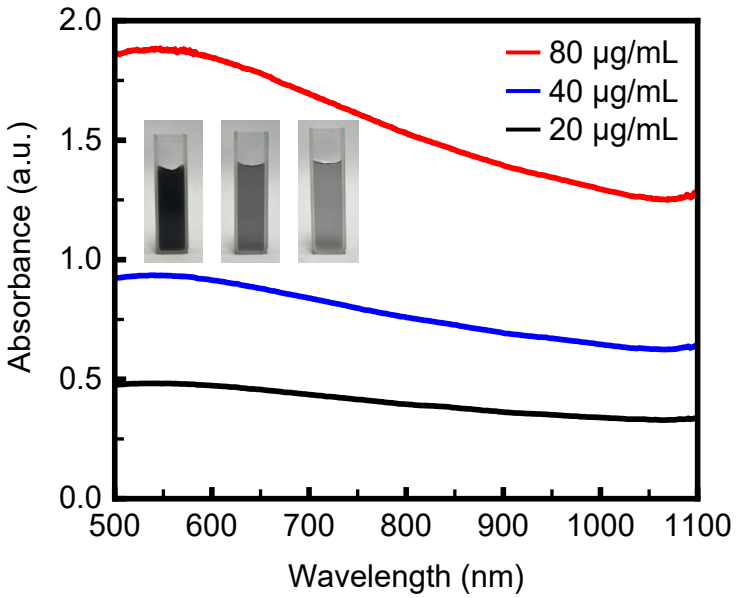

Figure 3.3 - 6 *UV-Vis-NIR absorbance spectra of $BiTiS_3$ nanosheets at different concentrations (80 µg/mL, 40 µg/mL, and 20 µg/mL) with corresponding digital photos (inset).*

The photothermal response of $BiTiS_3$ nanosheets was characterised with a 1064 nm laser. Suspensions of $BiTiS_3$ at concentrations of 20 µg/mL, 40 µg/mL, and 80 µg/mL, each with a volume of 3 mL, were exposed to laser irradiation at a power density of 0.75 W/cm² (Fig. 3.3-7a). It was investigated the trend in temperature elevation which depended on both time and concentration (Fig. 3.3-7b). After 10 minutes of laser irradiation, the temperature of the $BiTiS_3$ suspension rose to 36.2, 42.1, and 48.1 °C from the room temperature of 24.1 °C for the concentrations of 20, 40, and 80 µg/mL, respectively, where DI water increased to 29.5 °C only. The thermal image sequences showed in Fig. 3.3-7b were detected by the use of a thermal imaging camera (Fig. 3.3-7c). To evaluate the photothermal stability, photothermal cycling curves (Fig. 3.3-7d) were obtained using a $BiTiS_3$ suspension at a concentration of 40 µg/mL under the laser irradiation. Five heating-cooling cycles were performed by alternately switching the laser on for 10 minutes and off for 15 minutes. The temperature after heating up per cycle was stabilised at 42.1 °C to 43.3 °C range where the temperature was stabilised at ~ 25.5 °C after cooling down at each cycle. The photothermal performance remained stable without any signs of deterioration.

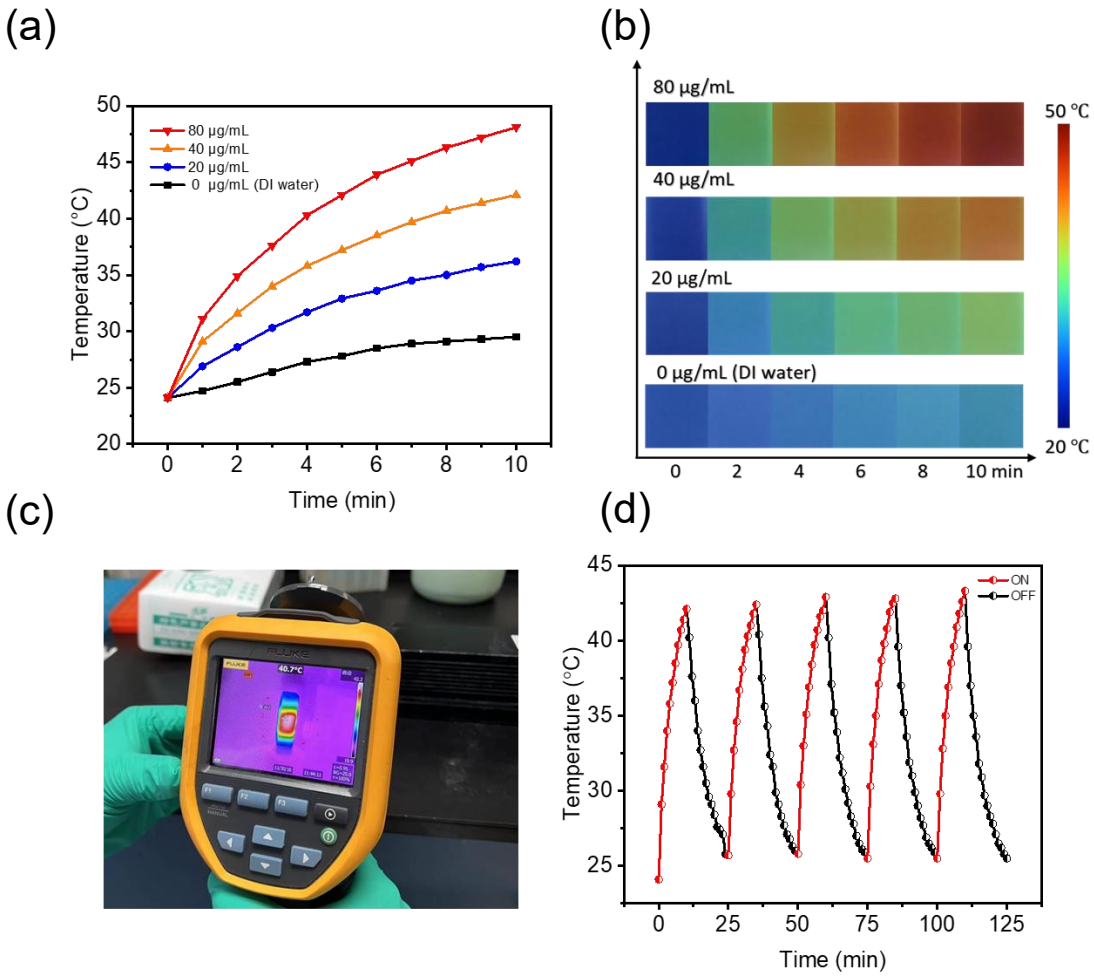

Figure 3.3 - 7 *(a) Photothermal-heating curves against $BiTiS_3$ suspension with different concentrations under 1064 nm laser irradiation at a power density of 0.75 W/cm^2. (b) Thermal images sequences. (c) A thermal imaging camera used for real-time temperature measurement (The temperature values were measured at a representative central region of the BP suspension, as indicated by the thermal images. The absolute temperature values were obtained using a thermal imaging camera and may be subject to uncertainty arising from factors such as emissivity assumptions and environmental conditions; however, the relative temperature changes are considered reliable for evaluating the photothermal performance). (d) Temperature changes of 40 µg/mL $BiTiS_3$ during five laser on/off cycles.*

3.3.3. Orthorhombic molybdenum trioxide (α-MoO_3) 2D nanoflakes

Orthorhombic molybdenum trioxide (α-MoO_3) is a layered metal oxide with pronounced in-plane anisotropy and distinctive optical properties, making it attractive for photonic and optoelectronic applications. It was therefore selected to demonstrate the versatility of the sonication-assisted liquid phase exfoliation method for layered metal oxides. For synthesis of α-MoO_3 2D nanoflakes, a high-yield liquid exfoliation method was carried out [73]. The exfoliation procedure involves three main steps: grinding, probe sonication, and centrifugation. Firstly, 1.0 g α-MoO_3 powder (Merck Life Science, UK) was ground for 30 minutes assisting with 0.2 mL acetonitrile for preventing agglomeration and

enhancing grinding efficiency. Secondly, the ground α-MoO_3 was dispersed in 15 mL of a mixed solution consisting of ethanol and DI water in a 1:1 volume ratio followed by a 2-hour probe sonication at 40W, operated in a cycle of 30 seconds power on and 30 seconds power off. During the probe sonication, the temperature was maintained at 0 ℃ by operating the process in a bath containing a mixture of ice and water. The mixture of ethanol and DI water was used to ensure the proper dispersion of α-MoO_3. Finally, the sonicated α-MoO_3 suspension was centrifuged at a speed of 6,000 rpm for 30 minutes followed by collecting the supernatant. The collected supernatant was further centrifuged at a speed of 12,000 rpm for 10 minutes. The desired α-MoO_3 nanoflakes were obtained by collecting sediment and re-dispersing them into DI water. Fig. 3.3-8a shows digital photos of α-MoO_3 suspensions at different stages: Sample1, 2, 3, and 4 correspond to the suspension (1) before sonication, (2) after sonication, (3) after centrifugation at 6,000 rpm, and (4) after centrifugation at 12,000 rpm followed by re-dispersion into DI water. Both sample 1 and sample 2 are not transparent where sample 2 shows a little bit bright with a slight blue. Sample 3 shows a transparent light blue solution. Sample 4 is the final α-MoO_3 suspension, containing only the sediment obtained after centrifugation at 12,000 rpm, which exhibits a transparent solution without any colour. The corresponding UV-Vis absorption characterization was subsequently performed. As shown in Fig. 3.3-8b, the UV-Vis absorption spectra of α-MoO_3 before and after sonication display broad absorption bands with high absorbance across the entire visible range, corresponding to their non-transparent solutions. The α-MoO_3 suspension after sonication exhibits lower absorbance, indicating the successful exfoliation of thinner nanoflakes. The UV-Vis absorption spectrum of sample 3 has a broad absorption band from 350 to 450 nm, corresponding to the wide band gap (~ 3.3eV) of α-MoO_3 nanoflakes. A very weak absorption signal with a slight increase near 350 nm is observed in the UV-Vis absorption spectrum of sample 4, suggesting that the concentration of dispersed α-MoO_3 nanoflakes in this sample is extremely low, leading to the absence of a pronounced absorption band. Moreover, the weak absorbance suggests that the sediment may contain fewer, thinner, and smaller nanoflakes, as will be further confirmed by subsequent characterisations.

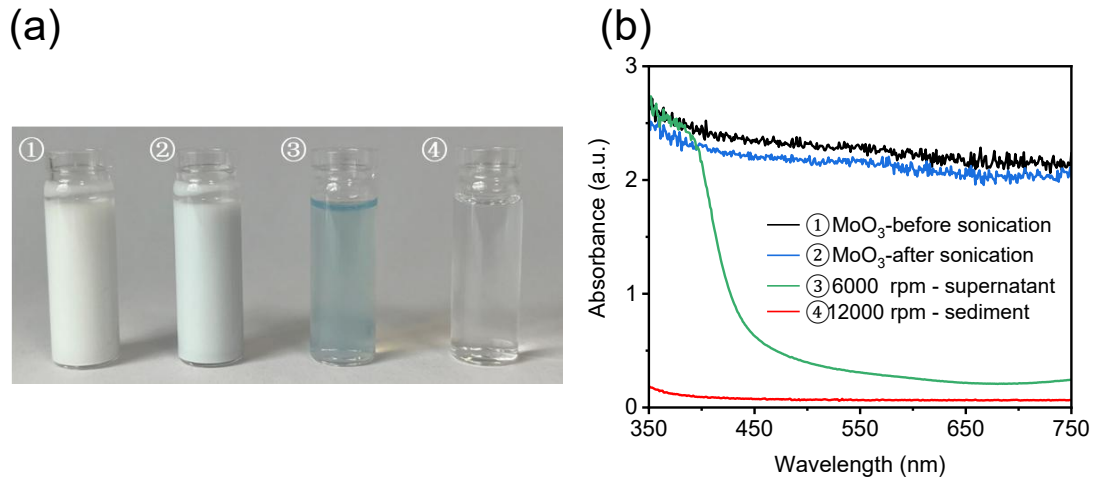

Figure 3.3 - 8 *(a) Digital photos of α-MoO_3 suspensions at different processing stages: (1) before sonication, (2) after sonication, (3) after 6,000 rpm centrifugation, and (4) re-dispersed sediment after 12,000 rpm centrifugation. (b) The corresponding UV-Vis absorption spectra.*

The X-ray diffraction (XRD) analysis was conducted to identify the crystal phase. As shown in Fig. 3.3-9, the dominant peaks at 12.8˚, 25.7 ˚, and 39.0 ˚ (2θ) corresponding to the (020), (040), and (060) planes of orthorhombic α-MoO_3 (DB card number 1537654) were observed in the patterns of both α-MoO_3 powder and α-MoO_3 2D nanoflakes. The lattice parameters of α-MoO_3 were calculated as a = 3.954 Å, b = 13.810 Å, c = 3.689 Å, which agreed with the following TEM and AFM analysis. Identifying the orthorhombic α-MoO_3 phase is essential, as the crystal structure governs the optical anisotropy, exfoliation behaviour, and subsequent device performance upon integration.

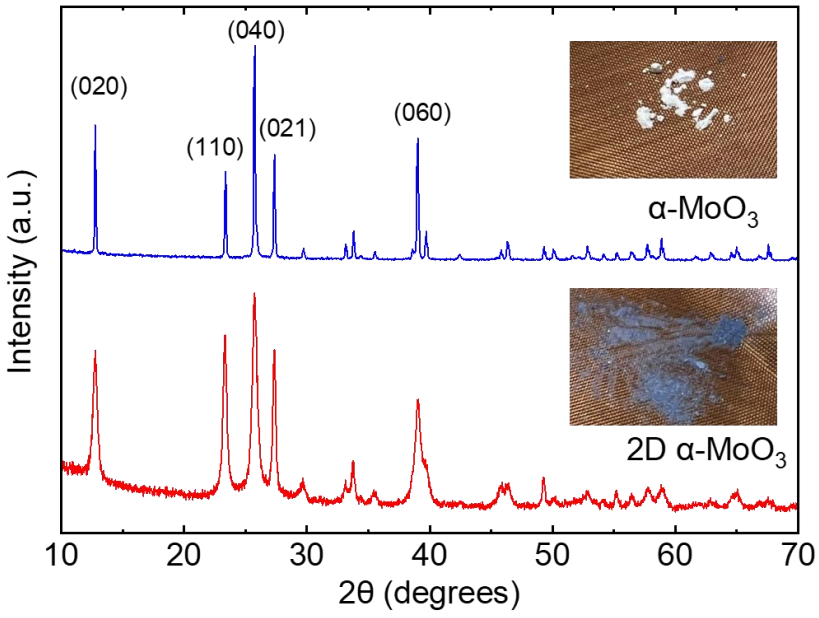

Figure 3.3 - 9 *XRD patterns of α-MoO_3 powder and α-MoO_3 2D nanoflakes (inset: photos of α-MoO_3 powder and α-MoO_3 2D nanoflakes).*

It is worth noting that a higher FWHM was observed in the XRD patterns of α-MoO_3 2D nanoflakes compared to that of α-MoO_3 powder, indicating a smaller grain size of α-MoO_3 2D nanoflakes (Table 3.3-1). The Scherrer formular gives the average grain size of the nanoflakes [102]:

$$\tau = \frac{K\lambda}{\beta \cos\theta} \qquad (3.3-1)$$

where τ is the average size of crystalline domains, K is the dimensionless shape factor with a typical value of ~0.9, λ is the wavelength of X-ray, β refers to the FWHM, and θ is the Bragg angle. α-MoO_3 2D nanoflakes exhibit the higher FWHM, demonstrating the smaller size has been successfully exfoliated. The most intense peaks at 12.8°, 25.7°, and 39.0° (2θ) suggest a preferred orientation along the (020), (040), and (060) planes, supporting the conclusion that the exfoliated 2D nanoflakes consist of parallel planes and maintain a lamellar structure. The relative enhancement of the (110) and (021) peaks in the α-MoO_3 2D nanoflakes may be attributed to preferred orientation effects.

Table 3.3 - 1 *Locations, FWHM, and grain size of α-MoO_3 powder and 2D α-MoO_3 nanoflakes from their XRD patterns.*

Peaks	Locations (˚)		FWHM (˚)		Size (nm)	
α-MoO_3	α-MoO_3 powder	α-MoO_3 2D nanoflakes	α-MoO_3 powder	α-MoO_3 2D nanoflakes	α-MoO_3 powder	α-MoO_3 2D nanoflakes
020	12.76	12.75	0.10	0.44	80.1	19.0
110	23.36	23.32	0.11	0.35	75.0	24.2
040	25.70	25.72	0.10	0.48	81.8	17.7
021	27.32	27.33	0.11	0.27	77.1	32.0
060	39.00	39.00	0.13	0.61	67.5	14.5

The exfoliated α-MoO_3 2D nanoflakes were characterised with TEM for identifying their lateral size and lattice spacing. Fig. 3.3-10a shows the morphologies and dimensions of the as-synthesised α-MoO_3 2D nanoflakes which consist rectangular, rhombic, and ellipsoidal shapes with lateral size ranging from 10 to 70 nm. As shown in HR-TEM image in Fig. 3.3-10b, two sets of parallel line, with lattice spacings of 0.398 nm and 0.374 nm corresponding to the interplanar distances of the (100) and (001) lattice planes, respectively. As the fast Fourier transform (FFT) displayed inset, the rectangular arrangement of diffraction spots confirms the orthorhombic lattice structure of α-MoO_3 2D nanoflakes.

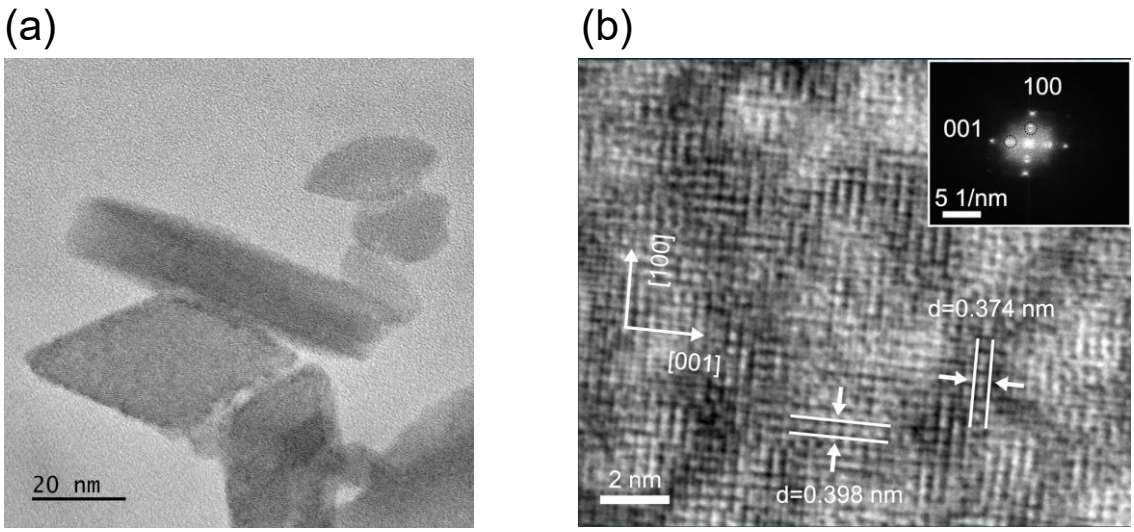

Figure 3.3 - 10 *(a) TEM image of atomically thin α-MoO_3 2D nanoflakes. (b) The HRTEM image with showing distance between lattice fringes (inset: the corresponding FFT image).*

TEMs reveal the in-plane structure of α-MoO_3 2D nanoflakes but lack of information of the out-of-plane structure. Orthorhombic α-MoO_3 is composed of double layers of edge-sharing, distorted MoO_6 octahedra, which are weakly bound vertically by vdW forces [61]. The weak vdW forces enable the exfoliation from bulk α-MoO_3 powder into α-MoO_3 2D nanoflakes, with a theoretical thickness of approximately 1.4 nm for a single unit cell along the (010) plane direction [103].

The AFM tapping mode scan was implemented for the thickness characterisation of α-MoO_3 2D nanoflakes (Fig. 3.3-11). The sediment from the α-MoO_3 suspension (after centrifugation at 12,000 rpm) was drop-cast onto an atomic flat mica film. The thinnest nanoflake was measured as 2.8 nm thick (profile-a in Fig. 3.3-11), which was approximately twice the thickness of one non-repeat unit cell. Another two nanoflakes were measured as 5.6 nm and 9.8 nm in thickness, corresponding to 4 layers (profile-b) and 7 layers (profile-c) of α-MoO_3 2D nanoflakes, respectively. Moreover, the lateral size of measured nanoflakes was found to range from 20 to 50 nm, which was in good agreement with the TEM characterisation.

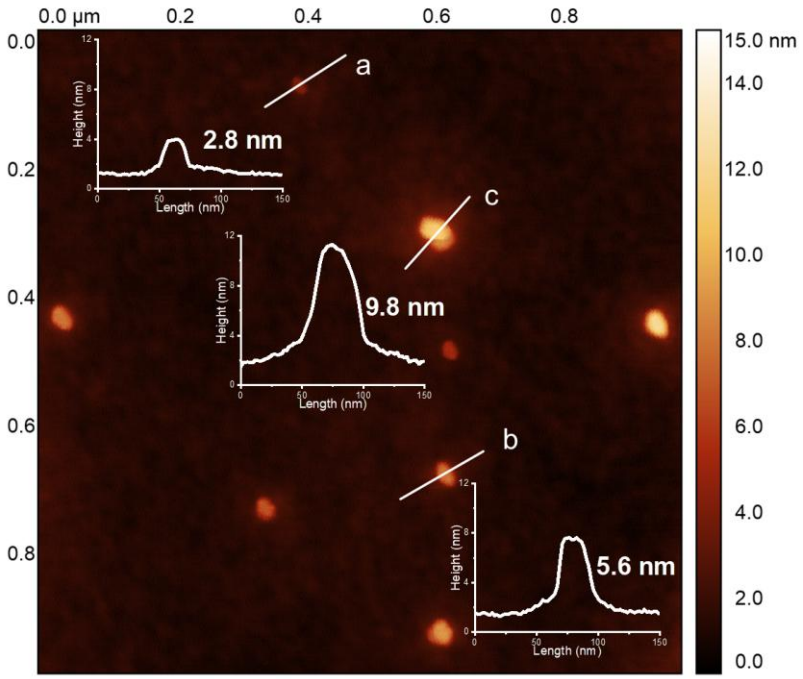

Figure 3.3 - 11 *AFM image of α-MoO_3 2D nanoflakes drop-cast onto a mica substrate (inset: height profiles of three measured α-MoO_3 nanoflakes along white lines).*

To select α-MoO_3 2D nanoflakes of the desired size corresponding to the centrifugation process, AFM characterisation was performed following differential centrifugation (Fig. 3.3-12). As shown in the original α-MoO_3 suspension (after probe sonication but without any centrifugation) in Fig. 3.3-12a, there were two distinct size ranges: the smaller ones ranged from 100 to 200 nm and were well separated, whilst the larger ones ranged from 500 to 1000 nm and tended to aggregate. The layered α-MoO_3 flakes, which were thicker at the centre and gradually thinner toward the edges, were considered to result from incomplete exfoliation. After centrifugation at 6,000 rpm, the sediment (Fig. 3.3-12b) contained mostly larger α-MoO_3 flakes ranging from 500 nm to 1000 nm, whilst the supernatant (Fig. 3.3-12c) contained smaller nanoflakes ranging from 10 to 200 nm. Additionally, some clusters of aggregated nanoflakes were randomly distributed on the mica substrate. Finally, well-dispersed 2D α-MoO_3 nanoflakes with a homogenous size were obtained from the sediment after centrifugation at 12,000 rpm (Fig. 3.3-12d).

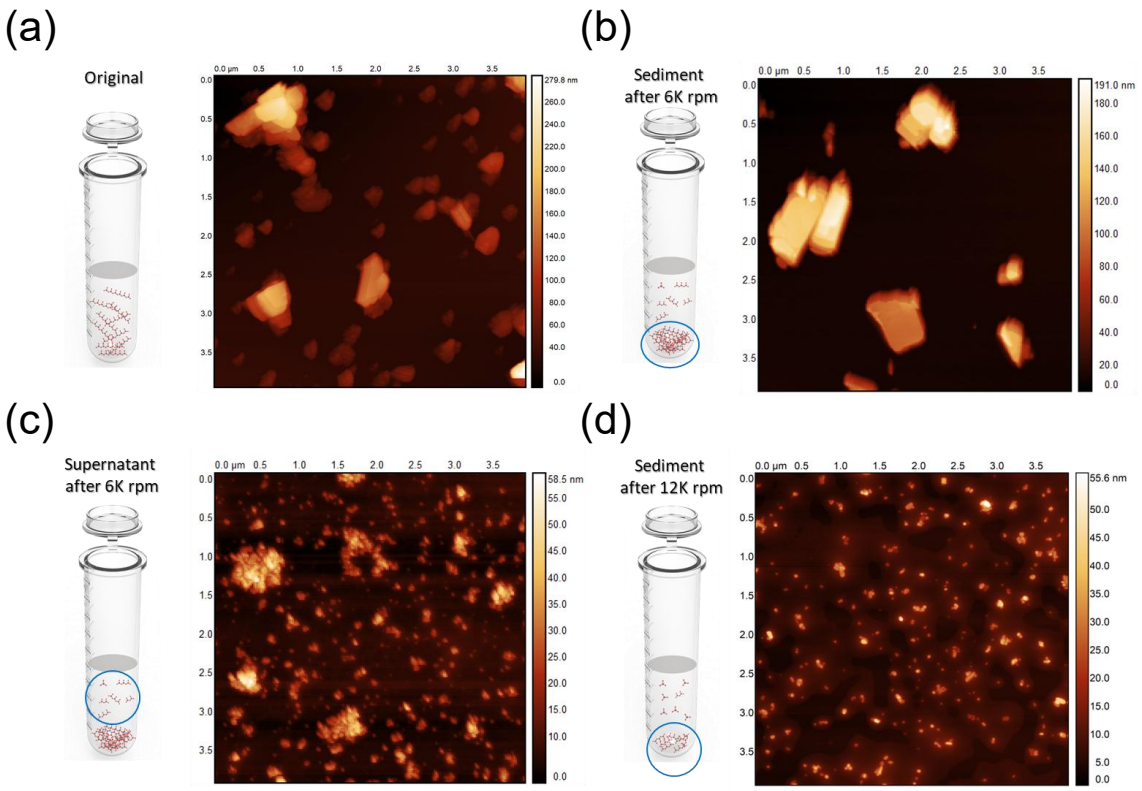

Figure 3.3 - 12 *AFM images of α-MoO_3 at different centrifugation stages, with schematic illustrations highlighting various components in suspensions. (a) The original suspension after probe sonication without any centrifugation. After centrifugation at 6,000 rpm, the sediment (b) and the supernatant (c). (d) The sediment after the centrifugation at 12,000 rpm.*

3.3.4. Graphene Oxide (GO)

Graphene oxide (GO) was selected owing to its unique optical properties, including broadband optical absorption and a high effective refractive index, which enable strong light-matter interaction while maintaining low optical loss in the telecommunication band. In addition, the abundant oxygen-containing functional groups on GO provide excellent aqueous dispersibility, bioaffinity, and surface functionalisation capability, making it highly suitable for chemical and biomedical sensing applications. GO nanosheets were exfoliated from the purchased GO nanocolloids (Merck Life Science, UK) by using bath sonication method. In brief, GO nanocolloids with the concentration of 2 mg/mL was diluted to 0.05 mg/mL followed by bath sonicating for 1 hour. The bath temperature was maintained at 0 °C by using an ice-water mixture during whole sonication process. The sonicated GO was subsequently centrifuged at 3000 rpm for 30 minutes. The desired GO nanosheets were ultimately obtained by collecting the supernatant from the centrifuged GO suspension.

Fig. 3.3-13 reveals the UV-Vis absorption spectrum of GO nanosheets suspension. A weak shoulder-like feature around 300 nm can be observed in the absorption spectrum, which is commonly attributed to the $\pi \rightarrow \pi^*$ transitions of C=O bonds, which is consistent with the presence of oxygen functional groups on GO nanosheets [104,105]. The GO suspension exhibits a dark colour (inset) due to its broad absorption band spanning the visible spectrum.

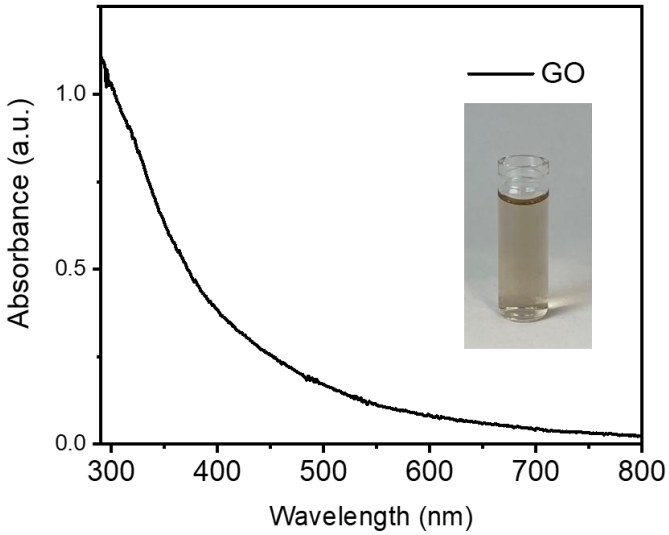

Figure 3.3 - 13 *The UV-Vis absorption spectrum of GO suspension (inset: digital photo of GO suspension).*

The exfoliated GO nanosheets were characterised with AFM (Fig. 3.3-14). The single-layer GO nanosheets were measured to have a thickness of 1.1 nm and a lateral size ranging from 1 to 20 μm. For the profile-c crossing a region with aggregated GO nanosheets, there were three boundary steps corresponding to 1-layer, 2-layer and 3-layer GO nanosheets [106].

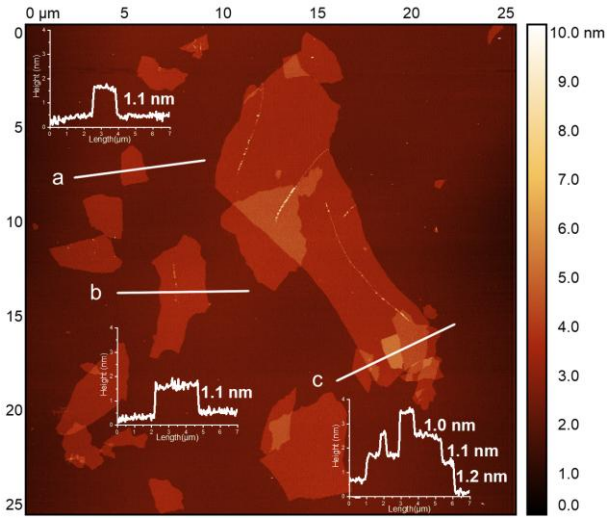

Figure 3.3 - 14 *AFM image of single-layer and few-layer GO nanosheets (inset: height profiles of three measured GO nanosheets along white lines).*

3.4. Electrochemical exfoliation method

Electrochemical exfoliation was employed in addition to sonication-assisted exfoliation to enable the preparation of BP nanosheets with larger lateral dimensions and reduced mechanical damage. While sonication-assisted exfoliation is effective for producing single- and few-layer nanosheets, the electrochemical approach offers improved control over flake size and is therefore suitable for applications requiring larger-area BP flakes and subsequent material loading. The BP nanosheets were synthesised by exfoliating bulk BP with electrochemical method [107]. As shown in Fig. 3.4-1a, the bulk BP was clamped as the cathode, whilst a platinum thin film was placed parallel to the BP at a distance ~ 5cm, serving as the anode. The electrolyte was prepared by mixing 500 mL DMF with 20 g TBAB in a beaker. The BP and platinum were fully immersed into electrolyte followed by applying a voltage of 5 V. The bulk BP was subsequently exfoliated due to the intercalation of TBA^+ ions (Fig. 3.4-1b). The BP was collected after it completely converted into a larger sponge-like structure, with some flakes detaching and settling at the bottom of the beaker. the collected BP was washed for 4 times with DMF for removing unwanted residual. After washing process accompanying with centrifugation at 12,000 rpm for 10 minutes, the sediments were collected, for further bath sonication for 2 minutes to obtain well-dispersed BP nanosheets. The as-prepared BP nanosheets were re-dispersed into DI water for downstream using (Fig. 3.4-1c). To prevent degradation and oxidation, the synthesised BP nanosheets were stored in a glove box filled with argon. Compared to ultrasonic exfoliation, BP nanosheets synthesised by electrochemical exfoliation exhibited larger lateral size which were suitable for further loading of nanomaterials.

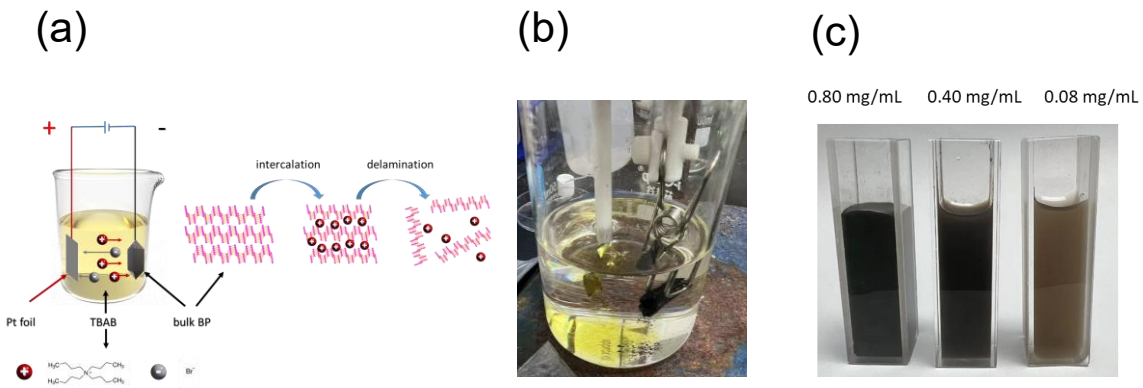

Figure 3.4 - 1 *(a) Schematic illustration of the electrochemical exfoliation of BP. (b) Photo of BP exfoliation. (c) Photo of BP nanosheets dispersed in water with different concentrations.*

The photothermal response of BP nanosheets was examined by the use of an 808 nm laser with a power density of 1.0 W/cm². The stored BP suspension was diluted into different concentrations (0.80, 0.40, and 0.08 mg/mL), then exposed to the laser irradiation at a power density of 1.0 W/cm². As shown in Fig. 3.4-2a, the temperature elevation trend was found to depend on both time and concentration. After 10-min's laser irradiation, the temperature of the BP suspension was increased by 18.1, 25.9, and 33.7 ℃ for the concentrations of 0.08, 0.40, and 0.80 mg/mL, respectively. By comparison, the temperature of DI water was increased by 1.4 ℃ only. A direct quantitative comparison with Fig. 3.3-7 is not appropriate due to differences in irradiation wavelength, power density, and suspension concentration. Qualitatively, the electrochemically exfoliated BP exhibits a more rapid temperature increase during the initial irradiation period, followed by a gradual saturation at longer times. This behaviour is consistent with the larger lateral size of electrochemically exfoliated BP flakes and the onset of thermal equilibrium with the surrounding environment.

To further evaluate the photothermal stability, the BP suspension at a concentration of 0.40 mg/mL was employed for the photothermal cycling with a laser on/off irradiation (Fig. 3.4-2b). Five heating-cooling cycles were performed by alternately switching the laser on for 2 minutes and off for 13 minutes. The temperatures of the BP suspension were stabilised at ~ 48.7 °C and ~ 25.5 °C after heating and cooling down, respectively. For the first cycle, the temperature was reached 46.9 °C only due to an initial lower temperature started. The photothermal performance remained stable without any sign of deterioration during the 5 heating-cooling cycles. Fig. 3.4-2c demonstrates thermal images of BP suspensions with various concentrations under different laser irradiation durations.

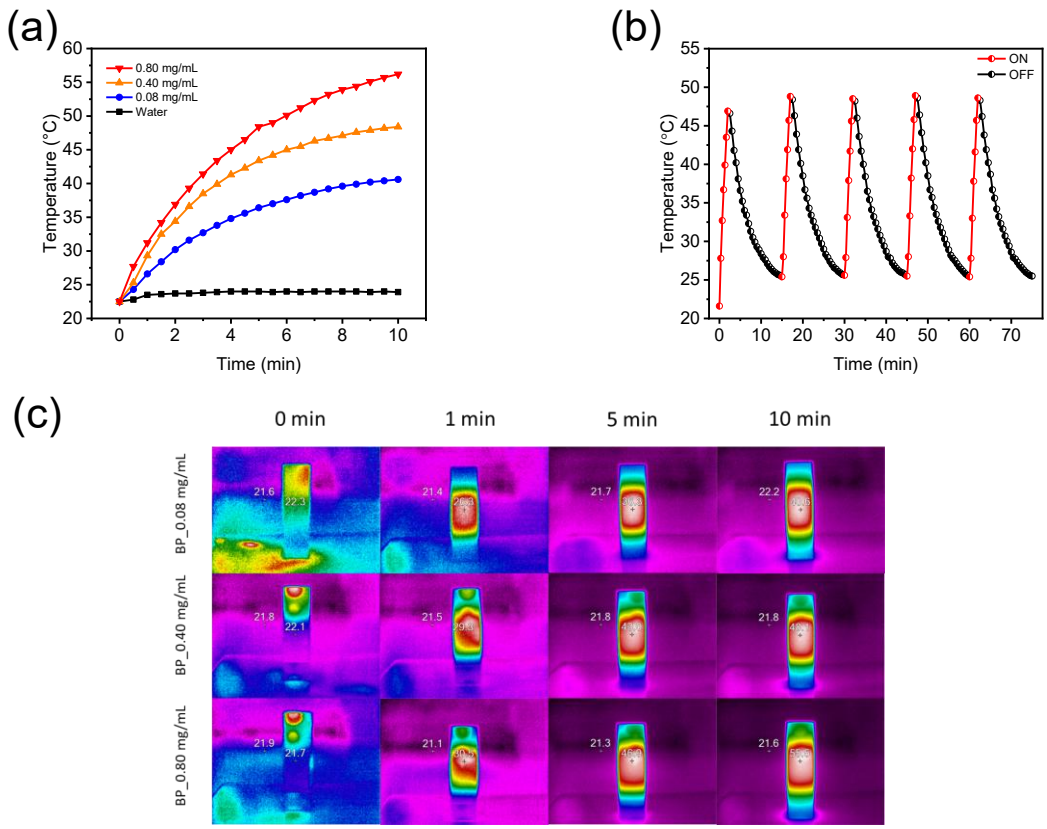

Figure 3.4 - 2 *(a) Photothermal-heating curves against BP suspension with different concentrations under laser irradiation (at 808 nm, 1.0 W/cm^2). (b) Temperature changes of 0.40 mg/mL BP during five laser on/off cycles. (c) Infrared thermographic maps of in vitro photothermal of BP suspensions (The temperature values were measured at a representative central region of the BP suspension, as indicated by the thermal images).*

3.5. Selective etching method

Selective etching was employed in this work to enable the controlled removal of the aluminium layer from the Ti_3AlC_2 MAX phase, thereby producing 2D $Ti_3C_2T_x$ MXene nanosheets. This chemical etching and delamination process transforms the parent MAX phase into a loosely stacked layered MXene structure, while preserving the integrity of the transition metal carbide layers. Here, the minimally intensive layer delamination (MILD) method with slight modification was developed for the synthesis of $Ti_3C_2T_x$ MXene nanosheets (Fig. 3.5-1). A mixture of a fluoride salt, lithium fluoride (LiF), and hydrochloric acid (HCl) was used to generate hydrofluoric acid (HF) in situ to selectively etch aluminium (Al), which is much milder and safer than using HF directly [108,109]. Firstly, 2 g LiF powder was dissolved in 35 mL of 10M HCl to form LiF/HCl mixture. 2 g of Ti_3AlC_2 MAX precursor was suspended into 5mL deionized (DI) water to form stable MAX suspension which was pipetted into the LiF/HCl mixture slowly and followed by mild string at 35 °C for 24 hours. Secondly, the above-prepared solution was centrifuged

(3500 rpm, 5 minutes) and washed with DI water multiple times until the pH of the supernatant reached 5.5. After discarding the supernatant, 40 mL of DI water was added to the sediment, primarily containing multi-layered $Ti_3C_2T_x$, followed by exfoliating with vortex for 1 hour. Finally, the single- or few-layered $Ti_3C_2T_x$ nanosheets suspension was obtained by collecting the supernatant after centrifugation at 3500 rpm for 1 hour. This process enabled the synthesis of high-quality MXene under mild reaction conditions, which was facilitated by the weak acidity of the solution. To determine the concentration, a dried film from vacuum filtration of a certain volume of the $Ti_3C_2T_x$ dispersion was weighed.

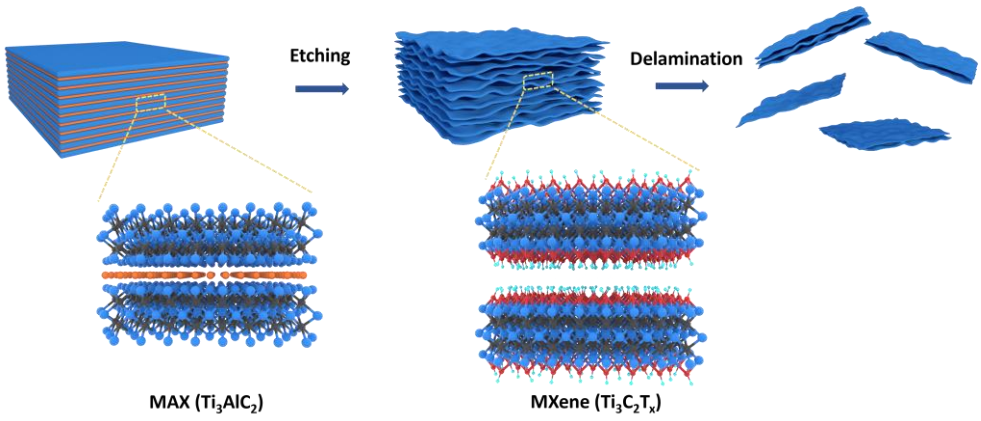

Figure 3.5 - 1 *The schematical diagram for the synthetic processes of $Ti_3C_2T_x$ MXene nanosheets, using in situ hydrofluoric acid (HF) method. (left) Parent layered Ti_3AlC_2 MAX phase, (middle) etched $Ti_3C_2T_x$ MXene, and (right) delaminated $Ti_3C_2T_x$ MXene nanosheets.*

The morphologies and elemental distribution of $Ti_3C_2T_x$ MXene were firstly characterised by SEM and EDS (Fig. 3.5-2a). The SEM image of $Ti_3C_2T_x$ MXene exhibited its accordion-like structure after the successful etching of the Al layer. The EDS elemental mapping revealed a uniform distribution of all elements across the $Ti_3C_2T_x$ MXene sheets, confirming their homogeneous elemental composition. AFM was utilised for characterising the height of MXene nanosheets. As shown in Fig. 3.5-2b, a single layer with height of 1.5 nm was observed, demonstrating the successful exfoliation of monolayer-thick MXene nanosheets. The lateral size of MXene nanosheets were found from 0.5 – 3.0 µm. The Raman spectrum of MXene was further characterised (Fig. 3.5-2c). The peaks at 199 and 723 cm^{-1} correspond to the out-of-plane vibrations of A_{1g} (Ti, O, C) and A_{1g} (C), respectively. The peaks at 286, 384, 577, and 623 cm^{-1} correspond to the E_g group vibrations associated with in-plane modes of Ti, C, and surface functional group atoms [110]. TEM was employed to investigate the exfoliated $Ti_3C_2T_x$ MXene nanosheets. As shown in Fig. 3.5-2d, a monolayer nanosheet with a lateral size of

approximately 0.8–1.0 µm is observed, which is consistent with the AFM measurements. The corresponding selected area electron diffraction (SAED) pattern (inset of Fig. 3.5-2d) exhibits clear hexagonal symmetry of the lattice planes. Additionally, the exfoliated mono- and bilayer of $Ti_3C_2T_x$ nanosheets were found in the cross-sectional TEM image (Fig. 3.5-2e).

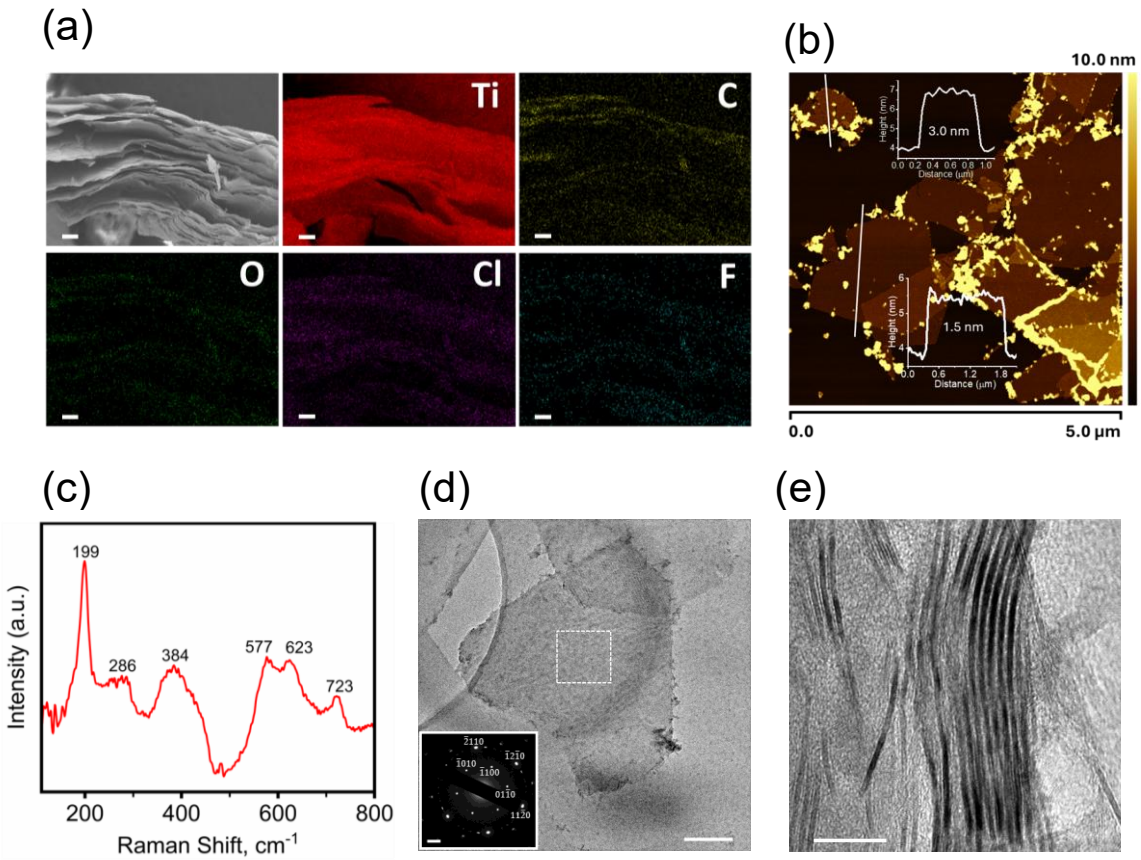

Figure 3.5 - 2 *(a) SEM image and corresponding elemental mapping of Ti, C, O, Cl, and F in layered $Ti_3C_2T_x$ MXene (scale bar = 20 µm). (b) AFM image of $Ti_3C_2T_x$ nanosheets with corresponding height profiles extracted from white lines (inset). (c) Raman spectrum of $Ti_3C_2T_x$ MXene. (d) TEM image of a monolayer $Ti_3C_2T_x$ nanosheet (scale bar: 200 nm) and selected area diffraction patterns (inset, scale bar: 2 nm^{-1}). (e) Cross-sectional TEM image of mono- and bilayer $Ti_3C_2T_x$ nanosheets.*

The optical absorbance of the $Ti_3C_2T_x$ MXene dispersion was characterised using UV–Vis-NIR spectroscopy, as presented in Fig. 3.5-3. The shoulder of the absorption spectrum, located at 300 nm, is characteristic of freshly prepared $Ti_3C_2T_x$ dispersions, as previously reported [111,112]. In addition, a broad absorption feature centred around 805 nm is attributed to the plasmonic response of the $Ti_3C_2T_x$ nanosheets [113]. The inset shows a clear linear correlation between absorbance at 755 nm and MXene concentration, indicating good dispersibility and stability of the nanosheets in the aqueous medium.

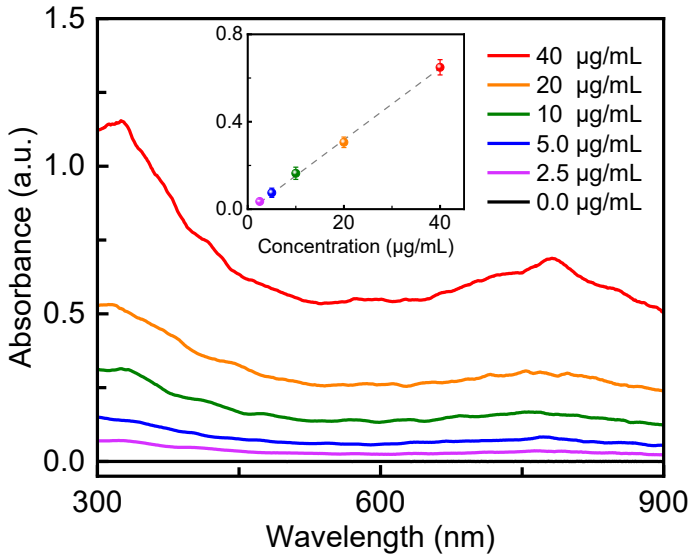

Figure 3.5 - 3 *The UV–Vis-NIR spectroscopy of diluted $Ti_3C_2T_x$ MXene dispersions. Inset: Absorbance values at 755 nm for dispersions with concentrations of 2.5, 5, 10, 20, and 40 µg/mL, demonstrating a linear relationship between concentration and absorbance (Data are presented as mean ± standard deviation from three independent experiments).*

3.6. 'One-pot' seedless synthesis

A new technique termed as 'one-pot' seedless was developed for synthesis of small gold nanorods (sAuNRs) (Fig. 3.6-1) [114]. Initially, a mixture was prepared by combining 5 mL of 0.2 M CTAB, 1 mL of 5 mM $HAuCl_4$, and 4.5 mL of deionized water in a 50 mL glass beaker. Subsequently, a volume of 250 µL of 4 mM $AgNO_3$ followed by 500 µL of 0.1 M NaOL was introduced into the solution under gentle stirring. This was followed by the addition of 8 mL of concentrated HCl (36%-38%), and finally 56 µL of 0.1 M ascorbic acid was introduced with slight swirling. The solution changed from dark orange to colourless, indicating the reduction of Au^{3+} to Au^{+}. Next, 15 µL of freshly prepared, ice-cold 10 mM $NaBH_4$ was added to the beaker. The solution was gently mixed for 10 seconds and then left undisturbed in an incubator at 35°C for 3 hours to facilitate the reduction of Au^{+} to Au^{0}. Subsequently, centrifugation was performed at 12,000 rpm for 20 minutes to collect the final product. The desired sAuNRs suspension was obtained by collecting the sediment and re-suspending it in DI water (Fig. 3.6-1b). In this method, the length and LSPR band of the sAuNRs can be readily tuned by modifying the quantity of NaOL. For example, a small diameter of ~7 nm of the AuNRs was achieved [114]. Fig. 3.6-1c shows the UV-vis-NIR absorption spectrum of the sAuNR with a strongest absorption at 809 nm, which is ideal for NIR-I photothermal therapy.

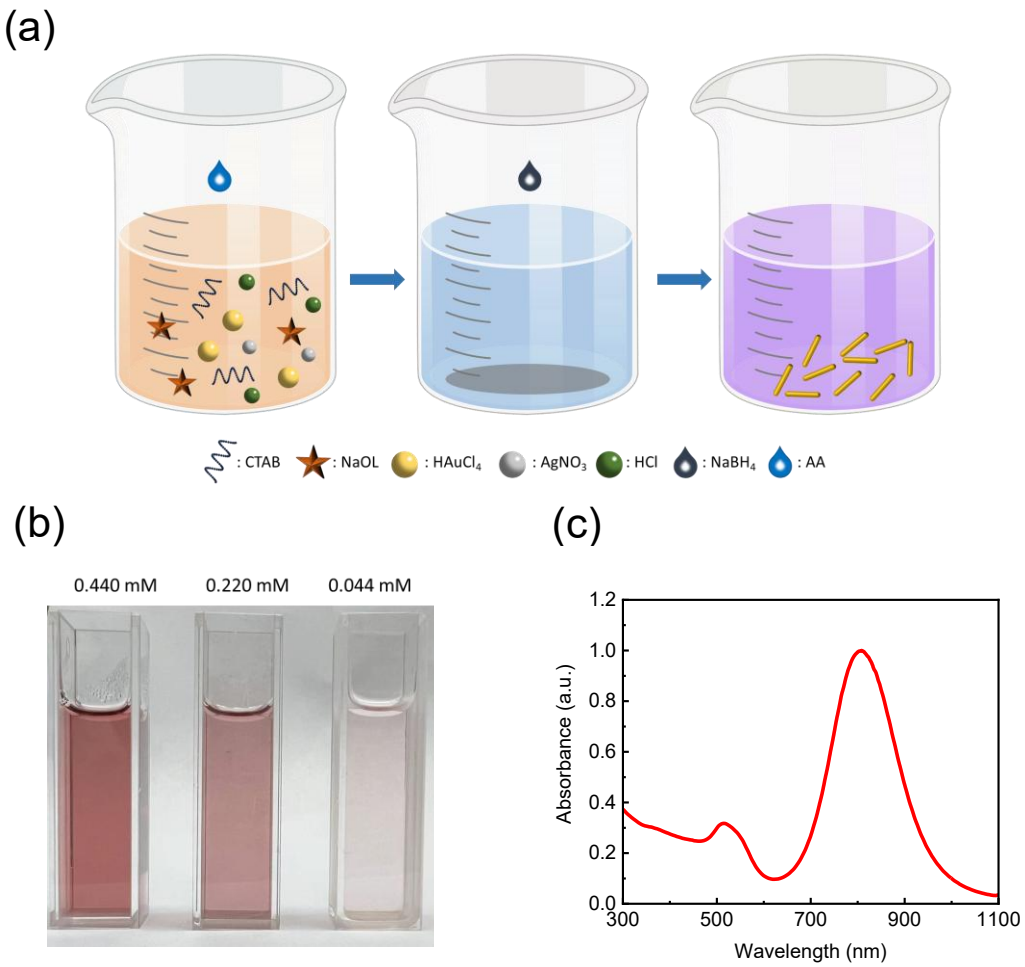

Figure 3.6 - 1 *(a) Schematic illustration of the 'one-pot' seedless synthesis of small gold nanorods. (b) Photographic image of aqueous dispersions of sAuNRs at different concentrations. (c) UV–Vis–NIR absorption spectrum of sAuNR with the concentration of 0.440 mM.*

3.7. Chapter summary

This chapter begins with an introduction to 2D materials, followed by an in-depth discussion of selected examples, including graphene, GO, MXenes, and α-MoO_3. Advanced synthesis techniques are then reviewed and categorised into 'top-down' and 'bottom-up' approaches. Commonly employed synthesis methods, such as mechanical cleavage, sonication-assisted liquid-phase exfoliation, and CVD, are examined in detail, highlighting their respective advantages and limitations. Finally, various synthesis methods implemented by the author for fabricating 2D materials are presented and discussed. The synthesis methods implemented in this chapter can be compared in terms of their governing mechanisms, material applicability, and downstream compatibility. Sonication assisted liquid phase exfoliation provides a general and scalable route for van der Waals layered crystals, enabling single- and few-layer nanosheets with good solution processability for subsequent coating and integration. Electrochemical exfoliation offers an alternative route that can yield larger lateral flakes and improved structural integrity, which is advantageous when larger area nanosheets are required for further material loading and device fabrication. In contrast, selective etching is specifically employed for MAX phase precursors to obtain $Ti_3C_2T_x$ MXene through controlled removal of the Al layer and subsequent delamination into a loosely stacked two-dimensional structure. Accordingly, the selection of synthesis strategy is primarily guided by the parent crystal structure and bonding characteristics of the material, together with practical requirements such as flake size and dispersion stability, surface chemistry and functionalisation capability, and compatibility with the integration routes used in the subsequent photonic and optoelectronic sensing applications. In addition, the surface morphology, elemental composition, structural properties, and optical properties characterisation are analysed using SEM, EDS, TEM, AFM, XRD, UV-Vis-NIR spectrophotometer, Raman spectrophotometer, and thermal imaging camera.

Chapter 4 2D materials deposition and integration

As outlined in the previous chapter, various 2D materials can be fabricated by different synthesis methods in either liquid or solid phases. However, the successful integration of 2D materials with the optoelectronic devices relies not only on 2D materials synthesis but also on reliable deposition techniques that preserve the intrinsic properties whilst ensuring uniform coverage, scalability, and compatibility with existing device architectures.

The choice of deposition method plays a crucial role in determining the material's structural quality, optical properties, and electronic performance. Conventional techniques such as wet transfer [115], dry transfer [116], spin coating [117], and dip coating [118] have been widely employed, each offering distinct advantages depending on the specific applications. However, challenges such as film uniformity, layer thickness, surface roughness, and interfacial adhesion remain critical considerations when selecting an appropriate deposition approach [119].

This chapter will provide an overview of conventional deposition techniques, highlighting their advantages and limitations. It will also discuss the deposition strategies developed by the author in this PhD programme, along with the corresponding characterisations including optical microscopy, SEM, AFM, EDS, XPS, and Raman spectroscopy to evaluate the morphologies and composition of the deposited 2D materials and nanocoatings.

4.1. Current deposition methods

The wet transfer method is a widely used technique for integrating 2D nanomaterials into optoelectronic devices for various downstream applications. This process involves using a liquid medium to facilitate the transfer of thin films or nanomaterials from one substrate to another. In wet transfer, based on the method used for sample delamination from the growth substrate, it can be categorized into (a) chemical etchant-assisted [120], (b) electrochemical [121], and (c) surface-energy-assisted wet transfer [122].

(a) In a typical etchant-assisted wet transfer process (Fig. 4.1-1a), the 2D material grown on metal substrate is firstly coated with a polymer support layer (e.g., PMMA) through spin coating. The metal substrate is then dissolved using an appropriate etchant, allowing the polymer/2D material stack to be separated. After thorough cleaning, the stack is transferred onto the target substrate, and the polymer layer is finally removed using organic solvents (Fig. 4.1-1a). The polymer supporting layer plays a crucial role in the wet transfer method. Its high flexibility, mechanical strength, and resistance to water and etchants ensure that the 2D materials are well protected throughout the transfer process, preserving their structural integrity and minimising potential damage. However, the high cost of noble metal substrates, the time-consuming etching process, and the environmental impact of chemical etchants limit the applicability of this method.

(b) The electrochemical transfer, also known as bubbling transfer method, utilise the bubbles generated at the interface between 2D materials and metal substrates to facilitate the delamination (Fig. 4.1-1b). During the delamination process, a direct current voltage is applied between the polymer/2D materials/substrate cathode and a counter anode within an electrolytic cell. An aqueous electrolyte solution, such as NaCl or KCl, is used. As the H_2O undergoes the reduction at the interface between 2D materials and metal substrate where hydrogen bubbles are generated. A persistent force is provided to lift the PMMA/2D material stack from the metal substrate. Unlike etchant-assisted transfer, this method eliminates the use of chemical etchants and allows for the recycling of metal substrates, making it both environmentally friendly and cost-effective. Additionally, the bubbling transfer process is generally faster, as the delamination time can be controlled by adjusting the applied voltage. However, this method requires the original substrate to be conductive, limiting its applicability to materials synthesised on dielectric substrates. Moreover, the formation of hydrogen bubbles may introduce mechanical damage to the transferred 2D materials [123,124].

(c) The surface-energy-assisted wet transfer (Fig. 4.1-1c) is an alternative etchant-free wet transfer technique [122] that employs capillary forces to delaminate and transfer 2D materials [125]. During the delamination process, hydrophilic dielectric growth substrates, such mica, SiO_2/Si wafer, and sapphire, are commonly used. As the hydrophilic substrates and hydrophobic polymer layer are penetrated by water, the polymer/2D material film is lifted off, enabling the further transfer of 2D materials onto target substrates (Fig. 4.1-1c). The surface-energy-assisted transfer method owns several advantages. It is simple to execute without involving complicated and potentially harmful

processes, such as etching or electrochemical delamination. However, applications of this transfer method are limited due to several drawbacks: i) the weak capillary force requires a long time to delaminate the polymer/2D material film. ii) the original substrates must be hydrophilic, with adhesion weaker than the capillary force. iii) it has been reported that 2D materials transferred using this method often exhibit non-ideal wrinkles and bubbles, caused by the strain generated during the delamination process [126–128].

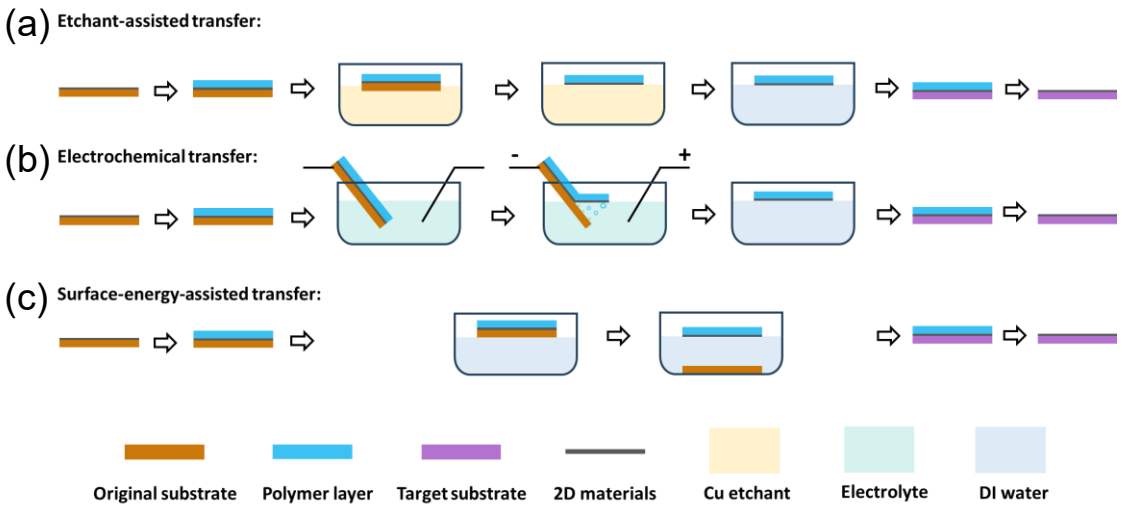

Figure 4.1 - 1 *Schematic illustration of (a) the etchant-assisted transfer, (b) electrochemical transfer, and (c) surface-energy-assisted transfer methods. reproduced with permission from Ref. [129].*

The dry transfer method is widely used in the fabrication of 2D vdW heterostructures which involves transferring 2D samples with an elastomer stamp as the supporting material. A PDMS supporting layer is typically used to pick up the 2D materials from the original substrate and release them onto the target substrate based on the principles of viscoelastic stamping [129]. During the 'pick up and release' process, a strong adhesion between samples and stamp is required to successfully 'pick-up' the 2D materials from their growth substrates, whilst a relatively weaker adhesion between samples and the target substrate is desired to facilitate the 'release' step. Fig. 4.1-2 illustrates the experimental setup and the process of the dry transfer method [130]. The experimental setup includes a 3-axis adjustable lower stage on which the sample (2D crystal flake/SiO_2 substrate) is placed, an upper stage with a polymer stamp fixed onto a glass slide, and an optical microscope for monitoring the stage movement and sample alignment (Fig. 4.1-2a). The dry transfer process (Fig. 4.1-2b) involves a pick-up step at 50 °C, where the adhesion of PVC stamp is strong to pick up the 2D crystal flake, followed by a release step at 100 °C where the adhesion of PVC is relatively weak to transfer the 2D crystal

flake onto a target substrate. Finally, the PVC stamp is slowly peeled off to complete the transfer.

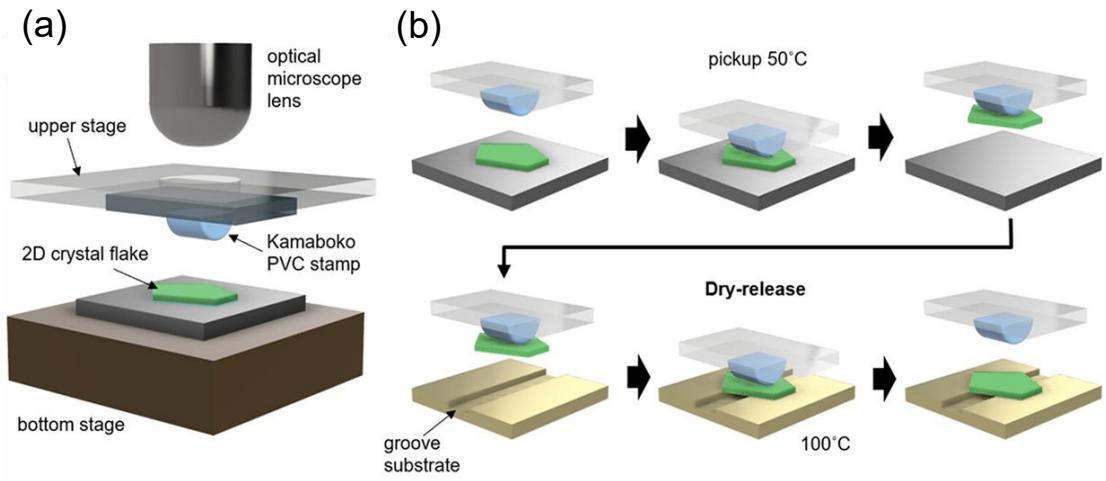

Figure 4.1 - 2 *Schematic illustration of 2D crystal flake transfer. (a) experimental setup. (b) The dry transfer process [130].*

Compared to the wet transfer methods, the dry transfer technique is more scalable for large-area or mass production since it does not rely on wet chemicals, which are difficult to control and replicate on a large scale. Additionally, it provides better alignment control during the transfer process, making it ideal for high-precision applications requiring accurate material positioning. Another advantage is the reduced risk of contamination, as eliminating liquid-based processes minimises impurities that could affect material quality. However, the dry transfer often involves direct physical contact or pressure, increasing the risk of cracks, wrinkles, or defects, particularly in delicate 2D materials or thin films. Moreover, methods utilising polymer stamps or mechanical exfoliation may require specialised equipment, adding complexity and cost compared to the wet transfer techniques [131,132].

Drop casting is a straightforward and rapid deposition technique, which has been widely used for coating 2D nanomaterials that suspended in liquid phase [133–135]. In this method, a specified amount of sample suspension is deposited onto a substrate and left to evaporate. As the solution dries, a thin film or dispersed 2D materials cluster is formed on the substrate. The primary advantage of this approach is its simplicity. However, its main drawbacks include challenges in achieving a uniform and continuous coating, as well as the inability to precisely control the thickness of the deposited layer [136]. Nevertheless, when a uniform coating is unnecessary, such as for analysing the surface morphology of 2D materials (nanosheet lateral size and thickness), the drop casting

method allows for the controlled dispersion of nanosheets or nanoparticles on a substrate by simply adjusting the material concentration and the volume of liquid dropped onto the substrate.

Spin coating is a technique used to deposit consistent and uniform thin films of 2D materials onto the flat substrates, ranging from nanometres to micrometres. Fig. 4.1-3 illustrates the process of spin coating. In brief, the solution is dropped onto a substrate held by the vacuum chuck within a spin coater, allowing it to spread evenly across the surface as the substrate rotates at a controlled speed. The spinning process begins with a set acceleration and maintains a constant speed for a specific duration, allowing the coating material to be evenly distributed by centrifugal force. Excess fluid is expelled from the edges until the desired film thickness is achieved through a combination of liquid flow and evaporation. The final thickness and film characteristics depend on the rotation speed (rpm) and duration [136,137]. Additional treatments, such as heat or UV exposure, may be required depending on the solution's properties [138]. However, the spin coating method still has some drawbacks that limit its use. First, achieving uniform film thickness can be challenging, especially for very thin layers or highly viscous liquids. Second, spin coating can produce inconsistent results, especially on substrates that are not flat or have varying surface energy, which may lead to non-uniform coatings. Third, the technique works best on flat surfaces. Coating irregular or non-planar surfaces can be difficult and lead to poor film quality [139,140].

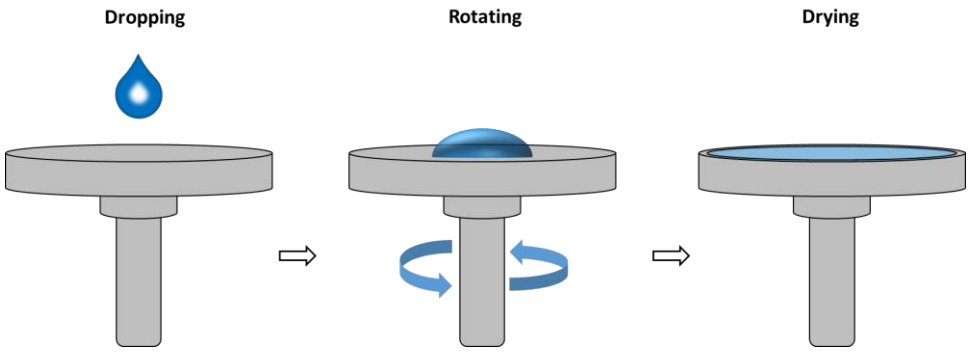

Figure 4.1 - 3 *Schematic illustration of the spin coating.*

Dip coating is another relatively simple, low-cost, and scalable deposition method, making it a widely used technique for applying 2D materials onto substrates such as Si/SiO_2 wafers, metal, fibres, etc., to achieve high uniformity thin-film deposition [141–143]. This method does not require any special or expensive equipment [144]. In a standard process, dip coating involves immersing a substrate into a precursor solution, followed by slowly lifting it out to form a liquid film. This process consists of four

stages [145]: 1) Immersion, where the substrate is dipped at a uniform speed; 2) Pull-up, where it is slowly lifted, allowing the film to deposit, with the speed affecting film thickness; 3) Deposition, where uniform layers form as the substrate is pulled up; 4) Evaporation, where the solvent evaporates to solidify the film. As mentioned, this approach is ideal for substrates that are flexible and irregularly shaped, as it enables the solution to cover the entire surface of the substrate. However, the control over the layer thickness is limited, as it is influenced by factors like the surface morphology and tension of the textile substrate [146], along with processing parameters including time, temperature, withdrawal speed, and the concentration and composition of the coating bath [144]. Additionally, the dip coating requires a large volume of precursor solution, leading to considerable material waste.

4.2. In-situ layer-by-layer (i-LbL) deposition technique

The in-situ layer-by-layer (i-LbL) deposition technique, combining chemical bonding and multiple physical adsorptions, has been developed for the deposition of 2D materials onto optical fibres [1]. In brief, the bare optical fibre undergoes a silanisation process to facilitate the deposition of 2D nanosheets. Then fibre is then immersed in the target suspension of 2D nanosheets within a home-made mini bath with gentle heating. As the water evaporates, 2D nanosheets gradually deposit onto the fibre surface. In this work, the method was further adapted and optimised by the author, particularly to improve coating uniformity through controlled fibre rotation between successive deposition cycles when thicker coating is required, as discussed later in this chapter.

4.2.1. Graphene oxide deposition on fibre and characterisation

The optical fibre is firstly cleaned with acetone (Fig. 4.2-1a) for 30 minutes, then immersed in 1.0 M NaOH solution for 1 hour, followed by washing with DI water and drying thoroughly (Fig. 4.2-1b). This alkaline treatment enriches the fibre surface with hydroxyl (-OH) groups, facilitating subsequent functionalization. The hydroxyl-enriched optical fibre is then silanised by incubating it in a 5% (v/v) (3-Aminopropyl)triethoxysilane (APTES) solution for 20 minutes at room temperature. Afterward, the fibre is rinsed with ethanol then baked in an oven at 70°C for 30 minutes to stabilise the Si-O-Si bonding (Fig. 4.2-1c). Next, the APTES-silanised optical fibre is immersed in a 1 mL suspension of GO nanosheets (0.10 mg/mL) contained in a custom-made mini-bath, which is placed on a hotplate at ~ 42°C for 40 minutes (Fig. 4.2-1d). As

the suspension evaporates, GO nanosheets chemically bond to the optical fibre surface through the reaction between epoxy groups of GO and amino groups of the APTES-silanised surface [147]. Once the suspension has completely evaporated, a second coating cycle is applied by adding another 1 mL of the GO suspension to facilitate physical adsorption between the pre-coated GO layer and newly introduced GO nanosheets. This coating process can be repeated multiple times to achieve the desired thicknesses of overlay. After completing the coating cycles, the GO-coated optical fibre is washed with DI water to remove any unbonded nanosheets and then baked in an oven at 35℃ for 12 h to enhance adhesion and stability of the GO overlay (Fig. 4.2-1e).

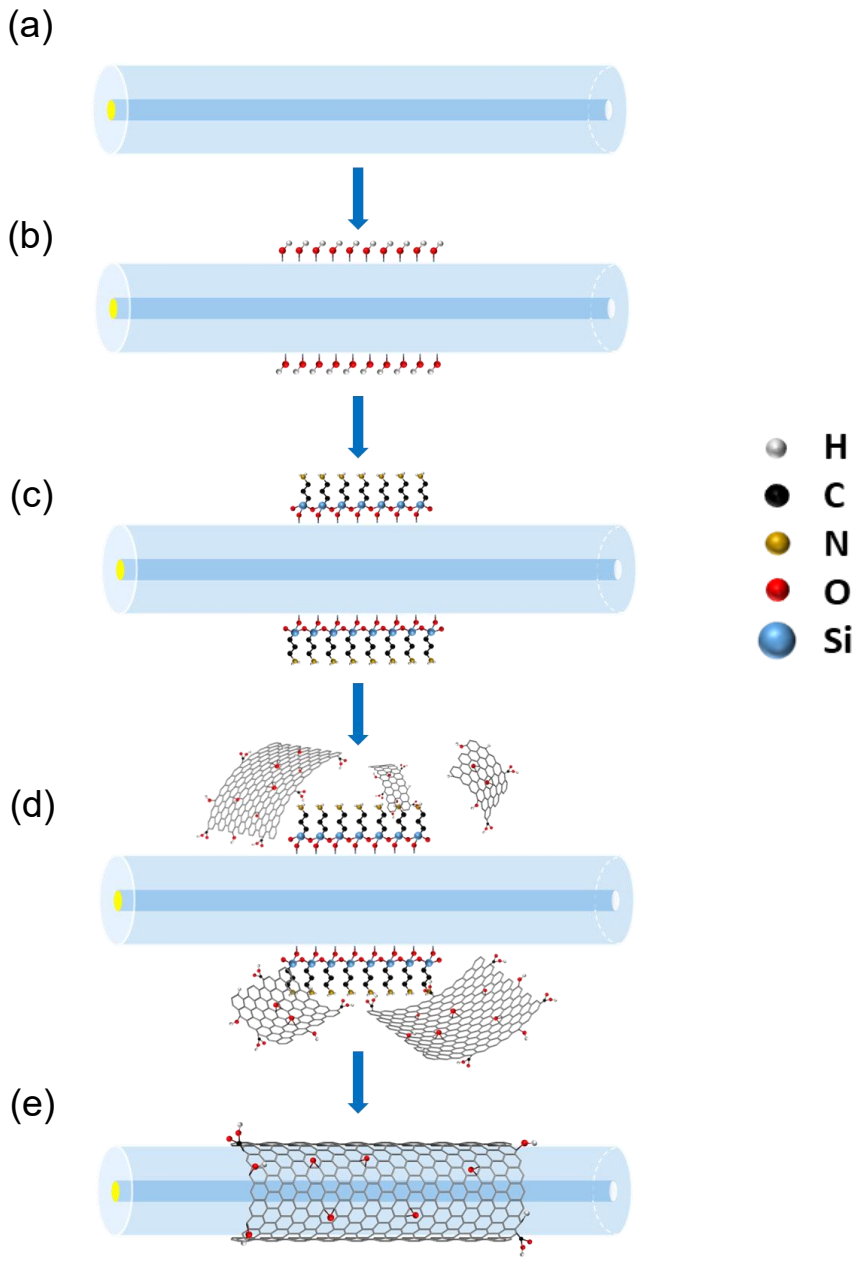

Figure 4.2 - 1 *Schematic illustration of in-situ i-LbL deposition technique for coating GO nanosheets onto an optical fibre. (a) Clean bare optical fibre, (b) Optical fibre with alkaline treatment, (c) Optical fibre with APTES silanisation, (d) layer-by-layer GO deposition, (e) GO-coated optical fibre.*

Followed by this i-LbL coating technique, the influence of coating parameters such as coating cycles and GO suspension concentration on the uniformity and thickness of coating overlay was investigated. A set of optical fibres was coated with GO nanosheets through varying coating cycles to examine the relationship between overlay thickness and the number of coating cycles. Additionally, to assess the minimum achievable overlay thickness, a diluted GO suspension (0.05 mg/mL) was used for a single-cycle coating on the optical fibre.

Fig. 4.2-2 presents optical microscope images of a bare and GO-coated fibre samples with varying coating cycles. As previously mentioned, a single-layer graphene sheet exhibits a high absorbance of 2.3% across the visible light spectrum [44]. Consequently, GO overlays with different thicknesses should display noticeable contrast in transmission-mode optical microscope images. Compared to the bare fibre (Fig. 4.2-2a), the GO-coated fibres (Fig. 4.2-2b-e) exhibit light to dark brown overlays with high uniformity, indicating the successful deposition of GO onto the optical fibres. The single-cycle overlay coated with 0.05 mg/mL GO suspension (Fig. 4.2-2b) displays higher transparency compared to those coated with 0.10 mg/mL GO suspension (Fig. 4.2-2c-e), confirming that a thinner overlay was achieved by using a lower GO concentration. Moreover, both Fig. 4.2-2b and Fig. 4.2-2c exhibits a smooth GO overlay that firmly wraps around optical fibre surface, attributed to the strong chemical bonding between the APTES-silanised fibre surface and GO nanosheets.

Based on the single-cycle GO overlay (0.10 mg/mL GO suspension), multiple coating cycles results in darker and rougher surface morphologies (Fig. 4.2-2d-e), indicating that increased coating cycles leads to a thicker GO overlay. In addition, the typical wrinkled and slightly wavy surface texture of GO is observed in the 5-cycle coated overlay [148], attributed to the physical adsorptions between GO layers formed during different coating cycles. It is worth noting that the observed macroscopic surface texture arises from the accumulation of the wavy and wrinkled structures of hundreds of individual layers. The surface of thinner GO overlays, such as in Fig. 4.2-2b, is inherently wavy and wrinkled, which will be further examined and discussed in the following SEM images.

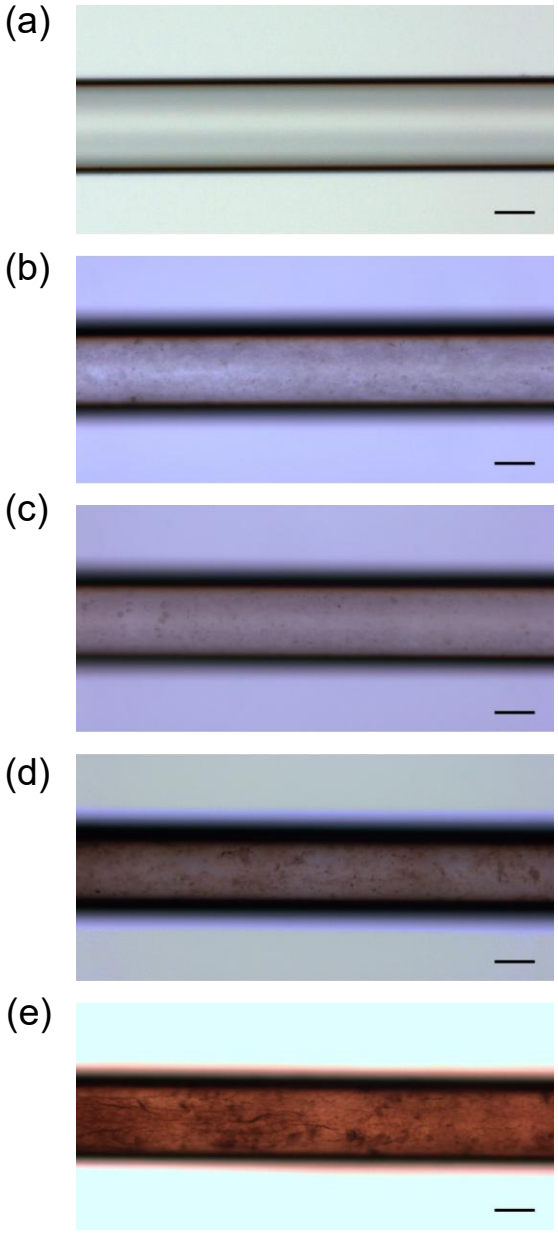

Figure 4.2 - 2 *Optical microscope images (scale bars = 50 μm) of (a) bare optical fibre, (b) 1-cycle GO-coated fibre (GO suspension concentration of 0.05 mg/mL), (c) 1-cycle GO-coated fibre (GO suspension concentration of 0.10 mg/mL), (d) 3-cycle GO-coated fibre (GO suspension concentration of 0.10 mg/mL), (e) 5-cycle GO-coated fibre (GO suspension concentration of 0.10 mg/mL).*

The surface morphologies of GO-coated fibre were characterised by SEM (Fig. 4.2-3) to further investigate the texture of GO overlays with varying thicknesses. Fig. 4.2-3a shows the SEM image of a cleaned bare optical fibre (e.g., without any coating), revealing a highly smooth surface. In contrast, a single-cycle GO-coated optical fibre (Fig. 4.2-3b) shows a success thin GO overlay coated on entire fibre surface with a slight rough texture. Meanwhile, 5-cycle GO-coated optical fibre (Fig. 4.2-3c) exhibits a rougher surface with more pronounced wrinkles distributed across the fibre surface, likely due to the accumulation and enlargement of defects on the basal plane of individual GO nanosheets.

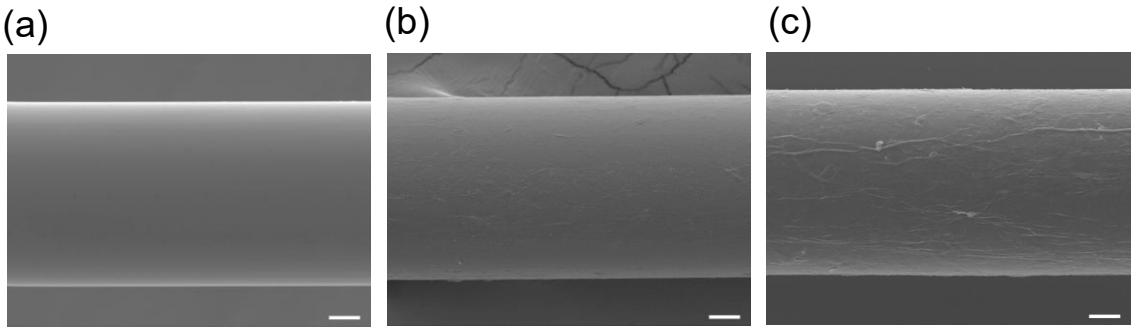

Figure 4.2 - 3 *SEM images of (a) bare fibre, (b) GO-coated fibre with thin overlay, (c) GO-coated fibre with thick overlay (scale bar = 20 µm).*

Apart from the characterisation of GO surface texture, the overlay thicknesses were characterised by AFM. Fig. 4.2-4 shows the thickness analysis of the GO overlay after a single-cycle deposition. A low concentration GO suspension (0.05 mg/mL) was employed for the deposition of an extremely thin GO overlay. As shown in Fig. 4.2-4a, there is a clear step boundary between the bare and GO-coated sections on fibre surface. The thickness of the GO overlay was measured to be between 10 nm and 15 nm (Fig. 4.2-4b). Fig. 4.2-4c presents the 3D AFM image of the single-cycle GO-coated fibre, where the curved surface corresponds to the cylindrical geometry of optical fibre. The sample was further characterised by SEM demonstrating the wrinkled texture of the GO overlay in contrast to the smooth surface of the bare fibre (Fig. 4.2-4d).

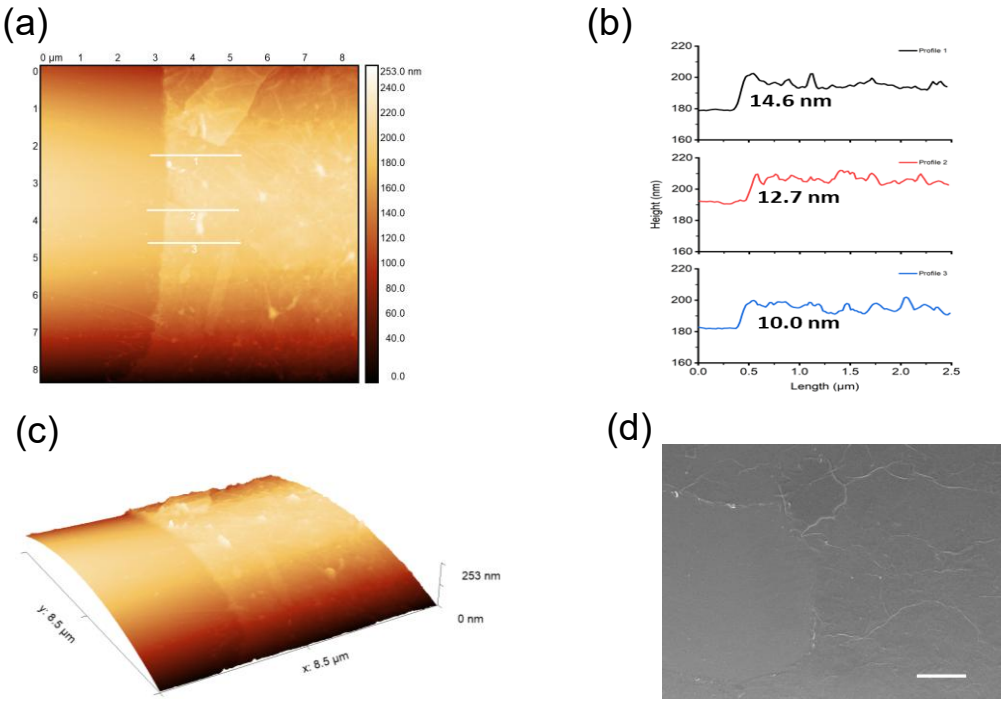

Figure 4.2 - 4 *Single-cycle deposited GO overlay thickness analysis (0.05 mg/mL GO suspension). (a) AFM image of the GO-fibre with a created step boundary. (b) Height profiles of GO overlay according to the white lines in (a). (c) 3D view of AFM image. (d) SEM image of the GO-fibre with a created step boundary (scale bar = 5 µm).*

As comparison, a thicker GO overlay was deposited on the optical fibre by applying multiple deposition cycles. Based on the step boundary shown in AFM image (Fig. 4.2-5a), the thickness of GO overlay is ranged from 170 nm to 200 nm (Fig. 4.2-5b). The 3D AFM image demonstrates a homogenous GO overlay with a heavily wrinkled texture alone the fibre cylindrical surface (Fig. 4.2-5c), which was further characterised using SEM to investigate the finer surface details (Fig. 4.2-5d).

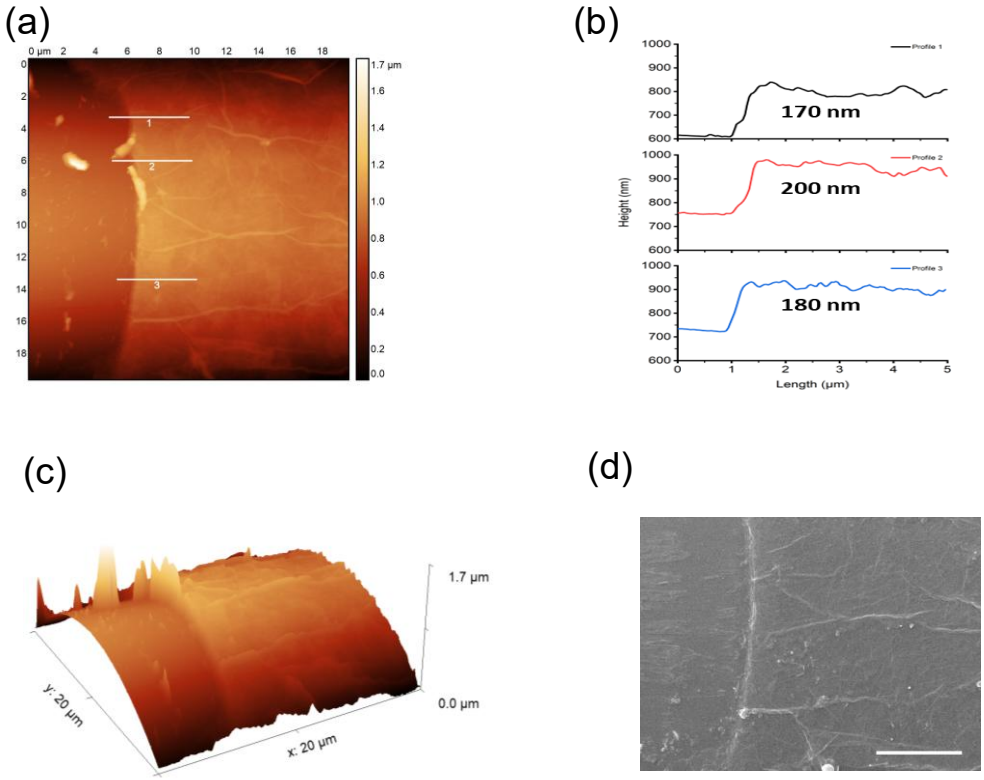

Figure 4.2 - 5 *Five-cycle deposited GO overlay thickness analysis (0.10 mg/mL GO suspension, with the fibre rotated every coating cycle). (a) AFM image of the GO-fibre with a created step boundary. (b) Height profiles of GO overlay according to the white lines in (a). (c) 3D view of AFM image. (d) SEM image of the GO-fibre with a created step boundary (scale bar = 5 μm).*

To understand the thickness distribution surround the fibre surface, the GO-coating from four azimuthal surfaces around the cylindrical surface (top, bottom, and two sides, as illustrated in Fig. 4.2 – 6) were investigated. As we know, the liquid level gradually decreased accompanying with water evaporation during the coating process, which could affect the coating process. In addition, the self-gravity and Brownian motion of GO nanosheets could influence their physical adhesion at various locations, contributing to variations in coating thickness. Two coating strategies were implemented. Firstly, a bare optical fibre was fixed and kept stationary in the mini bath throughout the whole GO deposition process where a GO concentration of 0.10 mg/mL was used and a 5-cycle

deposition was applied. Fig. 4.2-6a illustrates the coating setup, where the top, side, and bottom surfaces of the fibre are defined. Following the deposition process, step boundaries were created at these surfaces to enable thickness measurements. Fig. 4.2-6 (b-d) shows the top surface of the GO-fibre, where the thickness of the GO overlay is found to range from 110 nm to 150 nm. Based on the previously mentioned thickness of the GO overlay (top surface), which ranged from 10 nm to 15 nm when deposited using a 0.05 mg/mL GO suspension with a single-cycle coating, if we simply assume that doubling the concentration will double the thickness for each cycle. Therefore, a single-cycle coating using a 0.10 mg/mL GO suspension is expected to yield a thickness ranging from 20 nm to 30 nm. Given this, the measured thickness of 110 nm to 150 nm after 5-cycle coating is reasonable. Moreover, the thickest GO overlay is observed on the side surface of the GO-fibre, ranging from 275 nm to 290 nm (Fig. 4.2-6 (e-g)). This may be attributed to the longer contact time with the GO suspension during the deposition process compared to the top surface. In contrast, Fig. 4.2-6 (h-j) displays the thinnest GO overlay on the bottom surface of the GO-fibre, measuring between 70 nm and 90 nm. This is likely due to the need for GO nanosheets to overcome gravitational forces in order to adhere to the fibre. In addition, experimental observations indicate that the bottom surface of the optical fibre quickly separates from the GO suspension within the last couple seconds of deposition, potentially leading to incomplete or reduced GO nanosheets deposition. In contrast, the top and side surfaces undergo a smoother and slower separation process, which facilitates a thicker and firm GO coating.

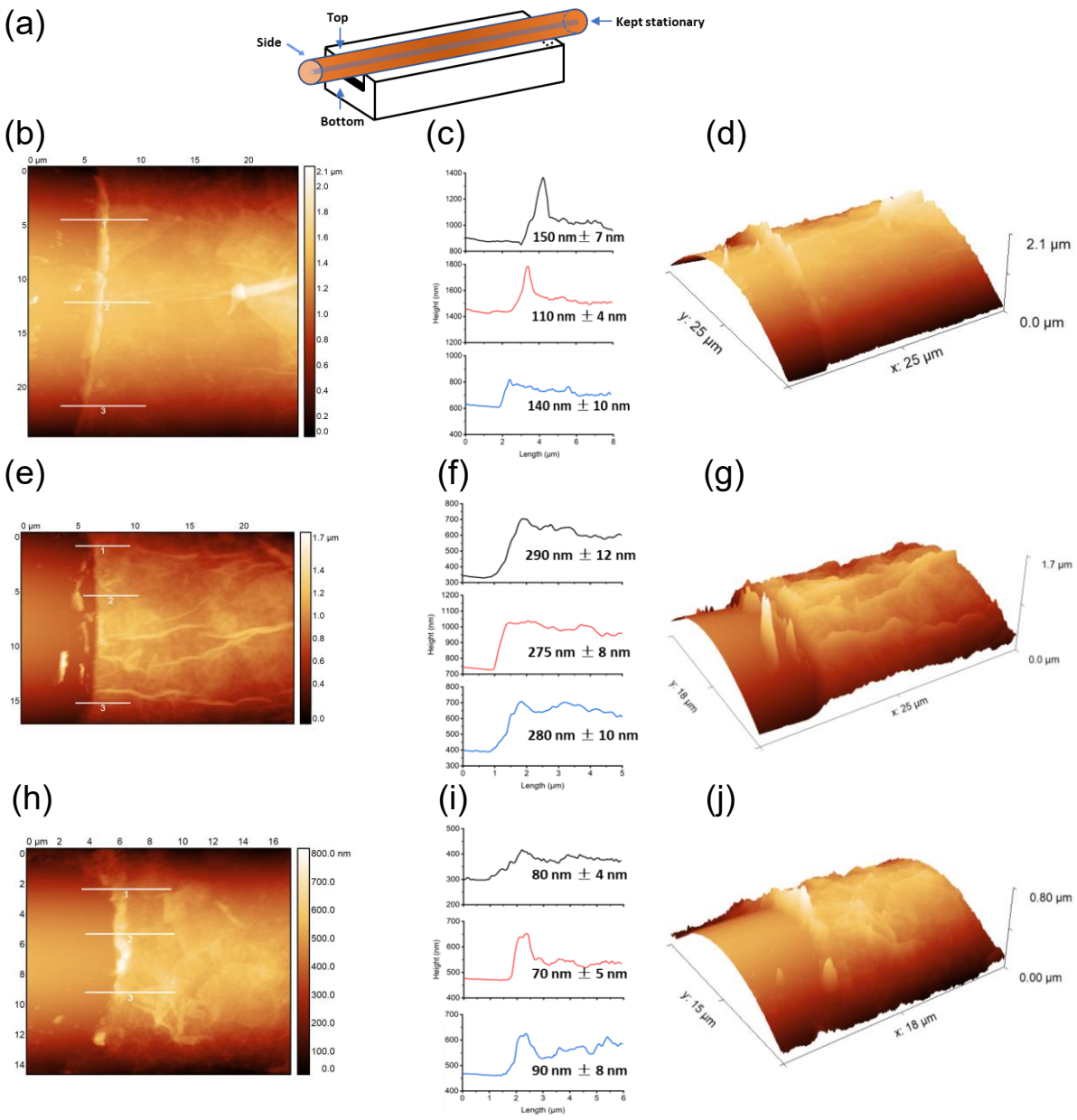

Figure 4.2 - 6 *Thickness analysis of GO overlay at four different azimuthal surfaces around the cylindrical surface (e.g., top, bottom, and two sides. Errors in (c), (f), and (i) represent the variation in measured thickness arising from the intrinsic surface roughness of the GO coatings). (a) Schematic illustration of GO deposition in a mini-bath with indicating different azimuthal of cylindrical geometry (the fibre was kept stationary). (b) AFM image of the top surface of GO-fibre with a created step boundary. (c) Height profiles of GO overlay along the white lines in (b). (d) 3D view AFM image of top surface. (e) AFM image of the side surface of GO-fibre with a created step boundary. (f) Height profiles of GO overlay along the white lines in (e). (g) 3D view AFM image of side surface. (h) AFM image of the bottom surface of GO-fibre with a created step boundary. (i) Height profiles of GO overlay along the white lines in (h). (j) 3D view AFM image of bottom surface.*

Since a standard single-mode optical fibre exhibits central symmetry in its cross-section, achieving a uniform coating is desirable for maintaining the integrity of light transmission, especially for guiding light beams in interferometric applications. To achieve a uniform GO overlay across four different azimuthal surfaces, a new coating strategy was

implemented by rotating the fibre by 90 degrees after each coating cycle during the multiple-cycle deposition process. This approach aimed to achieve coating consistency across different azimuthal fibre surfaces. As shown in Fig. 4.2-7, after 5-cycle deposition, the thickest GO overly remains ~242 nm on the side surface, while the thinnest coating is found on the bottom surface, averaging 170 nm. The top surface has an intermediate thickness of approximately 218 nm. The results indicate that the GO overlay achieves a more uniform distribution across different azimuthal of the fibre, highlighting the importance of the rotation step in obtaining a homogenous GO overlay.

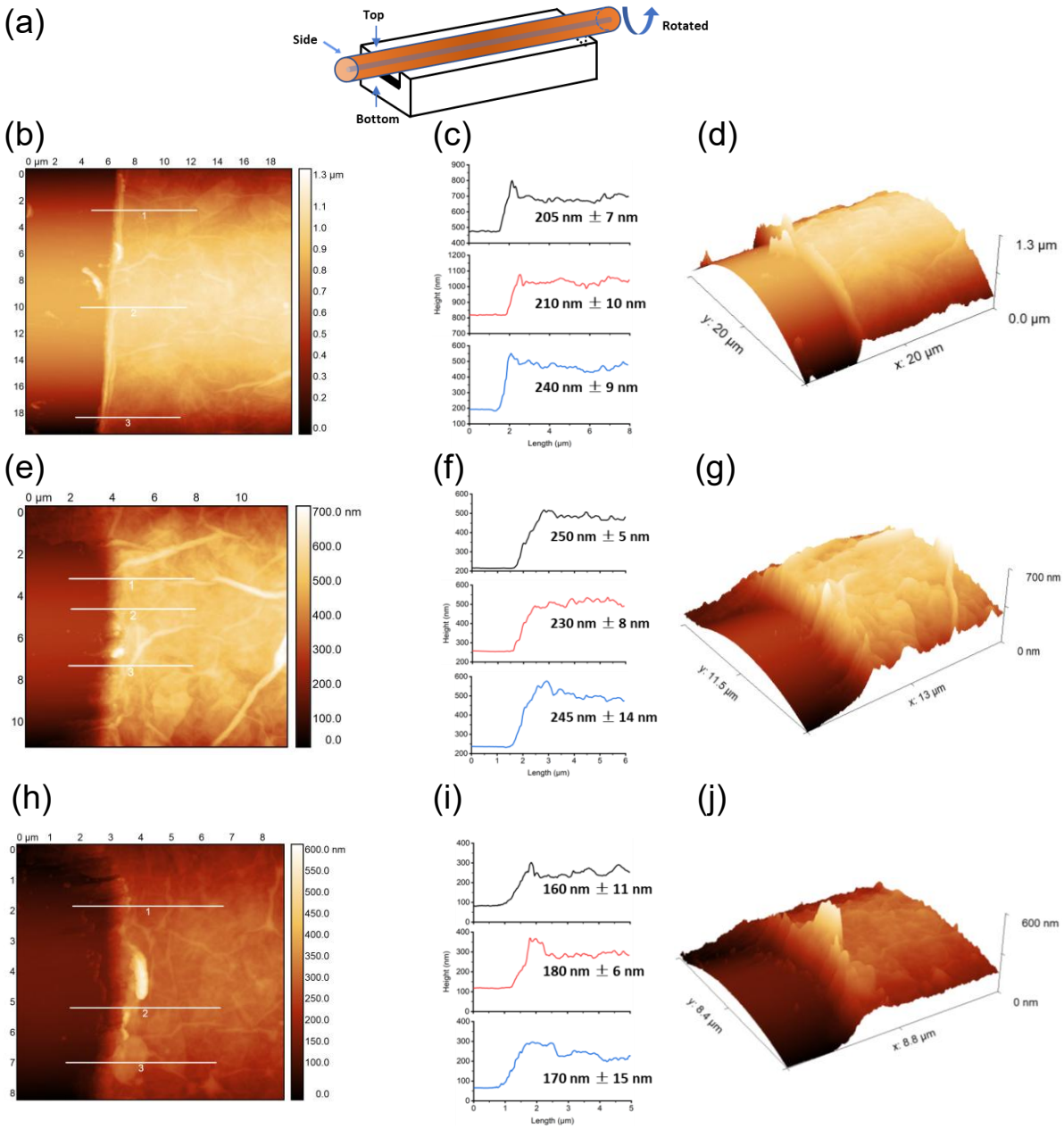

Figure 4.2 - 7 *Thickness analysis of GO overlay at four different azimuthal surfaces around the cylindrical surface (e.g., top, bottom, and two sides. Errors in (c), (f), and (i) represent the variation in measured thickness arising from the intrinsic surface roughness of the GO coatings). (a) Schematic illustration of GO deposition in a mini-bath, indicating different azimuthal of cylindrical geometry (the fibre was rotated 90˚ per coating cycle). (b) AFM*

image of the top surface of GO-fibre with a created step boundary. (c) Height profiles of GO overlay along the white lines in (b). (d) 3D view AFM image of top surface. (e) AFM image of the side surface of GO-fibre with a created step boundary. (f) Height profiles of GO overlay along the white lines in (e). (g) 3D view AFM image of side surface. (h) AFM image of the bottom surface of GO-fibre with a created step boundary. (i) Height profiles of GO overlay along the white lines in (h). (j) 3D view AFM image of bottom surface.

The chemical composition of the GO overlay was analysed using Raman spectroscopy, which detects molecular vibrational modes to provide a structural fingerprint for material identification [149]. A DXR Raman Microscope (Thermo Fisher Scientific Inc., UK) with a 532 nm excitation laser was used in this investigation. Fig. 4.2-8 presents the Raman spectra of the GO-coated fibre surface alongside that of a bare fibre for comparison. The presence of GO on the coated fibre is confirmed by its characteristic D and G peaks located at 1320 cm^{-1} and 1590 cm^{-1}, respectively, along with a second order 2D peak at 2640 cm^{-1} and a combination band (D + D′) at 2900 cm^{-1}. The D peak corresponds to the A_{1g} breathing mode, which is associated with defects on the basal plane of graphene oxide. These defects, induced by oxygen functional groups, lead to significant alterations in the structure of the carbon basal plane [150]. The G peak appears in sp^2 carbon materials and originates from the first order scattering of the E_{2g} in-plane vibrational mode. The 2D peak appears when momentum conservation is maintained by two photons with opposite wave vectors. It is always present in the spectrum since its activation does not rely on defects. In contrast, the D + D′ band requires defects for activation, as it arises from the combination of phonons with different momenta [151].

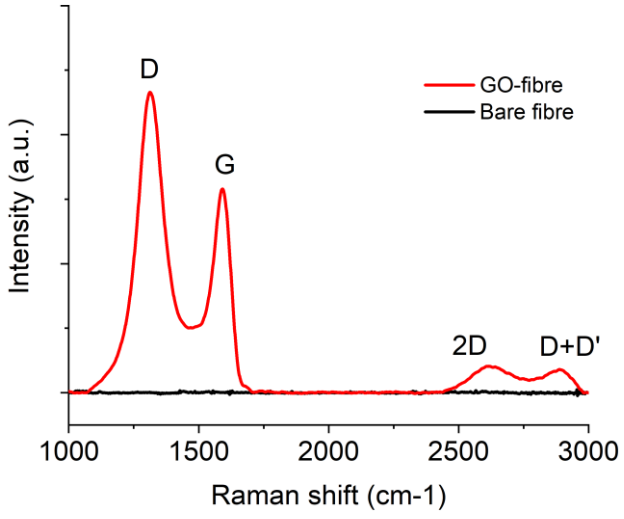

Figure 4.2 - 8 *Raman spectrum of the GO-coated optical fibre surface.*

4.2.2. $Ti_3C_2T_x$ MXene deposition on fibre and characterisation

The $Ti_3C_2T_x$ nanosheets are rich in oxygen-functional groups located on their basal planes as well as edges, allowing covalent bonding with the silanised fibre surface. Moreover, $Ti_3C_2T_x$ suspension has been reported to exhibit negative zeta potential [108], which facilitates electrostatic adhesion between the negatively charged $Ti_3C_2T_x$ nanosheets and the positively charged silanised fibre surface.

The $Ti_3C_2T_x$ nanosheets were deposited onto optical fibres with the i-LbL deposition technique. The SEM images in Fig. 4.2-9 illustrate the surface texture of the MXene-coated optical fibre and the bare fibre. Fig. 4.2-9a displays the SEM image of the entire MXene-fibre, showing a smooth and homogenous MXene overlay. In contrast, a darker surface of the bare fibre is observed in Fig. 4.2-9b, suggesting a clean, uncoated surface. The magnified SEM image of the MXene-fibre surface (Fig. 4.2-9c) exhibits densely packed wrinkles with random orientations, whereas the same magnified SEM image of the bare fibre (Fig. 4.2-9d) shows a clear and smooth surface. This contrast confirms the successful deposition of MXene nanosheets onto optical fibre, forming a uniform overlay.

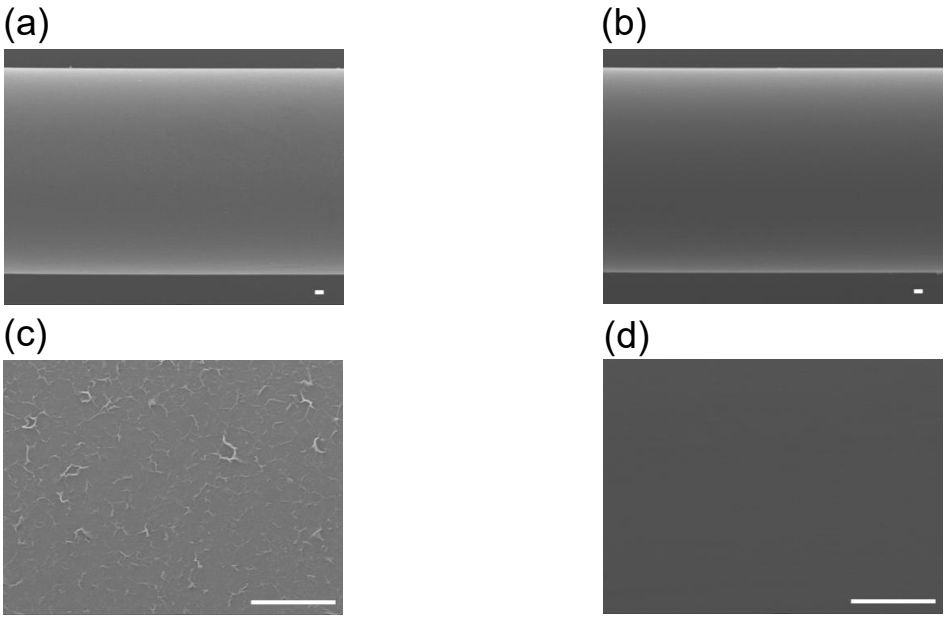

Figure 4.2 - 9 *SEM images (scale bar = 5 μm) of (a) MXene-coated optical fibre. (b) Bare fibre. (c) Magnified SEM image of MXene-fibre surface extracted from (a). (d) Magnified SEM image of bare fibre surface extracted from (b).*

The $Ti_3C_2T_x$ nanosheets were deposited onto optical fibre to form both thin and thick overlays. The thin MXene overlay was prepared using a 0.10 mg/mL MXene suspension with a single-cycle coating. Its thickness was characterised by AFM, as shown in Fig. 4.2. 10 (a, b), where the step boundary between the bare and coated fibre was measured,

revealing a thickness range of 45 to 60 nm. Additionally, the solid and dashed frames represent the bare fibre surface and the MXene-coated overlay surface, respectively. The coated region exhibits an increased surface roughness, as indicated by an RMS value of 17.0 nm. In contrast, the bare fibre section has an RMS roughness of only 5.5 nm, indicating that the MXene coating significantly increases surface texture. The 3D AFM image (Fig. 4.2-10c) confirms that the overlay is tightly wrapped around the fibre surface. The corresponding SEM image (Fig. 4.2-10d) further illustrates a homogenous coating, contrasting with the clean and smooth surface of the bare fibre.

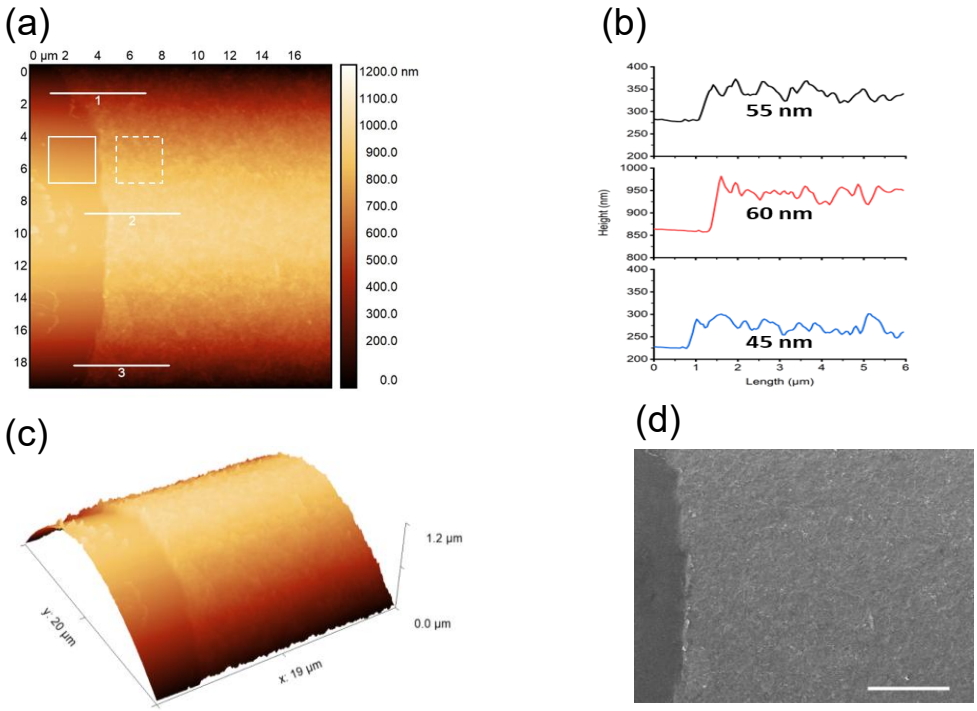

Figure 4.2 - 10 *Single-cycle deposited MXene overlay thickness analysis (0.10 mg/mL MXene suspension). (a) AFM image of the MXene-fibre with a created step boundary (inset: profile lines for height measurement; regions for roughness comparation). (b) Height profiles of MXene overlay according to the white lines in (a). (c) 3D view of AFM image. (d) SEM image of the MXene-fibre with a created step boundary (scale bar = 5 µm).*

The thick MXene overlay, using a 0.10 mg/mL MXene suspension with a 5-cycle coating, was analysed by AFM to determine its thickness and by EDS to investigate its elemental composition. The AFM images and corresponding height profiles in Fig. 4.2-11 (a-c) show that the thickness of the thick MXene overlay ranges from 260 nm to 310 nm, which is approximately five to six times that of above-mentioned thin overlay. This result demonstrates the stability and reliability of the coating technique. Furthermore, the SEM image of thicker MXene-fibre surface displays larger and more remarkable randomly distributed wrinkles compared to the thin MXene-fibre (Fig. 4.2-11d).

To investigate the chemical composition of the MXene overlay, EDS line scanning was performed. A region covering the step boundary was selected for elemental analysis (Fig. 4.2-11e). Fig. 4.2-11f shows the EDS line spectra, illustrating the elemental distribution along the scanned yellow line in Fig. 4.2-11e. A sharp decrease in Si and O signals, dropping by approximately 1500 cps and 1300 cps, respectively, is observed at the step boundary. These elements, which are the primary components of the optical fibre, experience this reduction due to the ~300 nm thick $Ti_3C_2T_x$ MXene overlay covering the underlying fibre. In contrast, Ti and C signals increase by approximately 500 cps and 300 cps, respectively, at the step boundary, providing elemental evidence of successful MXene deposition. Fig. 4.2-11g reveals the atomic concentrations of Ti and C are 23.0% and 14.8%, respectively, aligning with the theoretical ratio of 3:2 in $Ti_3C_2T_x$ MXene. Additionally, slight concentrations of F (3.1%) and Cl (1.1%) are observed, originating from functional groups (e.g., -F, -Cl) on the basal planes and edges of MXene nanosheets.

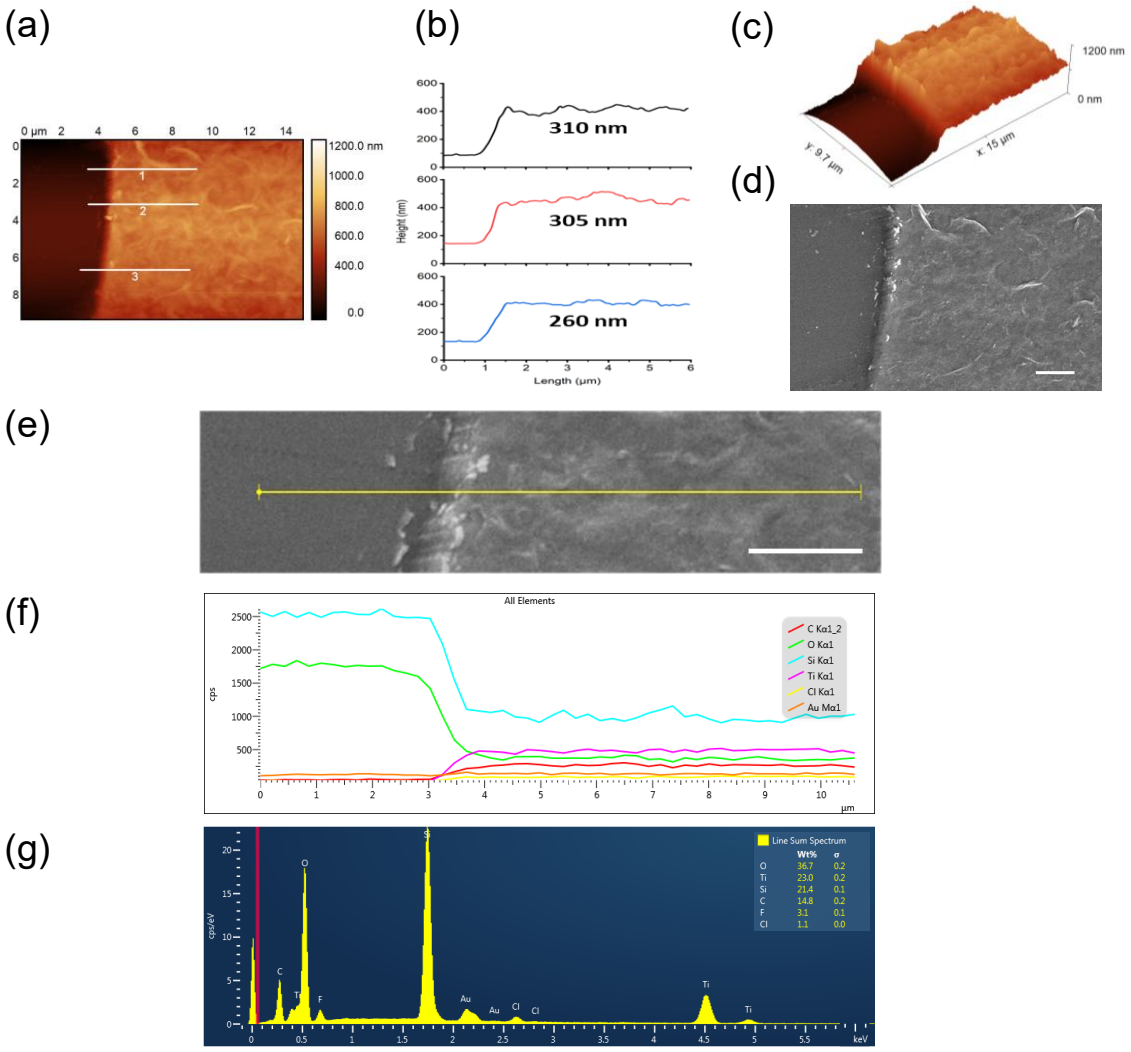

Figure 4.2 - 11 *Five-cycle deposited MXene overlay thickness and elemental composition analysis (0.10 mg/mL MXene suspension, with the fibre rotated 90˚ per coating cycle). (a) AFM image of the MXene-fibre with a created step boundary. (b) Height profiles of MXene overlay according to the white lines in (a). (c) 3D view of AFM image.*

(d) SEM image of the MXene-fibre with a created step boundary (scale bar = 2 µm). (e) SEM image of the MXene-fibre extracted from (d) with EDS line scanning. (scale bar = 2 µm). (f) EDS line spectra representing the elemental distribution along the yellow line in (e). (g) EDS line sum spectrum along the scanned line.

Furthermore, the cross-section of thick MXene-coated fibre was used to characterise the coating quality and thickness. Fig. 4.2-12a provides the SEM image of the MXene-fibre cross-section, where the optical fibre is centrally located and wrapped with MXene nanosheets, forming a uniform overlay around its surface. Since this inspection is conducted at the microscale, the nanoscale MXene overlay can hardly be observed. To address this, two regions (marked with solid and dotted frames) were selected for further analysis at higher magnification, as shown in Fig. 4.2-12b and Fig. 4.2-12c. In Fig. 4.2-12b, the MXene overlay was observed to fold from the side surface toward the top surface of the optical fibre, with its edge slightly curling and partially peeling, demonstrating a layered structure. Additionally, multiple layers of MXene are deposited on the fibre surface, forming an overlay with thickness of ~ 320 nm (Fig. 4.2-12c), which is consistent with the thickness measurements obtained via AFM. Furthermore, EDS elemental mapping was conducted to analyse the element distribution across the edge of the MXene-fibre cross-section (Fig. 4.2-12d). Si and O are found well-dispersed on the top surface of the optical fibre region, consistent with its SiO_2 composition. In contrast, Ti and C are concentrated along the coating overlay, exhibiting the successful deposition of $Ti_3C_2T_x$ MXene. Additionally, a slight presence of Cl is observed within the coating layer, attributed to the surface termination groups of $Ti_3C_2T_x$ (represented as 'T_x').

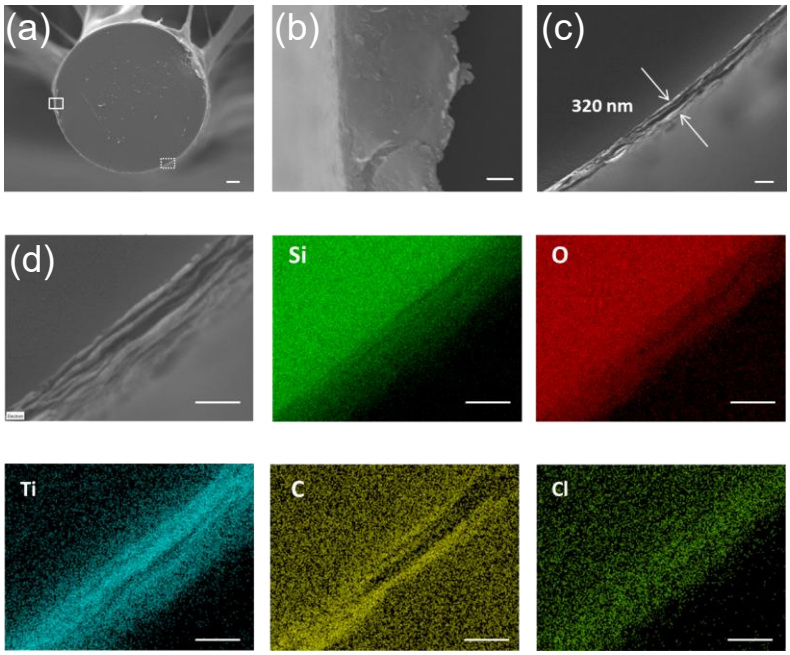

Figure 4.2 - 12 *SEM images of the MXene-fibre cross-section with corresponding EDS mapping. (a) SEM image of the MXene-coated optical fibre cross-section (inset: regions of MXene-fibre edges, scale bar = 10 µm). (b) The*

closeup SEM image extracted from the solid white frame in (a) (scale bar = 500 nm). (c) The closeup SEM image extracted from the dotted white frame in (a), displaying the MXene overlay thickness of ~320 nm (scale bar = 500 nm). (d) SEM image of the MXene-fibre edge with corresponding elemental mapping of Si, O, Ti, C, and Cl in the $Ti_3C_2T_x$ MXene overlay (scale bar = 500 nm).

4.2.3. $BiTiS_3$ nanosheets deposition on fibre and characterisation

The i-LbL deposition technique was developed to deposit $BiTiS_3$ nanosheets onto optical fibres. The $BiTiS_3$ nanosheet suspension was synthesised via the sonication-assisted liquid exfoliation (see Chapter 3) to get the concentrations of 80 µg/mL and 40 µg/mL, which were used for the deposition on fibres. Fig. 4.2-13 presents optical microscope images of $BiTiS_3$-coated fibres, single coating cycle but with varying concentrations. The dark and uniform coating overlays are observed on $BiTiS_3$-fibres with both suspension concentrations, in contrast to the transparent surface texture of the bare fibre. The fibre coated with 40 µg/mL $BiTiS_3$ suspension exhibits a smoother and finer surface morphologies than that of 80 µg/mL sample. Therefore, the concentration of 40 µg/mL $BiTiS_3$ was chosen for the subsequent multiple-cycle coating process for further applications.

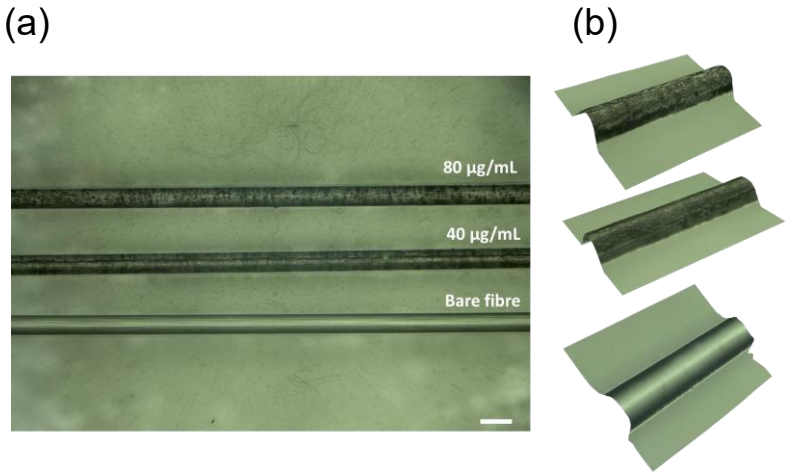

Figure 4.2 - 13 *(a) Optical microscope images of $BiTiS_3$-coated optical fibre prepared with different suspension concentrations and bare fibre (scale bar = 200 µm). (b) The corresponding 3D optical images.*

Further investigation of the surface morphologies of $BiTiS_3$-fibres was carried out using SEM. Fig. 4.2-14a reveals a rougher surface texture of the $BiTiS_3$-fibre after 5 coating cycles, in contrast to the clean and smooth surface of the bare fibre shown in Fig. 4.2-14b. Additionally, a magnified SEM image (specify the magnification) of the $BiTiS_3$-fibre is shown in Fig. 4.2-14c, where $BiTiS_3$ nanosheets/nanoflakes are observed aggregate on the fibres surface, rather than GO and MXene nanosheets, which wrap around the fibre

surface exhibiting a silk-like behaviour. Fig. 4.2-14d displays the magnified SEM image of the bare fibre, showing a smooth and clean surface.

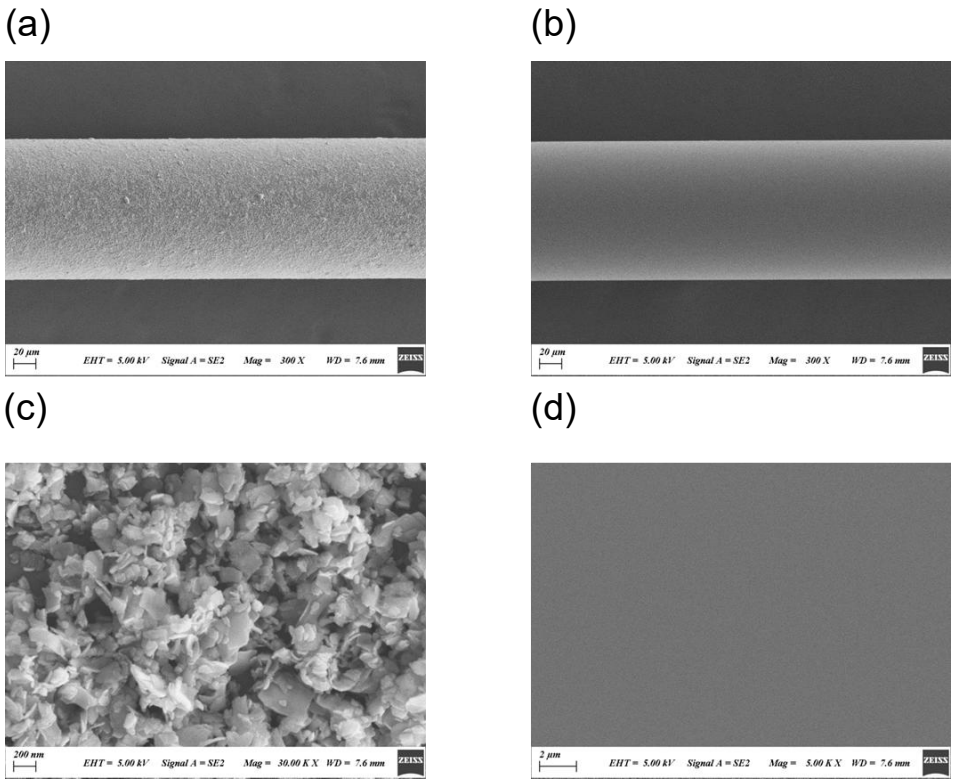

Figure 4.2 - 14 *SEM images of (a) $BiTiS_3$-coated optical fibre prepared using a 40 µg/mL $BiTiS_3$ suspension with 5 coating cycles (magnification: 300x). (b) The bare fibre. (c) The magnified (30,000x) SEM image extracted from (a). (d) The magnified SEM image extracted from (b).*

The $BiTiS_3$-fibre was subsequently characterised with EDS for evaluating its chemical composition and elemental distribution. Fig. 4.2-15a presents the SEM image of the entire $BiTiS_3$-coated fibre along with the corresponding EDS elemental mapping. As the main components of the optical fibre, Si and O are found distributed throughout the entire fibre. Additionally, the uniform dispersion of Bi, Ti, and S across the fibre surface confirms the successful and consistent deposition of $BiTiS_3$ coating. Fig. 4.2-15b reveals the atomic concentrations of Bi, Ti and S are 0.50% and 0.54%, and 1.61%, respectively, aligning with the theoretical ratio of 1:1:3 in $BiTiS_3$.

(a)

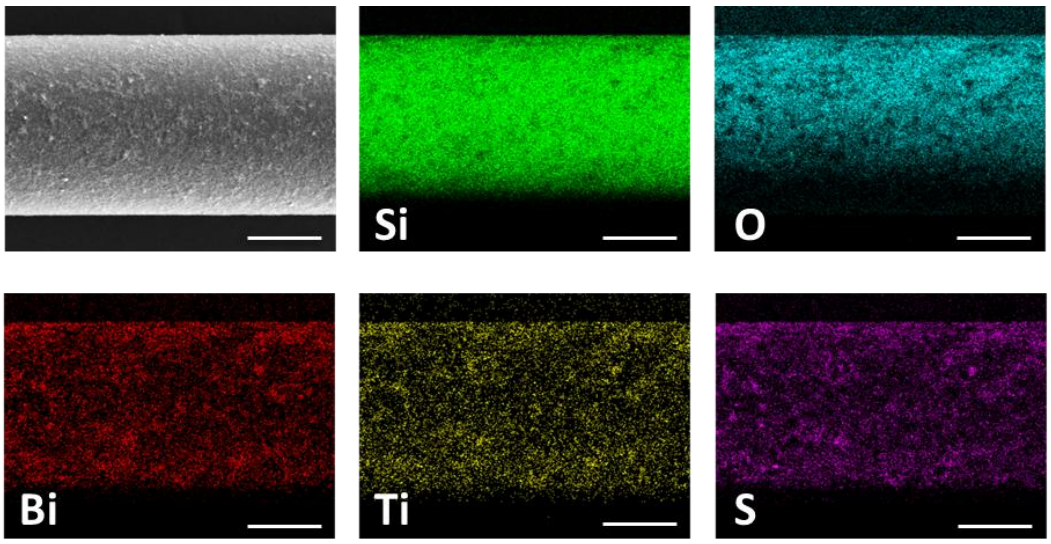

(b)

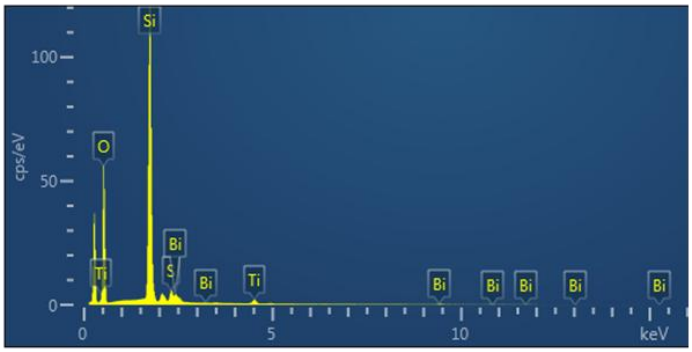

Elements	At%
O	67.74
Si	29.61
Bi	0.50
Ti	0.54
S	1.61
Total:	100.00

Figure 4.2 - 15 *(a) SEM image of the $BiTiS_3$-coated optical fibre with corresponding elemental mapping of Si, O, Bi, Ti, and S in the $BiTiS_3$ overlay (scale bar = 50 µm). (b) EDS map sum spectrum along with the atomic concentrations.*

Furthermore, the $BiTiS_3$ nanosheets were deposited onto 45˚ tilted fibre gratings (TFG) to evaluate its photothermal response as a solid overlay. $BiTiS_3$ is of particular interest due to its strong optical absorption and favourable photothermal response in the NIR-II window, making it a promising photothermal agent for biomedical applications. Evaluating its photothermal response at this stage provides a basis for its subsequent integration with tilted fibre gratings and photothermal therapeutic studies. As the experimental setup illustrated in Fig. 4.2-16a, the emitted light from a 1064 nm laser source was firstly focused by a collimator to ensure a parallel beam, then launched into a fibre polariser, a polarisation controller (PC) was then used to adjust different polarisation states before directing the light into the $BiTiS_3$ coated 45˚-TFG. This polarisation control is necessary to maximise the out-coupling efficiency of the 45°-TFG and enhance the interaction between the guided light and the $BiTiS_3$ coating.

The 45˚-TFG is designed to couple the s-polarised component of light out of the fibre core, while allowing the p-polarised component to propagate through the fibre. Acting as a photothermal agent, the $BiTiS_3$ nanosheets (coated on 45˚-TFG) absorbed the energy from the s-polarised component and converted it into heat, enabling potential applications such as directionally controlled photothermal therapy. To maximise the interaction between the $BiTiS_3$ overlay and the output light, the PC was adjusted to achieve a polarisation state with highest s-component intensity. Additionally, a thermocouple was placed onto the $BiTiS_3$-TFG for monitoring the temperature variations. Fig. 4.2-16b and Fig. 4.2-16c demonstrate the temperature variations of $BiTiS_3$-TFG and bare TFG under different laser intensities, respectively. To assess their photothermal response, the laser was switched on for 120 s, followed by an off period for 120 s. For the $BiTiS_3$-TFG, the temperature rises sharply within the first 10 s, then continues to increase at a slower rate between 10 and 60 s, eventually reaching saturation between 60 and 120 s. Once the laser is switched off, the $BiTiS_3$-TFG cools down rapidly during the first 40 s, followed by a more gradual cooling process from 40 to 120 s, ultimately dropping down to the initial temperature before heating. For the bare TFG, the temperature increases rapidly within the first 5 seconds and reaches a saturation state after 10 seconds, remaining steady until the laser is turned off. Upon switching off the laser, the temperature decreases quickly for the first 20 seconds, then gradually returns to its initial value after 60 seconds.

As shown in Fig. 4.2-16d, the temperature of $BiTiS_3$-TFG increases by 69.3℃ under laser irradiation at an intensity of 416 mW. In contrast, the temperature of bare TFG rises by only 4.3 ℃ under the same condition. The $BiTiS_3$-TFG exhibits a faster heating response and significantly higher temperature variations, which can be attributed to the light absorption and conversion by the $BiTiS_3$ nanosheets. Moreover, the photothermal performance of the $BiTiS_3$-TFG remains stable, showing no deterioration after five heating-cooling cycles (Fig. 4.2-16e). Fig. 4.2-16f shows infrared thermographic images of $BiTiS_3$-TFG under different laser intensities. As the laser intensity increases, the grating section gradually changes from blue to green, then to orange, and finally to dark red, indicating a progressive rise in temperature. Although the laterally emitted optical power is expected to decay along the grating, the temperature profile does not necessarily follow the same trend because thermal diffusion along the fibre and heat dissipation to the surroundings smooth the local temperature distribution. The non-uniform thermal pattern in Fig. 4.2-16 (f) may also arise from local variations in $BiTiS_3$ coating thickness/coverage and from non-ideal polarisation optimisation over the 50 mm grating length.

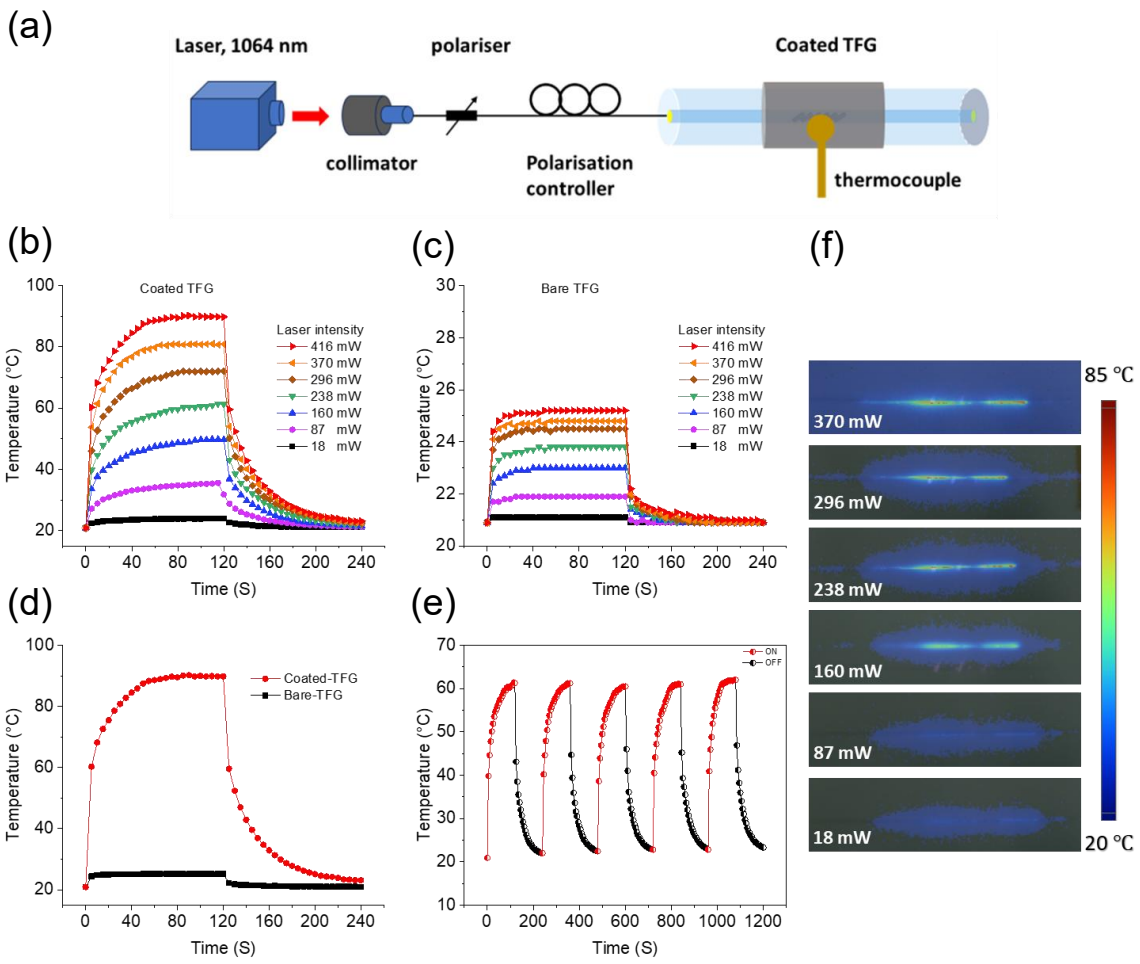

Figure 4.2 - 16 *The photothermal response of $BiTiS_3$-coated tilted fibre gratings (TFG). (a) Schematic illustration of the experimental setup (The temperature was measured using a thermocouple placed in direct contact with the target region of the coated fibre). (b) Photothermal heating curves of the BiTiS3-coated TFG under 1064 nm laser irradiation at different power levels. (c) Photothermal heating curves of the bare TFG under the same irradiation conditions. (d) Comparison of the photothermal response between the coated and bare TFGs (laser power: 416 mW). (e) Temperature variation of the coated TFG over five laser on/off cycles at an irradiation power of 238 mW. (f) Infrared thermographic images of the coated TFG under varying irradiation powers.*

4.2.4. α-MoO_3/GO heterostructure deposition and characterisation

Based on previous optimised deposition parameters, the ultrathin α-MoO_3/GO heterostructure overlays were successfully deposited onto optical fibres with the developed i-LbL approach. Firstly, one-cycle coating of α-MoO_3 suspension (see Chapter 3) was conducted. The formed nanolayer was attributed to the anchoring effect between α-MoO_3 and the amino-functionalised fibre surface, where the long-pair electrons of N atom in -NH_2 coordinated with the empty orbitals of Mo [152]. Subsequently, a second coating was performed using the supernatant of a 0.05 mg/mL GO suspension centrifugated at 3000 rpm for 30 minutes, to form the α-MoO_3/GO heterostructure overlay surround the optical fibre.

Fig. 4.2-17a and Fig. 4.2-17b present the SEM images of the α-MoO_3-coated fibre and α-MoO_3/GO heterostructure-coated fibre, respectively. The former exhibits high uniformity with a slightly rough surface texture (Fig. 4.2-17a) while the latter shows wrinkles texture (Fig. 4.2-17b). As the detailed surface texture of the α-MoO_3/GO heterostructure overlay presented in Fig. 4.2-17c, the labyrinthine-striped α-MoO_3 thin film is observed coved by the silk-like ultrathin GO layer.

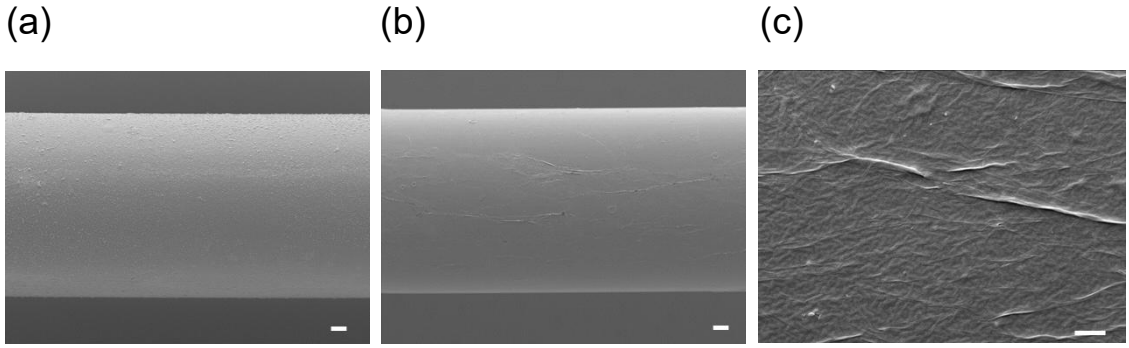

Figure 4.2 - 17 *SEM images. (a) α-MoO_3-coated optical fibre (scale bar = 10 μm). (b) α-MoO_3/GO heterostructure-coated optical fibre (scale bar = 10 μm). (c) the magnified region extracted from (b) to exhibit surface morphology (scale bar = 1 μm).*

For a better understanding of the 2D heterostructure-coated texture, a thin α-MoO_3 overlay was deposited on the fibre surface with a single-cycle coating process and was analysed by AFM and EDS (Fig. 4.2-18).

The AFM images and corresponding height profiles in Fig. 4.2-18 (a-b) reveal that the α-MoO_3 overlay has an average thickness of 15.6 nm, equivalent to 11 atomic layers of α-MoO_3. The 3D AFM image (Fig. 4.2-18c) further confirms the formation of a continuous thin film. Additionally, Fig. 4.2-18d presents the SEM image along with the EDS elemental mapping of the same sample with step boundary. Si and O, consistent with the SiO_2 composition of glass fibre, are well-dispersed on the fibre surface, whereas Mo is only observed in the deposition region. Fig. 4.2-18f displays the EDS line spectra, illustrating the elemental distribution of Mo along the scanned line shown in Fig. 4.2-18e. A step increase in the Mo signal, rising by approximately 40 cps, is observed in the α-MoO_3 deposited region. The atomic concentration of Mo along the scanned line is found to be 8.6%, whereas Si and O maintain high concentrations of 31.9% and 59.5%, respectively, corresponding to the typical 1:2 ratio of SiO_2, the primary component of the

glass fibre. The relatively low Mo concentration is attributed to the ultrathin nature of the α-MoO_3 film, hence with limited detectable signal in EDS line scanning.

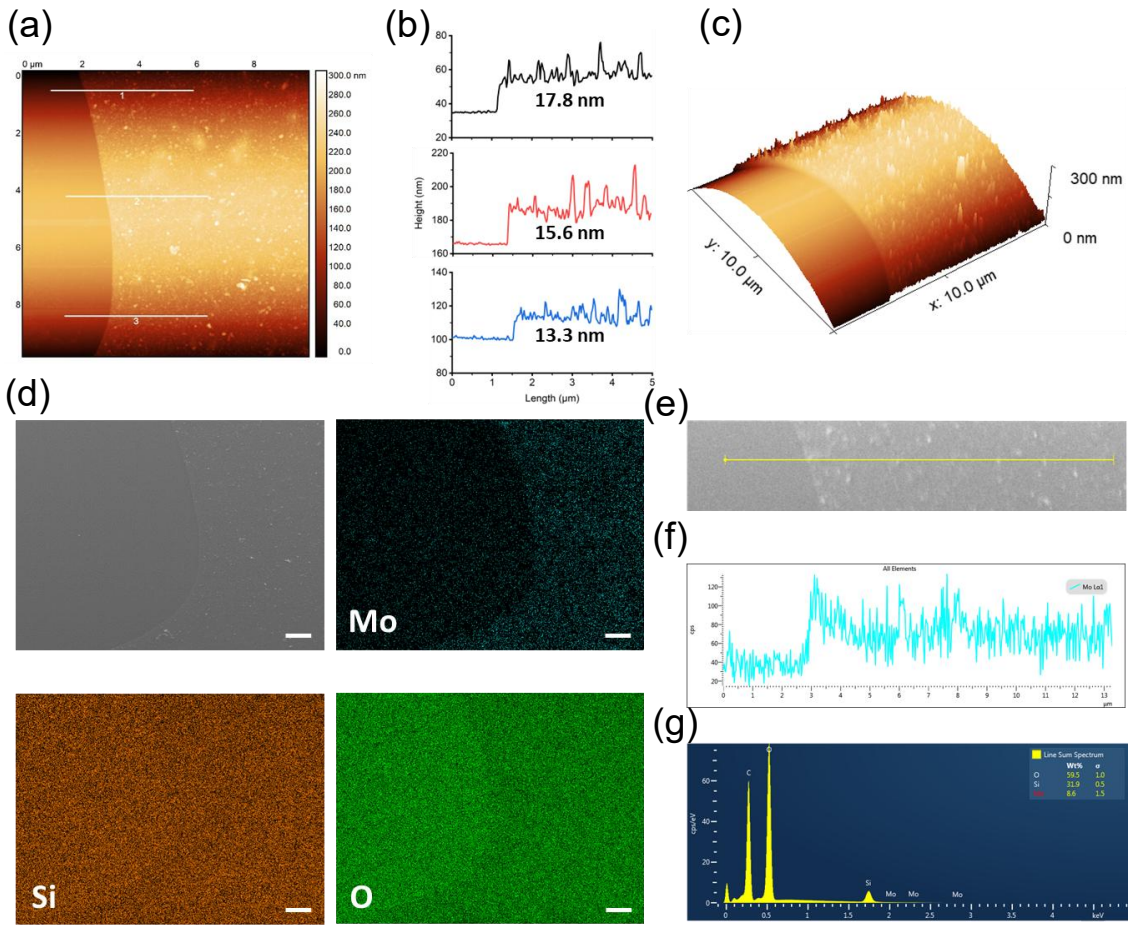

Figure 4.2 - 18 *The thickness and elemental composition analysis of α-MoO_3 overlay. (a) AFM image with a created step boundary (inset: profile lines for height measurement). (b) Height profiles according to the white lines in (a). (c) 3D view of AFM image. (d) SEM image of the α-MoO_3-coated optical fibre with corresponding elemental mapping of Mo, Si, and O in the coating overlay (scale bar = 2 μm). (e) SEM image of the coated fibre extracted from (d) with EDS line scanning. (f) EDS line spectra representing the elemental distribution along the yellow line in (e). (g) EDS line sum spectrum along the scanned line.*

The thickness of α-MoO_3/GO heterostructure overlay was then evaluated. As AFM image shown in Fig. 4.2-19a, a GO-on-α-MoO_3 heterostructure overlay is firmly wrapped the fibre cylindrical surface. Height measurements were conducted along three individual lines in Fig. 4.2-19a, giving an average thickness of 24.7 nm (Fig. 4.2-19b). This indicates that the heterostructure overlay consists of a ~16 nm α-MoO_3 thin film integrated with a ~9 nm GO thin film on top. The 3D AFM image of heterostructure overlay (Fig. 4.2-19c) further reveals the labyrinthine stripes of α-MoO_3, which are covered by the GO with characteristic wrinkled surface texture.

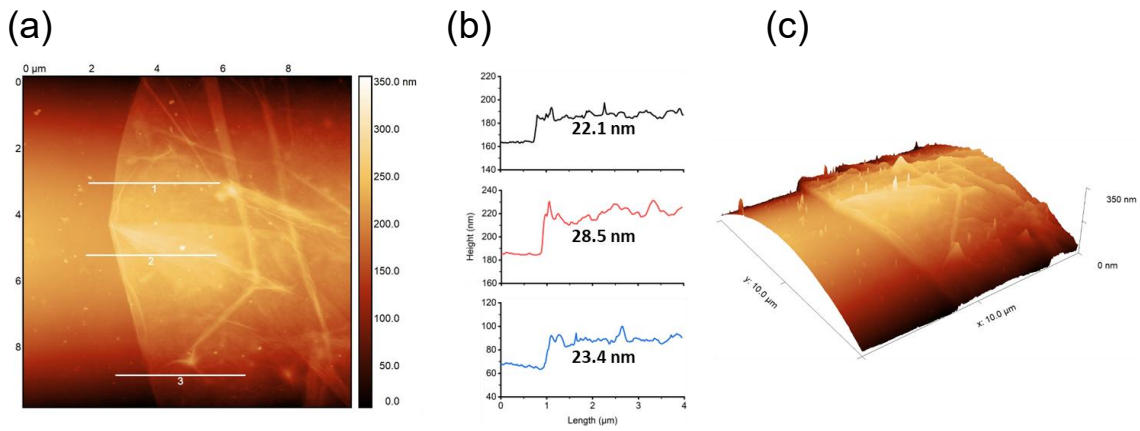

Figure 4.2 - 19 *The thickness analysis of α-MoO_3/GO heterostructure overlay. (a) AFM image with a created step boundary (inset: profile lines for height measurement). (b) Height profiles according to the white lines in (a). (c) 3D view of AFM image.*

Furthermore, Raman spectroscopy was performed on (1) α-MoO_3-coated fibre, (2) GO-coated fibre, and (3) α-MoO_3/GO heterostructure-coated fibre (Fig. 4.2-20). In the spectrum of α-MoO_3-coated fibre (blue line), three prominent peaks at 666, 820, and 996 cm^{-1} correspond to the stretching vibration modes of the Mo-O3 ', Mo-O2', and Mo-O1 bonds, respectively [153]. In the spectrum of GO-coated fibre (dark line), four characteristic peaks of D, G, 2D, and D+D' are observed at 1324, 1595, 2640, and 2900 cm^{-1}, respectively (see further details in Fig. 4.2-8). Apparently, the Raman spectrum of α-MoO_3/GO heterostructure-coated fibre (red line) presents characteristic peaks that appear in both α-MoO_3-coated fibre and GO-coated fibre, confirming the successful deposition of the 2D heterostructures onto fibres.

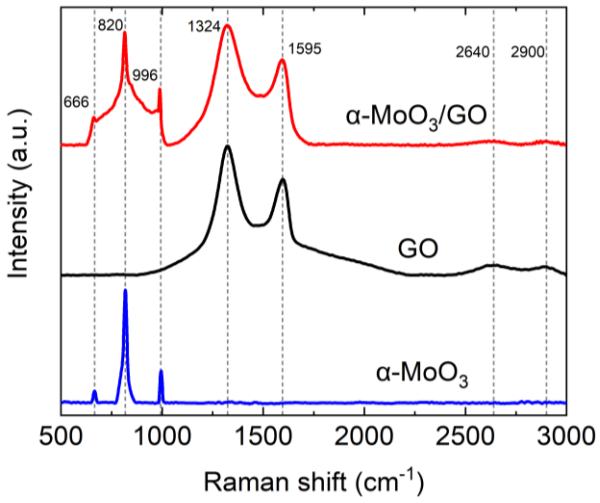

Figure 4.2 - 20 *Raman spectra of the optical fibre that coated with α-MoO_3 overlay, GO overlay, and α-MoO_3/GO heterostructure overlay.*

4.3. PMMA-assisted wet transfer method

The PMMA-assisted transfer and deposition process described in this section was carried out by the author. This method was selected for FET chip fabrication because it enables controlled placement of 2D nanomaterials onto pre-patterned device substrates, allowing effective functionalisation of the transistor channel while preserving channel integrity and minimising contamination or mechanical damage. The single layer graphene (SLG) was deposited onto a FET chip with using the PMMA-assisted wet transfer method. Figure 4.3-1a illustrates the transfer process of SLG onto a FET chip. In brief, a SLG on Cu film was firstly cropped into 5 × 5 mm pieces and immersed into 0.1 mg/mL $(NH_4)_2S_2O_8$ solution for 4h to etch away Cu (Fig. 4.3-1b), then the graphene pieces with PMMA were transferred into DI water (Fig. 4.3-1c) and followed by transferring onto SiO_2 substrate to cover drain/source electrodes and FET channel (Fig. 4.3-1d). Subsequently, the graphene-FET was stabilised by placing it in an oven at 80°C for 30 min (Fig. 4.3-1e), the PMMA was removed with acetone, followed by washing with ethanol and DI water, and drying thoroughly.

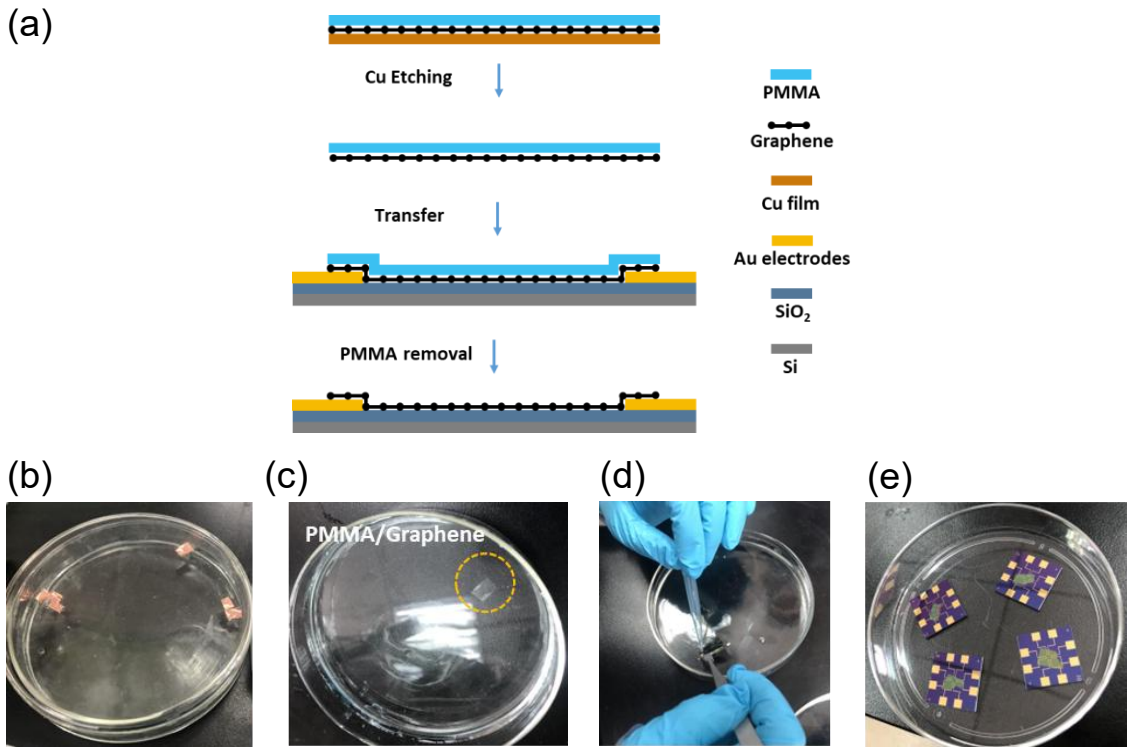

Figure 4.3 - 1 *(a) Schematic illustration of the SLG transfer process on an FET [6]. (b) SLG on Cu film prior to the etching process. (c) PMMA-supported SLG after etching process. (d) The transfer process. (e) FET chips coated with a piece of SLG.*

The SLG-FET after the transfer process was characterised with optical microscopy. Fig. 4.3-2a displays a digital photo of the SLG-deposited FET, demonstrating a tight contact

between the SLG and the FET substrate. The optical microscope image in Fig. 4.3-2b reveals a clear contrast between the graphene and the SiO_2 substrate.

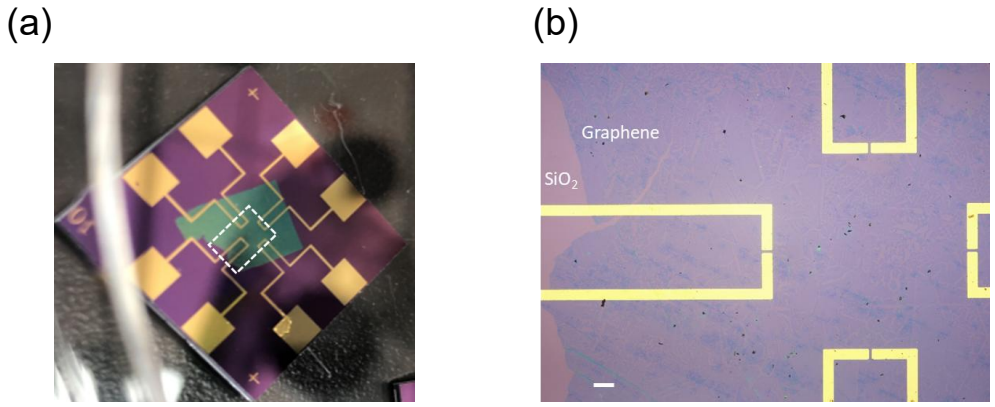

Figure 4.3 - 2 *(a) Digital photo of an FET deposited with SLG. (b) The microscope image of SLG-deposited FET, extracted from the white dashed frame in (a) (scale bar = 200 µm).*

4.4. Spin coating approach

The spin coating approach was developed for further deposition upon the SLG-FET. In brief, $CsPbI_3$ perovskite quantum dots (PQDs) with concentration of 2.5 µg/mL were spin-coated (800 rpm, 10 s) onto a graphene layer and crystalised by soft annealing at 80 °C for 30 min under N_2 environment.

The surface morphologies of the spin-coated $CsPbI_3$ PQDs were characterised by SEM and AFM. SEM image (Fig. 4.4-1a) reveals a granular surface texture [154]. Which AFM image (Fig. 4.4-1b) displays an increased surface roughness with a RMS roughness of 4.8 nm. The thickness of PQDs/SLG heterostructure layer was measured by the height profile of boundary, showing a thickness of 18.2 nm (Fig. 4.4-1c).

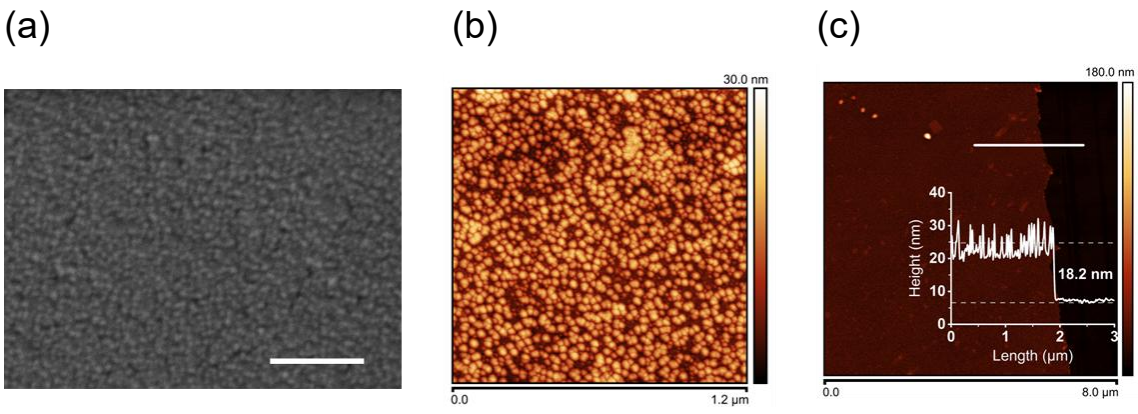

Figure 4.4 - 1 *(a) SEM image of $CsPbI_3$ PQDs film spin-coated upon SLG (scale bar: 500 nm). (b) AFM images of PQDs thin film surface. (c) AFM image of perovskite-on-graphene heterostructure with height profile (inset) [6].*

Additionally, the X-ray photoelectron spectroscopy (XPS) measurements were used to analyse the elements of $CsPbI_3$ PQDs (Fig. 4.4-2). The XPS spectra of $CsPbI_3$ exhibits (i) two characteristic peaks at 724.4 and 738.4 eV which corresponded to the elements of Cs $3d_{5/2}$ and Cd $3d_{3/2}$, respectively (Fig. 4.4-2a); (ii) two characteristic peaks at 619.1 and 630.6 eV that corresponded to the elements of I $3d_{5/2}$ and I $3d_{3/2}$, respectively (Fig. 4.4-2b); and (iii) two typical characteristic peaks at 138.6 and 143.4 eV that corresponded the elements of Pb $4f_{7/2}$ and Pb $4f_{5/2}$, respectively (Fig. 4.4-2c) [155].

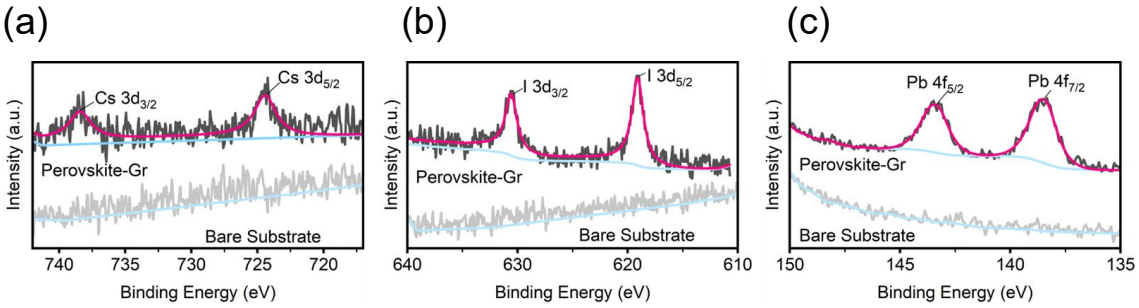

Figure 4.4 - 2 *High-resolution XPS spectra of $CsPbI_3$ perovskite/graphene heterostructure for (a) Cs, (b) I, and (c) Pb elements [6].*

4.5. Drop casting method

The drop casting method was used to deposit gold nanoparticles (AuNPs) onto a transparent glass substrate, forming an AuNP-functionalised nano-photonic filter (Fig. 4.5-1a). The AuNP-functionalised nano-photonic filter fabricated in this section is designed as a vertical bio–nano–photonic interface for subsequent FET-based sensing applications. By modulating the transmission of incident light through LSPR effects, the filter enables controlled optical delivery to the underlying FET channel, as demonstrated and utilised in Chapter 5.3. A thin SiO_2 substrate was rinsed with acetone, isopropanol, and DI water, then the surface was treated by O_2 plasma for 2 min at power of 150 W. Afterwards, the substrate was incubated in a 10% APTES solution for 2 h. AuNPs were drop-casted on the up-surface of substate to incubate the substrate up-surface for overnight. In this work, two AuNPs concentrations of 50 µg/mL and 5 µg/mL were used to fabricate the high-density and low-density AuNP filter, respectively.

The surface morphologies of the drop-coated AuNPs filters were characterised by AFM and SEM. The height, distribution, and density of AuNPs were analysed for both high-density (Fig. 4.5-1b-d) and low-density (Fig. 4.5-1e-g) filters, respectively. The high-

density AuNPs filter (Fig. 4.5-1b) shows a uniform distribution of AuNPs. By reviewing a typical profile line across the filter surface (Fig. 4.5-1c), there were 8 AuNPs distributed with an average spacing of 280 ± 5 nm and a height of 50 ± 10 nm. In contrast, the low-density filter (Fig. 4.5-1e) exhibits an irregular distribution of AuNPs across the surface, with particle heights ranging from 50 to 60 nm. Additionally, as SEM images shown, the high-density filter (Fig. 4.5-1d) demonstrates high-uniformity distribution of AuNPs upon SiO_2 layer with a high-density of ~50.6 particles μm^{-2} while the counterpart (Fig. 4.5-1g) shows less uniformity feature with a low-density of ~ 20.8 particles μm^{-2}.

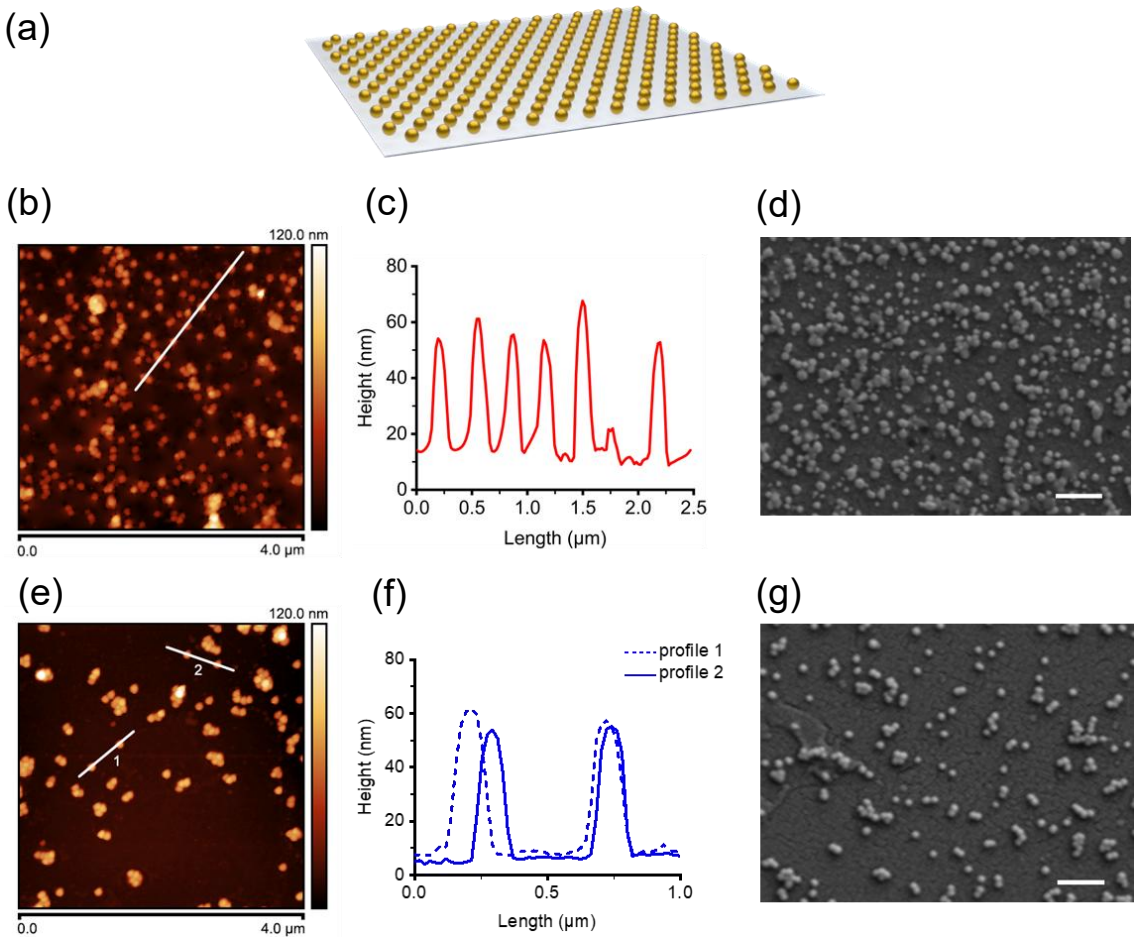

Figure 4.5 - 1 *(a) schematic illustration of AuNP filter. (b) AFM image of the high-density AuNPs filter. (c) AuNPs height profile according to the white line in (b). (d) SEM image of the high-density AuNPs filter. (e) AFM image of the low-density AuNPs filter. (f) AuNPs height profiles according to the white lines in (e). (g) SEM image of the low-density AuNPs filter [6].*

4.6. Chapter summary

In this chapter, several typical deposition techniques have been developed to deposit 2D nanomaterials onto optoelectronic device. Specifically, the i-LbL deposition technique is performed for depositing GO, MXene, $BiTiS_3$, and α-MoO_3/GO heterostructure onto optical fibres. A thinner GO coating has been achieved for a consistent and uniform overlay with a thickness of ~10 nm. With multiple coating cycles and rotating technique, the thicker and homogeneous overlays can be achieved. EDS analysis is important to confirm the deposition components of the 2D materials, such as MXene, $BiTiS_3$, etc. A 2D heterostructure overlay (α-MoO_3/GO) has been successfully deposited, with the advantage in enhancing light-matter interactions with optical fibre devices (see Chapter 6). Furthermore, the wet transfer technique, spin coating approach and drop casting method were employed to transfer the SLG, deposit $CsPbI_3$ quantum dots (QDs) and Au nanoparticles (AuNPs), respectively. The selection of deposition techniques in this chapter is guided by the intrinsic properties of the 2D materials and the functional requirements of the target optical or optoelectronic devices. In general, solution-based methods such as i-LbL deposition, wet transfer, spin coating, and drop casting are preferred for layered or dispersible nanomaterials, as they enable conformal coating, thickness control, and compatibility with fibre and planar device geometries. For optical fibre platforms, techniques that promote uniform surface coverage and strong interfacial adhesion are prioritised, whereas for chip-based devices, deposition approaches that preserve device integrity and enable localised material placement are selected. These considerations ensure that each deposition strategy is appropriately matched to both the material characteristics and the intended device functionality, forming a foundation for the sensing and optoelectronic applications explored in subsequent chapters.

Chapter 5 Label-free biosensors

5.1. GO-LPG based biosensor for detection of cancer cells

Cancer cells exhibit distinct metabolic characteristics compared to normal cells, notably the Warburg effect, where glycolysis remains the predominant energy production pathway even in the presence of oxygen [156]. These metabolic profiles not only offer early indicators of malignancy but also provide insight into tumour biology, enabling the development of personalized therapeutic strategies and facilitating treatment monitoring [157,158]. It is well known that cells consume nutrients and release metabolites into their culture medium during incubation. Cell metabolites are small molecules involved in or produced by metabolic processes, such as amino acids, sugars, lipids, and energy-related compounds. Changes in these metabolites can reflect the physiological state of cancer cells. Their concentrations in culture media change with cellular activity and quantity, making them attractive targets for non-invasive cancer diagnostics [159,160]. Dulbecco's Modified Eagle's Medium (DMEM), widely used in cell culture, mimics the in vivo environment by supplying essential nutrients for cellular proliferation. As cell number increases, metabolic activity alters the chemical composition of the media. Conventionally, cell counting is performed manually using a haemocytometer prior to incubation. However, a label-free sensing strategy that detects cumulative changes in secreted metabolites offers a more practical, indirect approach for monitoring cell quantity and viability over time. While advanced techniques such as mass spectrometry and nuclear magnetic resonance spectroscopy have been employed to profile these metabolites, they often involve complex sample preparations, lengthy analysis times, and high operational costs [161]. To address these limitations, optical biosensors have emerged as promising platforms for rapid, cost-effective, and label-free detection of metabolic variations in live cancer cell cultures [162–164].

Graphene oxide (GO), a derivative of graphene, has drawn great attention due to its large π-conjugated planar structure and abundance of oxygen, epoxy and hydroxyl groups on the basal plane and carboxyl groups at the edges [31,38,47,165,166]. These features endow GO with excellent aqueous dispersibility, biocompatibility, and surface modifiability, making it suitable for biomedical applications. Over the past decade, GO has been explored in various applications, including drug delivery [167,168],

photothermal therapy [169,170], and the detection of glucose [171], hemoglobin [16], cancer cell [172], microRNA [173], and antibodies [1]. Optical fibre technologies, particularly long-period fibre gratings (LPGs), are widely used in biochemical sensing due to their high sensitivity to surrounding refractive index (SRI) changes [174].

Functionalisation of LPGs with GO overlays has further enhanced the sensing performance. This enhancement is attributed to the increased light-matter interaction introduced by the GO overlay. The high RI and ultrathin nature of GO strengthen evanescent field interaction with the surrounding medium, thereby improving the sensor's sensitivity to RI variations. Depending on the application, GO coatings have varied from several micrometers [175] to hundreds of nanometers for humidity or hemoglobin sensing [16,176], to thinner coatings (~ 50 nm) for gas or immunosensing [1,177]. The optical properties of GO are critical to the next-generation nano-photonic devices [178]. However, very limited studies have investigated the effect of GO thickness on optical performance, mainly due to the lack of efficient methods for precisely determining and controlling nanocoating thickness [165].

Accurate and label-free quantification of cancer cells remains a key challenge for early-stage diagnostics and tumor monitoring. Although hemocytometry is commonly used for cell counting, it is limited by manual operation and sample preparation requirements. To address this challenge and demonstrate a viable approach for cancer cell quantification, a GO-functionalized LPG biosensor was developed as a label-free sensing platform for the quantification of MCF-7 human breast cancer cells.

5.1.1. Materials and device fabrication

The following materials were used to assist the functionalisation of the biosensor: The graphene oxide (GO) nanocolloids, (3-Aminopropyl)triethoxysilane (APTES), sodium hydroxide (NaOH), acetone, ethanol, methanol,

The MCF-7 (ATCC) human breast cancer cells were cultured with Dulbecco's Modified Eagle Medium (DMEM) and Fetal bovine serum (FBS). The CellTrackerTM Green was used for the fluorescent characterisation of cancer cells.

The LPG, with a period of 400 μm and a length of 15 mm, was fabricated in a hydrogen-loaded single-mode fibre using a continuous-wave and frequency-doubled Argon laser at

a wavelength of 244 nm and a point-by-point technique. The grating was subsequently annealed at 85°C for 48 h to remove residual hydrogen and stabilise its optical properties.

The GO nanosheets were subsequently coated onto the LPG using the developed improved layer-by-layer (i-LbL) deposition technique, as detailed in Section 4.2. The concentration of GO used in this process was 0.1 mg/mL.

5.1.2. Cell media preparation and cell staining

MCF-7 human breast cancer cells (Fig. 5.1-1a) were seeded into a 6-well plate (Fig. 5.1-1b) at the following cell numbers counted with a traditional hemocytometer: 1) 0 (control, DMEM medium only), 2) 1000, 3) 10,000, 4) 100,000, and 5) 500,000 cells per well, each in 5 mL of complete DMEM medium supplemented with 5% FBS. The plate was incubated for 72 h under standard growth conditions (37°C, 5% CO2). After the 72-h incubation, the cell culture media were carefully collected into sterile Eppendorf tubes (Fig. 5.1-1c), with the corresponding concentrations of 0, 2×10^2, 2×10^3, 2×10^4, and 1×10^5 cells/mL.

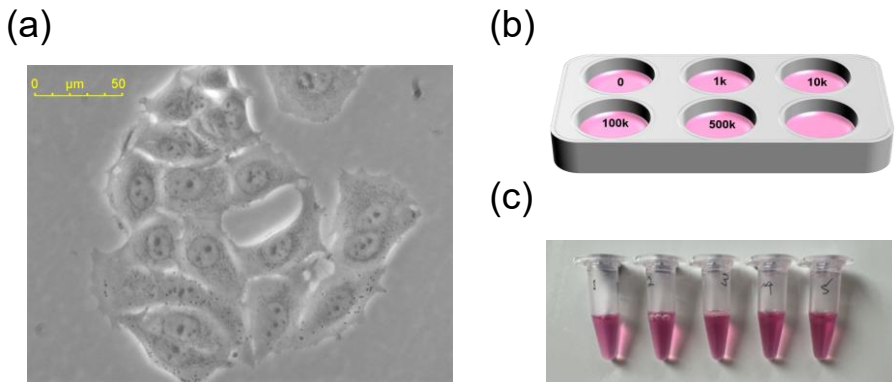

Figure 5.1 - 1 *(a) Bright-field image of viable MCF-7 cancer cells. (b) Schematic of MCF-7 cell culture setup in a 6-well plate. (c) Collection of conditioned culture media.*

To confirm the cells' density, the fluorescent imaging approach was applied. After the collection of culture media, the viable cells were incubated in CellTrackerTM Green at 0.1 nM final concentration for 15 min then imaged with a Leica DMI8 microscope with a 10× objective lens. The fluorescent images (Fig. 5.1-2a) presented the MCF-7 cancer cells at various seeding densities. An increase in fluorescent intensity was observed with increasing cell number, indicating good viability and effective staining of the cultured cells. MCF-7 cells were also stained with crystal violet solution for 10 min. The bright-field images of MCF-7 cells (Fig. 5.1-2b) further confirmed the differences in cell density across the wells.

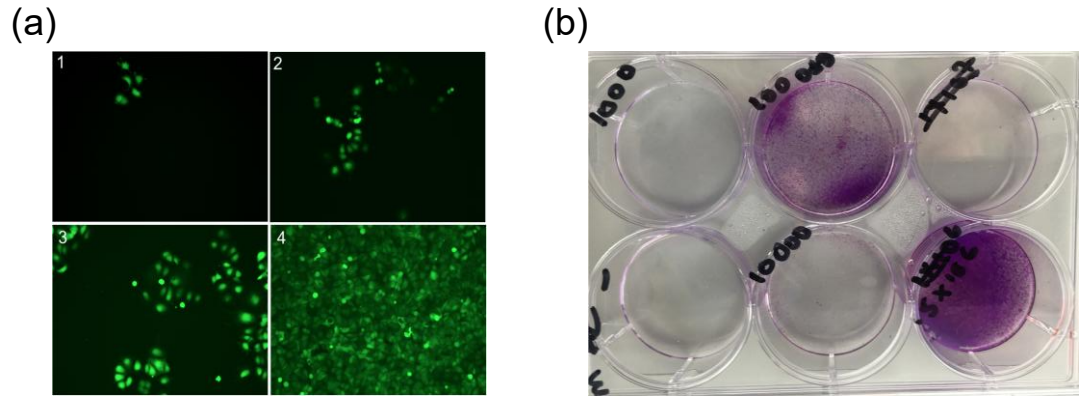

Figure 5.1 - 2 *(a) Fluorescent images of MCF-7 cells labelled with Cell Tracker Green at initial seeding densities of 1) 1000, 2) 10,000, 3) 100,000, and 4) 500,000 cells per well. (b) The Bright-field images of MCF-7 cells stained with crystal violet, highlighting differences in cell density across wells.*

5.1.3. Optical interrogation system

The GO-functionalised LPG biosensor operates based on RI modulation induced by changes in the surrounding medium, where variations in effective refractive index lead to shifts in the resonance wavelength, as described by the phase-matching condition introduced in Chapter 2. The GO overlay enhances evanescent field interaction with the external environment, thereby improving sensitivity to biochemical variations. To characterise the optical response of the GO-LPG device and evaluate its biosensing performance, an interrogation system was employed. As shown in Fig. 5.1-3, a superluminescent diode (SLD, S5FC1550S-A2, Thorlabs Ltd.) served as the light source to launch light into fibre, while the transmission spectra were monitored using an optical spectrum analyser (OSA, MS9740B, Anritsu Ltd.). To eliminate the cross-effects induced by bending and temperature, GO-LPG was placed in a custom-built container and kept straight while the external solution was applied. All measurements were conducted in a temperature-controlled room maintained at 21.0 ± 0.1 °C.

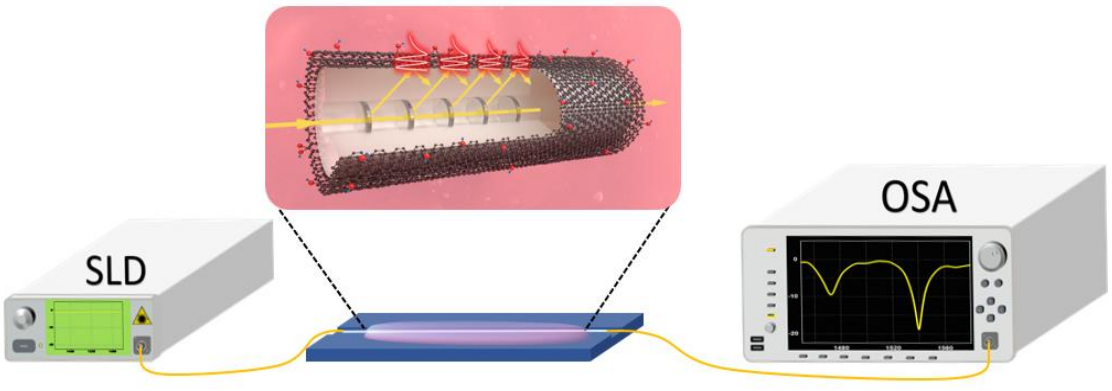

Figure 5.1 - 3 *Schematic illustration of the optical measurement setup.*

5.1.4. Effects of GO thicknesses on optical properties

The transmission spectra of the LPG attenuation band at 1538 nm were recorded before and after GO deposition (Fig. 5.1-4a, all measured in water). The thin 2GO-LPG (with 55 nm GO-overlay) resulted in a 3.5 dB increase in peak intensity with a slight red-shift of 0.4 nm, while the 4GO-LPG (with 125 nm GO-overlay) led to a 6.3 dB increase in intensity along with a slight red-shift of 0.7 nm. These results indicate that the GO overlay enhances evanescent field interaction with the surrounding medium, resulting in a progressively intensity-dominant spectral response as the coating thickness increases.

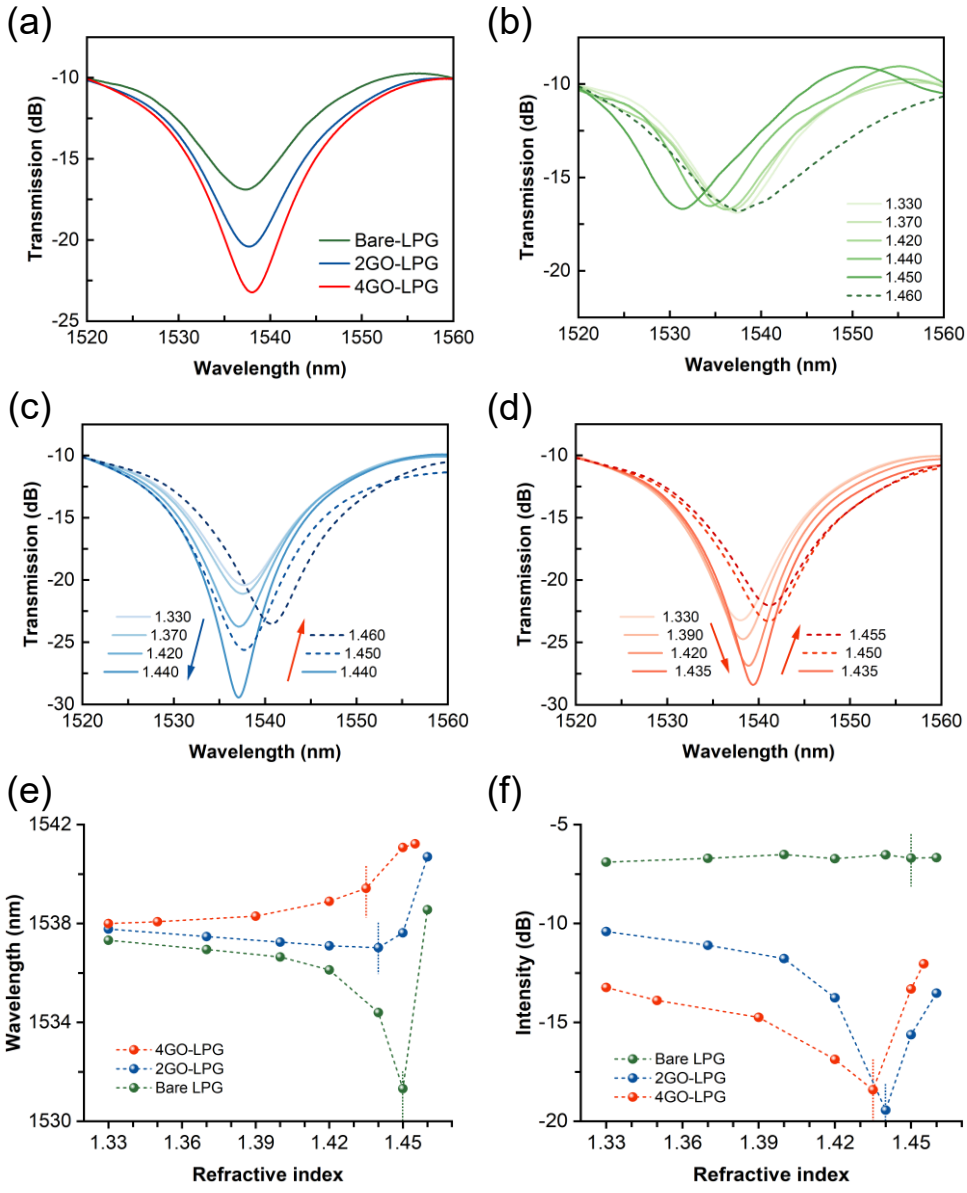

Figure 5.1 - 4 *(a) LPG transmission spectra (measured in water) with different GO thicknesses. Optical property evaluation under varying SRI for (b) bare-LPG, (c) 2GO-LPG, and (d) 4GO-LPG. LPG resonance wavelength shift (e) and intensity change (f) against SRI changes.*

The optical properties of GO-LPGs with different GO-overlay thicknesses were investigated under varying SRI (Fig. 5.1-4). The transmission spectra were monitored across a range of SRIs using the index-matching gels with RI from 1.330 to 1.460. For the bare-LPG (Fig. 5.1-4b), when the SRI increased from 1.330 to 1.450, the resonance showed a blue-shift of 6.01 nm while the peak intensity presented a negligible change (Table 5.1-1). This behaviour was consistent with that of the conventional LPGs *[21,174]*. For the thin coated 2GO-LPG (Fig. 5.1-4c), two distinct trends were observed in the attenuation band: (1) a blue-shift of 0.75 nm was detected along with a 9.03 dB increase in intensity when the SRI increased from 1.330 to 1.440; (2) the resonance exhibited a red-shift of 3.68 nm and a 5.91 dB decrease in intensity while the SRI increased from 1.440 to 1.460. As a contrast, the thick coated 4GO-LPG (Fig. 5.1-4d) showed a different behaviour: (1) an opposite red-shift of 1.43 nm to longer wavelength side accompanied by a 5.18 dB increase in intensity as the SRI increased from 1.330 to 1.435; (2) a further red-shift of 1.80 nm and a 6.37 dB decrease in intensity when the SRI reached to 1.455.

Table 5.1- 1 *Wavelength shift and intensity change under different SRIs (All wavelength shifts and intensity changes are referenced to the sensor response measured in DI water).*

	Sensor	SRI < TRI	SRI > TRI
Wavelength shift (nm)	Bare-LPG	- 6.01 nm	+ 7.24 nm
	2GO-LPG	- 0.75 nm	+ 3.68 nm
	4GO-LPG	+ 1.43 nm	+ 1.80 nm
Intensity change (dB)	Bare-LPG	- 0.21 dB	- 0.02 dB
	2GO-LPG	+ 9.03 dB	- 5.91 dB
	4GO-LPG	+ 5.18 dB	- 6.37 dB

As shown in Fig. 5.1-4e and 4f, there are three different transition refractive index (TRI) points of 1.450, 1.440, and 1.435 for bare LPG, 2GO-LPG, and 4GO-LPG, respectively. The TRI moved to a lower refractive index value as the GO thickness increased, which was consistent with previous findings [179,180].

It was reported that the real part of GO's complex refractive index ranged from 1.7 to 1.8, while the imaginary part lied between 0.3 and 0.4 in the 1550 nm wavelength region [180]. The presence of high refractive index (HRI) of GO coating could induce a transition from cladding-guided modes to overlay-guided modes. This transition could alter the effective refractive indices of cladding modes and consequently enhance the light-matter interaction between the optical device and the evanescent field [179,181]. In addition, since GO presented a complex refractive index, the cladding modes were more influenced

when the interaction was maximum at the light-matter interface at different GO thicknesses.

When the SRI was less than TRI, only a slight blue-shift was observed for the thin-coated 2GO-LPG. This behaviour could be attributed to the SRI increasing that facilitated the cladding mode transverse field profile to be stretched towards the HRI overlay, resulting in a reduction of the overlap integral between core and cladding modes [179,182]. In contrast, the thick-coated 4GO-LPG exhibited an immediate red-shift to an increasing of SRI, indicating that the presence of thicker HRI overlay induced the strong changes in the cladding mode distribution, where the mode transition occurred from cladding-guided to overlay-guided modes. The transition significantly enhanced the interaction between the evanescent wave and the surrounding medium.

In the region where the SRI was lower than the TRI, the coupling coefficient increased as the SRI rose, which led to an increase in the resonance intensity of GO-coated LPGs. This behaviour was consistent with the theoretical analysis [16]. Due to the complex refractive index of GO and the ongoing mode transition, both the coupling and extinction coefficients could be influenced. As the SRI approached the TRI, the GO-LPGs exhibited higher sensitivities of 283.95 and 102.47 dB/RIU for the thin- and thick-coated LPGs, respectively (Table 5.1-2). In the region where the SRI exceeded the TRI, the overlay-guided modes became dominant, and the coupling coefficient changed dramatically, with the light-matter interaction reaching its maximum at the interface. This resulted in the maximum RI sensitivities of -295.65 and -318.55 dB/RIU for the thin- and thick-coated LPGs, respectively.

Table 5.1- 2 *RI sensitivities of GO-LPGs at different RI regions (All wavelength shifts and intensity changes are referenced to the sensor response measured in DI water).*

RI region	2GO-LPG	4GO-LPG
1.330 – 1.420	+ 37.22 dB/RIU	+ 40.43 dB/RIU
1.420 – 1.440	+ 283.95 dB/RIU	+ 102.47 dB/RIU
1.440 – 1.460	- 295.65 dB/RIU	- 318.55 dB/RIU

5.1.5. Label-free quantification of cancer cells via culture media

The proposed sensor was utilized for the label-free quantitative detection of MCF-7 breast cancer cell via RI sensing of cancer cell media with initial concentrations of 0, 2×10^2, 2×10^3, 2×10^4, and 1×10^5 cells/mL, respectively. The cell media were mixed with a sucrose

solution (RI=1.455), which served as a high sensitivity RI buffer. It is important to note that the collected media contained no cells, only the metabolic byproducts secreted by the cancer cells during the culture period.

The 4GO-LPG was employed to detect the cell-conditioned media with the experimental setup in Fig. 5.1-3. An SLD source launched the light into the fibre sensor while the transmission spectra were monitored by the OSA. The fibre sensor was mounted in a custom-built container, which was fabricated from Teflon with a precision laser-cut groove along the centreline to hold the fibre sensor in a straight configuration. A pipette was used to manually introduce bio-samples and rinse the sensor during the measurements. As the transmission spectra recorded in Fig. 5.1-5a, a significant increase in resonance intensity of 2.95 dB was observed from media with increasing initial concentration from 0 to 1×10^5 cells/mL. The limit of detection (LOD) was determined to be 270 cells/mL, which was calculated based on the following equation [183]:

$$x_{\mathrm{LOD}} = f^{-1}(\bar{y}_{\mathrm{blank}} + 3\sigma_{\mathrm{max}}) \qquad (5.1-1)$$

where x_{LOD} is the limit of detection, $\bar{y}_{\mathrm{blank}}$ is the mean value of the blank sample, and σ_{max} represents the maximum standard deviation. The quantitative data (Fig. 5.1-5b) were expressed as the means $\pm$ standard deviations, with each data point averaged from a minimum of three independent measurements.

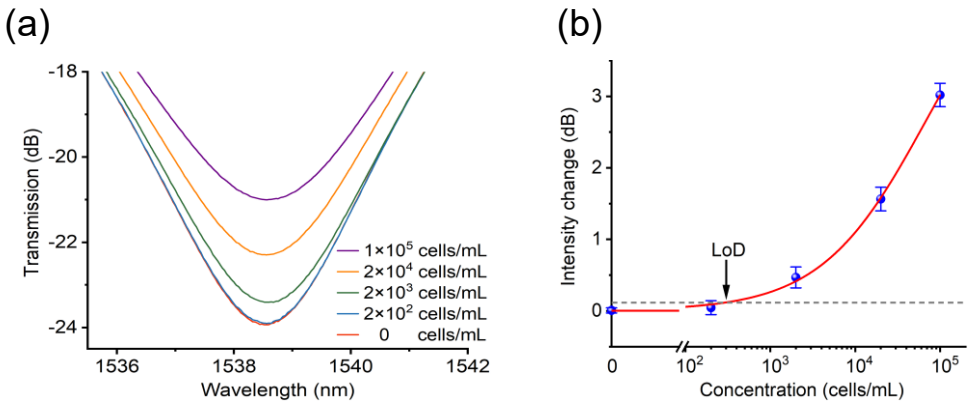

Figure 5.1 - 5 *(a) Transmission spectra corresponding to different cancer cell medium concentrations. (b) Intensity change of attenuation band against different cell medium concentrations.*

5.2. Hybrid short- and long-period gratings for label-free biodetection

5.2.1. Background of haemoglobin and hybrid gratings

Haemoglobin (Hb) plays a fundamental role in transporting oxygen throughout the body. Abnormalities in its concentration are closely associated with a variety of clinical conditions. For example, reduced Hb levels are a defining feature of anaemia and have been identified as an independent risk factor for cardiovascular disease and increased mortality in patients with coronary artery disease [184]. In oncology, baseline Hb concentration is widely recognised as a predictor of treatment outcomes. Patients with lower Hb levels often experience poorer responses to radiotherapy and shorter survival durations [185]. Despite its clinical significance, the detection of Hb in conventional settings commonly relies on techniques such as spectrophotometry, immunoassays, or surface plasmon resonance sensors. These methods usually require labelled reagents, extensive sample preparation, and specialised equipment, which makes them impractical for rapid testing in decentralised or resource-limited environments [186]. Optical fibre technologies have been widely investigated for biomedical applications by employing FBGs and LPGs with the advantages of label-free, real-time, multiplex and in-line determination [21,22]. However, the major challenge is the lack of high sensitivity and accuracy for the applications with small biomolecules and low concentration of analyte. FBG owns inherent advantage of narrow resonance due to the light coupling between counter propagating core modes but lack of the sensitivity for external refractive index (RI) detection as the light is confined in fibre core [22]. With the light coupling from core to cladding modes, LPG is a naturally good candidate for RI sensing but with the drawback of its broad bandwidth [1,187]. Therefore, A hybrid structure was formed by combining LPG and FBG, allowing the advantages of both short- and long-period gratings to be exploited, namely ultra-narrow resonances with high signal-to-noise ratio and enhanced refractive index sensitivity. In addition to the well-established core–core and core–cladding interactions [188,189], high order cladding–cladding mode coupling has also been observed for the first time in such a hybrid grating structure [190]. The proposed hybrid LPG/FBG has been implemented to detect the human haemoglobin demonstrating a high sensitivity.

5.2.2. Fabrication of hybrid LPG/FBG

The hybrid LPG/FBG structures were fabricated by collaborators at the University of Valencia and provided for use in this work, while all subsequent device characterisation and biosensing experiments were conducted by the author. The hybrid short- and long-period gratings are formed by a 10 mm-length LPG which couples the core mode to the $LP_{0,7}$ cladding mode [191,192], followed by a 5 mm gap, then a 24 mm-length FBG which acts as a reflector. Both gratings were inscribed in a boron/germania co-doped fibre (PS1250/1500, Fibercore Ltd.) by the use of a 244 nm argon-ion laser. The grating periods are Λ_{LPG} = 322 μm for the LPG and Λ_{FBG} = 538 nm for the FBG.

5.2.3. Multiple coupling mechanisms of hybrid LPG/FBG

The transmission spectrum of the hybrid gratings has been monitored (Fig. 5.2-1a), where the central wavelength of LPG resonance is 1543.50 nm with a bandwidth over 30 nm and depth of 19.23 dB while a Bragg peak is located at 1558.50 nm with a strong depth more than 30 dB. Over the bandwidth of LPG resonance, a series of resonances (i.e., loss spikes) appear at the short wavelength side of Bragg peak indicating the strong coupling to cladding modes. In the reflection spectra (Fig. 5.2-1b), along the left side of Bragg resonance, there are three ultra-narrow resonances at 1550.62, 1553.22, 1555.88 nm with FWHM of 53, 56, and 58 pm, respectively, due to the occurrence of cladding-mode assisted recoupling mechanisms by introducing the LPG.

When the light is launched into the fibre, a portion of core mode will be coupled by the LPG to the $LP_{0,7}$ cladding mode at 1543.50 nm while the remaining portion will keep travelling along the core. Subsequently, when the lights (both core and cladding modes) reach the FBG region, the strong FBG will couple the light by three main mechanisms (Fig. 5.2-1c): (1) the core-to-core (co-co) coupling is induced between the forward-propagating and counter-directional core modes, yielding a Bragg reflection peak at 1558.50 nm ($LP_{0,1}$ - $LP_{0,1}$ interaction). (2) the cladding-to-core (cl-co) coupling is observed at the left side of the Bragg peak in the transmission spectrum, where a comb of cladding modes is induced (Fig. 5.2-1a) by the coupling between the forward-propagating core mode and the backward-propagating cladding modes along the cladding [193], travelling close to the core/cladding boundary then consequently be selectively recoupled back to the core by the LPG, producing a reflective resonance at 1555.88 nm ($LP_{0,7}$ - $LP_{0,1}$ interaction). (3) the cladding-to-cladding (cl–cl) coupling occurs when the light, which is coupled to the $LP_{0,7}$ cladding mode by the LPG, travels through the 5 mm gap and meets

the strong FBG. It will be recoupled back to higher order cladding modes and finally be recaptured back to the core by the LPG ($LP_{0,7}$ - $LP_{0,n}$ interaction). These interactions are responsible for the reflective peaks at 1553.22 nm and 1550.62 nm, named cl-cl1 and cl-cl2, respectively.

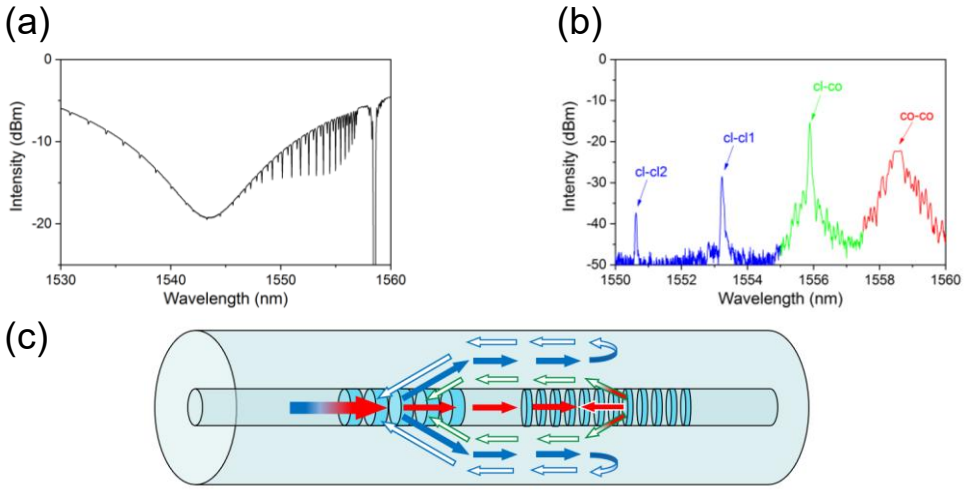

Figure 5.2 - 1 *(a) Transmission of the hybrid gratings. (b) Reflection spectrum. Four bands can be seen due to different coupling mechanisms. (c) Schematic of the hybrid LPG/FBG device. The arrows indicate light propagation and coupling paths, with colours corresponding to the reflection peaks shown in (b).*

A close inspection of the intensity profile (Fig. 5.2-1b) reveals a signal-to-noise ratio as large as 35 dB for the cl-co reflection, 21.5 dB for the cl-cl1 and 12.65 dB for the cl-cl2 reflection, respectively. This is attributed to the pronounced coupling strengths of the LPG and FBG, facilitating effective interaction with counterpropagating cladding modes.

Concerning the clad-clad coupling mechanisms, it is worth to note that the boundary between the gap and the LPG acts as a discontinuity in the structure, allowing the excitation and energy transfer between cladding modes and the core mode. This explains the two shorter wavelength reflection peaks. Such interaction between cladding modes can be found in other works, where the discontinuity can be a thin-core fibre [193], a mismatched splice [194] or a multi-mode fibre [195]. Furthermore, these interactions have also been reported in compound grating structures as described in [191].

5.2.4. Optical characterisation of the hybrid gratings

Reflection spectra in both directions: To verify the directional functionality of the hybrid LPG/FBG, the reflection spectra were measured by inducing light from both ends, as shown by the inset in Fig. 5.2-2. The results reveal the inherent asymmetry of the configuration. When the light is launched from the left side (e.g., LPG side), multiple reflection peaks are observed (blue colour spectrum), corresponding to the various modal

interactions enabled by the LPG-to-FBG device. In contrast, when the light is launched from the right side (e.g., FBG side), only the core mode reflection (i.e., Bragg peak) is detected (red colour spectrum), where its intensity is approximately 10 dB higher than former measurement due to the reflection occurring before the light reaches the LPG section downstream.

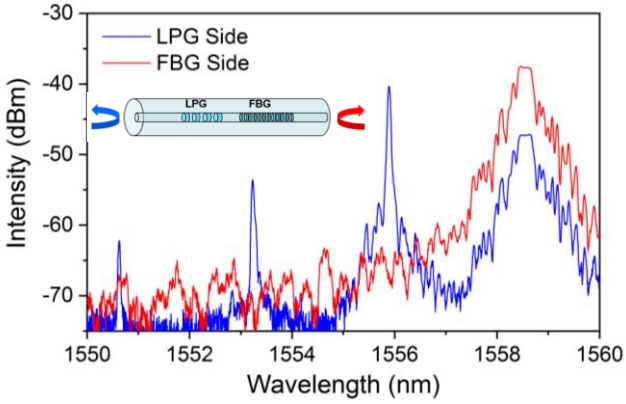

Figure 5.2 - 2 *Reflection spectra of light launched from different sides of the device (inset: light injection schematic).*

Mode couplings of hybrid LPG/FBG: In order to examine the cladding–cladding interactions and identify which region of the hybrid grating could be the most sensitive to external RI variations, the index-matching oil with a high refractive index (HRI) n = 1.460 (Cargille Inc., USA) was selected to apply to different regions of the hybrid LPG/FBG device, with the results shown in Fig. 5.2-3.

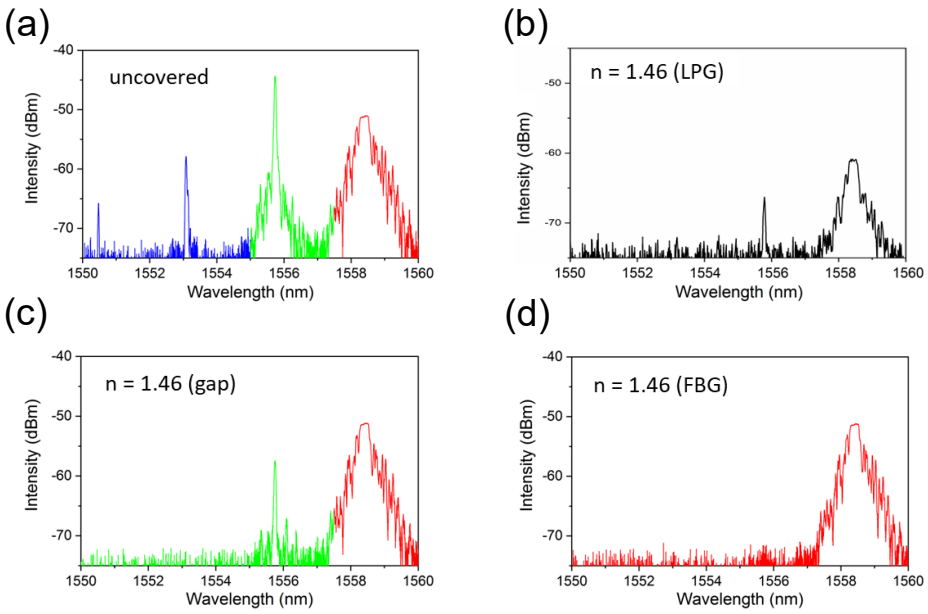

Figure 5.2 - 3 *Reflection spectra of the hybrid device under different refractive index (RI) conditions: (a) without RI liquid; (b) with n = 1.460 liquid applied over the LPG region; (c) with n = 1.460 liquid applied exclusively to the gap region between the LPG and FBG, and (d) with n = 1.460 liquid applied only over the FBG section.*

Under the condition without any external RI perturbation (Fig. 5.2–3a), all three reflection mechanisms are present: cladding–cladding (cl–cl1 and cl–cl2, blue), cladding–core (cl–co, green), and core–core (co–co, red).

Firstly, when the HRI liquid is applied over the LPG section (Fig. 5.2–3b), both cl-cl1 and cl-cl2 peaks disappear whilst a weakened cl–co and co-co peak remain. This can be attributed to the mode transition from cladding modes into leaky modes due to the HRI environment [22].

Secondly, when the HRI gel is applied to cover the gap region only (Fig. 5.2-3c), the co-co and co-cl peaks remain and with a slight enhanced intensity whilst the high cladding modes cl-cl1 and cl-cl2 are still eliminated. This can be attributed to the core-related couplings are less affected by the gap surrounded with the HRI gel, which causes the mode transition between cladding and leaky modes and prevents high-order cladding modes pass through the gap region.

Finally, when the HRI gel is applied to cover entire FBG, the co-co coupling remains unaffected whilst all cladding mode are completed prevented, hence all cladding-related peaks (couplings) have disappeared.

HRI against different length of FBG coverage:

The influence of the HRI environment to the hybrid gratings was further investigated. The HRI gel (n-1.460) was applied to cover the FBG region starting from the downstream end (e.g. right end of the FBG) with 8mm, 16mm, 24mm, respectively (Fig. 5.2-4). As the presence of the HRI medium prohibits higher-order cladding modes guidance, the effective length of the FBG is gradually reduced. Therefore, the modal coupling efficiency is subsequently decreased. The cladding-to-cladding reflections (cl-cl2 and cl-cl1) are firstly suppressed when 8 mm and 16 mm of the FBG are covered. When the full 24 mm length of the FBG is immersed in the HRI gel, the cladding–core (cl-co) reflection is also eliminated. Finally, when the HRI coverage is extended to cover entire FBG plus the gap region, all cladding-related couplings are inhibited.

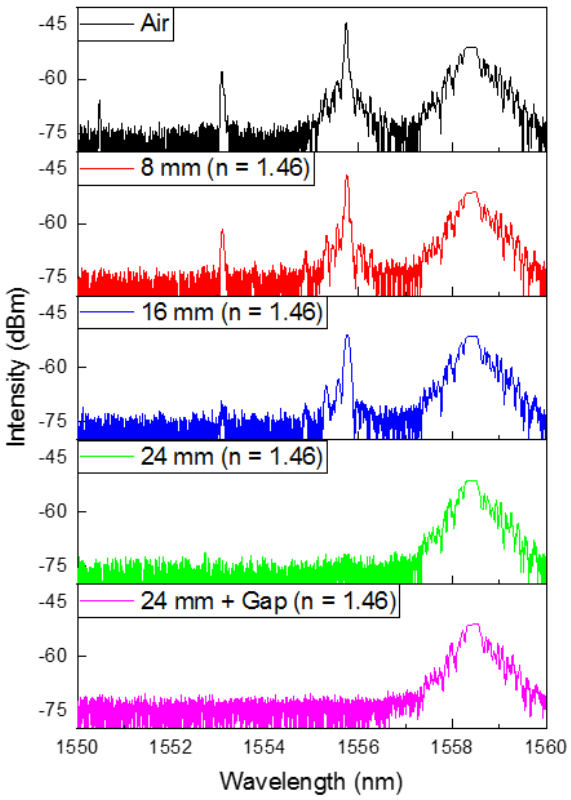

Figure 5.2 - 4 *Reflection for n = 1.46 oil covering different lengths of the FBG.*

Sensitivity of the hybrid grating: Considering its advance of narrow bandwidth of the reflection peaks (~10 GHz), the hybrid grating was performed for the RI test to evaluate its possibility for the external RI sensor. A set of RI solutions at lower RI region (1.333-1.360) was used to cover the FBG section whilst the spectra of the peaks were monitored. As we can see from Fig. 5.2-5a, the cl-cl2 peak showed a red shift of ~ 20 pm when the external RI increase from 1.333 to 1.360. Fig. 5.2-5b plots the wavelength shifts of four peaks when the FBG region was dipped into the RI gels. When the FBG was insert into water (from air), all three cladding-related peaks showed red-shift where cl-cl2 peak demonstrated a dramatic shift of 38 pm whilst the Bragg peak showed no noticeable change. Within the lower RI range (e.g., 1.333-1.360), all the peaks show a near linear relation between wavelength shift to the RI change. The RI sensitivities are 741 pm/RIU, 574 pm/RIU, and 426 pm/RIU for cl-cl2, cl-cl1, cl-co peaks, respectively. The higher cladding mode (cl-cl2) demonstrates the highest RI sensitivity.

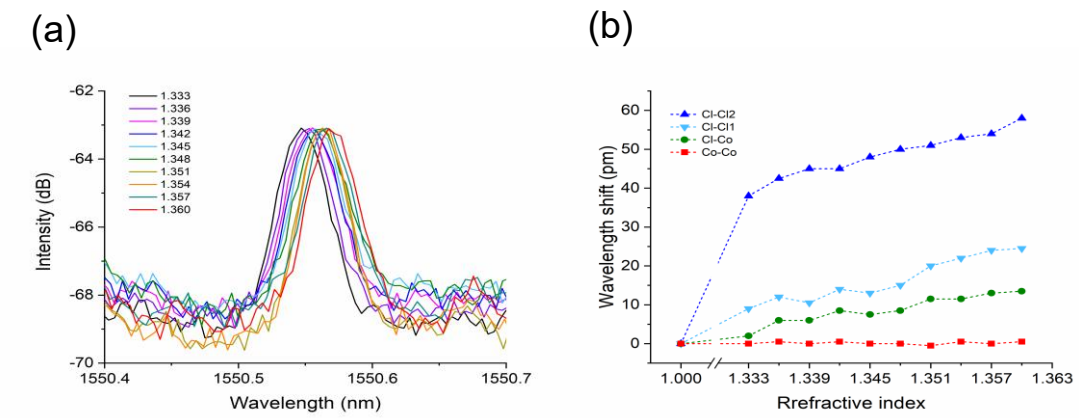

Figure 5.2 - 5 *(a) Reflection spectra of cl-cl2 peak under different RIs, (b) The wavelength shifts of four peaks against the RI changes.*

5.2.5. Label-free detection of haemoglobin

The proposed hybrid grating was implemented to detect human haemoglobin. A set of human haemoglobin concentrations (0.0%, 0.2%, 0.4%, 0.6%, 0.8%, 1.0%) was prepared. The reflection spectra of cl-cl2 peak were monitored and showed a clear red shift of 15.0 pm when the haemoglobin concentration increased from 0.0% to 1.0% (Fig. 5.2-6), giving a sensitivity of 1.5 pm/(mg/mL). By employing a low-noise interrogation system with a high resolution of 1.0 pm, the sensor is capable of detecting haemoglobin concentration changes as small as 0.67 mg/mL, which is far below the hemoglobin threshold value for anemia defined by WHO (120 mg/mL for women and 130 mg/mL for men).

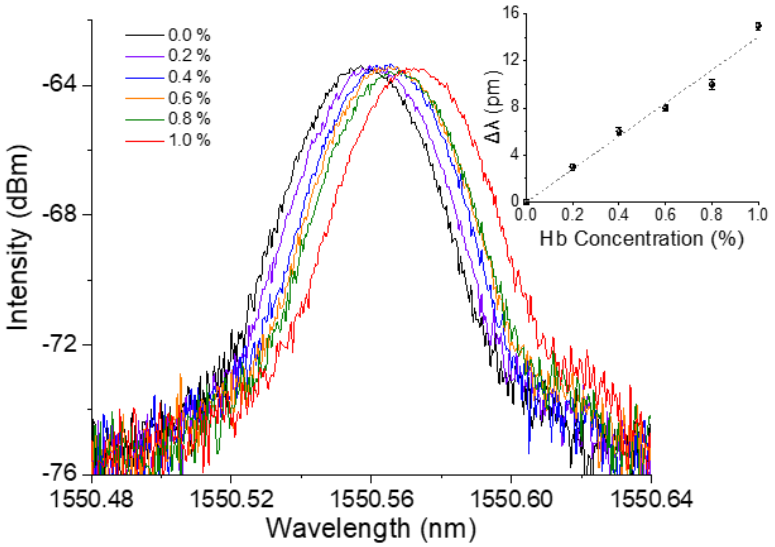

Figure 5.2 - 6 *Reflection spectra of the clad-clad 2 peak against haemoglobin concentrations (Inset: Linear relationship between the resonance wavelength shift of the cl–cl2 peak and haemoglobin concentration, extracted from the reflection spectra).*

5.3. Perovskite-graphene heterostructure biosensor for cytokine detection

5.3.1. Background of cytokines

Cytokines are crucial cell mediators in immune and inflammatory responses [196]. The determining cytokine levels in a variety of biological fluids (i.e., serum, blood, and saliva) provide valuable information in relation to the diagnosis and prognosis of different diseases and trauma [197,198]. Extremely high cytokine secretion may result in organ failure and death. For example, patients with Sars Cov2 (COVID-19) might suffer cytokine storm syndrome [199,200]. As one of the key human inflammatory cytokines, interleukin 6 (IL6) has an extensive impact on cells of the immune system and demonstrates hormone-like traits that influence the homeostatic balance [201]. The elevated circulating IL6 concentrations are concerned with numerous diseases, including cardiovascular disease [202,203], cancer [204], type 2 diabetes [198], and severe acute COVID-19 infection [205,206]. In general, it is required to detect IL6 concentrations down to pg/mL in human derived biological fluids [197,207]. Hence, it is crucial to develop biosensors with a limit of detection (LOD) in the range of sub pg/mL. Enzyme-linked immunosorbent assay (ELISA) has been the gold standard method for cytokine detection for many decades [208]. However, these methods are laborious and costly, limiting their wide usage in applications, particularly in emergency and urgent point-of-care settings where the rapid screening and diagnosis can be lifesaving.

5.3.2. 2D materials-based FET biosensor

Among various sensing methods, 2D materials-based field-effect transistors (FETs) [209–211] have attracted great research attention due to the advantages of label-free detection, high sensitivity, and fast response [11,212–225]. FET biosensors are electronic devices in which the binding of charged or dipolar biomolecules at the semiconductor surface modulates the carrier density and conductance of the transistor channel. Owing to their label-free operation, high sensitivity, and ease of electrical integration, FET-based biosensors have become an important class of devices for real-time biochemical detection. Compared with optical fibre sensors, FET biosensors are particularly attractive for compact, chip-based sensing systems, while optical fibre sensors provide superior performance for remote, optically interrogated, and electromagnetically robust sensing scenarios. Hao et al. proposed graphene-based FETs for IL6 detection with an LOD of hundreds of fM [212,213]. The molybdenum disulfide

(MoS_2)-based FET biosensors were developed for cytokine detection with an LOD down to tens of fM [216–218]. Very recently, van de Waals (vdW) heterostructures composed of atomically thin 2D materials have been extensively investigated, such as tin disulfide (SnS_2)/hexagonal boron nitride (h-BN), black arsenic (b-As)/SnS_2, and carbon nanomembrane (CNM)/graphene heterostructure-based FET biosensors [223–225]. The operating mechanism of the FET biosensor is to detect the electronic response induced by the binding between biomolecules. However, the electric field of FET is normally distributed throughout a bio-sample solution, which could perturb signal stability or cause unwanted leakage current and/or short circuits. Another challenge of 2D materials-based FETs is the degradation of 2D materials [209,226], which will affect the stability over long-term exposure to aqueous environments. An alternative scheme has been proposed to avoid the degradation by separating the FET detector and the biological solutions [218]. However, the rapid and highly sensitive bio-detection still remained as a major challenge.

5.3.3. Development of the biosensor

The perovskite/graphene heterostructure-based FET biosensor integrated with a biotunable nanoplasmonic ternary logic gate was developed for cytokine detection, operating with three modes (+1, 0, -1). As the diagram illustrated in Fig. 5.3-1, the biosensor is comprised of a lateral perovskite-on-graphene phototransistor integrated with a vertical bio-nano-photonic filter, with a decoupled construction inset. In the phototransistor, a thin film of perovskite quantum dots (PQDs) is spin-coated upon a single-layer graphene (SLG), where the photoactive PQDs capture the light and generate electro-hole pairs, while the photogenerated charges are transferred to the high mobility graphene layer. The vertical bio-nano-photonic filter consists of an anti-human interleukin 6 antibody (anti-IL6) immobilised gold nanoparticles (AuNPs) on a SiO_2 thin layer. Under laser illumination, the localised surface plasmon resonance (LSPR) induced by AuNPs in conjunction with the binding of antigen-antibody tunes the delivery of incident light passing through the filter and reaching the underlying FET.

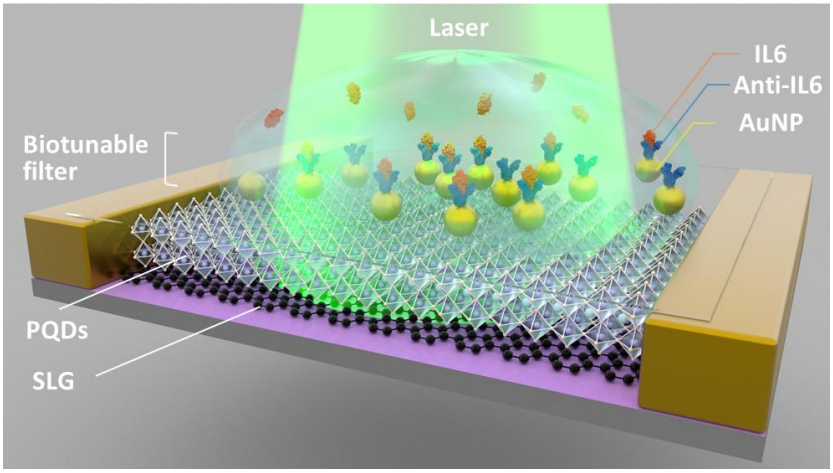

Figure 5.3 - 1 *PQDs/SLG heterostructure FET biosensor with biotunable nanoplasmonic ternary logic gating functionality. The biosensor was integrated by a lateral perovskite-on-graphene heterostructure phototransistor and a vertical bio-nano-photonic filter consisting of anti-IL6-immobilised AuNPs. The biosensing principle is based on the LSPR shifts induced by antigen-antibody binding, tuning the delivery of incident light passing through the bio-nano-photonic filter to the phototransistor.*

Materials and reagents used for functionalisation of the biosensor are list as follows:

Single-layer graphene (SLG) fabricated by chemical vapor deposition on copper, $CsPbI_3$ perovskite quantum dots (PQDs), Gold nanoparticles (AuNPs, d = 50 nm), acetone, ethanol, ammonium persulfate ($(NH_4)_2S_2O_8$), (3-Aminopropyl)triethoxysilane (APTES), deionized water, phosphate-buffered saline (PBS), neutravidin, SuperBlock, mouse biotinylated anti-human IL6 antibody (anti-IL6), recombinant human IL6 protein, goat Anti-Mouse IgG - AF488, serum, c-reactive protein (CRP), carcinoembryonic antigen (CEA), albumin (ALB), alpha-fetoprotein (AFP).

Fabrication of perovskite-on-graphene heterostructure based FET: The methods, including photolithography, metal sputtering, and lift-off, were utilised to fabricate the FET device with Ti(5 nm)/Au(52 nm) electrodes as the drain and source contacts on SiO_2/Si substrate. Then the single layer graphene (SLG) was deposited onto a FET chip using the PMMA-assisted wet transfer method (as detailed in section 4.3). Finally, the $CsPbI_3$ perovskite quantum dots were spin-coated onto the graphene layer (as detailed in section 4.4).

Fabrication and biofunctionalisation of nano-photonic filter: Distribution of AuNPs on a transparent substrate was used for LSPR biosensors. As shown in Fig. 5.3-2, a thin SiO_2 substrate was rinsed with acetone, isopropanol, and DI water, then the surface was treated with O_2 plasma for 2 min at a power of 150 W, and the SiO_2 substrate was incubated in a 10% APTES solution for 2 h. AuNPs were drop-casted on the upper-surface

of the substate by incubating the substrate in the AuNPs solution overnight with concentrations of 50 and 5 µg/mL to fabricate high- and low- density AuNPs filters, respectively. Subsequently, the AuNPs self-assembled filter was immersed in NeutrAvidin solution (0.1 mg/mL) at 4°C overnight. The 50 µL 0.1 mg/mL biotinylated anti-human IL6 antibody (anti-IL6) was loaded onto the filter at room temperature for 1 h to immobilise anti-IL6 onto the AuNPs surfaces. The non-bound anti-IL6 antibodies were washed away with PBS buffer. The unreacted sites on AuNPs surfaces were passivated with SuperBlock to block the remaining active carboxylic groups and prevent non-specific adsorption.

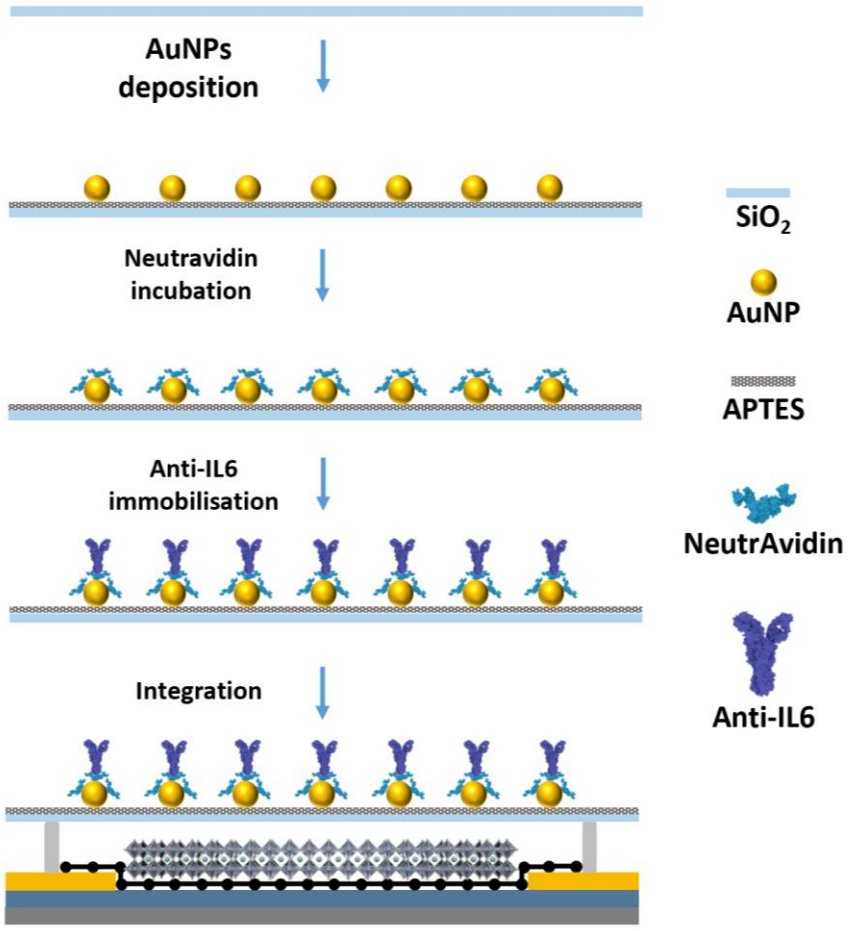

Figure 5.3 - 2 *Schematic illustration of the assembly of bio-nano-photonic filter [6].*

Fluorescent characterisation was employed using a secondary fluorescent antibody (Goat Anti-Mouse IgG-AF488) to verify the modification efficiency of anti-IL6 on the surface of the AuNPs filter (both for low- and high- density filters), as shown in Fig. 5.3-3. The fluorescence microscopy images and corresponding statistical analysis (Fig. 5.3-3 (b-d) for low-density, and Fig. 5.3-3 (e-g) for high-density), strong fluorescence signals were

observed in both cases compared to the control groups, indicating effective and consistent functionalisation of the AuNP surfaces with anti-IL6. These results demonstrate that the AuNP filters, regardless of nanoparticle density, provide a robust platform for antibody immobilisation. Finally, the anti-IL6 biofunctionalised AuNPs filter was assembled upon the PQDs/SLG, with a gap of 100 µm to form the sensor device.

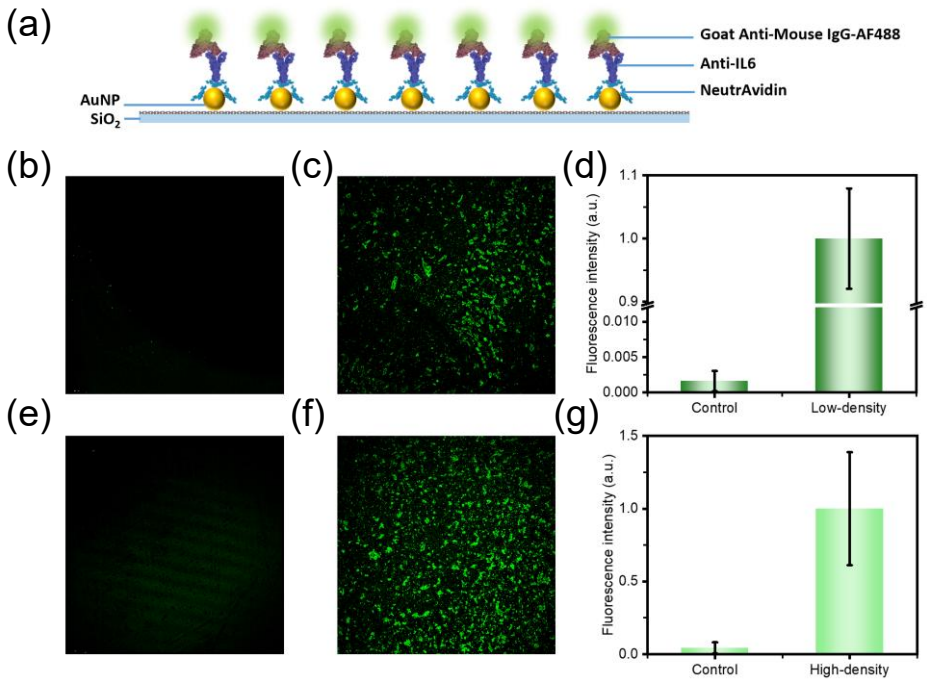

Figure 5.3 - 3 *Fluorescent characterisation of Mouse biotinylated anti-human IL6 antibody (anti-IL6) on AuNPs filter. (a) Schematic of secondary fluorescent antibody (Goat Anti-Mouse IgG-AF488) binding with anti-IL6. For low-density AuNP filter: (b) control group, (c) fluorescence microscopic image, (d) statistical values of fluorescence intensity in (b) and (c). For high-density AuNP filter: (e) control group, (f) fluorescence microscopic image, (g) statistical values of fluorescence intensity in (e) and (f) [6].*

5.3.4. Measurement system

All electronic characteristics of the FET were monitored using a Keithley 4200 semiconductor parameter analyzer. The Coherent Compass 115M-5 laser (λ = 532 nm) was used as a light source with intensity adjusted between 1 µW and 1000 µW using an optical attenuator (Thorlabs NDC-50C-4M). The surface morphology was examined by a Scanning Electron Microscope (SEM, JSM-7100F LV, JEOL Ltd.), Atomic Force Microscope (AFM, Bruker Dimension Icon, Bruker Ltd.), and X-ray Photoelectron Spectroscopy (XPS, Thermo Fisher Scientific Inc.).

5.3.5. Design and mechanism of PQDs/SLG heterostructure-based FET

The biosensor was integrated by a lateral phototransistor and a vertical bio-nano-photonic filter. In the lateral phototransistor, a perovskite-on-graphene heterostructure film bridged

the FET source and drain electrodes, photoactive PQDs served as sensitizers to absorb light and convert the photons to electric carriers, while high mobility SLG acted as an expressway for carrier transport. With this architecture, PQDs/SLG demonstrated synergistic effects, with each enhancing the other's capabilities for efficient light-carrier transition and high-speed electron transportation. From the top of the device, the bio-nano-photonic filter tuned the delivery of incident light by means of LSPR shift induced by antigen-antibody binding, operating as a biotunable gate with three logic modes (+1, 0, -1) [227].

Fig. 5.3-4 illustrates an insight into the mechanisms underpinning the biotunable ternary logic biosensor. As the cross-section in Fig. 5.3-4a, a decoupled construction (100 µm physical gap) was designed between AuNPs-filter and PQDs film to separate the 'wet' biosensing area and the 'dry' photodetection area, which not only simplified the complexities inherent in traditional FETs but also enhanced device stability without impairing the properties of the 2D materials. The vertical AuNPs-based nano-photonic filter functions to tune the delivery of incident light reaching the underlying FET channel via LSPR modulation induced by antigen-antibody binding, thereby enabling biotunable gating with ternary logic states. Two types of filters were developed: high- and low-density AuNPs filters. SEM images show the high-density filter (Fig. 5.3-4b) demonstrated high-uniformity in the distribution of AuNPs upon the SiO_2 layer with a high-density of ≈50.6 particles μm^{-2}, while the counterpart (Fig. 5.3-4c) showed less uniformity in features with a low-density of ≈20.8 particles μm^{-2}.

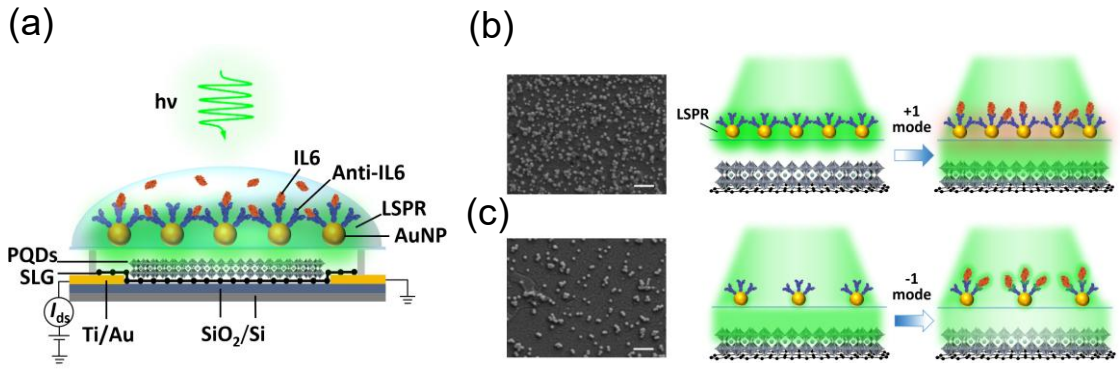

Figure 5.3 - 4 *(a) Schematic of biosensor with a decoupled construction between filter and phototransistor. The mechanism of the biotunable ternary logic gate is based on tuning the delivery of incident light to PQDs/SLG phototransistor by LSPR shifts induced by biomolecular binding by the use of: (b) high-density AuNPs filter for operating from 0 to +1 mode, (c) low-density AuNPs filter for operating from 0 to -1 mode (SEM image scale bar: 500 nm) [6].*

For the high-density filter (Fig. 5.3-4b) under laser illumination (0 mode), the initial photocurrent detected by the phototransistor was lower due to the strong LSPRs excited by the high-density and well-distributed gold nanoparticles under laser illumination, blocking the incident light passing through the filter. When the target human IL6 cytokines were present to bind with the anti-IL6 probe, a red shifted LSPR was induced due to the change of the local refractive index near the AuNPs surfaces [218,221], hence a larger amount of incident photons was transmitted through the filter increasing the photocurrent detected by the underlying phototransistor (+1 mode). The tuning was dependent on IL6 concentration as well as the antigen-antibody binding time. For the low-density filter (Fig. 5.3-4c), a strong photocurrent was initially detected (0 mode) due to very limited LSPRs generated by the poor-distributed low-density AuNPs, where a large fraction of incident light passed through the filter. When affinity binding increased, more antigens were attached to antibodies, shielding the light transportation and hence the photocurrent decreased (-1 mode).

5.3.6. Optical characterisation of PQDs/SLG heterostructure FET

The effect of the drain bias applied to the FET was plotted in Fig. 5.3-5a. The photocurrent I_{ds} was recorded while the source-drain voltage V_{ds} was swept from −2.0 to −1.8 V under the laser illumination with varying power (0, 1, 10, 100, and 1000 μW), revealing a noticeable increase in I_{ds} against the increased laser power. As an example (with a laser power of 1 μW), the photocurrent increased from −950.7 to −737.6 μA when the applied bias voltage was changed from −2.0 to −1.8 V. As a function of the incident laser power, for a fixed V_{ds} = −2.0 V, as shown in the inset figure in Fig. 5.3-5a, the photocurrent I_{ds} changed 63.7 μA when the laser power increased from 1 to 1000 μW. Fig. 5.3-5b shows the photo-switching response of the proposed device. The normalised photocurrent I_{ph} was defined by the ratio of photocurrent I_{ds} over the maximum drain-source current I_{ds_max} when the bias voltage was set as 0.1 V. The normalised photocurrent was stable as a function of time under the alternating illuminated and dark conditions with a duration of 55 s and a laser power of 500 μW. The On/Off photo-responses were well maintained for five repeated cycles. The high photoresponsivity of the proposed device facilitated its capability for rapid and ultrasensitive biosensing applications.

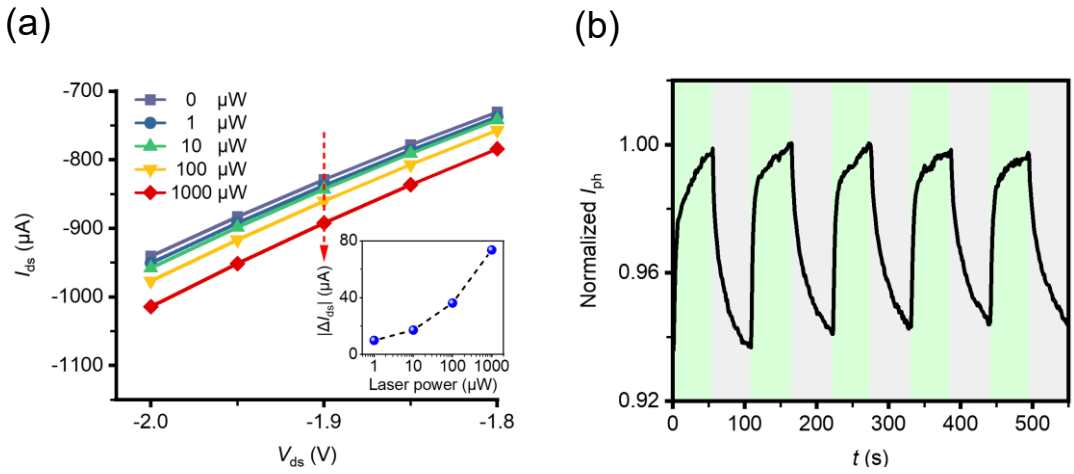

Figure 5.3 - 5 *(a) I_{ds}-V_{ds} curves of perovskite/graphene heterostructure FET under laser illumination with different powers (inset: the dependence of photocurrent against laser power at V_{ds} = −2 V). (b) Temporal I_{ph} response under alternating dark and light (λ = 532 nm, P = 500 μW) [6].*

5.3.7. Ultrasensitive detection of IL6 cytokines

The proposed device was able to detect IL6 cytokines. The anti-human IL6 antibody-immobilised AuNPs filter was loaded with human IL6 cytokine of different concentrations. During the antigen-antibody binding events, the corresponding photocurrent I_{ds} was monitored in real-time. The standard curve of photocurrent-time response provided the best Hill model fitting for the experimental data, where the photocurrent enhancement ΔI can be described by the Hill-Langmuir equation [228,229]:

$$\Delta I = \frac{C_{IL6}^n}{C_{IL6}^n + K_d^n} \Delta I_{max} \qquad (5.3-1)$$

where C_{IL6} is the ligand concentration, n is the Hill coefficient, which can determine the cooperative degree of ligand binding, K_d is the dissociation constant of ligand molecular interaction, and ΔI_{max} is the maximum photocurrent enhancement.

Under "0" mode: For "0" mode (i.e., the AuNPs-filter was immersed in 1×PBS buffer only), the base photocurrents I_{ds} of the biosensor were measured and plotted in Fig. 5.3-6. The I_{ds} - V_{ds} curves showed a non-linear relationship: when a bias voltage increased to 1 V, the photocurrent I_{ds} was 256.04 μA and 267.46 μA for the high- and low- density filters, respectively. As discussed in Section 5.3.5, high-density AuNPs excited stronger LSPR yielding less light flux to the phototransistor, hence its base I_{ds} was lower than that of the low-density filter.

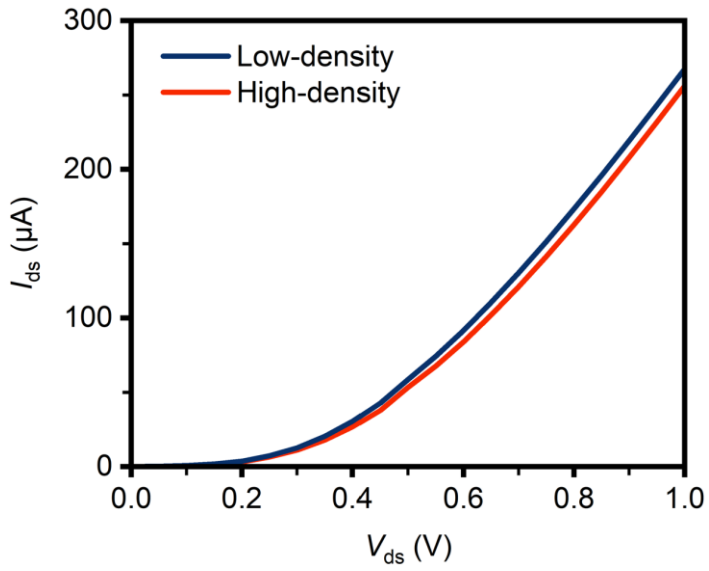

Figure 5.3 - 6 *I_{ds}-V_{ds} curves for the baseline photocurrent of biosensor with high-density (50.6 particles/μm²) and low-density (20.8 particles/μm²) filters (λ = 532 nm, P = 500 μW) [6].*

Detection of IL6 cytokines under "+1" mode: For operating on "+1" mode, the AuNPs filter with high-density (Fig. 5.3-7a) was employed. The I_{ds}-V_{ds} were monitored as a function of increasing incubation time, and the photocurrent variations $\Delta I_{ds}(t_n)$ were measured (at V_{ds} = 1.0 V) for the IL6 concentrations ranging from 0 to 10^5 fg/mL (results in Fig. 5.3-7b). At the initial "0" mode, the high-density and well-distributed AuNPs induced extremely strong LSPR to block the light passing through, remaining at the lower initial current. By loading IL6 cytokine in solution to the filter, a red shift of the LSPR peak was induced due to the local refractive index change accompanying the antigen-antibody binding [218,221], yielding a larger fraction of incident photons passing through the filter and reaching the photoconductive device. As depicted in Fig. 5.3-7b, in the first 5 min, there was a phase of rapid antibody-antigen binding during which the photocurrent increased dramatically, then the reaction rate began to asymptote to a steady-state and gradually achieved a stable-state. The rapid reaction and detection response of 5 min was 100% faster than that of a single graphene-FET biosensor [212]. As shown by I_{ds}-V_{ds} curves (Fig. 5.3-7c), the photocurrent increased as a function of increasing the IL6 concentration. As an example, at a bias voltage of 1.0 V and an incubation time of 5 min, the photocurrent increased from 256.0 to 267.9 μA (ΔI_{ds} = 11.9 μA) when IL6 concentration increased from 0 to 10^5 fg/mL. Based on the standard calibration curve of the biosensor (Fig. 5.3-7d), the LOD was as low as 3.7 fg/mL, showing an ultrahigh sensitivity for cytokine detection. The Hill equation offered a method to quantify the

degree of interaction between antigen-antibody binding. From Equation 5.3-1, the calculated value of ΔI_{max}, K_d, and n was 4.62, 87.92 fg/mL, and 0.47, respectively. The Hill coefficient n was less than 1, indicating a negative cooperativity in ligand binding to the receptor. To verify the reliability and reproducibility, another two devices with high-density AuNP filters (under "+1" mode) were used to detect IL6 with different concentrations (Fig. 5.3-7e & 7f).

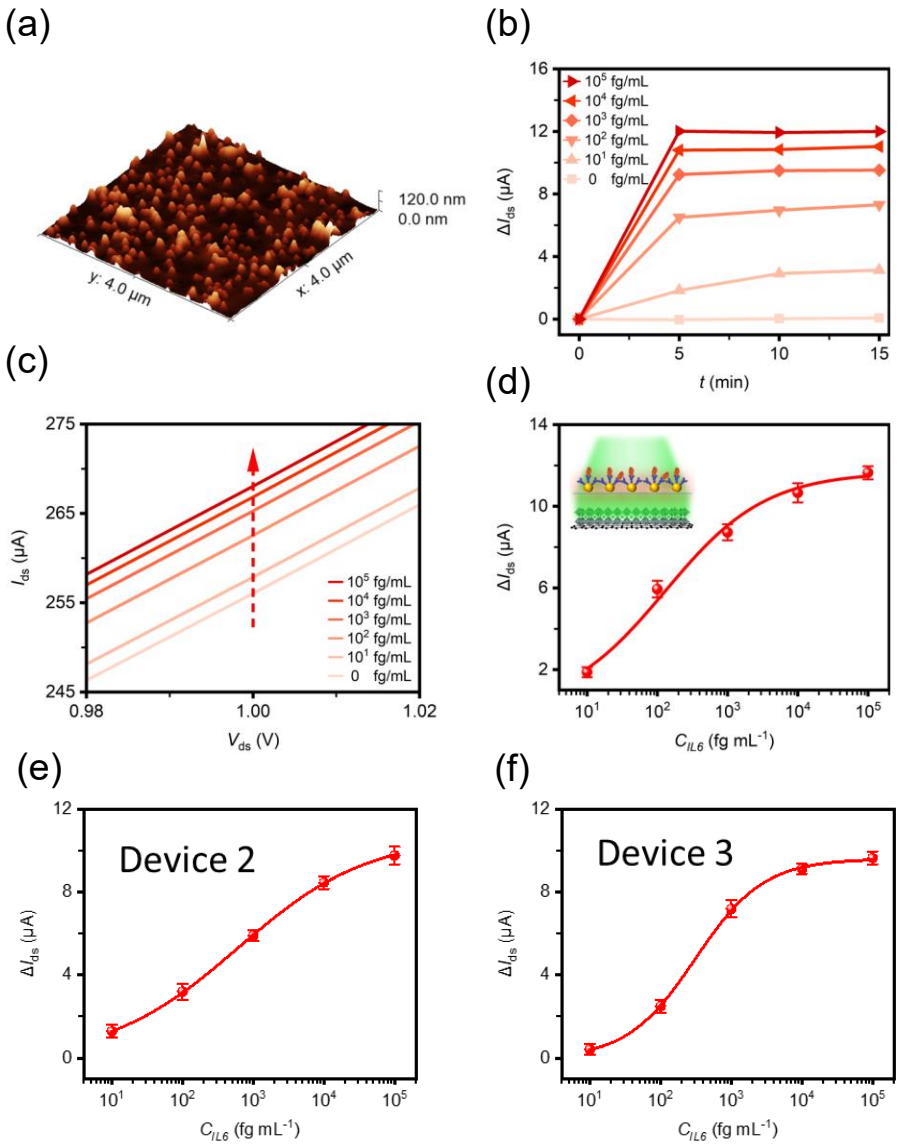

Figure 5.3 - 7 *Ultrasensitive bio-detection of IL6 cytokines under "+1" mode. (a) 3D AFM image of high-density AuNPs filter. (b) Photocurrent variation $\Delta I_{ds}(t_n)$ (at a bias V_{ds} = 1.0 V) during binding incubation with different IL6 concentrations. Each curve was measured under the same laser illumination (λ = 532 nm, P = 500 μW). (c) I_{ds}-V_{ds} curves for different IL6 concentrations (at an incubation time of 5 min). Standard curve of PQDs/SLG-based biosensor incorporating biotunable ternary logic gate under "+1" mode of (d) Device-1, (e) Device-2, and (f) Device-3 with ΔI_{ds} of 11.9 μA, 9.8 μA, and 9.6 μA, respectively, demonstrating great reliability and reproducibility [6].*

Detection of IL6 cytokines under "-1" mode: While operating on "-1" mode, the low-density AuNPs filter (Fig. 5.3-8a) was used. The I_{ds}-V_{ds} response was monitored, and the photocurrent variations with increasing binding time were plotted in Fig. 5.3-8b, which demonstrated the antigen-antibody kinetic binding processes. At the initial "0" mode, a high photocurrent was measured as a large proportional of incident light was easily transmitted through the filter due to a lower LSPR induced by the limited amount of AuNPs. By loading IL6 solutions onto the anti-IL6-AuNPs filter, the accumulation of antigen-antibody binding prevented the transmission of light through the filter. Consequently, the photocurrent decreased over the binding processes. As the I_{ds}-V_{ds} curves against IL6 concentrations shown in Fig. 5.3-8c, the photocurrent decreased as the IL6 concentrations increased. At a bias voltage of 1.0 V and time of 5 min, the photocurrent decreased from 267.5 to 253.4 μA ($\Delta I_{ds} = -14.1$ μA) when IL6 concentration increased from 0 to 10^5 fg/mL. Based on the standard calibration curve (Fig. 5.3-8d), the PQDs/SLG biosensor demonstrated an extremely high sensitivity with an LOD as low as 0.9 fg/mL (43 aM), which was 4 orders of magnitude more sensitive than conventional graphene-FET biosensors [212,213]. The enhanced performance could be attributed to the PQDs/SLG heterostructure, the ultrathin 2D-heterostructured materials exhibited superior electrical, optical, and physicochemical properties than their pristine materials due to the synergistic characteristics of the two different 2D materials [230]. The experimental data were fitted with the Hill model equation, and the calculated values of ΔI_{max}, K_d, and n were 13.57 μA, 1876.20 fg/mL, and 0.44, respectively. The Hill coefficient n is less than 1, showing a negative cooperativity in ligand binding to the receptor. Similarly, two more devices with low-density AuNP filters (under "-1" mode) were utilised for IL6 detection with results shown in Figure 5.3-8e & 8f, demonstrating good reliability and reproducibility.

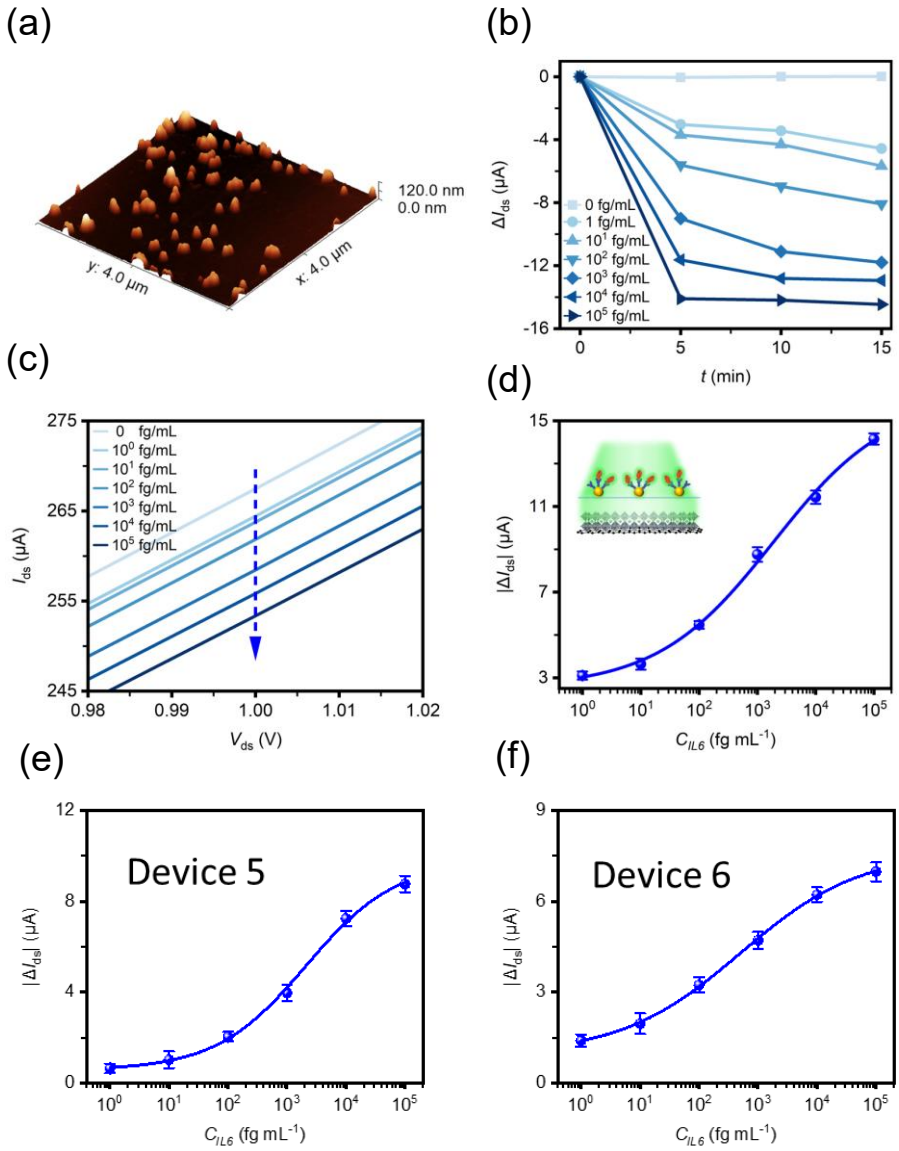

Figure 5.3 - 8 *Ultrasensitive bio-detection of IL6 cytokines under "-1" mode. (a) 3D AFM image of the low-density AuNPs filter. (b) Photocurrent variation $\Delta I_{ds}(t_n)$ (at a bias V_{ds} = 1.0 V) during antigen-antibody binding with different IL6 concentrations. (c) I_{ds}-V_{ds} curves for different IL6 concentrations (at an incubation time of 5 min). Standard curve obtained with the biosensor under "-1" mode of (d) Device-4, (e) Device-5, and (f) Device-6 with $|\Delta I_{ds}|$ of 14.1 µA, 12.4 µA, and 11.0 µA, respectively, showing great reliability and reproducibility [6].*

5.3.8. Specificity of the biotunable ternary logic biosensor

It was well known that the avidin-biotin complex is the established example of a strong noncovalent interaction between a protein and a ligand [231,232]. Compared to streptavidin, the neutral isoelectric point of neutravidin could minimise nonspecific binding caused by electrostatic interactions. Neutravidin provided a powerful and universal tool for biotin binding surfaces to construct different kinds of immunosensors. The specificity of the PQDs/SLG biosensor toward IL6 was evaluated to detect non-specific analytes (all with the same concentration of 100 pg/mL, and by using the low-

density filter). Fig.5.3-9 shows the results of the extended selectivity test by employing a variety of analytes, including CRP, CEA, ALB, and AFP. The maximum photocurrent variations were measured as 1.17, 4.67, 1.89, 1.36, and 14.15 µA for CRP, CEA, ALB, AFP, and IL6, respectively. The maximum signals for CRP, CEA, ALB, and AFP were only 8.2%, 33.0%, 13.4%, and 9.6% of IL6, respectively, indicating a high selectivity to IL6. To explore the interference in actual samples, the PQDs/SLG biosensor was evaluated toward serum samples and IL6 in serum (with IL6 concentration of 100 pg/mL). The photocurrent variation induced by IL6 in serum was ≈82% of that observed in PBS.

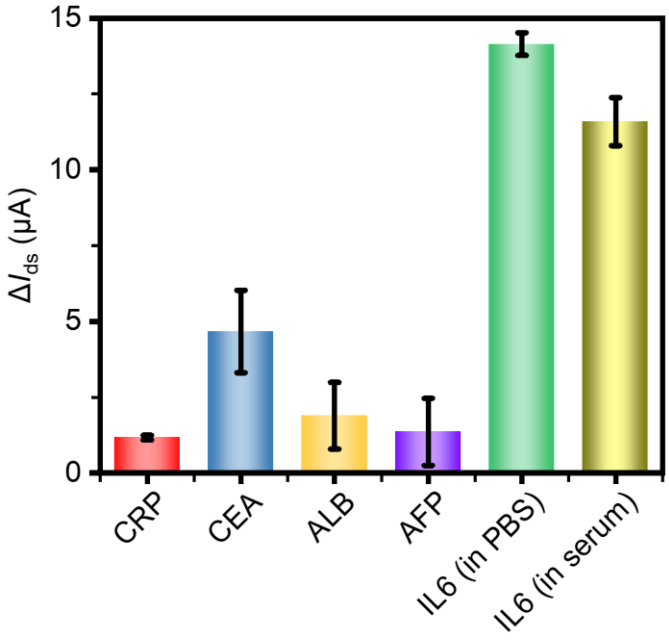

Figure 5.3 - 9 *Specificity of the PQDs/SLG biosensor, showing high selectivity specific to IL6, as the signals for IL6 (in PBS and in serum) are distinctly higher than other non-specific analytes [6].*

5.4. Chapter summary

This chapter has presented the development and implementation of three distinct optoelectronic biosensing platforms for biomedical and biochemical analysis, each tailored to address specific challenges in label-free, sensitive, and real-time molecular detection.

The first study introduced a GO-functionalised LPG biosensor designed for non-invasive quantification of cancer cells through their metabolic byproducts. By employing an improved in-situ layer-by-layer deposition technique, GO nanocoatings with controlled thicknesses of ~55 nm and ~ 125 nm were achieved, enabling precise tuning of the

evanescent field interactions. The influence of GO thickness on the sensor's optical response was systematically studied, revealing thickness-dependent resonance behaviour and enhanced RI sensitivity. This device achieved a detection limit as low as 198 cells/mL, demonstrating its promise for early-stage cancer diagnostics without the need for direct cell labelling or sample pre-treatment.

The second part of the chapter explored a novel hybrid grating biosensor that integrates a LPG and a FBG into a single reflective device. This hybrid structure exploited the strengths of both grating types, including the high RI sensitivity of LPGs and the ultra-narrow resonance with high signal-to-noise ratio of FBGs. In addition to the well-established core-core and core-cladding interactions, cladding-cladding mode coupling has been experimentally observed and systematically characterised for the first time in this hybrid grating structure. Detailed optical characterisation revealed distinct modal resonances with high signal-to-noise ratios. The device exhibited pronounced sensitivity to low refractive index environments in the range of 1.333 to 1.360, with the cladding–cladding resonance achieving an average sensitivity of 741 nm/RIU. The sensor was implemented for and haemoglobin detection, demonstrating a sensitivity of 1.5 pm/(mg/mL) and an estimated detection limit of 0.67 mg/mL, significantly below clinical thresholds for anaemia.

The final study presented the first perovskite/graphene heterostructure-based FET biosensor with uniquely biotunable ternary logic gating functionality for label-free, ultrasensitive, and rapid detection of human IL6 cytokines. PQDs/SLG heterostructure 2D materials were integrated into a FET, producing synergistic effects that enhanced the efficiency of light-carrier transition and high-speed electron transportation. An antibody-conjugated AuNPs filter acted as a tunable gate (with three logic modes: +1, 0, -1), by tuning the delivery of incident light that passed through the filter due to the LSPR shift induced by antibody-antigen binding. In particular, a decoupled construction was designed to separate the 'wet' biosensing area and the 'dry' photodetection area to enhance device stability without impairing the properties of the 2D materials. The proposed biosensor was proven to detect human IL6 cytokine, achieving ultrahigh sensitivity with an LOD as low as 0.9 fg mL−1 (43 aM) and a fast response time, with a sample-to-answer time of 5 min, which was 4 orders of magnitude more sensitive and 100% faster than graphene-FET biosensors. In addition, the specificity was investigated by running the analysis using CRP, CEA, ALB, and AFP analytes. These results

demonstrated excellent selectivity toward the IL6 cytokine and indicate strong potential for practical deployment in real-time inflammatory disease monitoring.

Together, these three approaches underline the versatility and performance potential of optoelectronic and fibre-based biosensors. By combining 2D materials, nanophotonics, and hybrid device architectures, the work reported in this chapter advances the capabilities of biosensing platforms in addressing unmet clinical and diagnostic needs.

Chapter 6 Functionalised fibre-optic sensors for chemical sensing and bioimaging

6.1. MXene based fibre-optic Fabry-Perot interferometer (FFPI) for heavy metal detection

The increase in human activities, along with industrialisation and population growth, has made heavy metal pollution in aquatic systems worse. Among these pollutants, mercury (Hg) is particularly dangerous [233–235], which was considered as the top ten chemicals of greatest public health concern by Word Health Organization (WHO) [236]. Prolonged exposure to excessive mercury can lead to severe health effects, including central nervous system damage, birth defects, and chromosomal alterations, primarily due to its bioaccumulation and biomagnification in the human body [237–240]. In water, mercury primarily exists as Hg^{2+}, with a permissible limit of 5 ppb in both surface and groundwater, which is a relatively low concentration that requires effective detection [241]. Therefore, developing ultrasensitive and rapid detection technologies for Hg^{2+} in water is essential, especially for on-site and portable detection applications. Several detection methods of Hg^{2+} have been reported, including traditional approaches such as atomic fluorescence spectrometry [242–244], atomic absorption spectrometry [245,246], and inductively coupled plasma mass spectrometry [247,248]. However, Traditional methods for detecting Hg^{2+} often rely on large, costly instruments and involve complex, time-consuming sample preparation, limiting their practical use. This highlights the urgent need to develop rapid, portable, and highly sensitive approaches to address these challenges.

As discussed in Chapter 3, the abundant surface functional groups and large surface area make the MXene as an excellent candidate for heavy metal adsorption. $Ti_3C_2T_x$ MXene has been utilised for Hg^{2+} ions removal, taking advantage of its adsorption capacity combined with a catalytic reduction mechanism, which leads to the formation of crystalline Hg_2Cl_2 on the surfaces of $Ti_3C_2T_x$ nanosheets [249,250].

Therefore, an ultrasensitive chemical sensor based on a MXene assisted FFPI was developed for the detection of mercury (Hg^{2+}) ions. MXene nanosheets that had captured Hg^{2+} ions significantly modified the RI of the analyte suspension in the FP cavity,

resulting in an extreme change in reflection intensity and free spectral range (FSR). Serving as both a signal transducer and a signal amplification medium, the MXene nanosheets enabled highly sensitive detection of Hg^{2+} ions.

6.1.1. Materials and fabrication of MXene based FFPI

The following materials were used to synthesis the $Ti_3C_2T_x$ MXene nanosheets: The Ti_3AlC_2 MAX (powder, 325 mesh), the lithium fluoride (LiF, powder, 300 mesh), mercury standard for ICP, hydrochloric acid (HCl), and UV curing optical adhesives.

The $Ti_3C_2T_x$ MXene nanosheets were synthesised with the minimally intensive layer delamination (MILD) method (see Section 3.5).

The FFPI was fabricated using two segments of single-mode fibre (SMF) and a hollow capillary tube (Fig. 6.1-1). In brief, two segments of SMF were inserted into a hollow capillary tube, with their finely cleaved end faces aligned to serve as two parallel reflecting mirrors (M1 and M2), forming the Fabry-Perot cavity. The hollow capillary tube permits the analyte solution to access the sensing region. A pair of 3-axis flexure stages was employed to adjust the separation between the fibre end faces, thereby defining the final F-P cavity length. To ensure structural stability, optical adhesive was applied to two ends of the capillary tube and fibres to secure the F-P cavity with a fixed length.

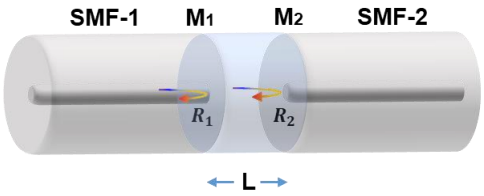

Figure 6.1 - 1 *Schematic illustration of FFPI.*

6.1.2. Optical characterisation of FFPI

Due to the low reflectance of the cleaved fibre surface, multiple reflections have negligible contributions to the optical interference [251]. The intensity of reflection from FFPI can be approximated with using the irradiance expression of two-beam optical interference (Eq. 2.4-9), where I, I_1, and I_2 represent total reflected irradiance and the irradiance contributions from mirrors M_1 and M_2, respectively. I_1 and I_2 are determined by the reflectance R_1 and R_2 at the cavity end faces M_1 and M_2. And the phase difference δ is given by:

$$\delta = \frac{4\pi nL}{\lambda} \qquad (6.1-1)$$

Here, λ, n, and L represent the central wavelength, the RI of the media within the cavity, and the cavity length, respectively. To validate the theoretical analysis and further investigate the optical properties of the proposed FFPI, experimental measurements were conducted.

Fineness against reflectance: Figure 6.1-2 demonstrates the reflection spectra of FFPI with a cavity length of 200 μm. The reflectance of the first fibre end face is fixed at 4%, while the second end face is varied with reflectance values of 4%, 15%, 22%, and 51% to form different F-P cavities in combination with the first end face. The varying reflectance of the second end faces is achieved by coating the fibre tips with gold films of different thickness. The total reflected intensity increases with the reflectance, as higher-reflectivity end faces produce stronger reflected beams. Furthermore, the spectrum exhibits shaper peaks as the second end face with higher reflectance, indicating increased fineness, which is in good agreement with Eq. 2.4-17.

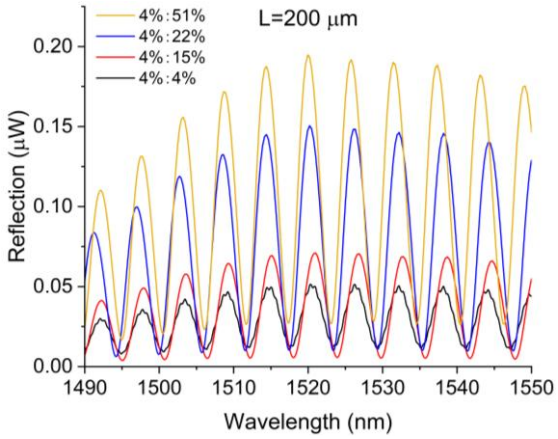

Figure 6.1 - 2 *Reflection spectra of FFPI with applying the second end faces with different reflectance.*

FSR against cavity length: Figure 6.1-3 exhibits the reflection spectra with cavity lengths of 40, 80, and 120 μm. An increase in cavity length results in a denser distribution of interference fringes in the reflection spectrum, as the FSR decreases inversely with the cavity length.

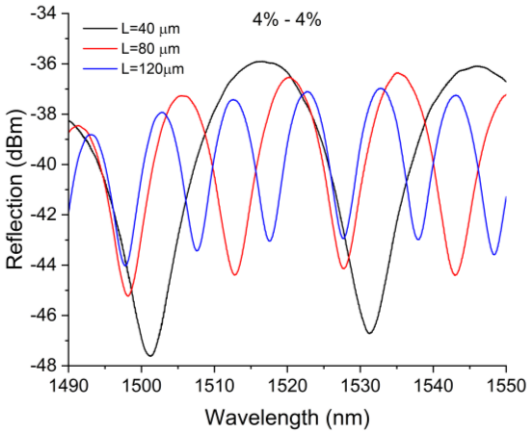

Figure 6.1 - 3 *Reflection spectra of FFPI with cavity lengths of 40, 80, and 120 µm.*

FSR against cavity RI: The spectra were monitored while varying the RI of the within the FFPI cavity by introducing Hg^{2+} solutions of different concentrations. A stock solution of Hg^{2+} at 5000 µM was serially diluted to a set of concentrations: 2500, 1000, 500, 100, 10, 1, 0.1, 0.01, and 0.001 µM. A control sample without Hg^{2+} was also included. Each diluted concentration was sequentially introduced into the FFPI cavity, followed by rinsing with DI water thoroughly between measurements. To ensure spectral stability, the sample concentration was maintained in the cavity for 1 min prior to each acquisition.

The interference spectra corresponding to the different Hg^{2+} concentrations are presented in Fig. 6.1-4a. As the Hg^{2+} concentration increases, the spectral fringes exhibit a noticeable redistribution, with a progressive shift in the positions of intensity maxima and minima across the wavelength axis. This reorganisation arises from a gradual reduction in the FSR, which in turn reflects changes in the effective RI of the cavity medium induced by the presence of Hg^{2+} ions. Hence, the change of FSR was utilised for determining the sensitivity of Hg^{2+} detection. As shown in Fig. 6.1-4b, the FSR exhibits two distinct linear responses with respect to two Hg^{2+} concentration ranges. A sensitivity of 1.90 pm/µM was obtained in the low Hg^{2+} concentration range (0–10 µM), while a lower sensitivity of 0.08 pm/µM was observed in the higher concentration range (100–5000 µM). As the refractive index of the intracavity medium increases with Hg^{2+} concentration, the fringe contrast (visibility) of the interference spectra gradually diminishes. This can be attributed to the reduced Fresnel reflection at the fibre-liquid interfaces, which weakens the multiple-beam interference. As a result, the interference fringes become less distinct.

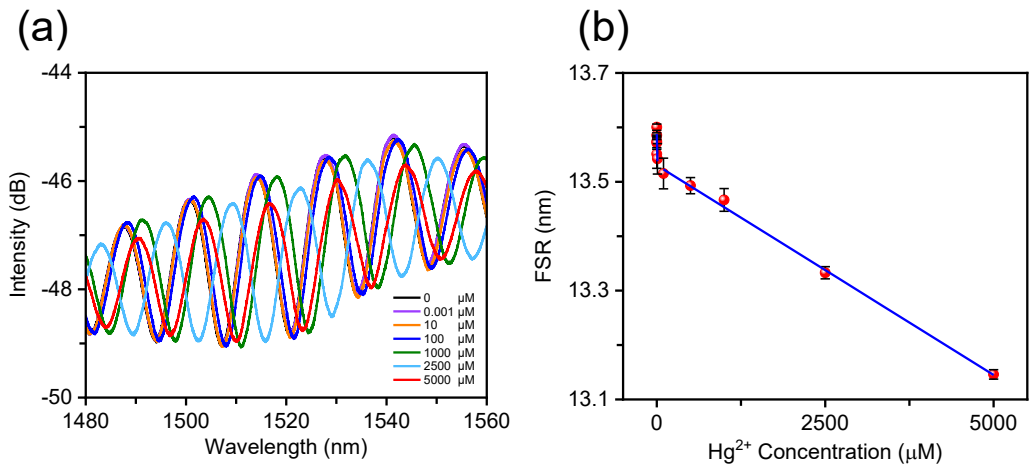

Figure 6.1 - 4 *(a) Interference spectra of FFPI at different concentrations of Hg^{2+} ions. (b) FSR against Hg^{2+} concentrations. The blue lines represent linear calibration curves for detecting Hg^{2+} in the ranges of 0–10 μM and 100–5000 μM, respectively.*

These results demonstrate the capability of the bare FFPI sensor to detect Hg^{2+} ions over a broad concentration range (0–5000 μM). However, its relatively low sensitivity in the sub-micromolar regime limits its practical applicability for trace detection. To address this limitation, MXene nanosheets were subsequently introduced into the cavity as signal-amplifying agents, enabling adsorption and crystallisation of Hg^{2+} ions on their surfaces, and thereby enhancing the optical response.

6.1.3. Mechanism of Hg^{2+} adsorption and crystallisation on MXene

The mechanism of mercury (Hg^{2+}) adsorption and catalytic reduction by $Ti_3C_2T_x$ has been investigated to aid in the removal of Hg^{2+} ions [249,250]. Fig. 6.1-5 schematically described the redox reaction between Hg^{2+} ions and $Ti_3C_2T_x$ MXene. The uptake of Hg^{2+} ions by $Ti_3C_2T_x$ MXene is attributed to its unique interaction mechanisms, including adsorption and catalytic reduction. The Ti atoms on the MXene surface preferentially adsorb Hg^{2+} in the form of Cl−Hg−OH. This intermediate undergoes homolytic cleavage, producing radical species such as −OH and −HgCl. The −HgCl radicals dimerize to form crystalline Hg_2Cl_2, which accumulates both on the surfaces and edges of $Ti_3C_2T_x$. The abundant −OH groups on the $Ti_3C_2T_x$ surfaces are further oxidised the $Ti_3C_2T_x$ to form TiO_2/C nanocomposites. The crystallised Hg_2Cl_2 clusters forming on the surfaces of $Ti_3C_2T_x$ MXene increase the RI of the surrounding medium in the FP cavity, alerting a change in the optical signal.

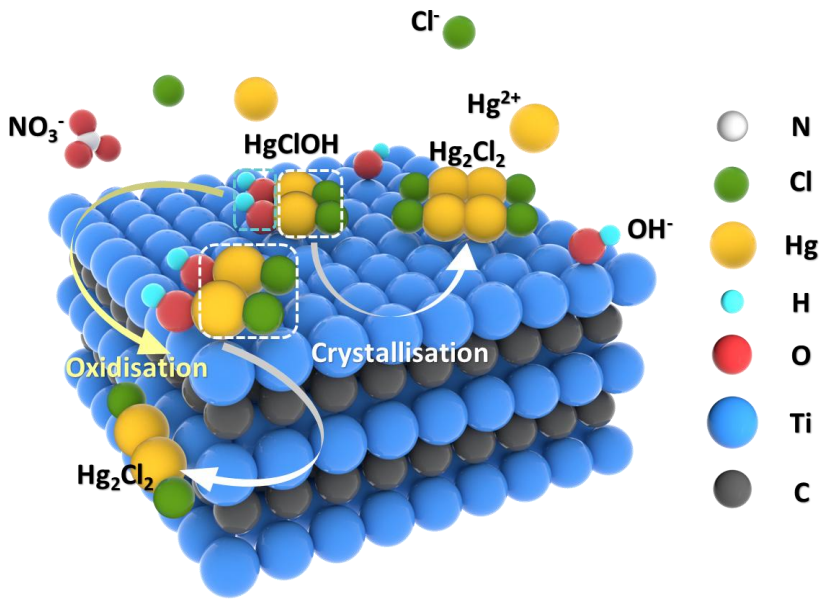

Figure 6.1 - 5 *Illustrations of Hg^{2+} ions uptake onto $Ti_3C_2T_x$ MXene surface, where Hg^{2+} is crystalised into Hg_2Cl_2. The $Ti_3C_2T_x$ MXene is oxidised by the residual OH^- groups.*

Fig. 6.1-6 demonstrates the SEM image and EDS mapping of $Ti_3C_2T_x$ adsorbed with Hg^{2+}. Clusters of Hg_2Cl_2 crystals gathered around surfaces and edges of $Ti_3C_2T_x$ can be observed from the SEM image. The elemental distribution of Hg and Cl was found to be almost identical, completely overlapping on the surfaces of $Ti_3C_2T_x$, indicating the successful adsorption and crystallisation of Hg^{2+} by MXene.

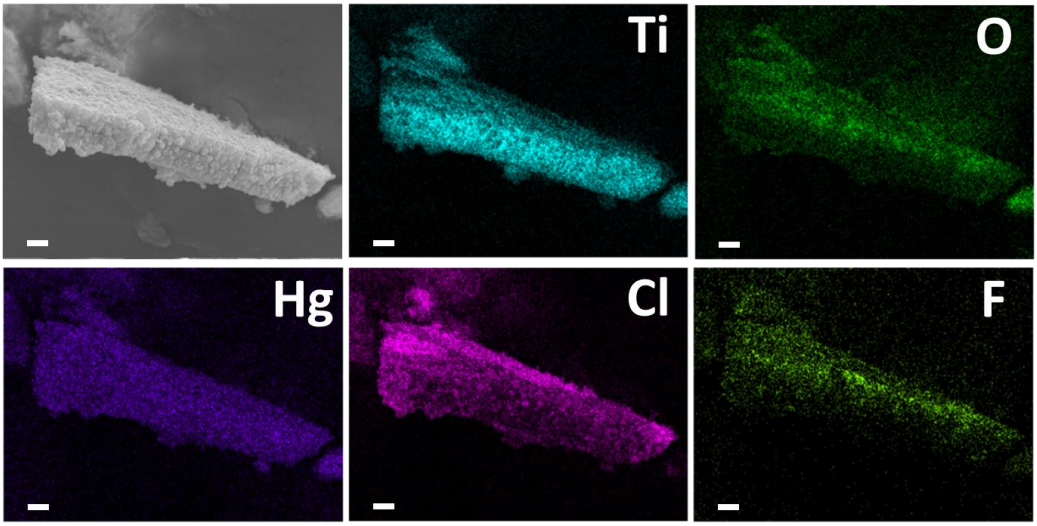

Figure 6.1 - 6 *SEM image and corresponding EDS elemental mapping of Ti, O, F, Hg, and Cl for layered $Ti_3C_2T_x$ MXene after adsorption of 2.5 mM Hg^{2+}. The distribution of each element confirms successful mercury uptake and the presence of surface terminations (scale bar: 2 μm).*

6.1.4. Sensing mechanism of MXene-based FFPI chemical sensor

The MXene-FFPI was employed for the detection of Hg^{2+} ions. As shown in Fig. 6.1-7, the light is launched into SMF-1 (from the left) and propagates through the FP cavity

enclosing the analyte solution, where the light undergoes multiple reflections between the parallel mirrors (end faces of SMF-1 & SMF-2). The reflected light guided by SMF-1 is monitored by an OSA, showing a distinct interference spectrum. As Hg^{2+} ions are increasingly captured by the $Ti_3C_2T_x$ MXene nanosheets within the F-P cavity, a reduction in the spectral FSR is observed accompanying by an increase in reflection intensity.

In this FFPI, the MXene suspension is employed to mix with Hg^{2+} ions with different concentrations. Upon the addition of Hg^{2+} ions, the ions are adsorbed onto the surfaces of the MXene nanosheets and subsequently crystallise to form Hg_2Cl_2 clusters. This crystallisation process induces a local RI increase of the cavity medium. Therefore, as the local RI increases with enhanced Hg^{2+} ion concentrations, a progressive narrowing of the FSR and a reduction in interference fringe visibility are theoretically expected and experimentally observed in the interference spectral pattern.

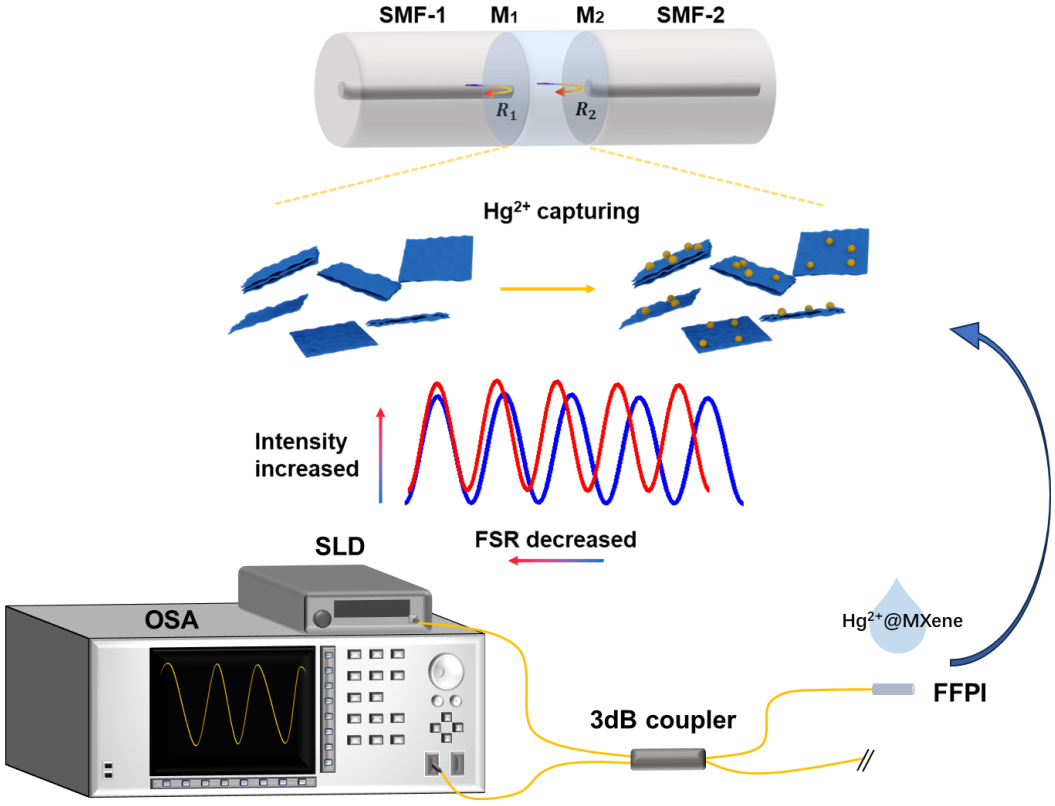

Figure 6.1 - 7 *Schematic illustration of $Ti_3C_2T_x$ MXene assisted FFPI for the detection of Hg^{2+} ions.*

6.1.5. MXene assisted Hg^{2+} sensing with enhanced sensitivity

For detecting low concentrations of Hg^{2+} ions with a higher sensitivity, a $Ti_3C_2T_x$ MXene suspension with a concentration of 0.5 mg/mL was prepared as the buffer solution to mix with Hg^{2+} concentrations, leveraging the strong adsorption of MXene toward Hg^{2+}. The MXene suspension was equally divided into multiple aliquots, and each aliquot was

mixed with a specific amount of Hg^{2+} solution to produce a series of test samples with final Hg^{2+} concentrations of 0, 0.001, 0.005, 0.01, 0.05, 0.1, 0.2, 0.3, 0.4, 0.5, and 1.0 μM, respectively. These mixtures were immediately introduced into the FFPI cavity (with a new cavity length of 50 μm) for spectral acquisition, followed by rinsing with DI water and complete drying. Each sample was held in the cavity for 1 minute to ensure sufficient time for Hg^{2+} adsorption and surface crystallisation prior to spectral acquisition.

The interference spectra obtained at different Hg^{2+} concentrations are plotted in Fig. 6.1-8a. As the concentration of Hg^{2+} increased, a redistribution of the interference fringes was observed, which corresponds to a reduction in the FSR due to an increase in the local RI. As illustrated in Fig. 6.1-8b, the FSR exhibited two distinct linear regimes as a function of Hg^{2+} concentration, with calculated sensitivities of 4580 pm/μM (0–0.01 μM) and 240 pm/μM (0.05–1.0 μM), respectively.

Notably, unlike the bare FFPI configuration, the interference intensity exhibited a consistent increase with rising Hg^{2+} concentration in the presence of MXene, as shown in Fig. 6.1-8a (with a close-up shown in Fig. 6.1-8c). This enhancement in total reflected intensity is attributed to the formation of Hg_2Cl_2 nanocrystallites on the surface and edges of MXene nanosheets, which results from the redox reaction between Hg^{2+} ions and Ti atoms in MXene. These crystallites, possessing a relatively high RI, serve as additional reflective domains or scattering centres within the cavity, thereby increasing the total effective reflection. However, as the RI of the reaction medium increases and local inhomogeneity develops, the interference fringe visibility gradually diminishes due to reduced coherence. The corresponding visibility-concentration relationship in Fig. 6.1-8d reveals three linear detection ranges, with sensitivities of 488%/μM (0–0.01 μM), 22.8%/μM (0.01–0.4 μM), and 2.5%/μM (0.4–1.0 μM), respectively. Owing to the strong signal amplification enabled by MXene and the use of a low-noise interrogation system with a resolution of 0.01 dB, corresponding to approximately 0.23% in visibility, the LOD of the MXene-functionalized FFPI sensor was determined to be as low as 0.47 nM.

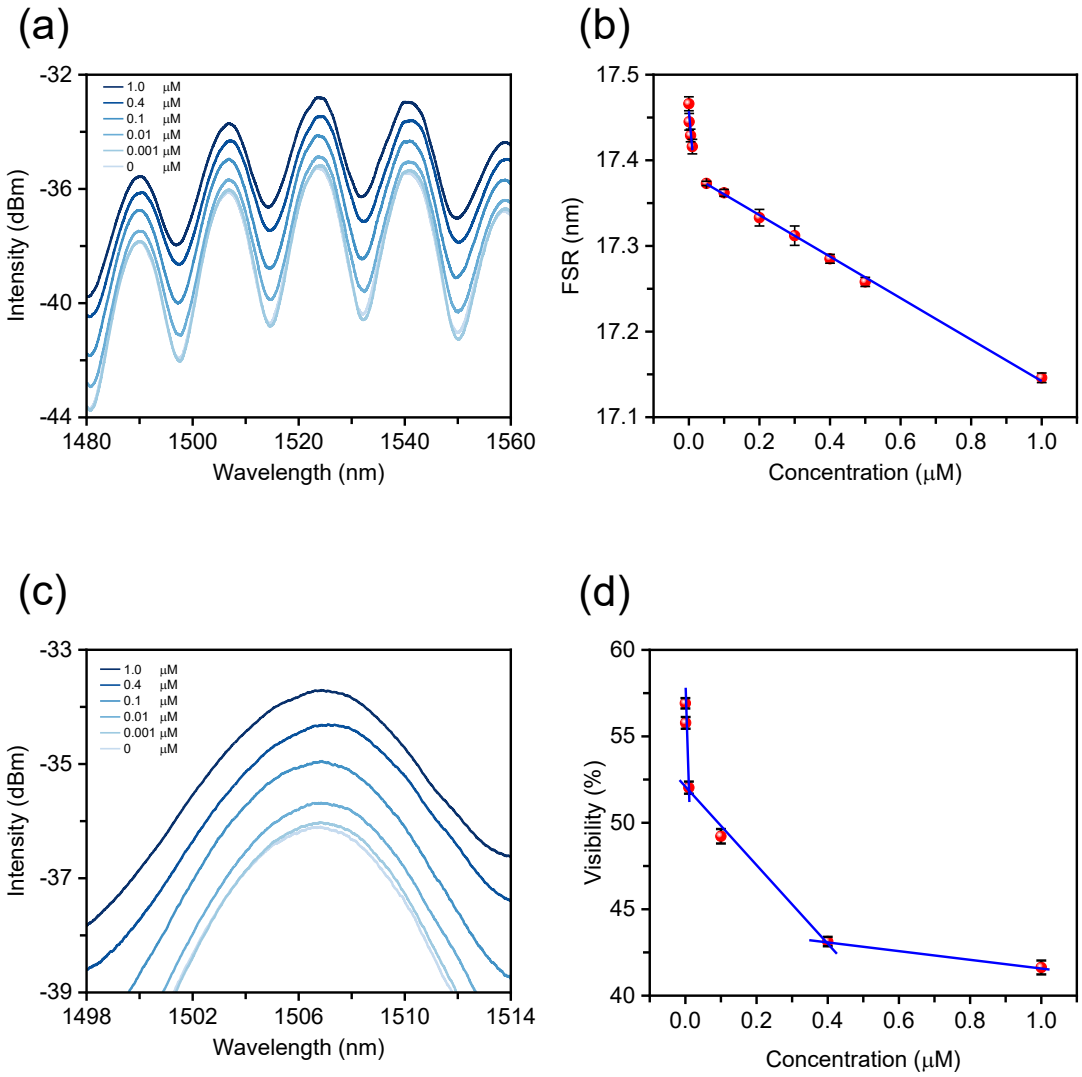

Figure 6.1 - 8 *(a) Interference spectra of FFPI at different concentrations of Hg^{2+} ions. (b) FSR against Hg^{2+} concentrations. The blue lines represent linear calibration curves for detecting Hg^{2+} in the ranges of 0–0.01 μM and 0.05–1.0 μM, respectively. (c) Closeup of (a) which shows a consistently increase of the intensity. (d) Visibility of interference fringes as a function of Hg^{2+} concentration for MXene-assisted Hg^{2+} detection. Data are mean ± s.d.*

6.2. GO-functionalised fibre optic probes for bioimaging

Due to the high surface-to-volume ratio and abundant oxygen functional groups, GO provides an ideal platform for biophilic binding interfaces [252]. After biofunctionalisation by EDC/NHS and immobilisation of fluorescent anti-IgG antibodies, the fluorescence images reveal that GO-coated fibres exhibit significantly higher fluorescence intensity compared to bare fibre probe. Here, the term "optical fibre probe" refers to a functional sensing and bio-interfacing platform, rather than a fluorescent molecular label used in conventional fluorescence microscopy. Notably, acid regeneration

enables the reusability of the GO-fibre probes, allowing repeated imaging cycles without compromising performance. The integration of high surface loading capacity, anti-quenching characteristics, and reversible bioconjugation makes the GO-functionalised miniaturised fibre probe a promising and versatile platform for real-time bioimaging [166,253]. This approach is particularly effective for detecting low-abundance biomarkers with high sensitivity. Importantly, the development of this GO-based fibre-optic imaging probe opens a new pathway for advancing label-based fibre-optic biosensing technologies, offering a scalable and adaptable solution for future applications in clinical diagnostics and point-of-care imaging.

6.2.1. Materials and device

The following materials were used to functionalise the GO-fibre optic probes: graphene oxide aqueous dispersion (2 mg/mL), NaOH, APTES, N-(3-Dimethylaminopropyl)-N′-ethylcarbodiimide hydrochloride (EDC) N-Hydroxysuccinimide (NHS), 1×PBS, pH 7.4, HCl, methanol, ethanol, acetone, Goat anti-Rabbit IgG Alexa Fluor^{TM} 488, silica single-mode fibre (SMF-28).

The deposition of GO on optical fibre follows the in-situ layer-by-layer coating technique (detailed in Section 4.2). All GO-fibre probes were fabricated with a 2-cycle GO deposition (0.10 mg/mL).

6.2.2. Measurement system and data analysis

The roughness of anti-IgG immobilised GO overlay was measured using an atomic force microscope (AFM, Bruker Dimension Icon, Bruker Ltd.). The substrate containing fluorescent signal was analysed using confocal microscopy (Leica TCS SP5) for fluorescence observation and z-axis scanning. Fluorescence quantification was conducted in ImageJ by converting raw images to 8-bit grayscale format followed by histogram-based threshold segmentation to isolate specific signals from background noise. Fourier transform infrared (FTIR) Spectra were acquired on a FTIR spectrometer (Thermo Scientific NICOLET iS50).

6.2.3. Biofunctionalisation of GO-fibre optic probes

To enable covalent immobilisation of fluorescent antibodies onto the surface of GO overlay, the EDC/NHS coupling strategy was employed (Fig. 6.2-1). EDC firstly activates the carboxyl groups (–COOH) on GO overlay surface to form a reactive but short-lived o-acylisourea active intermediate. The intermediate is highly susceptible to hydrolysis in

aqueous environments and exhibits the limited reactivity toward primary amines. To overcome this limitation, NHS has been added to convert the o-acylisourea into a more stable NHS ester intermediate. This activated ester readily reacts with the primary amine groups (–NH_2) on fluorescently labelled anti-IgG antibodies, resulting in the formation of stable amide bonds that anchor the biomolecules onto the GO surface. Compared to the use of EDC alone, the EDC/NHS strategy significantly improves the solubility and lifetime of the reactive intermediate, minimises premature hydrolysis, and enhances overall coupling efficiency [254]. This conjugation ensures the robust and reproducible functionalisation of GO-fibre probes for subsequent fluorescence-based bioimaging applications. In brief, The GO-coated fibre probes were immersed into a mixture of 20 mM EDC and 40 mM NHS in 1× PBS buffer for 1 h. Subsequently, the activated probes were immobilised with anti-IgG by incubating in anti-IgG solutions (with different concentrations of 2, 4, and 20 µg/mL, respectively) for 1 h. After incubation, the anti-IgG immobilised GO-probes were rinsed multiple times with PBS to remove any unbound anti-IgG.

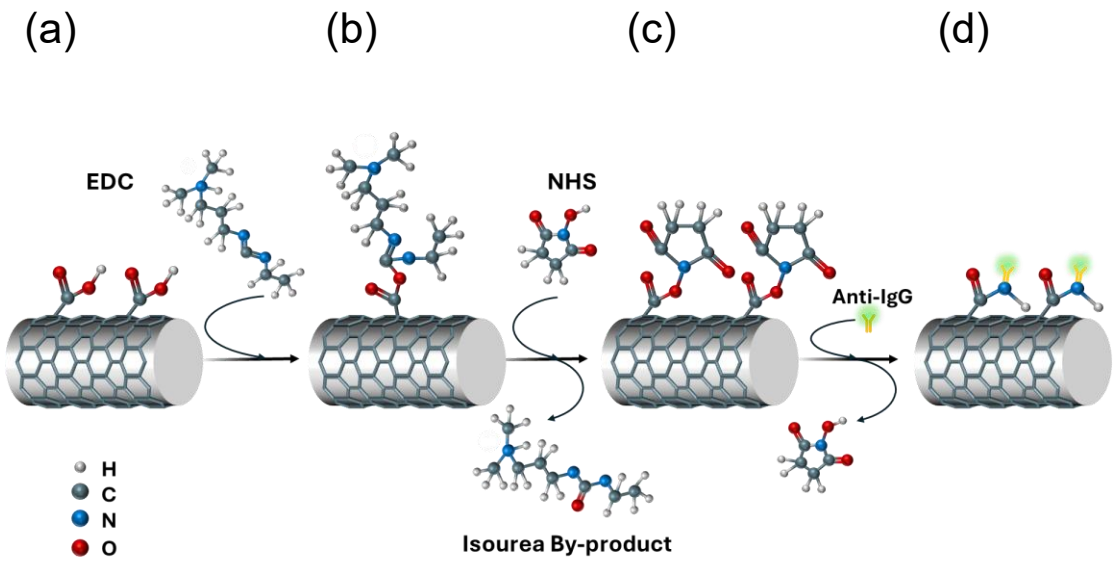

Figure 6.2 - 1 *Schematic illustration of biofunctionalisation of GO-fibre probe via EDC/NHS conjugation. (a) Carboxylic acid enriched GO-fibre probe surface. (b) GO-fibre probe bond with o-acylisourea active intermediate. (c) GO-fibre probe bond with NHS ester intermediate. (d) Anti-IgG immobilised GO-fibre probe.*

6.2.4. Surface morphological characterisation

Quantitative AFM analysis of fibre surfaces revealed a clear, concentration-dependent surface roughness evolution (Fig. 6.2-2a-d). The Probe-1 (Fig. 6.2-2a, bare fibre probe) treated with anti-IgG alone (with 2 µg/mL concentration) exhibited an RMS roughness of only 1.3 nm, reflecting minimal protein adsorption on an otherwise smooth substrate. By

contrast, Probe-2 (GO-coated fibre) incubated with 2 µg/mL low anti-IgG concentration showed a pronounced increase to 11.4 nm, while medium (4 µg/mL) and high (20 µg/mL) antibody concentrations yielded RMS values of 15.9 nm and 22.2 nm, for Probe-3 and Probe-4, respectively.

This dramatic increase in roughness on the GO-coated samples (Probe-2, 3, 4) can be attributed to the presence of the GO layer combined with the successful immobilisation of anti-IgG. GO nanosheets possess wrinkles, edges and oxygen-containing functional groups that create a heterogeneous topography and provide abundant binding sites for protein molecules [166]. When anti-IgG was applied, the NHS-activated carboxyl groups on the GO surface reacted with primary amines of the antibody molecules, forming stable covalent amide bonds. These reactions facilitated site-specific immobilisation of anti-IgG along the GO nanosheet wrinkles and step edges, where local topographical features further promoted efficient molecular attachment. At higher antibody concentrations, anti-IgG molecules cluster and bridge neighbouring GO sheets or span wrinkles, further amplifying surface undulations [255,256]. The textured GO nanosheets, together with the adsorbed anti-IgG, increase the surface roughness from 11.4 nm (Probe-2) to 15.9 nm (Probe-3) and 22.2 nm (Probe-4). While bare fibre probe (Probe-1) treated with anti-IgG shows only slight and isolated protein patches on the surface, the anti-IgG immobilised GO fibre probes (Probe-2, 3, 4) exhibit a high-roughness and richness surface morphologies. This comparison highlights the synergistic effect between the complex nanosheet architecture of GO and its abundant oxygenated functionalities, which collectively contribute to the increased surface roughness hence the improved biomolecular binding efficiency.

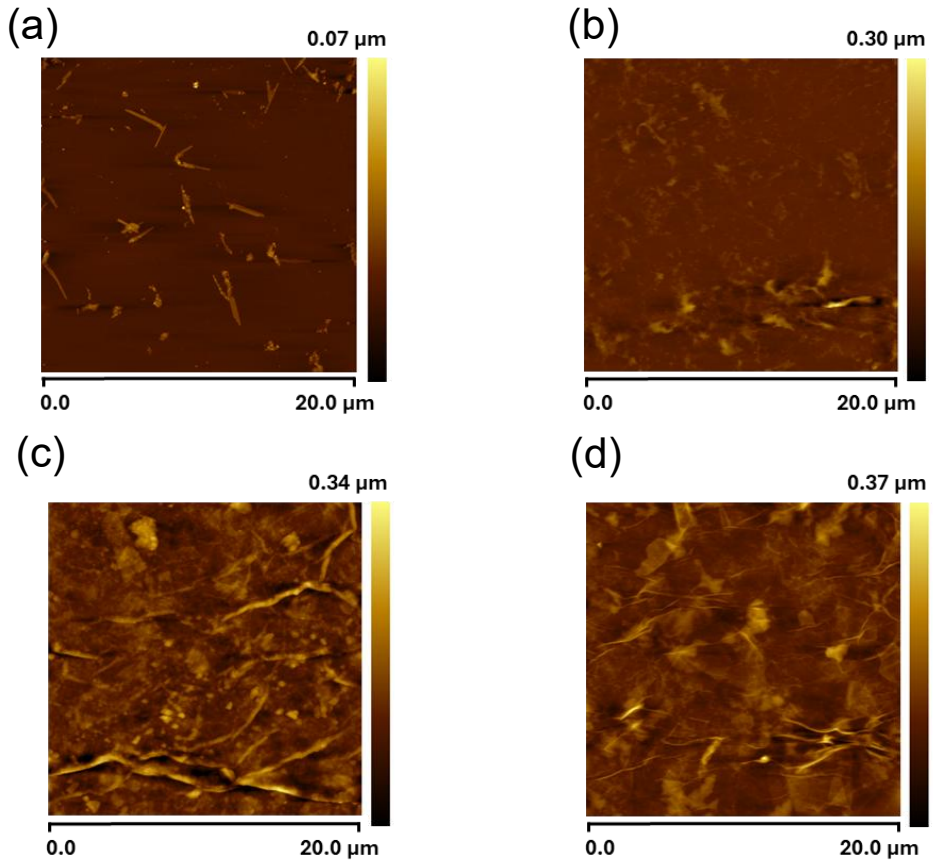

Figure 6.2 - 2 *AFM images of GO-fibre probes treated with different Anti-IgG concentrations. (a) Probe-1: bare fibre probe treated with 2 µg/mL anti-IgG, (b) Probe-2: GO-fibre probe treated with 2 µg/mL anti-IgG, (c) Probe-3: GO-fibre probe treated with 4 µg/mL anti-IgG, (d) Probe-4 treated with 20 µg/mL anti-IgG.*

6.2.5. Enhanced fluorescent intensity of GO-fibre probes

The confocal fluorescence micrographs (Fig. 6.2-3) show that GO-coated fibre probes (Probe-2, 3, and 4) exhibit significantly higher antibody loading and, consequently, stronger bio-fluorescence signals compared to the bare fibre probe (Probe-1). The confocal images with green fluorescence show denser and more uniform coverage of labelled antibodies on the GO fibre probes (Fig. 6.2-3b,c,d), whereas the bare Probe-1 appeares very weak fluorescence (Fig. 6.2-3a). These measurements confirm that the GO coating has greatly enhanced the immobilisation of antibodies on probe surfaces.

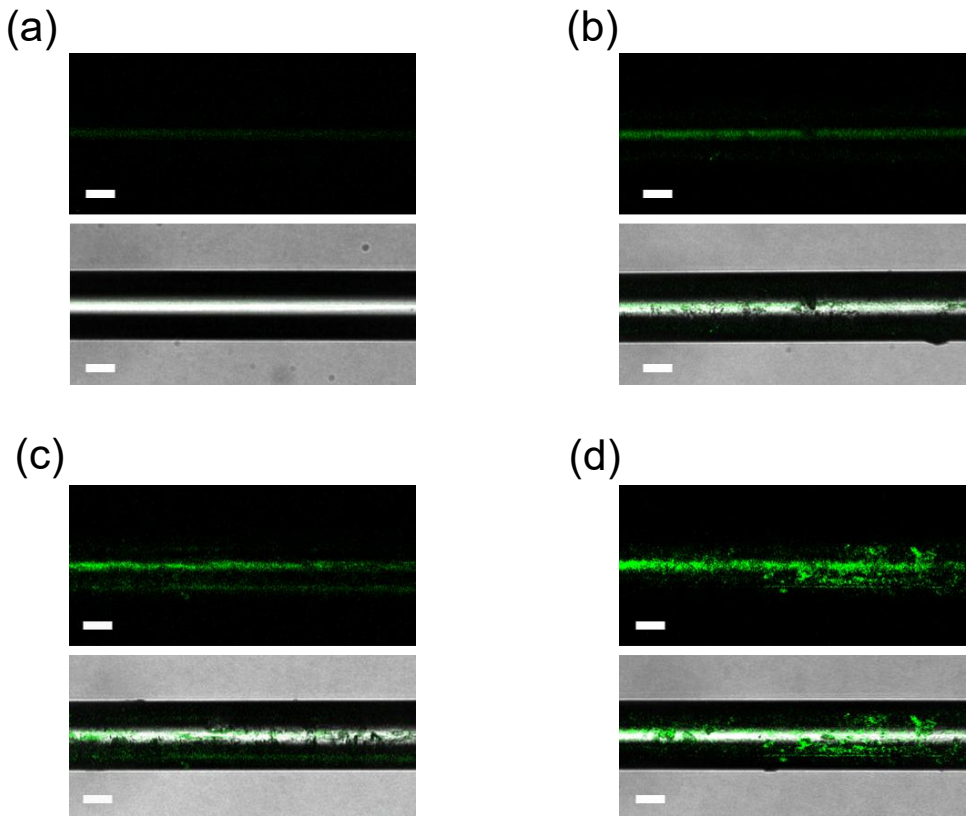

Figure 6.2 - 3 *Confocal microscopy observation of anti-IgG immobilised probes (a) Probe-1, (b) Probe-2, (c) Probe-3 and (d) Probe-4. (scale bar: 50 μm). For each probe, the upper panel shows the fluorescence image, and the lower panel displays the corresponding overlay image (bright-field and fluorescence merged). Increased fluorescence intensity and uniformity correlate with GO presence and higher antibody concentrations.*

Three-dimensional reconstructions of the fluorescent signals (Fig. 6.2-4a-d) and the comparison of fluorescence intensities (Fig. 6.2-4e) reveal that overall brightness of the emission of GO-fibre probes exceed those of bare sample (Probe-1). Under the same anti-IgG concentration (2 μg/mL), the GO-coated Probe-2 exhibited an average fluorescence intensity of 55.0 ± 3.0 a.u., approximately 14-fold higher than that of the bare Probe-1 (3.9 ± 1.0 a.u.). This pronounced enhancement reflects the superior capability of the GO coating to capture and retain biomolecules (e.g., antibodies in this work). When higher anti-IgG concentrations were applied, the fluorescence intensities increased to 85.0 ± 5.0 a.u. for Probe-3 (4 μg/mL) and 148.0 ± 4.5 a.u. for Probe-4 (20 μg/mL), representing approximately 1.5-fold and 2.7-fold enhancement to that of Probe-2, respectively.

These volumetric images confirm that the GO-functionalised and antibody-immobilised surfaces effectively amplify the fluorophore emission more than that of bare fibre probe, underscoring GO superior potential for high-contrast fluorescence analysis.

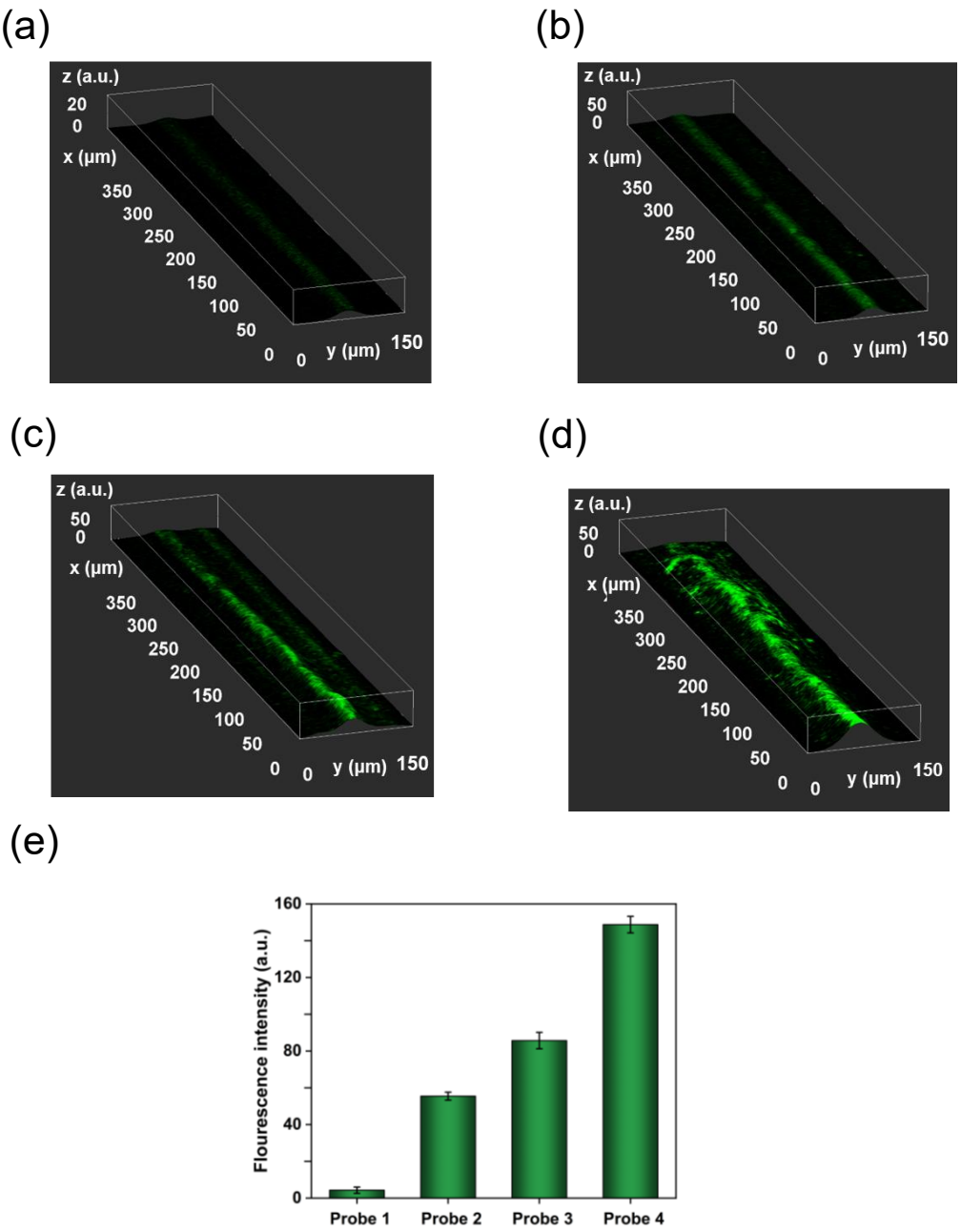

Figure 6.2 - 4 *Three-dimensional confocal fluorescence reconstructions of fibre probes functionalised with Alexa Fluor 488-conjugated anti-IgG: (a) Probe-1 (bare fibre, 2 µg/mL), (b) Probe-2 (GO-coated fibre, 2 µg/mL), (c) Probe-3 (GO-coated fibre, 4 µg/mL), and (d) Probe-4 (GO-coated fibre, 20 µg/mL). (e) Quantitative comparison of fluorescence intensities for all four probes, demonstrating enhanced antibody immobilisation on GO-functionalised surfaces.*

The abundant oxygenated functional groups of GO provide multivalent binding motifs for protein adsorption. Aromatic amino acid residues in the antibody can engage in π–π stacking with the graphitic regions of GO whilst polar side chains form the hydrogen bonds with GO's hydroxyl and carboxyl functionalities [257]. These interactions anchor each antibody to the GO surface in a relatively oriented manner, preserving the availability of its antigen-binding domains rather than flattening and denaturing the

molecule [258]. By contrast, an uncoated fibre probe surface (e.g., glass surface) has only a sparse density of Si-OH groups where antibodies tend to adsorb randomly, leading to partial unfolding and loss of bioactivity. Moreover, the sheet-like morphology of the GO dramatically increases the effective surface area for immobilisation, enabling a much higher antibody loading density than that on a bare glass fibre surface. The optical and electronic characteristics of GO could also mitigate fluorophore quenching and photobleaching effects [166,253]. Collectively, these features result in dense and uniform antibody coverage and correspondingly stronger, more reliable fluorescence signals. Such characteristics make GO-coated fibre probes a robust platform for sensitive and reproducible detection of low-abundance biomolecules.

6.2.6. Reusability of GO-fibre probes

To assess the reusability, the antibody-immobilised Probe-4 was immersed in 0.01 M HCl for 10 min at room temperature to disrupt the bonds between anti-IgG and the GO layer, followed by PBS rinsing and drying. After antibody removal, the fluorescence intensity dropped dramatically from 148.0 ± 4.5 a.u. to 14.0 ± 0.5 a.u. (Fig. 6.2-5a), indicating near-complete detachment of the conjugated antibodies. The probe was then re-incubated in a 20 µg/mL anti-IgG solution for 1 hour, restoring the fluorescence to 111.0 ± 7.9 a.u., which is approximately 75% of the original signal. To evaluate consistency, this regeneration and re-immobilisation processes were performed on three parallel Probe-4 samples, yielding similar fluorescence recovery with >70% retention, thereby confirming the reproducible reusability of the GO-fibre probes. The FTIR analysis was used to identify the presence of GO and its interaction with anti-IgG (Fig. 6.2-5b). The small peaks around 1516 cm^{-1} can be ascribed to the asymmetrically stretch of the C=C bonds in the aromatic ring or to the skeletal vibration of GO nanosheets [259]. Stretching vibration peak of O-H groups from carboxylic groups appears at 3585 cm^{-1} [260]. The presence of aliphatic amide (C-N) absorption band at 1086 cm^{-1} (red-curve) provides additional evidence of successful immobilisation of anti-IgG on GO fibre probe surface [261], which was disappeared after stripping off anti-IgG (blue-curve).

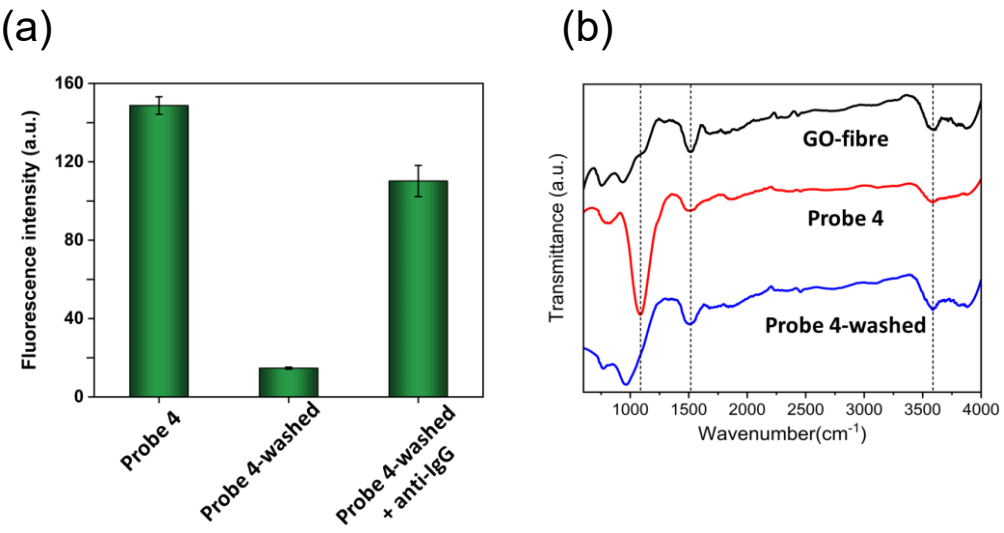

Figure 6.2 - 5 *(a) Reusability of GO-functionalised fibre probes evaluated using Probe-4. Fluorescence intensity significantly decreased after acid washing (Probe 4-washed) and partially recovered upon re-immobilisation of high-concentration anti-IgG (Probe 4-washed+anti-IgG). Error bars represent standard deviation from three parallel samples. (b) FTIR spectra of Probe-4 at different functionalisation stages: before bio-immobilisation (black), binding with high-concentration anti-IgG (red), and after antibody removal via acid wash (blue).*

6.3. Chapter summary

This chapter has presented the development of two functionalised fibre-optic sensors for the applications in heavy metal detection and bioimaging. (1) A fibre optic Fabry–Perot interferometer incorporating $Ti_3C_2T_x$ MXene nanosheets was designed for the detection of mercury (Hg^{2+}) ions in water. Upon Hg^{2+} adsorption and crystallisation on the MXene surface, notable changes in the refractive index within the cavity led to measurable modulation in the interference spectra. The MXene-assisted FFPI exhibited a low LOD of 0.47 nM, a broad detection range (from nanomolar to millimolar concentrations), and fast optical response, making it highly suitable for real-time, high-sensitive, and trace-level environmental monitoring. (2) The GO-functionalised fibre-optic probes were developed for fluorescence-based bioimaging. The GO nanosheets provided a high-density, chemically reactive surface enriched with oxygen-containing functional groups, enabling efficient covalent immobilisation of fluorescent anti-IgG antibodies via EDC/NHS coupling. Fluorescence imaging confirmed enhanced signal intensity and uniformity relative to uncoated probes, with performance strongly correlated to antibody concentration. Moreover, the biointerface allowed for probe regeneration through acidic treatment, achieving >70% fluorescence retention across parallel samples, thus demonstrating reusability. Overall, the results confirm that nanomaterial-modified fibre

platforms offer high sensitivity, strong reproducibility, and regeneration capability, supporting their potential as versatile sensing tools in both environmental diagnostics and biomedical imaging contexts.

Chapter 7 Conclusions and future work

7.1. Conclusions

This thesis has presented a comprehensive investigation of 2D materials-functionalised optoelectronic devices for biochemical sensing and biomedical applications. Through the synergistic combination of optoelectronic platforms and nanomaterials, a series of high performance, label-free, and application specific sensors have been developed to address critical challenges in cancer diagnostics, biomolecular analysis, bioimaging, and environmental monitoring.

The work began with the fundamental knowledge of light propagation and mode couplings. The principles of FBGs and LPGs were firstly derived using coupled-mode theory, enabling a clear understanding of resonant interactions between core and cladding modes. These models were fundamental for interpreting reflection and transmission characteristics in periodic fibre structures. The FPI was also analysed by the waveguide theory and interference principles, providing insight into resonance conditions in F-P cavity-based fibre sensors. Together, these theoretical foundations guided the design and optimisation of advanced fibre-optic sensing platforms explored in this thesis.

The subsequent chapters focused on the synthesis and characterisation of 2D materials including BP, $BiTiS_3$, α-MoO_3, GO, $Ti_3C_2T_x$ MXene, and small AuNRs. Various top-down exfoliation and bottom-up growth nanotechnologies, including sonication-assisted liquid exfoliation, electrochemical exfoliation, selective etching exfoliation, and 'one-pot' seedless synthesis were developed to produce atomically thin flakes with controlled dimensions and surface chemistry. A series of material characterisation techniques were employed to evaluate the morphological, structural, and optical properties of the synthesised 2D materials. SEM and AFM were used to assess surface morphology, flake size, and nanosheet thickness. TEM provided high-resolution imaging of internal lattice structures and edge morphology, offering further insight into the crystallinity and exfoliation quality of the materials. Raman spectroscopy was employed to evaluate the structural quality and disorder of the 2D materials by analysing characteristic vibrational modes. UV-Vis-NIR spectroscopy enabled the assessment of optical absorption characteristics, while XRD and FTIR provided insights into crystal structure and surface functional groups, respectively. These complementary techniques ensured a

comprehensive understanding of the materials' physical and chemical attributes, forming a robust basis for subsequent device-level integration.

Following material synthesis, various transfer and integration methods were employed to functionalise optoelectronic devices with 2D materials. The i-LbL deposition technique was systematically investigated for the deposition of 2D nanosheets onto fibre device surfaces. This method enabled controlled tuning of coating thickness and surface coverage by adjusting parameters such as concentration of materials suspension, coating time and number of coating cycles. The wet transfer was employed to transfer monolayer graphene onto planar FET substrates. The spin coating was used to deposit PQDs onto phototransistor channels. In addition, the drop casting was applied for the deposition of AuNPs onto photonic filters to enable surface functionalisation.

In the application-oriented study, five sensor devices were proposed and demonstrated, including GO-LPG based biosensor, hybrid gratings based biosensor, perovskite/graphene heterostructure based FET immunosensor, MXene based chemical sensor, and GO-fibre optic bioimaging probe. The proposed sensors exhibited excellent performance in terms of label-free, ultrasensitivity, and rapid responsivity. The GO-LPG biosensor was used for label-free quantification of breast cancer cell density with a LOD down to 270 cells/mL. The first perovskite/graphene heterostructure biosensor was reported for the detection of IL6 cytokines, achieving an ultralow LOD of 0.9 fg/mL, which is 4 orders of magnitude greater than graphene-FET biosensors. The LPG–FBG hybrid sensor exhibited a high RI sensitivity of 741 nm/RIU and enabled haemoglobin detection down to 0.67 mg/mL. The MXene-assisted FFPI sensor achieved a low LOD of 0.47 nM for the detection of Hg^{2+} ions, with a wide detection range from 0 to 5000 μM and a rapid response time of less than 1 minute. The GO-coated fibre probes enabled anti-IgG labelling and fluorescence bioimaging applications.

In conclusion, this thesis has advanced the field of fibre-optic and optoelectronic biosensing by integrating 2D materials with functional optoelectronic platforms. Through the rational design of material–device interfaces, it has been demonstrated that 2D materials can significantly enhance the sensitivity, specificity, and functional adaptability. These improvements were achieved across a range of device formats, including interferometers, fibre gratings, and phototransistors. Additionally, the thesis also explored the role of tailored photonic structures such as the hybrid LPG–FBG grating configuration, which enabled advanced light–matter interaction and mode-selective enhancement. Collectively, these contributions establish a robust foundation for the development of

compact, scalable, and application-specific sensing technologies with strong potential in healthcare, diseases diagnostics, environmental monitoring, and biological imaging.

7.2. Future work

7.2.1. 2D heterostructure based biosensor for cancer diagnostics

Extracellular vesicles (EVs) are naturally secreted by all types of cells, including both prokaryotic and eukaryotic cells, during normal physiological processes as well as in response to pathological conditions. These vesicles can transport a wide range of cellular components such as DNA, various forms of RNA, lipids, metabolites, and proteins located in the cytoplasm or on the cell surface. Through this mechanism, EVs facilitate the transfer of molecular information from donor cells to recipient cells. Research in EVs is driven by the potential of EVs to serve as diagnostic and therapeutic tools for the treatment of a range of diseases, including neurodegenerative disorders, cardiovascular dysfunction, and cancers [262–270].

Exosomes are a major class of EVs, originating from endosomes. They are characterised by a lipid-bilayer membrane and typically range in size from 50 to 150 nm in diameter. Exosomes are secreted by a wide range of cells and can remain stable while circulating in various body fluids. The bioactive contents of exosomes can be internalised by recipient cells, thereby contributing to the initiation and progression of tumours. Additionally, exosomes play a role in the formation of the pre-metastatic niche, tumour angiogenesis, and immune suppression. Furthermore, exosomes can reflect the altered physiological and pathological states of their parent cells [271–274].

However, exosomes research continues to face constraints due to experimental limitations in single particle detection and isolation, as well as the challenge of imaging and tracking exosomes in vivo with reliable resolution. Although Exosome-associated proteins such as tetraspanins (CD9, CD63, and CD81), components of the endosomal sorting complex (including TSG101 and Alix), and heat shock proteins (Hsp60, Hsp70, and Hsp90) have been widely investigated, specific markers that can reliably differentiate cancer-derived exosomes from those of normal cells remained unidentified until the discovery of glypican-1 (GPC1), a membrane protein recognised as a potential cancer-specific exosomal marker. GPC1+ circulating exosomes (crExos) have demonstrated 100% sensitivity and specificity across all stages of pancreatic cancer, highlighting their value

as a biomarker for disease detection at every stage and their potential for early diagnosis. [275,276].

Early diagnosis of pancreatic cancer (PC) is challenging, and its prognosis remains poor, with most patients seeking medical attention only after the disease has progressed and symptoms emerge. Based on GPC1was found as a pan-specific marker of cancer exosomes, research on related biosensing for the detection or diagnosis of PC were widely reported. Yin et al. presented graphene-FET sensor arrays for detection of pancreatic cancer exosomes, which found that GPC1 proteins were more strongly expressed on pancreatic cancer exosomes compared to the healthy ones [8]. A LPHN-CHDC biochip was reported for the detection of EV-associated RNAs, achieving an LOD of 0.01 pg for GPC1 mRNA [277]. A multiparametric plasma EV profiling promised a sensitivity of 86% for detecting PDAC and a specificity of 81% for differentiating PDAC from other pancreatic diseases [278]. A nanoliquid biopsy (nLB) assay was established for the diagnosis of pancreatic cancer with a LOD of 78 pg/mL of the GPC1 [279]. Li et al. reported a SERS immunoassay for exosome-based diagnosis and classification of pancreatic cancer, which realised a LOD of 544 particles/mL [10]. Though the published works distinguished Pancreatic cancer from healthy, the quantitative detection reaching single-exosome level remains a challenge.

The family of 2D materials has expanded significantly since the discovery of graphene [31,280]. In addition, different atomically thin 2D materials can be readily stacked together by vdW forces to make 2D heterostructures without the conventional 'lattice mismatch' issue, offering a flexible and easy approach to get the desired physical properties [281–283]. Tools for band-structure engineering in vdW heterostructures include the relative alignment of neighbouring crystals, surface reconstruction, charge transfer, and proximity effects. These effects allow one material to acquire properties from another through quantum tunnelling or Coulomb interactions. Such synergistic advantages will bring in enhanced sensitivities, heightened selectivity, and increased stability when the heterostructure are utilised for the integration with optoelectronic devices for the biochemical and biomedical applications.

Thereby, an α-MoO_3/GO heterostructure functionalised coaxial twin-tilted fibre Brag gratings (TFG) can be designed for the detection of PANC-1 cancer cell-secreted exosomes (Fig. 7.2-1). The strong in-plane anisotropy of α-MoO_3 is coated around TFG as the first layer to enhance the higher sensitivity to the surrounding-medium RI. The GO layer with abundant bio-affinity sites and a high surface-to-volume ratio is applied as the

second layer. Upon immobilisation of GPC-1 antibodies, the GO overlay provides an effective platform for capturing exosomes via specific antibody-antigen interactions.

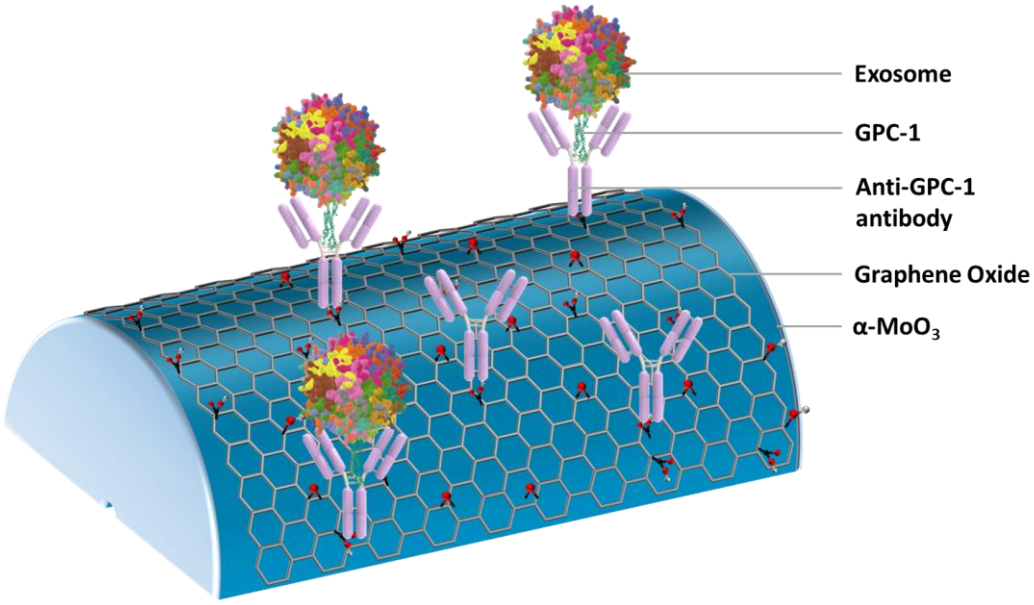

Figure 7.2 - 1 *Schematic illustration of α-MoO_3/GO heterostructure based biosensor for the detection of exosomes secreted from Pancreatic cancer cells.*

7.2.2. $BiTiS_3$ functionalised 45°-TFG for photothermal therapy

As one of the most life-threatening diseases, cancer remains a leading global cause of mortality. The International Agency for Research on Cancer (IARC) estimated that one in five individuals could face a cancer diagnosis during their lifetime [284–286]. Despite being a long-standing challenge in medical research, overcoming cancer requires precise and effective therapeutic interventions, informed by insights from various fields to address the complexities of treatment. Targeted therapies, particularly when initiated in the early stages of the disease, are crucial for enhancing survival rates and optimising patient outcomes [287,288].

Traditional cancer treatments like surgery, chemotherapy, and radiotherapy remain common clinical approaches; however, their effectiveness is often limited by resistance to drugs and radiation [289,290]. With revolutionary advances in photonics and optics, light has illuminated a new era in tumour treatment, providing abundant degrees of freedom for cancer theranostics [291]. Light-based therapy provides numerous advantages, such as high spatiotemporal controllability, ionization-free action, minimal invasiveness, and reduced side effects, making them an attractive option for modern oncology [292]. As one of the emerging treatment methods using light as the medium,

photothermal therapy (PTT) harnesses photon energy absorbed by nanomaterials to generate heat, which selectively destroys cancer cells. PTT not only offers a simpler procedure and shorter treatment duration but also promotes a quicker recovery and significantly reduces patient burden, positioning it as an efficient and targeted cancer treatment [293–295].

A wide variety of nanomaterials, including both inorganic and organic compounds, have been developed as photothermal agents for cancer treatment, utilizing their ability to absorb and convert light energy into heat, inducing localised hyperthermia and tumour ablation [296–299]. Recent advancements in material design have led to the creation of photothermal agents with improved properties, such as enhanced biocompatibility, biosafety, and modifiability, which have accelerated the development of PTT [300–302]. Among these, 2D materials such as graphene [303], MoS_2 [304], Bi_3Se_2 [294], and BP [305,306] have gained significant attention due to their unique structures, high surface-to-volume ratios, broad light absorption ranging from ultraviolet to near-infrared, and multifunctionality. 2D materials show great promise for integrating diagnosis and treatment, paving the way for more effective and practical PTT solutions [295].

Despite the rapid advancements in nanomaterials for PTT, significant challenges remain, particularly the limited penetration depth of light in human tissue, which poses a major barrier for treating deep-seated tumours [307,308]. While cutting-edge research has shifted the absorption wavelength of photothermal agents from visible region to the NIR-II region to enhance the penetration, this issue remains unresolved due to light scattering and absorption by the tissues [309–311]. Additionally, the photothermal agents injected into blood vessels may accumulate in the body, raising concerns about potential damage to healthy cells and the overall safety and precision of PTT [312–314]. Furthermore, whilst nanotechnology has advanced photoreporting and photosensitising drugs, uncertainties regarding the interaction of nanoparticles and organs, the circulatory system, and tumours continue to present risks for the in vivo application. These limitations hinder the use of PTT, especially for larger or deep-seated tumours, and complicate the regulation of laser illumination doses [315–317].

The limitations of light penetration in tissue during PTT can be effectively addressed through the use of optical fibres. As highly efficient light guides, optical fibres can deliver photons with minimal loss, making them ideal for internal, tumour-targeted light irradiation [299]. Their unique characteristics, including electrical isolation, resistance to corrosion, flexibility, and small size, allow them to be safely and precisely used for in

vivo applications. Photothermal agents can be integrated onto the specific surface of optical fibre to address issues of agent accumulation and reduce the risk of unintended harm to healthy tissues. Significant progress has recently been made in demonstrating the integration of optical fibres and nanomaterials for in vivo PTT. A tapered microfiber assembled with GO-Au nanorods and $Cu_{2-x}S$ has been developed for hyperthermal ablation of cancer cells, achieving an ablation rate of 89% [299]. A GO-Au@Ag_2S-VO_2 nanointerface was deposited on an optical microfiber for PTT by the use of temperature-tuneable enhancement of the evanescent field, resulting in an 82% ablation rate of cancer cells [318]. The thermal effect arises from the evanescent field at the interface of the tapered optical microfibre when the pump laser is launched. As a result, the light that propagates out of the tapered microfiber exhibits poor directional properties, making it challenging to control the direction of the emitted radiation. Controlling the direction of radiation is crucial when treating tumours located in sensitive areas of the human body. For instance, conditions such as angiosarcoma, cholangiocarcinoma, and ampullary cancer may require precisely directed light to ablate the tumour while minimizing damage to surrounding structures, such as blood vessels or the bile duct.

Hence, a $BiTiS_3$ nanosheets functionalised 45˚-TFG with controllable radiation direction can be designed for in vivo and in vitro cancer therapy. As shown in Fig. 7.2-2, an 45˚-TFG is designed to couple the s-polarisation component of light out of the fibre, whilst the p-polarisation component propagates pass through the fibre [319]. The radiated light from the TFG is confined strictly with a divergence angle at ~60˚. Recent studies have shown that elemental composition plays a key role in defining the properties of 2D materials. Ternary nanomaterials (e.g., contain three elements) have demonstrated superior physical and chemical properties compared to binary systems [320]. As a result, ternary transition metal dichalcogenides (TMDs) are expected to enhance the photothermal performance in cancer therapy. In this context, we introduce a novel type of 2D nanomaterial, $BiTiS_3$ nanosheets, which exhibit a broad and strong absorption band spanning both in NIR-I and NIR-II regions. $BiTiS_3$ nanosheets will be deposited around the 45˚-TFG, where the s-polarised light is radiated to the nanomaterials, which will convert the light energy into heat for directionally controlled tumour ablation. Guiding light through the $BiTiS_3$ nanosheet integrated 45˚ TFG not only fundamentally resolves the issue of limited light penetration depth in vivo but also provides a powerful tool for directionally controllable tumour theranostics, particularly in early-stage treatments.

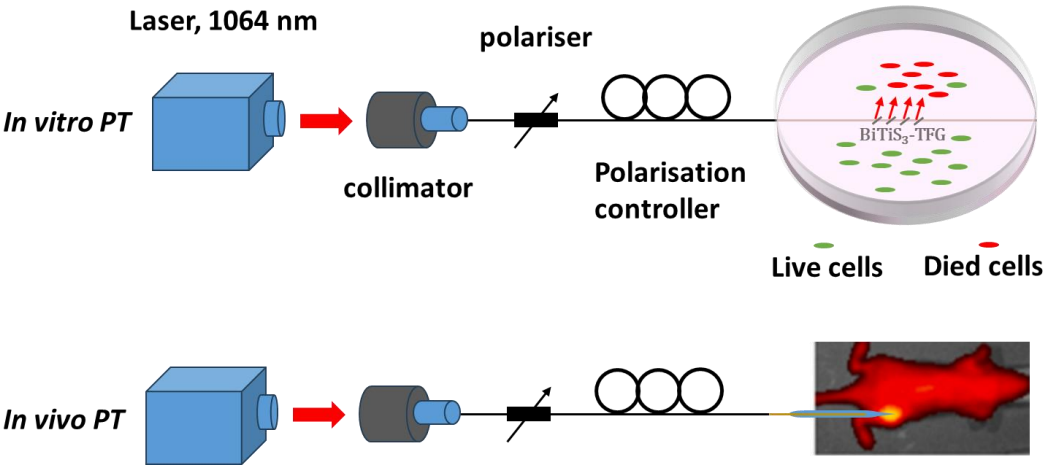

Figure 7.2 - 2 *Schematic illustration of $BiTiS_3$-TFG probe for in vitro (top) and in vivo (bottom) PT.*

References

1. C. Liu, Q. Cai, B. Xu, W. Zhu, L. Zhang, J. Zhao, and X. Chen, "Graphene oxide functionalized long period grating for ultrasensitive label-free immunosensing," Biosens. Bioelectron. **94**, 200–206 (2017).
2. B. Xu, M. Zhu, W. Zhang, X. Zhen, Z. Pei, Q. Xue, C. Zhi, and P. Shi, "Ultrathin MXene-Micropattern-Based Field-Effect Transistor for Probing Neural Activity," Adv. Mater. **28**, 3333–3339 (2016).
3. L. Zhou, C. Liu, Z. Sun, H. Mao, L. Zhang, X. Yu, J. Zhao, and X. Chen, "Black phosphorus based fiber optic biosensor for ultrasensitive cancer diagnosis," Biosens. Bioelectron. **137**, 140–147 (2019).
4. J. Zhao, C. He, W. Wu, H. Yang, L. Peng, L. Wen, Z. Hu, C. Hou, and D. Huo, "MXene-MoS2 carbon-fiber-based flexible electrochemical interface for multiple bioanalysis in biofluids," Chem. Eng. J. **446**, 136841 (2022).
5. C. Zhu, Z. Zeng, H. Li, F. Li, C. Fan, and H. Zhang, "Single-Layer MoS_2 -Based Nanoprobes for Homogeneous Detection of Biomolecules," J. Am. Chem. Soc. **135**, 5998–6001 (2013).
6. J. Sun, L. Zhou, Z. Li, G. He, H. Mao, J. Zhao, J. A. Hunt, and X. Chen, "Perovskite-Graphene Heterostructure Biosensor Integrated with Biotunable Nanoplasmonic Ternary Logic Gate for Ultrasensitive Cytokine Detection," Adv. Sci. **n/a**, e03124 (n.d.).
7. H. Xie, P. Li, J. Shao, H. Huang, Y. Chen, Z. Jiang, P. K. Chu, and X.-F. Yu, "Electrostatic Self-Assembly of $Ti_3C_2T_x$ MXene and Gold Nanorods as an Efficient Surface-Enhanced Raman Scattering Platform for Reliable and High-Sensitivity Determination of Organic Pollutants," ACS Sens. **4**, 2303–2310 (2019).
8. T. Yin, L. Xu, B. Gil, N. Merali, M. S. Sokolikova, D. C. A. Gaboriau, D. S. K. Liu, A. N. Muhammad Mustafa, S. Alodan, M. Chen, O. Txoperena, M. Arrastua, J. M. Gomez, N. Ontoso, M. Elicegui, E. Torres, D. Li, C. Mattevi, A. E. Frampton, L. R. Jiao, S. Ramadan, and N. Klein, "Graphene Sensor Arrays for Rapid and Accurate Detection of Pancreatic Cancer Exosomes in Patients' Blood Plasma Samples," ACS Nano **17**, 14619–14631 (2023).
9. G. Qiu, A. Thakur, C. Xu, S. Ng, Y. Lee, and C. L. Wu, "Detection of Glioma-Derived Exosomes with the Biotinylated Antibody-Functionalized Titanium Nitride Plasmonic Biosensor," Adv. Funct. Mater. **29**, 1806761 (2019).
10. T.-D. Li, R. Zhang, H. Chen, Z.-P. Huang, X. Ye, H. Wang, A.-M. Deng, and J.-L. Kong, "An ultrasensitive polydopamine bi-functionalized SERS immunoassay for exosome-based diagnosis and classification of pancreatic cancer," Chem. Sci. **9**, 5372–5382 (2018).
11. S. Chandra Barman, M. Sharifuzzaman, M. A. Zahed, C. Park, S. H. Yoon, S. Zhang, H. Kim, H. Yoon, and J. Y. Park, "A highly selective and stable cationic polyelectrolyte encapsulated black phosphorene based impedimetric immunosensor for Interleukin-6 biomarker detection," Biosens. Bioelectron. **186**, 113287 (2021).
12. P. Ferdinand, "The Evolution of Optical Fiber Sensors Technologies During the 35 Last Years and Their Applications in Structure Health Monitoring," (2014).
13. B. Lee, "Review of the present status of optical fiber sensors," Opt. Fiber Technol. **9**, 57–79 (2003).

14. B. Culshaw, "Optical Fiber Sensor Technologies: Opportunities and—Perhaps—Pitfalls," J. Light. Technol. **22**, 39–50 (2004).
15. Y. Zhao, S. Liu, J. Luo, Y. Chen, C. Fu, C. Xiong, Y. Wang, S. Jing, Z. Bai, C. Liao, and Y. Wang, "Torsion, Refractive Index, and Temperature Sensors Based on An Improved Helical Long Period Fiber Grating," J. Light. Technol. **38**, 2504–2510 (2020).
16. C. Liu, B. J. Xu, L. Zhou, Z. Sun, H. J. Mao, J. L. Zhao, L. Zhang, and X. Chen, "Graphene oxide functionalized long period fiber grating for highly sensitive hemoglobin detection," Sens. Actuators B Chem. **261**, 91–96 (2018).
17. F. Yu, Q. Liu, X. Gan, M. Hu, T. Zhang, C. Li, F. Kang, M. Terrones, and R. Lv, "Ultrasensitive Pressure Detection of Few-Layer MoS_2," Adv. Mater. **29**, 1603266 (2017).
18. E. Hecht, *Optics*, 5 ed (Pearson Education, Inc, 2017).
19. M. Bass and E. Van Stryland, "Fiber Optics Handbook—Fiber, Devices and Systems for Optical Communications," in (2002).
20. X. Chen, "Optical Fibre Gratings for Chemical and Bio - Sensing," in *Current Developments in Optical Fiber Technology*, S. W. Harun, ed. (InTech, 2013).
21. S. W. James and R. P. Tatam, "Optical fibre long-period grating sensors: characteristics and application," Meas. Sci. Technol. **14**, R49–R61 (2003).
22. T. Erdogan, "Fiber grating spectra," J. Light. Technol. **15**, 1277–1294 (1997).
23. T. Erdogan, "Cladding-mode resonances in short- and long-period fiber grating filters," J. Opt. Soc. Am. A **14**, 1760 (1997).
24. K. S. Lee and T. Erdogan, "Fiber mode coupling in transmissive and reflective tilted fiber gratings," (n.d.).
25. H. Kogelnik, "Theory of Optical Waveguides," in *Guided-Wave Optoelectronics*, T. Tamir, ed. (Springer, 1988), pp. 7–88.
26. M. Born and E. Wolf, *Principles of Optics: Electromagnetic Theory of Propagation, Interference and Diffraction of Light*, 7th ed. (Cambridge University Press, 1999).
27. K. Zhou, L. Zhang, X. Chen, and I. Bennion, "Low Thermal Sensitivity Grating Devices Based on Ex-45° Tilting Structure Capable of Forward-Propagating Cladding Modes Coupling," J. Light. Technol. **24**, 5087–5094 (2006).
28. C. Fabry, "Theorie et applications d'une nouvelle methods de spectroscopie intereferentielle," Ann Chim Ser 7 **16**, 115–144 (1899).
29. A. Perot and C. Fabry, "On the Application of Interference Phenomena to the Solution of Various Problems of Spectroscopy and Metrology," Astrophys. J. **9**, 87 (1899).
30. C. Tan, X. Cao, X.-J. Wu, Q. He, J. Yang, X. Zhang, J. Chen, W. Zhao, S. Han, G.-H. Nam, M. Sindoro, and H. Zhang, "Recent Advances in Ultrathin Two-Dimensional Nanomaterials," Chem. Rev. **117**, 6225–6331 (2017).
31. K. S. Novoselov, A. K. Geim, S. V. Morozov, D. Jiang, Y. Zhang, S. V. Dubonos, I. V. Grigorieva, and A. A. Firsov, "Electric Field Effect in Atomically Thin Carbon Films," Science **306**, 666–669 (2004).
32. F. Yang, P. Song, M. Ruan, and W. Xu, "Recent progress in two-dimensional nanomaterials: Synthesis, engineering, and applications," FlatChem **18**, 100133 (2019).
33. A. K. Geim and K. S. Novoselov, "The rise of graphene," Nat. Mater. **6**, 183–191 (2007).

34. H. Zhang, "Ultrathin Two-Dimensional Nanomaterials," ACS Nano **9**, 9451–9469 (2015).
35. M. D. Stoller, S. Park, Y. Zhu, J. An, and R. S. Ruoff, "Graphene-Based Ultracapacitors," Nano Lett. **8**, 3498–3502 (2008).
36. D. Zhang, W. Pan, M. Tang, D. Wang, S. Yu, Q. Mi, Q. Pan, and Y. Hu, "Diversiform gas sensors based on two-dimensional nanomaterials," Nano Res. **16**, 11959–11991 (2023).
37. Z. Zhen and H. Zhu, "1 - Structure and Properties of Graphene," in *Graphene*, H. Zhu, Z. Xu, D. Xie, and Y. Fang, eds. (Academic Press, 2018), pp. 1–12.
38. M. J. Allen, V. C. Tung, and R. B. Kaner, "Honeycomb Carbon: A Review of Graphene," Chem. Rev. **110**, 132–145 (2010).
39. D. R. Cooper, B. D'Anjou, N. Ghattamaneni, B. Harack, M. Hilke, A. Horth, N. Majlis, M. Massicotte, L. Vandsburger, E. Whiteway, and V. Yu, "Experimental Review of Graphene," ISRN Condens. Matter Phys. **2012**, 1–56 (2012).
40. K. I. Bolotin, K. J. Sikes, Z. Jiang, M. Klima, G. Fudenberg, J. Hone, P. Kim, and H. L. Stormer, "Ultrahigh electron mobility in suspended graphene," Solid State Commun. **146**, 351–355 (2008).
41. S. V. Morozov, K. S. Novoselov, M. I. Katsnelson, F. Schedin, D. C. Elias, J. A. Jaszczak, and A. K. Geim, "Giant Intrinsic Carrier Mobilities in Graphene and Its Bilayer," Phys. Rev. Lett. **100**, 016602 (2008).
42. J.-H. Chen, C. Jang, S. Xiao, M. Ishigami, and M. S. Fuhrer, "Intrinsic and extrinsic performance limits of graphene devices on SiO2," Nat. Nanotechnol. **3**, 206–209 (2008).
43. J. Wang, R. Zhao, M. Yang, Z. Liu, and Z. Liu, "Inverse relationship between carrier mobility and bandgap in graphene," J. Chem. Phys. **138**, 084701 (2013).
44. R. R. Nair, P. Blake, A. N. Grigorenko, K. S. Novoselov, T. J. Booth, T. Stauber, N. M. R. Peres, and A. K. Geim, "Fine Structure Constant Defines Visual Transparency of Graphene," Science **320**, 1308–1308 (2008).
45. G.-K. Lim, Z.-L. Chen, J. Clark, R. G. S. Goh, W.-H. Ng, H.-W. Tan, R. H. Friend, P. K. H. Ho, and L.-L. Chua, "Giant broadband nonlinear optical absorption response in dispersed graphene single sheets," Nat. Photonics **5**, 554–560 (2011).
46. K. P. Loh, Q. Bao, G. Eda, and M. Chhowalla, "Graphene oxide as a chemically tunable platform for optical applications," Nat. Chem. **2**, 1015–1024 (2010).
47. D. R. Dreyer, S. Park, C. W. Bielawski, and R. S. Ruoff, "The chemistry of graphene oxide," Chem Soc Rev **39**, 228–240 (2010).
48. G. Eda, C. Mattevi, H. Yamaguchi, H. Kim, and M. Chhowalla, "Insulator to Semimetal Transition in Graphene Oxide," J. Phys. Chem. C **113**, 15768–15771 (2009).
49. J. Wu, Y. Yang, Y. Qu, X. Xu, Y. Liang, S. T. Chu, B. E. Little, R. Morandotti, B. Jia, and D. J. Moss, "Graphene Oxide Waveguide and Micro-Ring Resonator Polarizers," Laser Photonics Rev. **13**, 1900056 (2019).
50. Y. Yang, J. Wu, X. Xu, Y. Liang, S. T. Chu, B. E. Little, R. Morandotti, B. Jia, and D. J. Moss, "Invited Article: Enhanced four-wave mixing in waveguides integrated with graphene oxide," APL Photonics **3**, 120803 (2018).
51. M. R. Lukatskaya, O. Mashtalir, C. E. Ren, Y. Dall'Agnese, P. Rozier, P.-L. Taberna, M. Naguib, P. Simon, M. W. Barsoum, and Y. Gogotsi, "Cation Intercalation and High Volumetric Capacitance of Two-Dimensional Titanium Carbide," (n.d.).

52. M. Han, K. Maleski, C. E. Shuck, Y. Yang, J. T. Glazar, A. C. Foucher, K. Hantanasirisakul, A. Sarycheva, N. C. Frey, S. J. May, V. B. Shenoy, E. A. Stach, and Y. Gogotsi, "Tailoring Electronic and Optical Properties of MXenes through Forming Solid Solutions," J. Am. Chem. Soc. **142**, 19110–19118 (2020).
53. X. Yu, X. Cai, H. Cui, S.-W. Lee, X.-F. Yu, and B. Liu, "Fluorine-free preparation of titanium carbide MXene quantum dots with high near-infrared photothermal performances for cancer therapy," Nanoscale **9**, 17859–17864 (2017).
54. A. Shahzad, M. Nawaz, M. Moztahida, J. Jang, K. Tahir, J. Kim, Y. Lim, V. S. Vassiliadis, S. H. Woo, and D. S. Lee, "Ti3C2Tx MXene core-shell spheres for ultrahigh removal of mercuric ions," Chem. Eng. J. **368**, 400–408 (2019).
55. M. Naguib, M. Kurtoglu, V. Presser, J. Lu, J. Niu, M. Heon, L. Hultman, Y. Gogotsi, and M. W. Barsoum, "Two-Dimensional Nanocrystals Produced by Exfoliation of $Ti_3 AlC_2$," Adv. Mater. **23**, 4248–4253 (2011).
56. M. Naguib, O. Mashtalir, J. Carle, V. Presser, J. Lu, L. Hultman, Y. Gogotsi, and M. W. Barsoum, "Two-Dimensional Transition Metal Carbides," ACS Nano **6**, 1322–1331 (2012).
57. X. Hong, Z. Xu, Z. Lv, Z. Lin, M. Ahmadi, L. Cui, V. Liljeström, V. Dudko, J. Sheng, X. Cui, A. P. Tsapenko, J. Breu, Z. Sun, Q. Zhang, E. Kauppinen, B. Peng, and O. Ikkala, "High-permittivity Solvents Increase MXene Stability and Stacking Order Enabling Ultraefficient Terahertz Shielding," Adv. Sci. **11**, 2305099 (2024).
58. M. Naguib, V. N. Mochalin, M. W. Barsoum, and Y. Gogotsi, "25th Anniversary Article: MXenes: A New Family of Two-Dimensional Materials," Adv. Mater. **26**, 992–1005 (2014).
59. K. Hantanasirisakul and Y. Gogotsi, "Electronic and Optical Properties of 2D Transition Metal Carbides and Nitrides (MXenes)," Adv. Mater. **30**, 1804779 (2018).
60. A. VahidMohammadi, J. Rosen, and Y. Gogotsi, "The world of two-dimensional carbides and nitrides (MXenes)," Science **372**, eabf1581 (2021).
61. I. A. de Castro, R. S. Datta, J. Z. Ou, A. Castellanos-Gomez, S. Sriram, T. Daeneke, and K. Kalantar-zadeh, "Molybdenum Oxides – From Fundamentals to Functionality," Adv. Mater. **29**, 1701619 (2017).
62. W. Ma, P. Alonso-González, S. Li, A. Y. Nikitin, J. Yuan, J. Martín-Sánchez, J. Taboada-Gutiérrez, I. Amenabar, P. Li, S. Vélez, C. Tollan, Z. Dai, Y. Zhang, S. Sriram, K. Kalantar-Zadeh, S.-T. Lee, R. Hillenbrand, and Q. Bao, "In-plane anisotropic and ultra-low-loss polaritons in a natural van der Waals crystal," Nature **562**, 557–562 (2018).
63. L. Lajaunie, F. Boucher, R. Dessapt, and P. Moreau, "Strong anisotropic influence of local-field effects on the dielectric response of α -MoO 3," Phys. Rev. B **88**, 115141 (2013).
64. S. Puebla, R. D'Agosta, G. Sanchez-Santolino, R. Frisenda, C. Munuera, and A. Castellanos-Gomez, "In-plane anisotropic optical and mechanical properties of two-dimensional MoO3," Npj 2D Mater. Appl. **5**, 37 (2021).
65. H. Hu, N. Chen, H. Teng, R. Yu, M. Xue, K. Chen, Y. Xiao, Y. Qu, D. Hu, J. Chen, Z. Sun, P. Li, F. J. G. De Abajo, and Q. Dai, "Gate-tunable negative refraction of mid-infrared polaritons," Science **379**, 558–561 (2023).
66. X. Guo, C. Wu, S. Zhang, D. Hu, S. Zhang, Q. Jiang, X. Dai, Y. Duan, X. Yang, Z. Sun, S. Zhang, H. Xu, and Q. Dai, "Mid-infrared analogue polaritonic reversed Cherenkov radiation in natural anisotropic crystals," Nat. Commun. **14**, 2532 (2023).

67. A. Bouzidi, N. Benramdane, H. Tabet-Derraz, C. Mathieu, B. Khelifa, and R. Desfeux, "Effect of substrate temperature on the structural and optical properties of MoO3 thin films prepared by spray pyrolysis technique," Mater. Sci. Eng. B **97**, 5–8 (2003).
68. K. Kalantar-zadeh, J. Tang, M. Wang, K. L. Wang, A. Shailos, K. Galatsis, R. Kojima, V. Strong, A. Lech, W. Wlodarski, and R. B. Kaner, "Synthesis of nanometre-thick MoO_3 sheets," Nanoscale **2**, 429–433 (2010).
69. B. Zheng, Z. Wang, Y. Chen, W. Zhang, and X. Li, "Centimeter-sized 2D α -MoO_3 single crystal: growth, Raman anisotropy, and optoelectronic properties," 2D Mater. **5**, 045011 (2018).
70. A. J. Molina-Mendoza, J. L. Lado, J. O. Island, M. A. Niño, L. Aballe, M. Foerster, F. Y. Bruno, A. López-Moreno, L. Vaquero-Garzon, H. S. J. Van Der Zant, G. Rubio-Bollinger, N. Agraït, E. M. Pérez, J. Fernández-Rossier, and A. Castellanos-Gomez, "Centimeter-Scale Synthesis of Ultrathin Layered MoO_3 by van der Waals Epitaxy," Chem. Mater. **28**, 4042–4051 (2016).
71. L. Cai, P. M. Rao, and X. Zheng, "Morphology-Controlled Flame Synthesis of Single, Branched, and Flower-like α-MoO_3 Nanobelt Arrays," Nano Lett. **11**, 872–877 (2011).
72. M. B. Sreedhara, H. S. S. R. Matte, A. Govindaraj, and C. N. R. Rao, "Synthesis, Characterization, and Properties of Few-Layer MoO_3," Chem. – Asian J. **8**, 2430–2435 (2013).
73. S. Balendhran, S. Walia, M. Alsaif, E. P. Nguyen, J. Z. Ou, S. Zhuiykov, S. Sriram, M. Bhaskaran, and K. Kalantar-zadeh, "Field Effect Biosensing Platform Based on 2D α-MoO3," ACS Nano **7**, 9753–9760 (2013).
74. M. Yi and Z. Shen, "A review on mechanical exfoliation for the scalable production of graphene," J. Mater. Chem. A **3**, 11700–11715 (2015).
75. V. Nicolosi, M. Chhowalla, M. G. Kanatzidis, M. S. Strano, and J. N. Coleman, "Liquid Exfoliation of Layered Materials," Science **340**, 1226419 (2013).
76. K. R. Paton, E. Varrla, C. Backes, R. J. Smith, U. Khan, A. O'Neill, C. Boland, M. Lotya, O. M. Istrate, P. King, T. Higgins, S. Barwich, P. May, P. Puczkarski, I. Ahmed, M. Moebius, H. Pettersson, E. Long, J. Coelho, S. E. O'Brien, E. K. McGuire, B. M. Sanchez, G. S. Duesberg, N. McEvoy, T. J. Pennycook, C. Downing, A. Crossley, V. Nicolosi, and J. N. Coleman, "Scalable production of large quantities of defect-free few-layer graphene by shear exfoliation in liquids," Nat. Mater. **13**, 624–630 (2014).
77. K. Parvez, Z.-S. Wu, R. Li, X. Liu, R. Graf, X. Feng, and K. Müllen, "Exfoliation of Graphite into Graphene in Aqueous Solutions of Inorganic Salts," J. Am. Chem. Soc. **136**, 6083–6091 (2014).
78. R. Ma and T. Sasaki, "Two-Dimensional Oxide and Hydroxide Nanosheets: Controllable High-Quality Exfoliation, Molecular Assembly, and Exploration of Functionality," Acc. Chem. Res. **48**, 136–143 (2015).
79. S. Stankovich, D. A. Dikin, R. D. Piner, K. A. Kohlhaas, A. Kleinhammes, Y. Jia, Y. Wu, S. T. Nguyen, and R. S. Ruoff, "Synthesis of graphene-based nanosheets via chemical reduction of exfoliated graphite oxide," Carbon **45**, 1558–1565 (2007).
80. M. Naguib, J. Halim, J. Lu, K. M. Cook, L. Hultman, Y. Gogotsi, and M. W. Barsoum, "New Two-Dimensional Niobium and Vanadium Carbides as Promising Materials for Li-Ion Batteries," J. Am. Chem. Soc. **135**, 15966–15969 (2013).

81. S. Gao, Y. Lin, X. Jiao, Y. Sun, Q. Luo, W. Zhang, D. Li, J. Yang, and Y. Xie, "Partially oxidized atomic cobalt layers for carbon dioxide electroreduction to liquid fuel," Nature **529**, 68–71 (2016).
82. X. Chen, Y. Zhou, Q. Liu, Z. Li, J. Liu, and Z. Zou, "Ultrathin, Single-Crystal WO_3 Nanosheets by Two-Dimensional Oriented Attachment toward Enhanced Photocatalystic Reduction of CO_2 into Hydrocarbon Fuels under Visible Light," ACS Appl. Mater. Interfaces **4**, 3372–3377 (2012).
83. Z. Wu, Y. Li, J. Liu, Z. Lu, H. Zhang, and B. Yang, "Colloidal Self-Assembly of Catalytic Copper Nanoclusters into Ultrathin Ribbons," Angew. Chem. **126**, 12392–12396 (2014).
84. Y. Liu, J. Goebl, and Y. Yin, "Templated synthesis of nanostructured materials," Chem Soc Rev **42**, 2610–2653 (2013).
85. J. S. DuChene, W. Niu, J. M. Abendroth, Q. Sun, W. Zhao, F. Huo, and W. D. Wei, "Halide Anions as Shape-Directing Agents for Obtaining High-Quality Anisotropic Gold Nanostructures," Chem. Mater. **25**, 1392–1399 (2013).
86. X.-J. Wu, J. Chen, C. Tan, Y. Zhu, Y. Han, and H. Zhang, "Controlled growth of high-density CdS and CdSe nanorod arrays on selective facets of two-dimensional semiconductor nanoplates," Nat. Chem. **8**, 470–475 (2016).
87. H. Li, J. Wu, Z. Yin, and H. Zhang, "Preparation and Applications of Mechanically Exfoliated Single-Layer and Multilayer MoS_2 and WSe_2 Nanosheets," Acc. Chem. Res. **47**, 1067–1075 (2014).
88. J. Liu, Y. Xue, Z. Wang, Z.-Q. Xu, C. Zheng, B. Weber, J. Song, Y. Wang, Y. Lu, Y. Zhang, and Q. Bao, "Two-Dimensional $CH_3 NH_3 PbI_3$ Perovskite: Synthesis and Optoelectronic Application," ACS Nano **10**, 3536–3542 (2016).
89. X.-Q. Zhang, C.-H. Lin, Y.-W. Tseng, K.-H. Huang, and Y.-H. Lee, "Synthesis of Lateral Heterostructures of Semiconducting Atomic Layers," Nano Lett. **15**, 410–415 (2015).
90. A. J. Pollard, R. R. Nair, S. N. Sabki, C. R. Staddon, L. M. A. Perdigao, C. H. Hsu, J. M. Garfitt, S. Gangopadhyay, H. F. Gleeson, A. K. Geim, and P. H. Beton, "Formation of Monolayer Graphene by Annealing Sacrificial Nickel Thin Films," J. Phys. Chem. C **113**, 16565–16567 (2009).
91. Y. Shi, C. Hamsen, X. Jia, K. K. Kim, A. Reina, M. Hofmann, A. L. Hsu, K. Zhang, H. Li, Z.-Y. Juang, Mildred. S. Dresselhaus, L.-J. Li, and J. Kong, "Synthesis of Few-Layer Hexagonal Boron Nitride Thin Film by Chemical Vapor Deposition," Nano Lett. **10**, 4134–4139 (2010).
92. B. Liu, L. Chen, G. Liu, A. N. Abbas, M. Fathi, and C. Zhou, "High-Performance Chemical Sensing Using Schottky-Contacted Chemical Vapor Deposition Grown Monolayer MoS_2 Transistors," ACS Nano **8**, 5304–5314 (2014).
93. M. Okada, T. Sawazaki, K. Watanabe, T. Taniguch, H. Hibino, H. Shinohara, and R. Kitaura, "Direct Chemical Vapor Deposition Growth of WS_2 Atomic Layers on Hexagonal Boron Nitride," ACS Nano **8**, 8273–8277 (2014).
94. B. Liu, M. Fathi, L. Chen, A. Abbas, Y. Ma, and C. Zhou, "Chemical Vapor Deposition Growth of Monolayer WSe_2 with Tunable Device Characteristics and Growth Mechanism Study," ACS Nano **9**, 6119–6127 (2015).
95. J. C. Shaw, H. Zhou, Y. Chen, N. O. Weiss, Y. Liu, Y. Huang, and X. Duan, "Chemical vapor deposition growth of monolayer MoSe2 nanosheets," Nano Res. **7**, 511–517 (2014).
96. A. Roy, H. C. P. Movva, B. Satpati, K. Kim, R. Dey, A. Rai, T. Pramanik, S. Guchhait, E. Tutuc, and S. K. Banerjee, "Structural and Electrical Properties of

$MoTe_2$ and $MoSe_2$ Grown by Molecular Beam Epitaxy," ACS Appl. Mater. Interfaces **8**, 7396–7402 (2016).
97. K. Keyshar, Y. Gong, G. Ye, G. Brunetto, W. Zhou, D. P. Cole, K. Hackenberg, Y. He, L. Machado, M. Kabbani, A. H. C. Hart, B. Li, D. S. Galvao, A. George, R. Vajtai, C. S. Tiwary, and P. M. Ajayan, "Chemical Vapor Deposition of Monolayer Rhenium Disulfide (ReS_2)," Adv. Mater. **27**, 4640–4648 (2015).
98. C. Huang, S. Wu, A. M. Sanchez, J. J. P. Peters, R. Beanland, J. S. Ross, P. Rivera, W. Yao, D. H. Cobden, and X. Xu, "Lateral heterojunctions within monolayer MoSe2–WSe2 semiconductors," Nat. Mater. **13**, 1096–1101 (2014).
99. Y. Yu, S. Hu, L. Su, L. Huang, Y. Liu, Z. Jin, A. A. Purezky, D. B. Geohegan, K. W. Kim, Y. Zhang, and L. Cao, "Equally Efficient Interlayer Exciton Relaxation and Improved Absorption in Epitaxial and Nonepitaxial MoS_2 /WS_2 Heterostructures," Nano Lett. **15**, 486–491 (2015).
100. Y. Gong, S. Lei, G. Ye, B. Li, Y. He, K. Keyshar, X. Zhang, Q. Wang, J. Lou, Z. Liu, R. Vajtai, W. Zhou, and P. M. Ajayan, "Two-Step Growth of Two-Dimensional WSe_2 /$MoSe_2$ Heterostructures," Nano Lett. **15**, 6135–6141 (2015).
101. M. Jiang, Z. Cheng, T. Luo, C. Chu, Z. Zhang, Y. Hui, P. K. Chu, X.-F. Yu, J. Wang, W. Zhou, and S. Geng, "BiTiS3 bio-transducer with explosive on-demand generation of NO gas for synergetic cancer therapy," Biosens. Bioelectron. **246**, 115895 (2024).
102. P. Scherrer, "Göttinger Nachrichten Gesell., vol. 2," (1918).
103. M. M. Y. A. Alsaif, S. Balendhran, M. R. Field, K. Latham, W. Wlodarski, J. Z. Ou, and K. Kalantar-zadeh, "Two dimensional α-MoO3 nanoflakes obtained using solvent-assisted grinding and sonication method: Application for H2 gas sensing," Sens. Actuators B Chem. **192**, 196–204 (2014).
104. Rattana, S. Chaiyakun, N. Witit-anun, N. Nuntawong, P. Chindaudom, S. Oaew, C. Kedkeaw, and P. Limsuwan, "Preparation and characterization of graphene oxide nanosheets," Procedia Eng. **32**, 759–764 (2012).
105. X. Sun, Z. Liu, K. Welsher, J. T. Robinson, A. Goodwin, S. Zaric, and H. Dai, "Nano-graphene oxide for cellular imaging and drug delivery," Nano Res. **1**, 203–212 (2008).
106. L. J. Cote, F. Kim, and J. Huang, "Langmuir−Blodgett Assembly of Graphite Oxide Single Layers," J. Am. Chem. Soc. **131**, 1043–1049 (2009).
107. D. Liu, J. Wang, J. Lu, C. Ma, H. Huang, Z. Wang, L. Wu, Q. Liu, S. Jin, P. K. Chu, and X. Yu, "Direct Synthesis of Metal-Doped Phosphorene with Enhanced Electrocatalytic Hydrogen Evolution," Small Methods **3**, 1900083 (2019).
108. K. Maleski, "Solution Processing and Optical Properties of 2D Transition Metal Carbides (MXenes)," Doctor of Philosophy, Drexel University (2019).
109. M. Ghidiu, M. R. Lukatskaya, M.-Q. Zhao, Y. Gogotsi, and M. W. Barsoum, "Conductive two-dimensional titanium carbide 'clay' with high volumetric capacitance," Nature **516**, 78–81 (2014).
110. A. Sarycheva and Y. Gogotsi, "Raman Spectroscopy Analysis of the Structure and Surface Chemistry of $Ti_3C_2T_x$ MXene," Chem. Mater. **32**, 3480–3488 (2020).
111. L. Yu, A. S. R. Bati, T. S. L. Grace, M. Batmunkh, and J. G. Shapter, "Ti3C2Tx (MXene)-Silicon Heterojunction for Efficient Photovoltaic Cells," Adv. Energy Mater. **9**, 1901063 (2019).

112. L. Chen, M. Wakeel, T. U. Haq, C. Chen, and X. Ren, "Insight into UV-induced simultaneous photocatalytic degradation of Ti3C2Tx MXene and reduction of U(VI)," J. Hazard. Mater. **430**, 128377 (2022).
113. J. Li, R. Qin, L. Yan, Z. Chi, Z. Yu, N. Li, M. Hu, H. Chen, and G. Shan, "Plasmonic Light Illumination Creates a Channel To Achieve Fast Degradation of $Ti_3C_2T_x$ Nanosheets," Inorg. Chem. **58**, 7285–7294 (2019).
114. Z. Li, S. Tang, B. Wang, Y. Li, H. Huang, H. Wang, P. Li, C. Li, P. K. Chu, and X.-F. Yu, "Metabolizable Small Gold Nanorods: Size-dependent Cytotoxicity, Cell Uptake and *In Vivo* Biodistribution," ACS Biomater. Sci. Eng. **2**, 789–797 (2016).
115. Y. Chen, X.-L. Gong, and J.-G. Gai, "Progress and Challenges in Transfer of Large-Area Graphene Films," Adv. Sci. **3**, 1500343 (2016).
116. L.-P. Ma, W. Ren, and H.-M. Cheng, "Transfer Methods of Graphene from Metal Substrates: A Review," Small Methods **3**, 1900049 (2019).
117. M. S. Ozório, S. A. Camacho, N. J. A. Cordeiro, J. L. Duarte, and N. Alves, "Solvent Effect on Morphology and Optical Properties of Poly(3-hexylthiophene):TIPS-Pentacene Blends," J. Electron. Mater. **47**, 1353–1361 (2018).
118. C. W. Sele, B. K. C. Kjellander, B. Niesen, M. J. Thornton, J. B. P. H. Van Der Putten, K. Myny, H. J. Wondergem, A. Moser, R. Resel, A. J. J. M. Van Breemen, N. Van Aerle, P. Heremans, J. E. Anthony, and G. H. Gelinck, "Controlled Deposition of Highly Ordered Soluble Acene Thin Films: Effect of Morphology and Crystal Orientation on Transistor Performance," Adv. Mater. **21**, 4926–4931 (2009).
119. Z. Cai, L. Liu, and P. Zhou, "The development of transfer technologies for advanced 2D circuits integration," Inf. Funct. Mater. **1**, 304–322 (2024).
120. X. Li, W. Cai, J. An, S. Kim, J. Nah, D. Yang, R. Piner, A. Velamakanni, I. Jung, E. Tutuc, S. K. Banerjee, L. Colombo, and R. S. Ruoff, "Large-Area Synthesis of High-Quality and Uniform Graphene Films on Copper Foils," Science **324**, 1312–1314 (2009).
121. Y. Wang, Y. Zheng, X. Xu, E. Dubuisson, Q. Bao, J. Lu, and K. P. Loh, "Electrochemical Delamination of CVD-Grown Graphene Film: Toward the Recyclable Use of Copper Catalyst," ACS Nano **5**, 9927–9933 (2011).
122. G. F. Schneider, V. E. Calado, H. Zandbergen, L. M. K. Vandersypen, and C. Dekker, "Wedging Transfer of Nanostructures," Nano Lett. **10**, 1912–1916 (2010).
123. C. T. Cherian, F. Giustiniano, I. Martin-Fernandez, H. Andersen, J. Balakrishnan, and B. Özyilmaz, "'Bubble-Free' Electrochemical Delamination of CVD Graphene Films," Small **11**, 189–194 (2015).
124. X. Wang, L. Tao, Y. Hao, Z. Liu, H. Chou, I. Kholmanov, S. Chen, C. Tan, N. Jayant, Q. Yu, D. Akinwande, and R. S. Ruoff, "Direct Delamination of Graphene for High-Performance Plastic Electronics," Small **10**, 694–698 (2014).
125. A. Gurarslan, Y. Yu, L. Su, Y. Yu, F. Suarez, S. Yao, Y. Zhu, M. Ozturk, Y. Zhang, and L. Cao, "Surface-Energy-Assisted Perfect Transfer of Centimeter-Scale Monolayer and Few-Layer MoS2 Films onto Arbitrary Substrates," ACS Nano **8**, 11522–11528 (2014).
126. Z.-Q. Xu, Y. Zhang, S. Lin, C. Zheng, Y. L. Zhong, X. Xia, Z. Li, P. J. Sophia, M. S. Fuhrer, Y.-B. Cheng, and Q. Bao, "Synthesis and Transfer of Large-Area Monolayer WS2 Crystals: Moving Toward the Recyclable Use of Sapphire Substrates," ACS Nano **9**, 6178–6187 (2015).

127. H. Liu, Q. H. Thi, P. Man, X. Chen, T. Chen, L. W. Wong, S. Jiang, L. Huang, T. Yang, K. H. Leung, T. T. Leung, S. Gao, H. Chen, C.-S. Lee, M. Kan, J. Zhao, Q. Deng, and T. H. Ly, "Controlled Adhesion of Ice—Toward Ultraclean 2D Materials," Adv. Mater. **35**, 2210503 (2023).
128. T. Zhang, K. Fujisawa, T. Granzier-Nakajima, F. Zhang, Z. Lin, E. Kahn, N. Perea-López, A. L. Elías, Y.-T. Yeh, and M. Terrones, "Clean Transfer of 2D Transition Metal Dichalcogenides Using Cellulose Acetate for Atomic Resolution Characterizations," ACS Appl. Nano Mater. **2**, 5320–5328 (2019).
129. H. Liu, J. Zhao, and T. H. Ly, "Clean Transfer of Two-Dimensional Materials: A Comprehensive Review," ACS Nano **18**, 11573–11597 (2024).
130. M. Onodera, M. Ataka, Y. Zhang, R. Moriya, K. Watanabe, T. Taniguchi, H. Toshiyoshi, and T. Machida, "Dry Transfer of van der Waals Junctions of Two-Dimensional Materials onto Patterned Substrates Using Plasticized Poly(vinyl chloride)/Kamaboko-Shaped Polydimethylsiloxane," ACS Appl. Mater. Interfaces **16**, 62481–62488 (2024).
131. B. Jang, C.-H. Kim, S. T. Choi, K.-S. Kim, K.-S. Kim, H.-J. Lee, S. Cho, J.-H. Ahn, and J.-H. Kim, "Damage mitigation in roll-to-roll transfer of CVD-graphene to flexible substrates," 2D Mater. **4**, 024002 (2017).
132. C. Kim, M.-A. Yoon, B. Jang, H.-D. Kim, J.-H. Kim, A. T. Hoang, J.-H. Ahn, H.-J. Jung, H.-J. Lee, and K.-S. Kim, "Damage-free transfer mechanics of 2-dimensional materials: competition between adhesion instability and tensile strain," NPG Asia Mater. **13**, 44 (2021).
133. A. Kaliyaraj Selva Kumar, Y. Zhang, D. Li, and R. G. Compton, "A mini-review: How reliable is the drop casting technique?," Electrochem. Commun. **121**, 106867 (2020).
134. M. Eslamian, "Inorganic and Organic Solution-Processed Thin Film Devices," Nano-Micro Lett. **9**, 3 (2016).
135. J.-M. Park, I.-B. Sohn, C. Kang, C.-S. Kee, I.-W. Hwang, H. Keun Yoo, and J. Wook Lee, "Terahertz modulation using TIPS-pentacene thin films deposited on patterned silicon substrates," Opt. Commun. **359**, 349–352 (2016).
136. Y. Yunus, N. A. Mahadzir, M. N. Mohamed Ansari, T. H. Tg Abd Aziz, A. Mohd Afdzaluddin, H. Anwar, M. Wang, and A. G. Ismail, "Review of the Common Deposition Methods of Thin-Film Pentacene, Its Derivatives, and Their Performance," Polymers **14**, 1112 (2022).
137. H. A. M. Mustafa and D. A. Jameel, "Modeling and the main stages of spin coating process: A review," J. Appl. Sci. Technol. Trends **2**, 119–123 (2021).
138. C. Glynn and C. O'Dwyer, "Solution Processable Metal Oxide Thin Film Deposition and Material Growth for Electronic and Photonic Devices," Adv. Mater. Interfaces **4**, 1600610 (2017).
139. Y. Yin, "Advances and perspectives of spin coating techniques," Appl. Comput. Eng. **7**, 291–301 (2023).
140. R. Nisticò, D. Scalarone, and G. Magnacca, "Sol-gel chemistry, templating and spin-coating deposition: A combined approach to control in a simple way the porosity of inorganic thin films/coatings," Microporous Mesoporous Mater. **248**, 18–29 (2017).
141. Y. A. Olcer, M. Tascon, A. E. Eroglu, and E. Boyacı, "Thin film microextraction: Towards faster and more sensitive microextraction," TrAC Trends Anal. Chem. **113**, 93–101 (2019).

142. S. Hilliard, G. Baldinozzi, D. Friedrich, S. Kressman, H. Strub, V. Artero, and C. Laberty-Robert, "Mesoporous thin film WO3 photoanode for photoelectrochemical water splitting: a sol–gel dip coating approach," Sustain. Energy Fuels **1**, 145–153 (2017).
143. F. Esposito, L. Sansone, C. Taddei, S. Campopiano, M. Giordano, and A. Iadicicco, "Ultrasensitive biosensor based on long period grating coated with polycarbonate-graphene oxide multilayer," Sens. Actuators B Chem. **274**, 517–526 (2018).
144. A. Ojstršek, L. Jug, and O. Plohl, "A Review of Electro Conductive Textiles Utilizing the Dip-Coating Technique: Their Functionality, Durability and Sustainability," Polymers **14**, 4713 (2022).
145. M. N. Rahaman, *Ceramic Processing and Sintering*, 2nd ed. (CRC Press, 2017).
146. P. Mostafalu, M. Akbari, K. A. Alberti, Q. Xu, A. Khademhosseini, and S. R. Sonkusale, "A toolkit of thread-based microfluidics, sensors, and electronics for 3D tissue embedding for medical diagnostics," Microsyst. Nanoeng. **2**, 1–10 (2016).
147. S. Wang, P. Chia, L. Chua, L. Zhao, R. Png, S. Sivaramakrishnan, M. Zhou, R. G. -S. Goh, R. H. Friend, A. T. -S. Wee, and P. K. -H. Ho, "Band-like Transport in Surface-Functionalized Highly Solution-Processable Graphene Nanosheets," Adv. Mater. **20**, 3440–3446 (2008).
148. D. A. Dikin, S. Stankovich, E. J. Zimney, R. D. Piner, G. H. B. Dommett, G. Evmenenko, S. T. Nguyen, and R. S. Ruoff, "Preparation and characterization of graphene oxide paper," Nature **448**, 457–460 (2007).
149. A. Kudelski, "Analytical applications of Raman spectroscopy," Talanta **76**, 1–8 (2008).
150. L. G. Cançado, A. Jorio, E. H. M. Ferreira, F. Stavale, C. A. Achete, R. B. Capaz, M. V. O. Moutinho, A. Lombardo, T. S. Kulmala, and A. C. Ferrari, "Quantifying Defects in Graphene via Raman Spectroscopy at Different Excitation Energies," Nano Lett. **11**, 3190–3196 (2011).
151. D. López-Díaz, M. López Holgado, J. L. García-Fierro, and M. M. Velázquez, "Evolution of the Raman Spectrum with the Chemical Composition of Graphene Oxide," J. Phys. Chem. C **121**, 20489–20497 (2017).
152. J. Wang, W. Wu, Q. Yang, W.-H. Wang, and M. Bao, "Improving the stability of subnano-MoO_3 /meso-SiO_2 catalyst through amino-functionalization," Funct. Mater. Lett. **11**, 1850003 (2018).
153. Y. Wu, Q. Ou, Y. Yin, Y. Li, W. Ma, W. Yu, G. Liu, X. Cui, X. Bao, J. Duan, G. Álvarez-Pérez, Z. Dai, B. Shabbir, N. Medhekar, X. Li, C.-M. Li, P. Alonso-González, and Q. Bao, "Chemical switching of low-loss phonon polaritons in α-MoO3 by hydrogen intercalation," Nat. Commun. **11**, 2646 (2020).
154. L. Hu, Q. Zhao, S. Huang, J. Zheng, X. Guan, R. Patterson, J. Kim, L. Shi, C.-H. Lin, Q. Lei, D. Chu, W. Tao, S. Cheong, R. D. Tilley, A. W. Y. Ho-Baillie, J. M. Luther, J. Yuan, and T. Wu, "Flexible and efficient perovskite quantum dot solar cells via hybrid interfacial architecture," Nat. Commun. **12**, 466 (2021).
155. X. Ling, S. Zhou, J. Yuan, J. Shi, Y. Qian, B. W. Larson, Q. Zhao, C. Qin, F. Li, G. Shi, C. Stewart, J. Hu, X. Zhang, J. M. Luther, S. Duhm, and W. Ma, "14.1% CsPbI3 Perovskite Quantum Dot Solar Cells via Cesium Cation Passivation," Adv. Energy Mater. **9**, 1900721 (2019).

156. M. G. Vander Heiden, L. C. Cantley, and C. B. Thompson, "Understanding the Warburg Effect: The Metabolic Requirements of Cell Proliferation," Science **324**, 1029–1033 (2009).
157. I. Elia and M. C. Haigis, "Metabolites and the tumour microenvironment: from cellular mechanisms to systemic metabolism," Nat. Metab. **3**, 21–32 (2021).
158. T. S. Martins, J. L. Bott-Neto, and O. N. Oliveira, "Label- and Redox Probe-Free Bioelectronic Chip for Monitoring Vitamins C and the 25-Hydroxyvitamin D3 Metabolite," ACS Appl. Nano Mater. **7**, 4938–4945 (2024).
159. D. Hanahan and R. A. Weinberg, "Hallmarks of Cancer: The Next Generation," Cell **144**, 646–674 (2011).
160. M. Tufail, C.-H. Jiang, and N. Li, "Altered metabolism in cancer: insights into energy pathways and therapeutic targets," Mol. Cancer **23**, 203 (2024).
161. M. P. M. Letertre, P. Giraudeau, and P. de Tullio, "Nuclear Magnetic Resonance Spectroscopy in Clinical Metabolomics and Personalized Medicine: Current Challenges and Perspectives," Front. Mol. Biosci. **8**, (2021).
162. S. Madhurantakam, K. Jayanth Babu, J. B. Balaguru Rayappan, and U. M. Krishnan, "Fabrication of mediator-free hybrid nano-interfaced electrochemical biosensor for monitoring cancer cell proliferation," Biosens. Bioelectron. **87**, 832–841 (2017).
163. S. Bose, H. Yao, Q. Huang, R. Whitaker, C. D. Kontos, R. A. Previs, and X. Shen, "Using genetically encoded fluorescent biosensors to interrogate ovarian cancer metabolism," J. Ovarian Res. **15**, 114 (2022).
164. S. Burgstaller, H. Bischof, L. Matt, and R. Lukowski, "Assessing K+ ions and K+ channel functions in cancer cell metabolism using fluorescent biosensors," Free Radic. Biol. Med. **181**, 43–51 (2022).
165. H. S. Skulason, P. E. Gaskell, and T. Szkopek, "Optical reflection and transmission properties of exfoliated graphite from a graphene monolayer to several hundred graphene layers," Nanotechnology **21**, 295709 (2010).
166. K. P. Loh, Q. Bao, G. Eda, and M. Chhowalla, "Graphene oxide as a chemically tunable platform for optical applications," Nat. Chem. **2**, 1015–1024 (2010).
167. L. Deng, Q. Li, S. Al-Rehili, H. Omar, A. Almalik, A. Alshamsan, J. Zhang, and N. M. Khashab, "Hybrid Iron Oxide–Graphene Oxide–Polysaccharides Microcapsule: A Micro-Matryoshka for On-Demand Drug Release and Antitumor Therapy In Vivo," ACS Appl. Mater. Interfaces **8**, 6859–6868 (2016).
168. F. Nasrollahi, J. Varshosaz, A. A. Khodadadi, S. Lim, and A. Jahanian-Najafabadi, "Targeted Delivery of Docetaxel by Use of Transferrin/Poly(allylamine hydrochloride)-functionalized Graphene Oxide Nanocarrier," ACS Appl. Mater. Interfaces **8**, 13282–13293 (2016).
169. L. Yang, Y.-T. Tseng, G. Suo, L. Chen, J. Yu, W.-J. Chiu, C.-C. Huang, and C.-H. Lin, "Photothermal Therapeutic Response of Cancer Cells to Aptamer–Gold Nanoparticle-Hybridized Graphene Oxide under NIR Illumination," ACS Appl. Mater. Interfaces **7**, 5097–5106 (2015).
170. Q. Li, J. Wen, C. Liu, Y. Jia, Y. Wu, Y. Shan, Z. Qian, and J. Liao, "Graphene-Nanoparticle-Based Self-Healing Hydrogel in Preventing Postoperative Recurrence of Breast Cancer," ACS Biomater. Sci. Eng. **5**, 768–779 (2019).

171. Y. Song, K. Qu, C. Zhao, J. Ren, and X. Qu, "Graphene Oxide: Intrinsic Peroxidase Catalytic Activity and Its Application to Glucose Detection," Adv. Mater. **22**, 2206–2210 (2010).
172. Y. Tao, Y. Lin, Z. Huang, J. Ren, and X. Qu, "Incorporating Graphene Oxide and Gold Nanoclusters: A Synergistic Catalyst with Surprisingly High Peroxidase-Like Activity Over a Broad pH Range and its Application for Cancer Cell Detection," Adv. Mater. **25**, 2594–2599 (2013).
173. R.-C. Huang, W.-J. Chiu, Y.-J. Li, and C.-C. Huang, "Detection of microRNA in Tumor Cells using Exonuclease III and Graphene Oxide-Regulated Signal Amplification," ACS Appl. Mater. Interfaces **6**, 21780–21787 (2014).
174. H. J. Patrick, A. D. Kersey, and F. Bucholtz, "Analysis of the response of long period fiber gratings to external index of refraction," J. Light. Technol. **16**, 1606–1612 (1998).
175. Y. Wang, C. Shen, W. Lou, and F. Shentu, "Polarization-dependent humidity sensor based on an in-fiber Mach-Zehnder interferometer coated with graphene oxide," Sens. Actuators B Chem. **234**, 503–509 (2016).
176. B. Xia, B. Liu, N. Wang, C. Liao, G. Long, C. Zhao, Z. Liao, and D. Lyu, "Polyelectrolyte/Graphene Oxide Nano-Film Integrated Fiber-Optic Sensors for High-Sensitive and Rapid-Response Humidity Measurement," ACS Appl. Mater. Interfaces **14**, 41379–41388 (2022).
177. B. Xu, J. Huang, X. Xu, A. Zhou, and L. Ding, "Ultrasensitive NO Gas Sensor Based on the Graphene Oxide-Coated Long-Period Fiber Grating," ACS Appl. Mater. Interfaces **11**, 40868–40874 (2019).
178. T. Tene, M. Guevara, F. Benalcázar Palacios, T. P. Morocho Barrionuevo, C. Vacacela Gomez, and S. Bellucci, "Optical properties of graphene oxide," Front. Chem. **11**, 1214072 (2023).
179. A. Cusano, A. Iadicicco, P. Pilla, L. Contessa, S. Campopiano, A. Cutolo, and M. Giordano, "Mode transition in high refractive index coated long period gratings," Opt. Express **14**, 19 (2006).
180. L. Coelho, D. Viegas, J. L. Santos, and J. M. M. M. De Almeida, "Characterization of zinc oxide coated optical fiber long period gratings with improved refractive index sensing properties," Sens. Actuators B Chem. **223**, 45–51 (2016).
181. I. Del Villar, I. R. Matias, F. J. Arregui, and M. Achaerandio, "Nanodeposition of materials with complex refractive index in long-period fiber gratings," J. Light. Technol. **23**, 4192–4199 (2005).
182. A. V. Hine, X. Chen, M. D. Hughes, K. Zhou, E. Davies, K. Sugden, I. Bennion, and L. Zhang, "Optical fibre-based detection of DNA hybridization," Biochem. Soc. Trans. **37**, 445–449 (2009).
183. F. Chiavaioli, C. Gouveia, P. Jorge, and F. Baldini, "Towards a Uniform Metrological Assessment of Grating-Based Optical Fiber Sensors: From Refractometers to Biosensors," Biosensors **7**, 23 (2017).
184. M. J. Sarnak, H. Tighiouart, G. Manjunath, B. MacLeod, J. Griffith, D. Salem, and A. S. Levey, "Anemia as a risk factor for cardiovascular disease in the atherosclerosis risk in communities (aric) study," J. Am. Coll. Cardiol. **40**, 27–33 (2002).
185. U. Schäfer, O. Micke, S. B. Müller, P. Schüller, and N. Willich, "Hemoglobin as an Independent Prognostic Factorin the Radiotherapy of Head and Neck Tumors," Strahlenther. Onkol. **179**, 527–534 (2003).

186. R. D. Whitehead, Z. Mei, C. Mapango, and M. E. D. Jefferds, "Methods and analyzers for hemoglobin measurement in clinical laboratories and field settings," Ann. N. Y. Acad. Sci. **1450**, 147–171 (2019).
187. X. C. Chen Liu, "EDC-Mediated Oligonucleotide Immobilization on a Long Period Grating Optical Biosensor," J. Biosens. Bioelectron. **06**, (2015).
188. M. Han, F. Guo, and Y. Lu, "Optical fiber refractometer based on cladding-mode Bragg grating," Opt. Lett. **35**, 399 (2010).
189. M.-Y. Fu, "Refractive Index Sensing Based on the Reflectivity of the Backward Cladding-Core Mode Coupling in a Concatenated Fiber Bragg Grating and a Long Period Grating," IEEE Sens. J. **12**, 1415–1420 (2012).
190. J. Sun, L. Poveda-Wong, H. Jiang, J. Cascante-Vindas, J. L. Cruz, M. V. Andrés, and X. Chen, "Hybrid optical fibre grating for label-free biodetection," in *Specialty Optical Fibres VIII*, C.-A. Bunge, K. Kalli, and P. Peterka, eds. (SPIE, 2024), p. 20.
191. D. Sáez-Rodriguez, J. L. Cruz, A. Díez, and M. V. Andrés, "Coupling between counterpropagating cladding modes in fiber Bragg gratings," Opt. Lett. **36**, 1518 (2011).
192. L. Poveda-Wong, J. L. Cruz, M. Delgado-Pinar, X. Roselló-Mechó, A. Díez, and M. V. Andrés, "Fabrication of long period fiber gratings of subnanometric bandwidth," Opt. Lett. **42**, 1265 (2017).
193. Y. Ma, X. Qiao, T. Guo, R. Wang, J. Zhang, Y. Weng, Q. Rong, M. Hu, and Z. Feng, "Reflective fiber-optic refractometer based on a thin-core fiber tailored Bragg grating reflection," Opt. Lett. **37**, 323 (2012).
194. X. Zhang, W. Peng, Y. Liu, and L. Pan, "Core–cladding mode recoupling based fiber optic refractive index sensor," Opt. Commun. **294**, 188–191 (2013).
195. Q. Wu, Y. Semenova, B. Yan, Y. Ma, P. Wang, C. Yu, and G. Farrell, "Fiber refractometer based on a fiber Bragg grating and single-mode–multimode–single-mode fiber structure," Opt. Lett. **36**, 2197 (2011).
196. J. Bienvenu, G. Monneret, N. Fabien, and J. P. Revillard, "The Clinical Usefulness of the Measurement of Cytokines," cclm **38**, 267–285 (2000).
197. C. Liu, D. Chu, K. Kalantar-Zadeh, J. George, H. A. Young, and G. Liu, "Cytokines: From Clinical Significance to Quantification," Adv. Sci. **8**, 2004433 (2021).
198. A. D. Pradhan, "C-Reactive Protein, Interleukin 6, and Risk of Developing Type 2 Diabetes Mellitus," JAMA **286**, 327 (2001).
199. P. Mehta, D. F. McAuley, M. Brown, E. Sanchez, R. S. Tattersall, and J. J. Manson, "COVID-19: consider cytokine storm syndromes and immunosuppression," The Lancet **395**, 1033–1034 (2020).
200. J. B. Moore and C. H. June, "Cytokine release syndrome in severe COVID-19," Science **368**, 473–474 (2020).
201. C. A. Hunter and S. A. Jones, "IL-6 as a keystone cytokine in health and disease," Nat. Immunol. **16**, 448–457 (2015).
202. P. M. Ridker, "C-Reactive Protein and Other Markers of Inflammation in the Prediction of Cardiovascular Disease in Women," N. Engl. J. Med. (2000).
203. P. M. Ridker, N. Rifai, M. J. Stampfer, and C. H. Hennekens, "Plasma Concentration of Interleukin-6 and the Risk of Future Myocardial Infarction Among Apparently Healthy Men," Circulation **101**, 1767–1772 (2000).

204. K. Heikkilä, S. Ebrahim, and D. A. Lawlor, "Systematic review of the association between circulating interleukin-6 (IL-6) and cancer," Eur. J. Cancer **44**, 937–945 (2008).
205. C. Phetsouphanh, D. R. Darley, D. B. Wilson, A. Howe, C. M. L. Munier, S. K. Patel, J. A. Juno, L. M. Burrell, S. J. Kent, G. J. Dore, A. D. Kelleher, and G. V. Matthews, "Immunological dysfunction persists for 8 months following initial mild-to-moderate SARS-CoV-2 infection," Nat. Immunol. **23**, 210–216 (2022).
206. R. Batool, M. Soler, F. Colavita, L. Fabeni, G. Matusali, and L. M. Lechuga, "Biomimetic nanoplasmonic sensor for rapid evaluation of neutralizing SARS-CoV-2 monoclonal antibodies as antiviral therapy," Biosens. Bioelectron. **226**, 115137 (2023).
207. A. Shakeri, N. A. Jarad, J. Terryberry, S. Khan, A. Leung, S. Chen, and T. F. Didar, "Antibody Micropatterned Lubricant-Infused Biosensors Enable Sub-Picogram Immunofluorescence Detection of Interleukin 6 in Human Whole Plasma," Small **16**, 2003844 (2020).
208. X. Zhou, M. S. Fragala, J. E. McElhaney, and G. A. Kuchel, "Conceptual and methodological issues relevant to cytokine and inflammatory marker measurements in clinical research:," Curr. Opin. Clin. Nutr. Metab. Care **13**, 541–547 (2010).
209. C. Dai, Y. Liu, and D. Wei, "Two-Dimensional Field-Effect Transistor Sensors: The Road toward Commercialization," Chem. Rev. **122**, 10319–10392 (2022).
210. H. H. Yoon, H. A. Fernandez, F. Nigmatulin, W. Cai, Z. Yang, H. Cui, F. Ahmed, X. Cui, M. G. Uddin, E. D. Minot, H. Lipsanen, K. Kim, P. Hakonen, T. Hasan, and Z. Sun, "Miniaturized spectrometers with a tunable van der Waals junction," Science **378**, 296–299 (2022).
211. M. G. Uddin, S. Das, A. M. Shafi, V. Khayrudinov, F. Ahmed, H. Fernandez, L. Du, H. Lipsanen, and Z. Sun, "Engineering the Dipole Orientation and Symmetry Breaking with Mixed-Dimensional Heterostructures," Adv. Sci. **9**, 2200082 (2022).
212. Z. Hao, Y. Pan, C. Huang, Z. Wang, and X. Zhao, "Sensitive detection of lung cancer biomarkers using an aptameric graphene-based nanosensor with enhanced stability," Biomed. Microdevices **21**, 65 (2019).
213. Z. Hao, Y. Luo, C. Huang, Z. Wang, G. Song, Y. Pan, X. Zhao, and S. Liu, "An Intelligent Graphene-Based Biosensing Device for Cytokine Storm Syndrome Biomarkers Detection in Human Biofluids," Small **17**, 2101508 (2021).
214. D. Kwong Hong Tsang, T. J. Lieberthal, C. Watts, I. E. Dunlop, S. Ramadan, A. E. Del Rio Hernandez, and N. Klein, "Chemically Functionalised Graphene FET Biosensor for the Label-free Sensing of Exosomes," Sci. Rep. **9**, 13946 (2019).
215. R. Hasler, C. Reiner-Rozman, S. Fossati, P. Aspermair, J. Dostalek, S. Lee, M. Ibáñez, J. Bintinger, and W. Knoll, "Field-Effect Transistor with a Plasmonic Fiber Optic Gate Electrode as a Multivariable Biosensor Device," ACS Sens. **7**, 504–512 (2022).
216. B. Ryu, H. Nam, B.-R. Oh, Y. Song, P. Chen, Y. Park, W. Wan, K. Kurabayashi, and X. Liang, "Cyclewise Operation of Printed MoS2 Transistor Biosensors for Rapid Biomolecule Quantification at Femtomolar Levels," ACS Sens. **2**, 274–281 (2017).
217. T. De Silva, M. Fawzy, A. Hasani, H. Ghanbari, A. Abnavi, A. Askar, Y. Ling, M. R. Mohammadzadeh, F. Kabir, R. Ahmadi, M. Rosin, K. L. Kavanagh, and M. M.

Adachi, "Ultrasensitive rapid cytokine sensors based on asymmetric geometry two-dimensional MoS2 diodes," Nat. Commun. **13**, 7593 (2022).
218. Y. Park, B. Ryu, B.-R. Oh, Y. Song, X. Liang, and K. Kurabayashi, "Biotunable Nanoplasmonic Filter on Few-Layer MoS_2 for Rapid and Highly Sensitive Cytokine Optoelectronic Immunosensing," ACS Nano **11**, 5697–5705 (2017).
219. C. De-Eknamkul, X. Zhang, M.-Q. Zhao, W. Huang, R. Liu, A. T. C. Johnson, and E. Cubukcu, "MoS2-enabled dual-mode optoelectronic biosensor using a water soluble variant of μ-opioid receptor for opioid peptide detection," 2D Mater. **7**, 014004 (2019).
220. P. Fathi-Hafshejani, N. Azam, L. Wang, M. A. Kuroda, M. C. Hamilton, S. Hasim, and M. Mahjouri-Samani, "Two-Dimensional-Material-Based Field-Effect Transistor Biosensor for Detecting COVID-19 Virus (SARS-CoV-2)," ACS Nano **15**, 11461–11469 (2021).
221. F. Walters, S. Rozhko, D. Buckley, E. D. Ahmadi, M. Ali, Z. Tehrani, J. Mitchell, G. Burwell, Y. Liu, O. Kazakova, and O. J. Guy, "Real-time detection of hepatitis B surface antigen using a hybrid graphene-gold nanoparticle biosensor," 2D Mater. **7**, 024009 (2020).
222. C. Dou, Z. Wu, W. Chen, H. Yan, D. Li, X.-Q. You, Y.-S. Chen, C. Zhou, S. Chen, P. Zhuang, and J. Liu, "Au-functionalized wrinkle graphene biosensor for ultrasensitive detection of Interleukin-6," Carbon **216**, 118556 (2024).
223. S. Nisar, B. Basha, G. Dastgeer, Z. M. Shahzad, H. Kim, I. Rabani, A. Rasheed, M. S. Al-Buriahi, A. Irfan, J. Eom, and D. Kim, "A Novel Biosensing Approach: Improving SnS2 FET Sensitivity with a Tailored Supporter Molecule and Custom Substrate," Adv. Sci. **10**, 2303654 (2023).
224. G. Dastgeer, S. Nisar, Z. M. Shahzad, A. Rasheed, D. Kim, S. H. A. Jaffery, L. Wang, M. Usman, and J. Eom, "Low-Power Negative-Differential-Resistance Device for Sensing the Selective Protein via Supporter Molecule Engineering," Adv. Sci. **10**, 2204779 (2023).
225. D. Kaiser, N. Meyerbroeker, W. Purschke, S. Sell, C. Neumann, A. Winter, Z. Tang, D. Hüger, C. Maasch, L. Bethge, T. Weimann, G. Ferwerda, M. I. de Jonge, A. Schnieders, A. Vater, and A. Turchanin, "Ultrasensitive Detection of Chemokines in Clinical Samples with Graphene-Based Field-Effect Transistors," Adv. Mater. **36**, 2407487 (2024).
226. S. Nisar, G. Dastgeer, Z. M. Shazad, M. W. Zulfiqar, A. Rasheed, M. Z. Iqbal, K. Hussain, I. Rabani, D. Kim, A. Irfan, and A. R. Chaudhry, "2D Materials in Advanced Electronic Biosensors for Point-of-Care Devices," Adv. Sci. **11**, 2401386 (2024).
227. Z. Deng, Y. Yu, Y. Zhou, J. Zhou, M. Xie, B. Tao, Y. Lai, J. Wen, Z. Fan, X. Liu, D. Zhao, L. Feng, Y. Cheng, C. Huang, W. Yue, and W. Huang, "Ternary Logic Circuit and Neural Network Integration via Small Molecule-Based Antiambipolar Vertical Electrochemical Transistor," Adv. Mater. **36**, 2405115 (2024).
228. Z. Hao, Y. Pan, W. Shao, Q. Lin, and X. Zhao, "Graphene-based fully integrated portable nanosensing system for on-line detection of cytokine biomarkers in saliva," Biosens. Bioelectron. **134**, 16–23 (2019).
229. Y. Ohno, K. Maehashi, and K. Matsumoto, "Label-Free Biosensors Based on Aptamer-Modified Graphene Field-Effect Transistors," J. Am. Chem. Soc. **132**, 18012–18013 (2010).
230. C. Hu, D. Dong, X. Yang, K. Qiao, D. Yang, H. Deng, S. Yuan, J. Khan, Y. Lan, H. Song, and J. Tang, "Synergistic Effect of Hybrid PbS Quantum Dots/2D-WSe2

Toward High Performance and Broadband Phototransistors," Adv. Funct. Mater. **27**, 1603605 (2017).
231. M. J. Swamy, "Thermodynamic analysis of biotin binding to avidin. A high sensitivity titration calorimetric study," Biochem. Mol. Biol. Int. **36**, 219–225 (1995).
232. B. Kuhn and P. A. Kollman, "A Ligand That Is Predicted to Bind Better to Avidin than Biotin: Insights from Computational Fluorine Scanning," J. Am. Chem. Soc. **122**, 3909–3916 (2000).
233. R. Bruno, M. Mon, P. Escamilla, J. Ferrando-Soria, E. Esposito, A. Fuoco, M. Monteleone, J. C. Jansen, R. Elliani, A. Tagarelli, D. Armentano, and E. Pardo, "Bioinspired Metal-Organic Frameworks in Mixed Matrix Membranes for Efficient Static/Dynamic Removal of Mercury from Water," Adv. Funct. Mater. **31**, 2008499 (2021).
234. G. Nabi, M. Ali, S. Khan, and S. Kumar, "The crisis of water shortage and pollution in Pakistan: risk to public health, biodiversity, and ecosystem," Environ. Sci. Pollut. Res. **26**, 10443–10445 (2019).
235. H. Ali, E. Khan, and I. Ilahi, "Environmental Chemistry and Ecotoxicology of Hazardous Heavy Metals: Environmental Persistence, Toxicity, and Bioaccumulation," J. Chem. **2019**, 1–14 (2019).
236. "10 chemicals of public health concern," (n.d.).
237. B. Li, Y. Zhang, D. Ma, Z. Shi, and S. Ma, "Mercury nano-trap for effective and efficient removal of mercury(II) from aqueous solution," Nat. Commun. **5**, 5537 (2014).
238. M. McNutt, "Mercury and Health," Science **341**, 1430–1430 (2013).
239. C. Namasivayam and K. Kadirvelu, "Uptake of mercury (II) from wastewater by activated carbon from an unwanted agricultural solid by-product: coirpith," Carbon **37**, 79–84 (1999).
240. S. Hao, C. Liu, X. Chen, B. Zong, X. Wei, Q. Li, H. Qin, and S. Mao, "Ti3C2Tx MXene sensor for rapid Hg2+ analysis in high salinity environment," J. Hazard. Mater. **418**, 126301 (2021).
241. World Health Organization, *Guidelines for Drinking-Water Quality [Electronic Resource]: Incorporating 1st and 2nd Addenda,Vol.1, Recommendations*, 3rd ed (World Health Organization, 2008).
242. Z. Zhang, "Hg2+ ion-imprinted polymers sorbents based on dithizone–Hg2+ chelation for mercury speciation analysis in environmental and biological samples," (n.d.).
243. B. Campanella, "Determination of thiomersal by flow injection coupled with microwave-assisted photochemical online oxidative decomposition of organic mercury and cold vapor atomic fluorescence spectroscopy," (n.d.).
244. J. Fu, "Current status and challenges of ion imprinting," (n.d.).
245. A. Q. Shah, "Simultaneously determination of methyl and inorganic mercury in fish species by cold vapour generation atomic absorption spectrometry," (n.d.).
246. M. K. Rofouei, "Solid phase extraction of ultra traces mercury (II) using octadecyl silica membrane disks modified by 1,3-bis(2-ethoxyphenyl)triazene (EPT) ligand and determination by cold vapor atomic absorption spectrometry," (n.d.).

247. X. Chen, "Rapid speciation analysis of mercury in seawater and marine fish by cation exchange chromatography hyphenated with inductively coupled plasma mass spectrometry," (n.d.).
248. S. S. De Souza, A. D. Campiglia, and F. Barbosa, "A simple method for methylmercury, inorganic mercury and ethylmercury determination in plasma samples by high performance liquid chromatography–cold-vapor-inductively coupled plasma mass spectrometry," Anal. Chim. Acta **761**, 11–17 (2013).
249. K. Fu, X. Liu, D. Yu, J. Luo, Z. Wang, and J. C. Crittenden, "Highly Efficient and Selective Hg(II) Removal from Water Using Multilayered $Ti_3 C_2 O_x$ MXene via Adsorption Coupled with Catalytic Reduction Mechanism," Environ. Sci. Technol. **54**, 16212–16220 (2020).
250. X. Chen, X. Tong, J. Gao, L. Yang, J. Ren, W. Yang, S. Liu, M. Qi, J. Crittenden, and R. Hao, "Simultaneous Nitrite Resourcing and Mercury Ion Removal Using MXene-Anchored Goethite Heterogeneous Fenton Composite," Environ. Sci. Technol. **56**, 4542–4552 (2022).
251. T. Wei, Y. Han, Y. Li, H.-L. Tsai, and H. Xiao, "Temperature-insensitive miniaturized fiber inline Fabry-Perot interferometer for highly sensitive refractive index measurement," Opt. Express **16**, 5764 (2008).
252. M. Zhang, T. Okazaki, Y. Iizumi, E. Miyako, R. Yuge, S. Bandow, S. Iijima, and M. Yudasaka, "Preparation of small-sized graphene oxide sheets and their biological applications," J. Mater. Chem. B **4**, 121–127 (2016).
253. J. Lee, J. Kim, S. Kim, and D.-H. Min, "Biosensors based on graphene oxide and its biomedical application," Adv. Drug Deliv. Rev. **105**, 275–287 (2016).
254. G. T. Hermanson, "The Reactions of Bioconjugation," in *Bioconjugate Techniques* (Elsevier, 2013), pp. 229–258.
255. K. S. Kim, Y. Zhao, H. Jang, S. Y. Lee, J. M. Kim, K. S. Kim, J.-H. Ahn, P. Kim, J.-Y. Choi, and B. H. Hong, "Large-scale pattern growth of graphene films for stretchable transparent electrodes," Nature **457**, 706–710 (2009).
256. D. Bitounis, H. Ali-Boucetta, B. H. Hong, D. Min, and K. Kostarelos, "Prospects and Challenges of Graphene in Biomedical Applications," Adv. Mater. **25**, 2258–2268 (2013).
257. J. Kim, S.-J. Park, and D.-H. Min, "Emerging Approaches for Graphene Oxide Biosensor," Anal. Chem. **89**, 232–248 (2017).
258. E. Morales-Narváez and A. Merkoçi, "Graphene Oxide as an Optical Biosensing Platform," Adv. Mater. **24**, 3298–3308 (2012).
259. D. Prodan, M. Moldovan, G. Furtos, C. Saroși, M. Filip, I. Perhaița, R. Carpa, M. Popa, S. Cuc, S. Varvara, and D. Popa, "Synthesis and Characterization of Some Graphene Oxide Powders Used as Additives in Hydraulic Mortars," Appl. Sci. **11**, 11330 (2021).
260. P. Liu, Z. Yao, and J. Zhou, "Controllable synthesis and enhanced microwave absorption properties of silane-modified $Ni_{0.4} Zn_{0.4} Co_{0.2} Fe_2 O_4$ nanocomposites covered with reduced graphene oxide," RSC Adv. **5**, 93739–93748 (2015).
261. C. T. P. Da Silva, J. P. Monteiro, E. Radovanovic, and E. M. Girotto, "Unprecedented high plasmonic sensitivity of substrates based on gold nanoparticles," Sens. Actuators B Chem. **191**, 152–157 (2014).
262. C. Théry, K. W. Witwer, E. Aikawa, M. J. Alcaraz, J. D. Anderson, R. Andriantsitohaina, A. Antoniou, T. Arab, F. Archer, G. K. Atkin-Smith, D. C. Ayre, J. Bach, D. Bachurski, H. Baharvand, L. Balaj, S. Baldacchino, N. N. Bauer, A. A.

Baxter, M. Bebawy, C. Beckham, A. Bedina Zavec, A. Benmoussa, A. C. Berardi, P. Bergese, E. Bielska, C. Blenkiron, S. Bobis-Wozowicz, E. Boilard, W. Boireau, A. Bongiovanni, F. E. Borràs, S. Bosch, C. M. Boulanger, X. Breakefield, A. M. Breglio, M. Á. Brennan, D. R. Brigstock, A. Brisson, M. L. Broekman, J. F. Bromberg, P. Bryl-Górecka, S. Buch, A. H. Buck, D. Burger, S. Busatto, D. Buschmann, B. Bussolati, E. I. Buzás, J. B. Byrd, G. Camussi, D. R. Carter, S. Caruso, L. W. Chamley, Y. Chang, C. Chen, S. Chen, L. Cheng, A. R. Chin, A. Clayton, S. P. Clerici, A. Cocks, E. Cocucci, R. J. Coffey, A. Cordeiro-da-Silva, Y. Couch, F. A. Coumans, B. Coyle, R. Crescitelli, M. F. Criado, C. D'Souza-Schorey, S. Das, A. Datta Chaudhuri, P. De Candia, E. F. De Santana, O. De Wever, H. A. Del Portillo, T. Demaret, S. Deville, A. Devitt, B. Dhondt, D. Di Vizio, L. C. Dieterich, V. Dolo, A. P. Dominguez Rubio, M. Dominici, M. R. Dourado, T. A. Driedonks, F. V. Duarte, H. M. Duncan, R. M. Eichenberger, K. Ekström, S. El Andaloussi, C. Elie-Caille, U. Erdbrügger, J. M. Falcón-Pérez, F. Fatima, J. E. Fish, M. Flores-Bellver, A. Försönits, A. Frelet-Barrand, F. Fricke, G. Fuhrmann, S. Gabrielsson, A. Gámez-Valero, C. Gardiner, K. Gärtner, R. Gaudin, Y. S. Gho, B. Giebel, C. Gilbert, M. Gimona, I. Giusti, D. C. Goberdhan, A. Görgens, S. M. Gorski, D. W. Greening, J. C. Gross, A. Gualerzi, G. N. Gupta, D. Gustafson, A. Handberg, R. A. Haraszti, P. Harrison, H. Hegyesi, A. Hendrix, A. F. Hill, F. H. Hochberg, K. F. Hoffmann, B. Holder, H. Holthofer, B. Hosseinkhani, G. Hu, Y. Huang, V. Huber, S. Hunt, A. G. Ibrahim, T. Ikezu, J. M. Inal, M. Isin, A. Ivanova, H. K. Jackson, S. Jacobsen, S. M. Jay, M. Jayachandran, G. Jenster, L. Jiang, S. M. Johnson, J. C. Jones, A. Jong, T. Jovanovic-Talisman, S. Jung, R. Kalluri, S. Kano, S. Kaur, Y. Kawamura, E. T. Keller, D. Khamari, E. Khomyakova, A. Khvorova, P. Kierulf, K. P. Kim, T. Kislinger, M. Klingeborn, D. J. Klinke, M. Kornek, M. M. Kosanović, Á. F. Kovács, E. Krämer-Albers, S. Krasemann, M. Krause, I. V. Kurochkin, G. D. Kusuma, S. Kuypers, S. Laitinen, S. M. Langevin, L. R. Languino, J. Lannigan, C. Lässer, L. C. Laurent, G. Lavieu, E. Lázaro-Ibáñez, S. Le Lay, M. Lee, Y. X. F. Lee, D. S. Lemos, M. Lenassi, A. Leszczynska, I. T. Li, K. Liao, S. F. Libregts, E. Ligeti, R. Lim, S. K. Lim, A. Linē, K. Linnemannstöns, A. Llorente, C. A. Lombard, M. J. Lorenowicz, Á. M. Lörincz, J. Lötvall, J. Lovett, M. C. Lowry, X. Loyer, Q. Lu, B. Lukomska, T. R. Lunavat, S. L. Maas, H. Malhi, A. Marcilla, J. Mariani, J. Mariscal, E. S. Martens-Uzunova, L. Martin-Jaular, M. C. Martinez, V. R. Martins, M. Mathieu, S. Mathivanan, M. Maugeri, L. K. McGinnis, M. J. McVey, D. G. Meckes, K. L. Meehan, I. Mertens, V. R. Minciacchi, A. Möller, M. Møller Jørgensen, A. Morales-Kastresana, J. Morhayim, F. Mullier, M. Muraca, L. Musante, V. Mussack, D. C. Muth, K. H. Myburgh, T. Najrana, M. Nawaz, I. Nazarenko, P. Nejsum, C. Neri, T. Neri, R. Nieuwland, L. Nimrichter, J. P. Nolan, E. N. Nolte-'t Hoen, N. Noren Hooten, L. O'Driscoll, T. O'Grady, A. O'Loghlen, T. Ochiya, M. Olivier, A. Ortiz, L. A. Ortiz, X. Osteikoetxea, O. Østergaard, M. Ostrowski, J. Park, D. M. Pegtel, H. Peinado, F. Perut, M. W. Pfaffl, D. G. Phinney, B. C. Pieters, R. C. Pink, D. S. Pisetsky, E. Pogge Von Strandmann, I. Polakovicova, I. K. Poon, B. H. Powell, I. Prada, L. Pulliam, P. Quesenberry, A. Radeghieri, R. L. Raffai, S. Raimondo, J. Rak, M. I. Ramirez, G. Raposo, M. S. Rayyan, N. Regev-Rudzki, F. L. Ricklefs, P. D. Robbins, D. D. Roberts, S. C. Rodrigues, E. Rohde, S. Rome, K. M. Rouschop, A. Rughetti, A. E. Russell, P. Saá, S. Sahoo, E. Salas-Huenuleo, C. Sánchez, J. A. Saugstad, M. J. Saul, R. M. Schiffelers, R. Schneider, T. H. Schøyen, A. Scott, E. Shahaj, S. Sharma, O. Shatnyeva, F. Shekari, G. V. Shelke, A. K. Shetty, K. Shiba, P. R.

Siljander, A. M. Silva, A. Skowronek, O. L. Snyder, R. P. Soares, B. W. Sódar, C. Soekmadji, J. Sotillo, P. D. Stahl, W. Stoorvogel, S. L. Stott, E. F. Strasser, S. Swift, H. Tahara, M. Tewari, K. Timms, S. Tiwari, R. Tixeira, M. Tkach, W. S. Toh, R. Tomasini, A. C. Torrecilhas, J. P. Tosar, V. Toxavidis, L. Urbanelli, P. Vader, B. W. Van Balkom, S. G. Van Der Grein, J. Van Deun, M. J. Van Herwijnen, K. Van Keuren-Jensen, G. Van Niel, M. E. Van Royen, A. J. Van Wijnen, M. H. Vasconcelos, I. J. Vechetti, T. D. Veit, L. J. Vella, É. Velot, F. J. Verweij, B. Vestad, J. L. Viñas, T. Visnovitz, K. V. Vukman, J. Wahlgren, D. C. Watson, M. H. Wauben, A. Weaver, J. P. Webber, V. Weber, A. M. Wehman, D. J. Weiss, J. A. Welsh, S. Wendt, A. M. Wheelock, Z. Wiener, L. Witte, J. Wolfram, A. Xagorari, P. Xander, J. Xu, X. Yan, M. Yáñez-Mó, H. Yin, Y. Yuana, V. Zappulli, J. Zarubova, V. Žėkas, J. Zhang, Z. Zhao, L. Zheng, A. R. Zheutlin, A. M. Zickler, P. Zimmermann, A. M. Zivkovic, D. Zocco, and E. K. Zuba-Surma, "Minimal information for studies of extracellular vesicles 2018 (MISEV2018): a position statement of the International Society for Extracellular Vesicles and update of the MISEV2014 guidelines," J. Extracell. Vesicles **7**, 1535750 (2018).

263. R. Kalluri, "The biology and function of exosomes in cancer," J. Clin. Invest. **126**, 1208–1215 (2016).
264. C. Kahlert and R. Kalluri, "Exosomes in tumor microenvironment influence cancer progression and metastasis," J. Mol. Med. **91**, 431–437 (2013).
265. G. Van Niel, G. D'Angelo, and G. Raposo, "Shedding light on the cell biology of extracellular vesicles," Nat. Rev. Mol. Cell Biol. **19**, 213–228 (2018).
266. K. M. McAndrews and R. Kalluri, "Mechanisms associated with biogenesis of exosomes in cancer," Mol. Cancer **18**, 52 (2019).
267. D. Yu, Y. Li, M. Wang, J. Gu, W. Xu, H. Cai, X. Fang, and X. Zhang, "Exosomes as a new frontier of cancer liquid biopsy," Mol. Cancer **21**, 56 (2022).
268. S. Lin, Z. Yu, D. Chen, Z. Wang, J. Miao, Q. Li, D. Zhang, J. Song, and D. Cui, "Progress in Microfluidics-Based Exosome Separation and Detection Technologies for Diagnostic Applications," Small **16**, 1903916 (2020).
269. Y.-C. Zhang, Q. Zhou, and Y.-L. Wu, "The emerging roles of NGS-based liquid biopsy in non-small cell lung cancer," J. Hematol. Oncol.J Hematol Oncol **10**, 167 (2017).
270. A. Becker, B. K. Thakur, J. M. Weiss, H. S. Kim, H. Peinado, and D. Lyden, "Extracellular Vesicles in Cancer: Cell-to-Cell Mediators of Metastasis," Cancer Cell **30**, 836–848 (2016).
271. A. Hoshino, B. Costa-Silva, T.-L. Shen, G. Rodrigues, A. Hashimoto, M. Tesic Mark, H. Molina, S. Kohsaka, A. Di Giannatale, S. Ceder, S. Singh, C. Williams, N. Soplop, K. Uryu, L. Pharmer, T. King, L. Bojmar, A. E. Davies, Y. Ararso, T. Zhang, H. Zhang, J. Hernandez, J. M. Weiss, V. D. Dumont-Cole, K. Kramer, L. H. Wexler, A. Narendran, G. K. Schwartz, J. H. Healey, P. Sandstrom, K. Jørgen Labori, E. H. Kure, P. M. Grandgenett, M. A. Hollingsworth, M. De Sousa, S. Kaur, M. Jain, K. Mallya, S. K. Batra, W. R. Jarnagin, M. S. Brady, O. Fodstad, V. Muller, K. Pantel, A. J. Minn, M. J. Bissell, B. A. Garcia, Y. Kang, V. K. Rajasekhar, C. M. Ghajar, I. Matei, H. Peinado, J. Bromberg, and D. Lyden, "Tumour exosome integrins determine organotropic metastasis," Nature **527**, 329–335 (2015).
272. S. Kawamura, H. Iinuma, K. Wada, K. Takahashi, S. Minezaki, M. Kainuma, M. Shibuya, F. Miura, and K. Sano, "Exosome-encapsulated microRNA-4525, microRNA-451a and microRNA-21 in portal vein blood is a high-sensitive liquid

biomarker for the selection of high-risk pancreatic ductal adenocarcinoma patients," J. Hepato-Biliary-Pancreat. Sci. **26**, 63–72 (2019).
273. M. Nimir, Y. Ma, S. A. Jeffreys, T. Opperman, F. Young, T. Khan, P. Ding, W. Chua, B. Balakrishnar, A. Cooper, P. De Souza, and T. M. Becker, "Detection of AR-V7 in Liquid Biopsies of Castrate Resistant Prostate Cancer Patients: A Comparison of AR-V7 Analysis in Circulating Tumor Cells, Circulating Tumor RNA and Exosomes," Cells **8**, 688 (2019).
274. X. Cai, F. Janku, Q. Zhan, and J.-B. Fan, "Accessing Genetic Information with Liquid Biopsies," Trends Genet. **31**, 564–575 (2015).
275. R. Kalluri and V. S. LeBleu, "The biology, function, and biomedical applications of exosomes," Science **367**, eaau6977 (2020).
276. S. A. Melo, L. B. Luecke, C. Kahlert, A. F. Fernandez, S. T. Gammon, J. Kaye, V. S. LeBleu, E. A. Mittendorf, J. Weitz, N. Rahbari, C. Reissfelder, C. Pilarsky, M. F. Fraga, D. Piwnica-Worms, and R. Kalluri, "Glypican-1 identifies cancer exosomes and detects early pancreatic cancer," Nature **523**, 177–182 (2015).
277. J. Hu, Y. Sheng, K. J. Kwak, J. Shi, B. Yu, and L. J. Lee, "A signal-amplifiable biochip quantifies extracellular vesicle-associated RNAs for early cancer detection," Nat. Commun. **8**, 1683 (2017).
278. K. S. Yang, H. Im, S. Hong, I. Pergolini, A. F. Del Castillo, R. Wang, S. Clardy, C.-H. Huang, C. Pille, S. Ferrone, R. Yang, C. M. Castro, H. Lee, C. F. Del Castillo, and R. Weissleder, "Multiparametric plasma EV profiling facilitates diagnosis of pancreatic malignancy," Sci. Transl. Med. **9**, eaal3226 (2017).
279. Z. Yu, Y. Yang, W. Fang, P. Hu, Y. Liu, and J. Shi, "Dual Tumor Exosome Biomarker Co-recognitions Based Nanoliquid Biopsy for the Accurate Early Diagnosis of Pancreatic Cancer," ACS Nano **17**, 11384–11395 (2023).
280. K. S. Novoselov, D. Jiang, F. Schedin, T. J. Booth, V. V. Khotkevich, S. V. Morozov, and A. K. Geim, "Two-dimensional atomic crystals," Proc. Natl. Acad. Sci. **102**, 10451–10453 (2005).
281. A. K. Geim and I. V. Grigorieva, "Van der Waals heterostructures," Nature **499**, 419–425 (2013).
282. K. S. Novoselov, A. Mishchenko, A. Carvalho, and A. H. C. Neto, "2D materials and van der Waals heterostructures," (n.d.).
283. Z. Sun, A. Martinez, and F. Wang, "Optical modulators with 2D layered materials," Nat. Photonics **10**, 227–238 (2016).
284. Mohd. F. Ullah and M. Aatif, "The footprints of cancer development: Cancer biomarkers," Cancer Treat. Rev. **35**, 193–200 (2009).
285. H. Sung, J. Ferlay, R. L. Siegel, M. Laversanne, I. Soerjomataram, A. Jemal, and F. Bray, "Global Cancer Statistics 2020: GLOBOCAN Estimates of Incidence and Mortality Worldwide for 36 Cancers in 185 Countries," CA. Cancer J. Clin. **71**, 209–249 (2021).
286. P. Yingchoncharoen, D. S. Kalinowski, and D. R. Richardson, "Lipid-Based Drug Delivery Systems in Cancer Therapy: What Is Available and What Is Yet to Come," Pharmacol. Rev. **68**, 701–787 (2016).
287. J. Wu, Z. Fu, F. Yan, and H. Ju, "Biomedical and clinical applications of immunoassays and immunosensors for tumor markers," TrAC Trends Anal. Chem. **26**, 679–688 (2007).
288. M. Hasanzadeh, N. Shadjou, and M. de la Guardia, "Early stage screening of breast cancer using electrochemical biomarker detection," TrAC Trends Anal. Chem. **91**, 67–76 (2017).

289. J. Chen, M. Gong, Y. Fan, J. Feng, L. Han, H. L. Xin, M. Cao, Q. Zhang, D. Zhang, D. Lei, and Y. Yin, "Collective Plasmon Coupling in Gold Nanoparticle Clusters for Highly Efficient Photothermal Therapy," ACS Nano **16**, 910–920 (2022).
290. A. B. Sarmento-Ribeiro, A. Scorilas, A. C. Gonçalves, T. Efferth, and I. P. Trougakos, "The emergence of drug resistance to targeted cancer therapies: Clinical evidence," Drug Resist. Updat. **47**, 100646 (2019).
291. H. Xiang, L. Zhao, L. Yu, H. Chen, C. Wei, Y. Chen, and Y. Zhao, "Self-assembled organic nanomedicine enables ultrastable photo-to-heat converting theranostics in the second near-infrared biowindow," Nat. Commun. **12**, 218 (2021).
292. H. Shi and P. J. Sadler, "How promising is phototherapy for cancer?," Br. J. Cancer **123**, 871–873 (2020).
293. J. Shao, H. Xie, H. Huang, Z. Li, Z. Sun, Y. Xu, Q. Xiao, X.-F. Yu, Y. Zhao, H. Zhang, H. Wang, and P. K. Chu, "Biodegradable black phosphorus-based nanospheres for in vivo photothermal cancer therapy," Nat. Commun. **7**, 12967 (2016).
294. H. Xie, Z. Li, Z. Sun, J. Shao, X.-F. Yu, Z. Guo, J. Wang, Q. Xiao, H. Wang, Q.-Q. Wang, H. Zhang, and P. K. Chu, "Metabolizable Ultrathin Bi2Se3 Nanosheets in Imaging-Guided Photothermal Therapy," Small **12**, 4136–4145 (2016).
295. X. Yu, X. Cai, H. Cui, S.-W. Lee, X.-F. Yu, and B. Liu, "Fluorine-free preparation of titanium carbide MXene quantum dots with high near-infrared photothermal performances for cancer therapy," Nanoscale **9**, 17859–17864 (2017).
296. Q. Chen, Q. Hu, E. Dukhovlinova, G. Chen, S. Ahn, C. Wang, E. A. Ogunnaike, F. S. Ligler, G. Dotti, and Z. Gu, "Photothermal Therapy Promotes Tumor Infiltration and Antitumor Activity of CAR T Cells," Adv. Mater. **31**, 1900192 (2019).
297. G. Gao, X. Sun, and G. Liang, "Nanoagent-Promoted Mild-Temperature Photothermal Therapy for Cancer Treatment," Adv. Funct. Mater. **31**, 2100738 (2021).
298. H. Zhou, X. Zeng, A. Li, W. Zhou, L. Tang, W. Hu, Q. Fan, X. Meng, H. Deng, L. Duan, Y. Li, Z. Deng, X. Hong, and Y. Xiao, "Upconversion NIR-II fluorophores for mitochondria-targeted cancer imaging and photothermal therapy," Nat. Commun. **11**, 6183 (2020).
299. H. Wu, P. Chen, X. Zhan, K. Lin, T. Hu, A. Xiao, J. Liang, Y. Huang, Y. Huang, and B. Guan, "Marriage of a Dual-Plasmonic Interface and Optical Microfiber for NIR-II Cancer Theranostics," Adv. Mater. **36**, 2310571 (2024).
300. B. Lü, Y. Chen, P. Li, B. Wang, K. Müllen, and M. Yin, "Stable radical anions generated from a porous perylenediimide metal-organic framework for boosting near-infrared photothermal conversion," Nat. Commun. **10**, 767 (2019).
301. J. Zhang, C. Yang, R. Zhang, R. Chen, Z. Zhang, W. Zhang, S.-H. Peng, X. Chen, G. Liu, C.-S. Hsu, and C.-S. Lee, "Biocompatible D–A Semiconducting Polymer Nanoparticle with Light-Harvesting Unit for Highly Effective Photoacoustic Imaging Guided Photothermal Therapy," Adv. Funct. Mater. **27**, 1605094 (2017).

302. S. Zhu, L. Gong, J. Xie, Z. Gu, and Y. Zhao, "Design, Synthesis, and Surface Modification of Materials Based on Transition-Metal Dichalcogenides for Biomedical Applications," Small Methods **1**, 1700220 (2017).
303. K. Yang, S. Zhang, G. Zhang, X. Sun, S.-T. Lee, and Z. Liu, "Graphene in Mice: Ultrahigh In Vivo Tumor Uptake and Efficient Photothermal Therapy," Nano Lett. **10**, 3318–3323 (2010).
304. T. Liu, C. Wang, X. Gu, H. Gong, L. Cheng, X. Shi, L. Feng, B. Sun, and Z. Liu, "Drug delivery with PEGylated MoS2 nano-sheets for combined photothermal and chemotherapy of cancer," Adv. Mater. Deerfield Beach Fla **26**, 3433–3440 (2014).
305. Z. Sun, H. Xie, S. Tang, X.-F. Yu, Z. Guo, J. Shao, H. Zhang, H. Huang, H. Wang, and P. K. Chu, "Ultrasmall Black Phosphorus Quantum Dots: Synthesis and Use as Photothermal Agents," Angew. Chem. Int. Ed. **54**, 11526–11530 (2015).
306. W. Tao, X. Zhu, X. Yu, X. Zeng, Q. Xiao, X. Zhang, X. Ji, X. Wang, J. Shi, H. Zhang, and L. Mei, "Black Phosphorus Nanosheets as a Robust Delivery Platform for Cancer Theranostics," Adv. Mater. Deerfield Beach Fla **29**, 10.1002/adma.201603276 (2017).
307. Y. Yang, W. Zhu, Z. Dong, Y. Chao, L. Xu, M. Chen, and Z. Liu, "1D Coordination Polymer Nanofibers for Low-Temperature Photothermal Therapy," Adv. Mater. **29**, 1703588 (2017).
308. H. Luo, Q. Wang, Y. Deng, T. Yang, H. Ke, H. Yang, H. He, Z. Guo, D. Yu, H. Wu, and H. Chen, "Mutually Synergistic Nanoparticles for Effective Thermo-Molecularly Targeted Therapy," Adv. Funct. Mater. **27**, 1702834 (2017).
309. H. Bian, D. Ma, X. Zhang, K. Xin, Y. Yang, X. Peng, and Y. Xiao, "Tailored Engineering of Novel Xanthonium Polymethine Dyes for Synergetic PDT and PTT Triggered by 1064 nm Laser toward Deep-Seated Tumors," Small **17**, 2100398 (2021).
310. Y. Dai, H. Zhao, K. He, W. Du, Y. Kong, Z. Wang, M. Li, Q. Shen, P. Sun, and Q. Fan, "NIR-II Excitation Phototheranostic Nanomedicine for Fluorescence/Photoacoustic Tumor Imaging and Targeted Photothermal-Photonic Thermodynamic Therapy," Small **17**, 2102527 (2021).
311. M. Zhang, W. Wang, M. Mohammadniaei, T. Zheng, Q. Zhang, J. Ashley, S. Liu, Y. Sun, and B. Z. Tang, "Upregulating Aggregation-Induced-Emission Nanoparticles with Blood–Tumor-Barrier Permeability for Precise Photothermal Eradication of Brain Tumors and Induction of Local Immune Responses," Adv. Mater. **33**, 2008802 (2021).
312. X. Meng, B. Zhang, Y. Yi, H. Cheng, B. Wang, Y. Liu, T. Gong, W. Yang, Y. Yao, H. Wang, and W. Bu, "Accurate and Real-Time Temperature Monitoring during MR Imaging Guided PTT," Nano Lett. **20**, 2522–2529 (2020).
313. F. Yang, Q. Yang, L. Yang, J. Li, Y. Zhang, H. Lu, H. Dong, and X. Zhang, "Endogenous MicroRNA Accurate Diagnostics to Guide Photothermal Therapy," Anal. Chem. **94**, 6599–6606 (2022).
314. X. Zhu, W. Feng, J. Chang, Y.-W. Tan, J. Li, M. Chen, Y. Sun, and F. Li, "Temperature-feedback upconversion nanocomposite for accurate photothermal therapy at facile temperature," Nat. Commun. **7**, 10437 (2016).
315. Y. Liu, P. Bhattarai, Z. Dai, and X. Chen, "Photothermal therapy and photoacoustic imaging via nanotheranostics in fighting cancer," Chem. Soc. Rev. **48**, 2053–2108 (2019).

316. X. Li, J. F. Lovell, J. Yoon, and X. Chen, "Clinical development and potential of photothermal and photodynamic therapies for cancer," Nat. Rev. Clin. Oncol. **17**, 657–674 (2020).
317. F. Peng, M. I. Setyawati, J. K. Tee, X. Ding, J. Wang, M. E. Nga, H. K. Ho, and D. T. Leong, "Nanoparticles promote in vivo breast cancer cell intravasation and extravasation by inducing endothelial leakiness," Nat. Nanotechnol. **14**, 279–286 (2019).
318. A. Xiao, J. Zheng, X. Wu, W. Cui, P. Chen, J. Liang, J. Zhong, Y. Huang, Y. Huang, and B.-O. Guan, "Ultrasensitive Detection and Cellular Photothermal Therapy via a Self-Photothermal Modulation Biosensor," Adv. Opt. Mater. **11**, 2202711 (2023).
319. Z. Yan, C. Mou, K. Zhou, X. Chen, and L. Zhang, "UV-Inscription, Polarization-Dependant Loss Characteristics and Applications of 45° Tilted Fiber Gratings," J. Light. Technol. **29**, 2715–2724 (2011).
320. L. Wang, P. Hu, Y. Long, Z. Liu, and X. He, "Recent advances in ternary two-dimensional materials: synthesis, properties and applications," J. Mater. Chem. A **5**, 22855–22876 (2017).

Publication list

Journal publications

[1] **J. Sun**, L. Zhou, Z. Li, G. He, H. Mao, J. Zhao, J. A. Hunt, X. Chen, “Perovskite-graphene heterostructure biosensor integrated with biotunable ternary logic gate for ultrasensitive cytokine detection,” *Advanced Science* **2025**, *e03124*, DOI: 10.1002/advs.202503124.

[2] **J. Sun**, H. Jiang, A. Coutts, J. A. Hunt, X. Chen, “Graphene-based optical biosensor for detection of breast cancer cells”, *ACS Applied Nano Materials* (Accepted for publication).

[3] J. Zheng, D. Li, X. Cui, P. Liu, Q. Zhang, Z. Zhu, S. Yang, Y. Zhang, **J. Sun**, X. Chen, H. Yang, Z. Sun. “Temporal soliton dynamics of synchronised ultrafast fibre lasers”, *Optics Express* **2023**, *31 (20)*, 32373-32382. DOI: 10.1364/OE.492450.

[4] **J. Sun**, H. Jiang, C.C Perry, X. Chen, “MXene based fibre-optic Fabry-Perot interferometer chemical sensor for heavy metal detection”, *Journal of Hazardous Materials* (Submitted).

[5] **J. Sun**, L. Wong, J. Vindas, J.L. Cruz, M.V. Andrés, X. Chen, “Hybrid long-period and short-period gratings for biosensing”, under construction.

[6] **J. Sun**, H. Jiang, A. Coutts, C.C Perry, X. Chen, "α-MoO3/GO heterostructure functionalised in-fibre Mach-Zehnder interferometer for single exosome detection", under construction.

[7] H. Jiang, **J. Sun**, C.C Perry, X. Chen, "GO-functionalised fibre optic probes for bioimaging", *ACS Biomaterials Science & Engineering* (Submitted).

Conference publications

[8] **J. Sun**, H. Jiang, A. Coutts, W. Zhu, J. Hunt, X. Chen, "Graphene integrated optical biosensor for detection of breast cancer cell media", *Proc. SPIE 12835, Optical Fibers and Sensors for Medical Diagnostics, Treatment, and Environmental Applications XXIV* **2025**, 1283502. DOI: 10.1117/12.3000582.

[9] **J. Sun**, L. Wong, H. Jiang, J. Vindas, J.L. Cruz, M.V. Andrés, X. Chen, "Hybrid optical fibre grating for label-free biodetection", *Proc. SPIE 13001, SPIE Specialty Fibres VIII* **2024**, 13001B. DOI: 10.1117/12.3016659.

[10] **J. Sun**, H. Jiang, M. Buchanan, R. Wain, X. Chen, "MXene based fibre optic Fabry-Perot interferometer for heavy metal detection", *Proc. SPIE 13083, SPIE Future Sensing Technologies* **2024**, 1308312. DOI: 10.1117/12.3023050.

[11] **J. Sun**, L. Zhou, H. Mao, X. Chen, "An integrated nano-plasmonic graphene-quantum dots photoelectronic biosensor", *Opto-Electronics and Communications Conference (OECC)* **2023**, 1-3. DOI: 10.1109/OECC56963.2023.10209966.

[12] H. Jiang, **J. Sun**, M. Mahmoodi, C.C Perry, X. Chen, "Nano-fibre optic probe for label-free bioimaging detection", *Proc. SPIE 13331, Label-free Biomedical Imaging and Sensing (LBIS)* **2025**, 133310A. DOI: 10.1117/12.3041678.

[13] L. Wong, **J. Sun**, J. Vindas, X. Chen, J.L. Cruz, M.V. Andrés, "High-order mode coupling by cascaded long- and short-period gratings for enhanced physical magnitude sensing", *RIAO OPTILAS 2023 Congress (Latin-American Meeting on Optics, Lasers, and Applications)*, Costa Rica, Mar. 2023.